# Southern Ocean Circulation from Hydrographic Data: A Finite Difference Inverse Model.

by

Jeremy L. Harris, BSc, Grad Dip ASOS (Hons.)

Submitted in fulfilment of the requirements

for the degree of

Doctor of Philosophy

Institute of Antarctic and Southern Ocean Studies

University of Tasmania

August, 1996

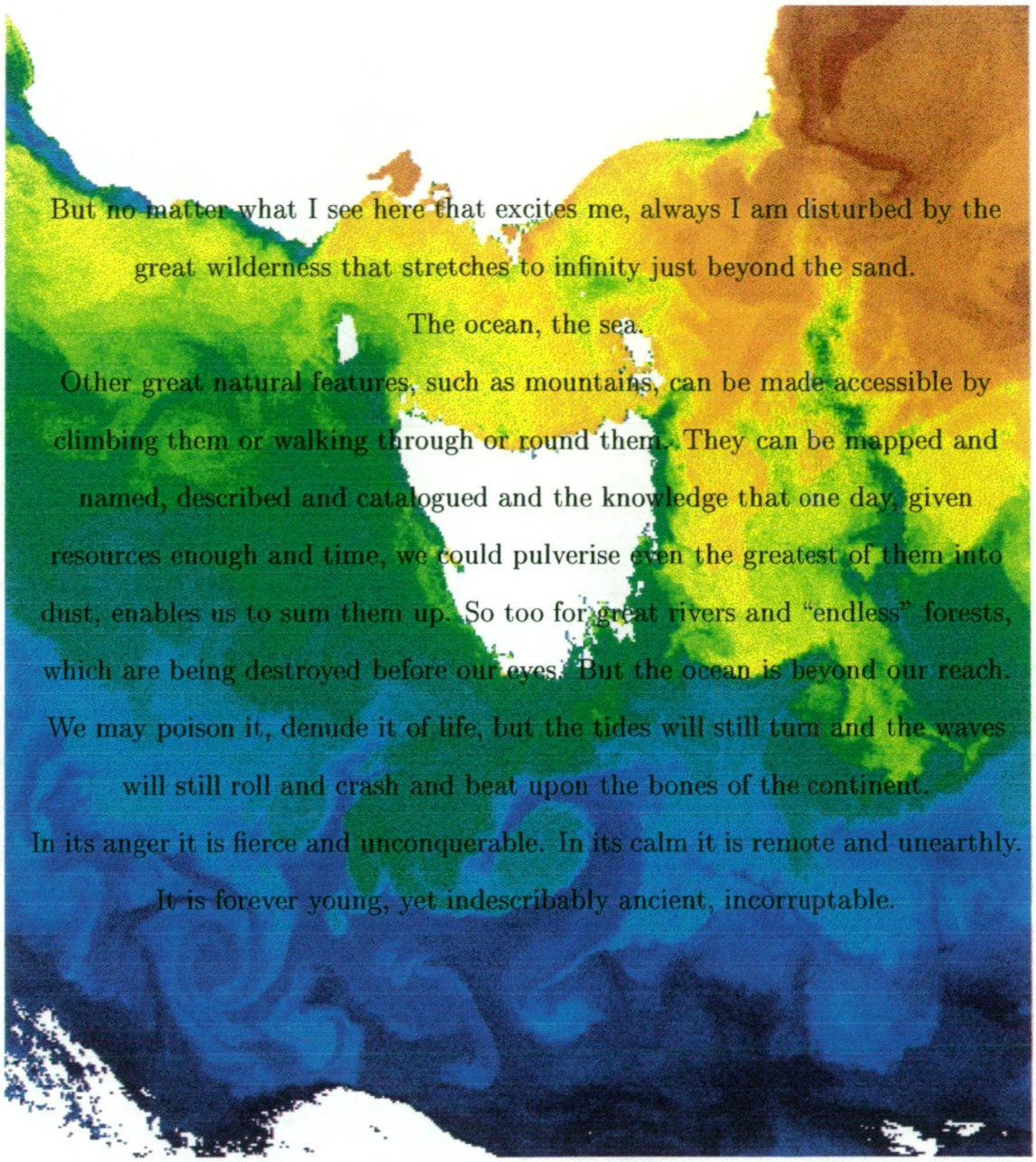

But no matter what I see here that excites me, always I am disturbed by the great wilderness that stretches to infinity just beyond the sand.

The ocean, the sea.

Other great natural features, such as mountains, can be made accessible by climbing them or walking through or round them. They can be mapped and named, described and catalogued and the knowledge that one day, given resources enough and time, we could pulverise even the greatest of them into dust, enables us to sum them up. So too for great rivers and "endless" forests, which are being destroyed before our eyes. But the ocean is beyond our reach. We may poison it, denude it of life, but the tides will still turn and the waves will still roll and crash and beat upon the bones of the continent.

In its anger it is fierce and unconquerable. In its calm it is remote and unearthly. It is forever young, yet indescribably ancient, incorruptable.

Quote: Ross Brownscombe,
Wilderness News Oct/Nov 1992, No. 129.

Image: CSIRO
Remote Sensing Department
Division of Oceanography,
NOAA 14, orbit 793, Feb. 24 1995 1528Z

## DECLARATION

This is to certify that the material comprising this thesis has never been accepted for any other degree or award in any tertiary institution and, to the best of my knowledge and belief, is solely the work of the author and contains no material previously published or written by another person, except where due reference is made in the text.

Jeremy L. Harris

August, 1996

## Authority of Access

This thesis may be made available for loan and limited copying in accordance with the Copyright Act 1968.

Jeremy L. Harris

August, 1996

## Abstract

A finite difference inverse model is developed to investigate the circulation of the Southern Ocean. The circulation of the Southern Ocean is largely unknown, and yet the heat and freshwater transported by the circulation plays an important role in maintaining the global climate [Rintoul 1988].

Previous inverse studies of the Southern Ocean, and inverse studies in general, suffer from relatively poor average spatial resolution [Martel and Wunsch 1993]. This study presents an inverse model of the Southern Ocean (SOINV) that begins to improve the spatial resolution of inverse investigations. In a move away from the quasi-synoptic approach of previous inverse models, the SOINV utilises all available hydrographic data measured between 1901 and 1990 to estimate a time averaged thermal wind circulation that is added to a mean Ekman circulation on a $1° \times 1°$ grid of the Southern Ocean. By applying conservation equations on each $1° \times 1°$ grid, a mass conserving, weakly vorticity conserving circulation of the Southern Ocean is developed that is dynamically consistent with the observations. The SOINV solves 26,945 equations to determine 28,480 unknowns using weighted damped least squares.

By comparing with in-situ observations, it is found that the SOINV circulation: underestimated velocities, developed comparable mass transports across sections in the model domain, and was in high qualitative agreement with the observations. The special features of the SOINV circulation are then highlighted by comparing the circulation to satellite measurements, a forward eddy-resolving numerical model and surface velocity estimates. None of these comparisons are possible with more traditional inverse studies. All of these comparisons show that the circulation developed by the inverse model is internally consistent, and is in close agreement with observations.

Using the mass circulation developed by the inverse model, the heat and fresh-

water transports are diagnosed. Comparing the heat and freshwater transports highlight that there are some inconsistencies within the global circulation. Despite these inconsistencies, this investigation demonstrates that a finite difference $1° \times 1°$ grid inverse model is possible. The resultant circulation is statistically consistent with the observations and gives a higher average spatial resolution than previous inverse investigations.

## Acknowledgments

Many generous people have assisted me in completing this thesis. First and foremost I would like to thank my main supervisor, Nathan Bindoff. His door was always open for many hours of discussions and the unwavering support and encouragement he showed during my research was much appreciated. I must also thank Richard Coleman for his many suggestions and time. The final thesis was much improved by his careful reading of the early drafts.

Many of the staff at the Division of Oceanography and Antarctic CRC have assisted me at sometime during my research. At the Division of Oceanography Steve Rintoul, John Wilkin and Peter McIntosh were always accommodating with any question I put to them. At the Antarctic CRC I am indebted to James Paterson for allowing me to, at times, completely hog the department's computer systems, without which I would not have finished.

I must thank the students of IASOS for keeping me sane. Particularly Bernadette Sloyan and Lousie Minty whose many deep and meaningful (and not so deep and meaningful) conversations helped me get through each day.

I would like to save my greatest thanks to my family. My wife Nichola, who has supported me every step of the way and her contribution to this thesis cannot be overstated; Nichola's family who have given me a home away from home; and most importantly my parents, who, throughout my life have shown the confidence in me that only parents can have.

I would like to acknowledge that this thesis would not have been possible without the financial support of an Antarctic CRC Post-Graduate Research Award.

Finally, to anyone else out there who I have not mentioned, well life's like that sometimes, but you know who you are.

Jeremy Harris

August, 1996

# Contents

# List of Figures

# List of Tables

# Chapter 1

# Introduction

The importance of ocean heat and freshwater transport in understanding the global climate system has been recognised for many years [Callahan 1971; de Szoeke and Levine 1981; Toole 1981; Georgi and Toole 1982; Hastenrath 1982; Wolff and Olbers 1989; van Ballegooyen et al. 1994]. The oceans maintain the global heat balance by transporting warm, shallow water poleward and returning cold, deep water equatorward [Rintoul 1988]. Because the Southern Ocean is the main route of connection between the Atlantic, Indian and Pacific Oceans, it plays an important role in the transportation of heat and freshwater around the globe, therefore making an important contribution to maintaining the earth's climate [Callahan 1971; Toole 1981; Georgi and Toole 1982; England et al. 1993]. The aim of this thesis is to gain a better understanding of the circulation of the Southern Ocean, and the implied transport of heat and freshwater budgets using inverse techniques.

For the purpose of this thesis, the Southern Ocean is defined as the ocean south of 30°S. This region contains several water masses that transport mass, heat, salt and other properties into, out of, and around the Southern Ocean, the deepest of which is Antarctic Bottom Water (ABW) (See figure 1.1). ABW is the major source of cold water for the worlds oceans and can be found as far north as 40°-50°N [Tchernia 1980; Mantyla and Reid 1983]. It is thought to be primarily produced in the Weddell Sea region, although there are known production sites in the Ross Sea and off the coast of East Antarctica [Tchernia 1980; Gordon and Tchernia 1972]. ABW is extremely cold, between -0.7°C to -0.5°C, and dense with salinities ranging between 34.64 psu to 34.7 psu. From

the formation site on the continental margin, ABW slides over the continental sill, down to abyssal plains before moving east and north across the ocean floor. ABW is the major reason for the low ocean temperatures and thus has a significant effect on the ocean's heat flow [Foster and Carmack 1976; Tchernia 1980; Carmack 1990].

Overlying the ABW is the relatively warm (0.5° to 2.5°C), salty (34.70 to 34.76 psu) Circumpolar Deep Water (CDW) (See figure 1.1). As the name suggests, CDW extends around the continent of Antarctica transporting heat, salt and nutrients southward. CDW is thought to have several origins. Lower CDW (LCDW), is cooler and more saline and is thought to originate from North Atlantic Deep Water (NADW), while upper CDW (UCDW) shows temperature and salinity signatures that suggest an origin in the mid-depth waters of the Indian and Pacific Oceans [Sievers and Nowlin 1984; Orsi et al. 1993; Roether et al. 1993]. UCDW is associated with an oxygen minimum layer suggesting that UCDW is also older than LCDW. As the relatively oxygen poor, but nutrient rich, CDW moves south, it shoals to the surface mixing and cooling with the surface waters making nutrients available to the biology of the region [Orsi et al. 1993]. Some CDW impinges on the continental margin to assist in the production of ABW [Orsi et al. 1993]. The rest mixes and cools, but does not sink, to form northward flowing Antarctic Surface Water (AASW) [Pickard and Emery 1990]. The movement of heat and salt by CDW, the largest water mass of the Southern Ocean, plays an important role in the global transport of heat and freshwater.

AASW is the relatively cold (<0°C) and fresh (<34.0 psu) surface waters surrounding Antarctica. AASW moves north until meeting warmer southward flowing water masses. The location of this confluence is termed the Polar Front (PF) (also known as the Antarctic Convergence, figure 1.1) and is signalled by

strong surface temperature and salinity gradients. The AASW is extremely oxygen rich and extends to a depth of 100 - 200 metres and shows strong seasonal signals [Sievers and Nowlin 1984; Orsi et al. 1993]. It is thought that at least some of the AASW mixes with the warmer waters north of the PF to form Antarctic Intermediate Water (AAIW). AAIW is characterised by a salinity minimum, oxygen maximum water found under the warmer Subantarctic waters north of the PF (see figure 1.1). Temperature and salinity characteristics of AAIW vary around the globe. Atlantic AAIW salinities range from 34.20 to 34.22 psu. Salinity steadily increases to the east, reaching a maximum of approximately 34.40 psu near 160°E, before decreasing to a minimum of 34.24 psu in the Pacific. Temperatures of AAIW range from 3° to 7°C throughout the Southern Ocean [Piola and Georgi 1982]. The variability in temperature and salinity shown by AAIW, lead McCartney [1977] to suggest that there were several processes involved in the formation of AAIW arising from winter cooling of Subantarctic Surface Waters (SASW) and Subantarctic Mode Water (SAMW).

SASW is a shallow (150 metres) layer thought to be the result of seasonal warming during summer which isolates the deeper SAMW from the atmosphere. Surface temperatures reach values of >7°C with relatively low salinities of less than 34.1 psu. The oxygen concentration is nearly 100% of saturation value and has associated low nutrient concentrations. During autumn and winter SASW disappears exposing the deeper SAMW to renewal by convective overturning in the Subantarctic Zone [McCartney 1977]. Temperatures associated with the deeper SAMW range from 4°C up to 6°C while salinities range from 34.0 psu to greater than 34.2 psu [McCartney 1977; Sievers and Nowlin 1984]. SAMW ranges in thickness from 300 metres near the PF to greater than 700 metres to the north [McCartney 1977; Sievers and Nowlin 1984]. The importance of these

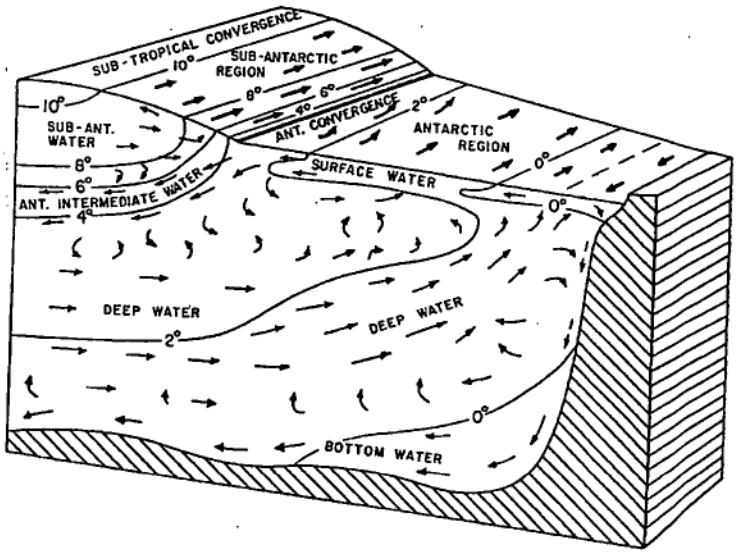


Figure 1.1: Water masses of the Southern Ocean Circulation, from Sverdrup et al. [1942].

relatively shallow water masses on the transport of properties around the Southern Ocean was noted by Rintoul [1988] who calculated that AAIW was the dominant water mass of the Southern Ocean in terms of transport and so their contribution to heat and salt transport is significant.

Associated with the PF is the Antarctic Circumpolar Current (ACC) which circulates around the globe as an uninterrupted jet at approximately 50°S, meandering north and south forced by dynamics and underlying topography [Nowlin and Klinck 1986]. There are many tributaries and offshoots of the ACC that assist in the transport of properties between the ocean basins and across the ACC. How the ACC assists or hinders the transport of mass, heat and freshwater around the globe is still largely undetermined [Rintoul 1988; Vassie et al. 1994]. There are several other major current systems that enter the Southern Ocean either as intense boundary currents or large subtropical gyers [Grundlingh 1980; deSzoeke 1987; Zemba and McCartney 1988; Peterson and Stramma 1991; Ridgway and Godfrey 1994; Stramma et al. 1995]. How these currents move properties around the Southern Ocean is also important in

understanding the Southern Ocean's impact on the heat and freshwater budget.

Our present knowledge about how these water masses and circulation of the Southern Ocean move heat and freshwater around the globe is uncertain. For example, estimates of meridional heat transport in each of the three ocean basins vary considerably. Macdonald [1993] presents a comprehensive review of heat transport estimates in the three ocean basins (see Tables 1, 2 and 3 of [Macdonald 1993]) and highlight a variation of estimates between +.15 PW to -2.3 PW of heat transport in the Pacific (positive transport is north), +1.76 PW to -1.6 PW in the Indian, and +1.5 PW to -2.3 PW in the Atlantic. It is generally accepted that the Indian and Pacific Oceans have a net southward heat transport and that the Atlantic has a net northward heat transport [Rintoul 1988; Macdonald 1993], but as Toole and Raymer [1985] point out, a net northward transport of heat by the oceans is contrary to the premise that the oceans must transport heat poleward from the equator. With such variation on the net heat transports, it is little wonder that the influence the individual water masses have on the heat transport is even less clear, with recent discussion centering on the relative importance of the "cold water" and "warm water" thermohaline circulation [Schmitz 1995].

The heat transport of the world's oceans is probably the most investigated property of the ocean after mass transport. Our uncertainty about the ocean's heat transport, given the amount of research into it, gives an indication on our lack of knowledge on the freshwater budget of the global oceans. There is even some debate about the definition of freshwater transport [Fu 1986; Bryden et al. 1991; Wijffels et al. 1992].

It is the aim of this thesis to further our knowledge about the mass circulation of the Southern Ocean and the implied transport of heat and freshwater that this mass circulation generates. This will be carried out by

developing a high resolution, single layer, inverse model that conserves mass and weakly conserves linear vorticity. Instead of following the usual synoptic approach of previous inverse models, all of the available hydrographic data in the Southern Ocean will be utilised to develop a mean, dynamically consistent circulation of the Southern Ocean. There are no constraints, apart from mass conserving boundary conditions, applied to the circulation. Previous inverse studies have constrained the circulation by imposing a transport, for example 130±13 Sv through Drake Passage [Rintoul 1988], on the circulation. The lack of these constraints, and the simple boundary conditions results in a inverse model that is relatively simple to implement and could be applied to any or all of the worlds oceans given sufficient computer resources.

Chapter 2 of the thesis reviews techniques and results from previous inverse models, highlighting the theory and limitations of each that lead to the development of the inverse model used in this thesis. Chapter 3 presents the investigation and processing of the windstress and hydrographic data for use in the inverse model. Chapter 4 presents the development of the model: the equations, the method of solving and a discussion of the solution, mainly from the mathematical point of view, inspecting the residuals of the model. An oceanographic discussion of the solution is presented in chapter 5 with the implied heat and freshwater transports presented in chapter 6. Finally, chapter 7, presents a summary and conclusions of the research.

# Chapter 2

# Review

Inverse techniques have been applied to the problem of determining the large scale ocean circulation since Wunsch [1978] attempted to claim Worthington's case of scotch by developing a dynamically consistent circulation of the western North Atlantic. The circulation conserved mass and maintained the geostrophic balance within multiple layers of the ocean which Worthington had stated could not be done [Wunsch 1978]. Wunsch only received a case of scotch miniatures because, in Worthington's opinion, he had only answered part of the question. Worthington felt that Wunsch's approach failed to completely solve the problem because a different choice of initial reference level resulted in a different solution. However, an advantage of the inverse technique is that an estimate of how good or bad the solution is can be made [Fiadeiro and Veronis 1982].

Wunsch's [1978] original model assumes that the ocean is in steady state, in hydrostatic equilibrium, and geostrophic balance which can be used to generate the thermal wind equation

$$f\frac{\partial v}{\partial z} = \frac{g}{\rho_0}\frac{\partial \rho}{\partial x} \tag{2.1}$$

where $f$ is the Coriolis parameter, $z$ is the vertical coordinate, $g$ is acceleration due to gravity and $\rho_0$ is the constant reference density [Wunsch 1978]. Equation 2.1, can be integrated once to give the velocity field $v$ normal to the hydrographic section

$$v(x,z) = \frac{g}{\rho_0 f}\int_{z_0}^{z}\frac{\partial \rho}{\partial x}dz + b = v_r + b \tag{2.2}$$

where $v_r$ is the velocity relative to the reference velocity, b, which is the integration constant. As Wunsch points out, the difficulty is in determining the integration constant $b$.

Wunsch used the fact that in any region of the ocean, discounting river runoff and evaporation and precipitation, mass into any volume must equal mass out. In a volume bounded by hydrographic sections, the nondivergence of mass can be written from equation 2.2 as

$$\sum_{j=1}^{N} \delta \left( \int_0^{d_j} v_j(p)dp + b_j d_j \right) \Delta x_j = 0 \tag{2.3}$$

where $\delta = \pm 1$ depending on the unit normal relative to the adopted sign convention (+ into the box, − out of the box), $j = 1, \ldots, N$ number of station pairs, $d_j$ is the mean depth of the ocean between station pair $j$, and $\Delta x_j$ is the horizontal distance between station pair $j$. For equation 2.3 to be satisfied, the condition equation is simply that

$$b_j + v_j(p) = 0 \qquad j = 1, \ldots, N \tag{2.4}$$

In attempting to answer Worthington's question, Wunsch also added the constraint that mass must be conserved in isopycnal layers and divided the ocean up into 5 vertical layers on the basis of temperature. This introduced a further set of equations, derived from equation 2.3, for each isopycnal layer.

$$\sum_{j=1}^{N} \delta \left( \int_{p_{j1}}^{p_{j2}} v_j(p)dp + b_j(p_{j2} - p_{j1}) \right) \Delta x_j = 0 \tag{2.5}$$

where $p_{j1}$ and $p_{j2}$ are the pressure levels at the top and bottom of the isopycnal layer. Note that there is no exchange of mass between isopycnal layers.

Given an initial estimate of the reference level (which could be a function of space, usually determined from water mass analysis), the mass imbalance

over the total depth and within each isopycnal layer could be calculated. Using least squares techniques, equations 2.3 and 2.5 can be solved simultaneously to estimate dynamically consistent velocities ($v_j + b_j$) along the hydrographic sections bounding the model domain. The bounding of the region by hydrographic casts has resulted in the approach being termed the "box model" inverse and has been applied in many areas of the world's oceans such as the north Atlantic [Wunsch and Grant 1982], Pacific [Bingham and Tally 1991] and Tasman and Coral Seas [Thompson and Veronis 1980; Fiadeiro and Veronis 1982]. Wunsch [1978] pointed out that the conservation equation (equation 2.5) could be applied to other conservative properties including, salt, heat and potential vorticity which would then decrease the degree to which the system was underdetermined. By introducing more conservative properties, there are more equations to solve for the same number of unknowns. The number of isopycnal layers can be increased, as Fu [1981] carried out in the subtropical south Atlantic, to increase the number of equations. When investigating the south Pacific Ocean, Wunsch et al. [1983] acknowledged the contribution surface Ekman transport makes to the mass transport by including the Ekman component into the mass conservation equations.

The key point of the above discussion is that, mass over the total water column is the most important conservation equation in the model. As Wunsch [1978] describes it, the reference velocities are modified in such a way that the total depth integral (equation 2.3) remains satisfied until the layer conservation equations (equation 2.5) are satisfied, or in practice most closely satisfied. Therefore, any inverse model is required to satisfy the total depth integration equation first and foremost.

As noted above, Wunsch's [1978] original model did not allow for the exchange of mass between isopycnal layers. It has been observed, particularly in

the meridional direction that water mass properties can change, therefore mass can apparently cross isopycnal boundaries [McCartney 1977; Bindoff and McDougall 1994]. This inability of Wunsch's [1978] model to allow cross-isopycnal exchange of mass lead to the estimation of reference velocities that varied quite largely between neighbouring station pairs. Wunsch defended these varying reference velocities by suggesting that each station pair is sampling a new circulation and so will have different reference velocities. However, the need to allow mixing between the isopycnal layers was acknowledged and introduced into later applications of the inverse technique [Wunsch and Minster 1982].

The concept of mixing was introduced by including vertical eddy coefficients into the layer conservation equations [Wunsch 1984], modifying equation 2.5 to

$$\sum_{j=1}^{N} \delta \left( \int_{p_{j1}}^{p_{j2}} v_j(p)dp + b_j(p_{j2} - p_{j1}) + (w^*a)_{j2} - (w^*a)_{j1} \right) \Delta x_j = 0 \qquad (2.6)$$

where $w^*$ is the vertical transfers across the isopycnal layers that have area $a$.

The validity of these vertical coefficients and their application has been debated by McDougall [1987] among others, as to whether they are physically meaningful, because they are introduced into the conservation equation in terms of a velocity. McDougall [1987] had shown that the vertical advection velocities could not be introduced without including the vertical diffusion fluxes into the conservation equation. Rintoul [1988] defended the cross-isopycnal fluxes in box models by stating that they do not represent cross-isopycnal velocities, but rather a cross-isopycnal transfer of the conservative property by a "variety of unresolved processes" which could include the diffusion processes discussed by McDougall [1987]. Using the form of the layer conservation outlined in equation

2.6 resulted in smoother variations in reference velocities between neighbouring station pairs [Wunsch 1984]. These smoother reference velocities suggested that if the inverse model is going to have layers that allow some form of mixing across the layer boundaries,then the implementation of the mixing coefficients must be carefully considered. Because the ACC has been shown to extend to the bottom [Callahan 1971; Bryden and Pillsbury 1977], and the difficulties encountered in including vertical mass flux on depth layers, it should be possible to simply use a single layer model.

With all of these approaches, the reference velocities are only resolved at the location of the bounding hydrographic sections and at the spacing of the actual casts within each section. This results in very low horizontal resolution estimates, (final resolution controlled by location of hydrographic sections) which makes it difficult to compare to observations that may be available inside the inverse box (such as float or current metre data). The best horizontal resolution study, using box model inverse techniques was carried out by Martel and Wunsch [1993], who attempted to determine reference velocities on a 1°× 1° grid for the north Atlantic Ocean. They achieved this resolution by dividing the north Atlantic into 85 boxes (the smallest of which was 9° longitude × 6° latitude) with 11 vertical layers and optimally interpolating hydrographic data onto the edges of each region at each layer. Conservation constraints were written for each layer in each box using fixed depth levels and solved simultaneously. The reference velocities were then interpolated onto the final 1°× 1° grid, hence, mass was only conserved on the smallest box scale of 6°× 9°. The minimum size of the mass conserving boxes, 6°× 9°in Martel and Wunsch's [1993] model, was controlled by the amount of noise introduced when the hydrographic data was optimally interpolated onto the edges of the 85 regions. Martel and Wunsch [1993] lamented that the circulation they had

developed was still not resolving the observed circulation satisfactorily and that the only way to compute the unresolved circulation was to increase the resolution, a process that was not justified with the data at their disposal.

At this point several decisions can be made and outlined about the form of the model presented in this thesis. From the experiences of Martel and Wunsch [1993], it is clear that spatial resolution of the hydrographic data is crucial. Previous inverse studies have tried to use a synoptic approach using hydrographic sections taken close in time that bound the inverse region. The use of synoptic data means that the system of equations is greatly underdetermined because there are so few conservation equations compared to the number of unknown reference velocities, but there is very little smoothing involved. However, all data can contribute some useful information to the inverse model and it will be shown that by utilising all hydrographic measurements observed in the Southern Ocean that optimal interpolation errors are sufficiently small to allow resolution of both the $u$ and $v$ components of the thermal wind on a $1° \times 1°$ grid. This will decrease the degree to which the model is underdetermined but it does introduce increased smoothing. In essence, a trade-off is made between the degree of smoothing and the degree to which the system is underdetermined.

The justification of making such a trade-off can be found in the work of Martel and Wunsch [1993] who note that ocean physics have strong regional variations with spatial scales of only a few hundred kilometres and that these must be resolved before an understanding of the circulation it obtained. Rintoul and Wunsch [1991] also note that the fluxes and flux divergences of climatologically important fields, such as carbon and oxygen, are sensitive to the spatial resolution of the velocity fields and with increasing interest in global climate, estimates of these fluxes are required to higher levels of accuracy than

previously acceptable. There is, as noted by Martel and Wunsch [1993], the obvious justification that most hydrographic measurements are best interpreted as point data and comparison of these data are difficult with the coarse resolution models of the past.

By generating an inverse model of the Southern Ocean at 1°× 1° grid spacing, the number of equations that are to be solved simultaneously exceed 18,000 for a single layer for each conservative property. If two layers are used, the number of equations jumps to over 54,000 if only simple interlayer exchanges are included. Solving this many equations simultaneously in order to maintain mass conservation over the model domain, quickly consumes the limits of available computational resources.

As stated above, it is the total depth integral of mass that is the key equation of inverse modeling. With the inherent difficulties of satisfactorily including interlayer exchanges, not to mention the drain on computational power, it was decided to use only a single layer, (top-to bottom) inverse model using all hydrographic data. Depth-integrated thermal wind transports are optimally interpolated onto the 1°× 1° grid for use in the model. However, the system of equations is still 50% underdetermined with an infinite numbers of solutions. By introducing another set of independent equations, the degree of underdeterminicy can be reduced which helps to constrain the solution. By dividing the model into two layers does introduce extra equations, however, this as been ruled out because of computational limitations. At less computational cost than introducing a second layer to the model is the introduction of a second conservative property in the single layer model, reducing the problem to only slightly underdetermined.

The conservative property selected for use in this thesis was the conservation of linear vorticity based on the work originating from Schott and

Stommel [1978] who derived a technique that made use of the conservation of linear vorticity on the beta plane expressed as

$$\beta v = f\frac{\partial w}{\partial z} \tag{2.7}$$

where $\beta$ is the gradient of the Coriolis parameter $f$ in the northward $y$ direction, and $v$ and $w$ are the $y$ and $z$ components of velocity. Schott and Stommel [1978] were able to apply the conservation of linear vorticity with the steady-state heat transport and geostrophic shear equations to generate a suite of equations on density layers which could be solved simultaneously for the horizontal components of velocity. Because this method takes advantage of the theory behind beta-spirals in the ocean, it has been termed the "beta-spiral" inverse method.

The formulation presented by Schott and Stommel [1978] calculated an estimate of the absolute velocities at one location, given information about the local density field by conserving density. It assumed that the cross-isopycnal mixing is negligible, potential vorticity was conserved and that relative vorticity is small. Because of these assumptions, in regions of strong currents where there is large relative vorticity, ie., western boundary currents, frontal regions and jets, the technique cannot be expected to hold. In practice, Schott and Stommel [1978] found that the beta-spiral technique is only applicable to mid-ocean regions where there is a significant north-south component of geostrophic velocity. Therefore in the Southern Ocean, with the strong east-west ACC, the approach is most likely to work in the subtropical regions north of the ACC where there will be an appreciable $v$ component. This should assist in generating Sverdrup like circulation balances in the subtropical gyres.

The beta spiral technique only estimates local reference velocities and so the technique does not conserve mass between points. Subsequent applications

of the beta spiral over large regions of the oceans were formulated in such a way that the final solution produces a minimum mass imbalance [Olbers 1989].

In addition to the effect geostrophic circulation has on vorticity, there is an appreciable influence by topography on vorticity. Mellor et al. [1982] and Olbers [1989], among others, have investigated the circulation of the world's oceans along lines of constant planetary vorticity, defined as the ratio of the Coriolis parameter divided by the depth of the ocean ($H$), $\frac{f}{H}$. As $H$ changes, the vorticity conservation requires a shift of the water column, the direction depending on whether $H$ increases or decreases. In the Southern Ocean there are many ridges and abyssal plains that can change the value of $H$ by up to 4000 metres. The directional control these ridges have on the circulation is significant, particularly the ACC, and need to be included in the model [Mellor et al. 1982; Colton and Chase 1983; Marshall 1995].

So at this point, the inverse model to be used will conserve mass and linear vorticity on a single layer for the Southern Ocean, making use of all available hydrographic data to get the highest horizontal resolution while conserving mass and vorticity.

In utilising all the available data of the Southern Ocean, there are several practical problems associated with calculating thermal wind velocities and interpolating the velocities onto a regular grid for use in the inverse solution. As was highlighted by Martel and Wunsch [1993], the errors introduced during the optimal interpolation of hydrographic data can limit model resolution. There is also the question to be answered; at what stage of data processing is it best to interpolate? The options are:(i) should the temperature and salinity fields be interpolated before calculating thermal wind velocities, or (ii) should the thermal wind velocities be calculated and then interpolated onto the regular grid.

Martel and Wunsch [1993] noted that the averaging of data carried out by Levitus [1982] tended to "smear out" some features of the world's ocean to the point that some water masses, and water mass extremes disappeared. This smoothing has an obvious and not so obvious effect on the resultant smooth velocity field. If one thinks of the raw temperature ($T$) and salinity ($S$) fields having two components, the mean temperature ($\overline{T}$) and salinity ($\overline{S}$) field, and the perturbation about the mean field of temperature ($T'$) and salinity ($S'$), giving

$$T = \overline{T} + T' \qquad S = \overline{S} + S' \tag{2.8}$$

The perturbation fields, $T'$ and $S'$, can contain signals from several sources such as errors introduced during the sampling like instrumental biases and inaccuracies (remember some of the data dates back to the early 1900's) or observational errors. The instrumental and observational errors are considered random and so are treated as noise that should not be introduced into the model. Depending on the time and length scales used during the averaging process, the perturbations can also contain signals from natural sources that should be included in the model. On long time scale averaging, as carried out during this research, the perturbations contain signals from longterm climate change, seasonal variations, and short term variations in the circulation such as meanders and eddies. With long length scale averaging, the mean field will have very little fluctuation and so the the perturbations contain local phenomena such as temperature changes due to boundary currents. As the length scales shorten, more of the local phenomena will be transferred into the mean fields, however, at excessively short length scales the observational noise is also transferred to the mean field.

By simply calculating the velocities from the mean fields, $\overline{T}$ and $\overline{S}$, the natural signals present with the perturbation about the mean, $T'$ and $S'$, are not included. So the trick is to include the natural perturbation signal while excluding the observational noise.

Because of the non-linearity of the density equation, the velocity field calculated from the raw temperature and salinity fields will be different than the velocity field calculated from the smoothed field, ie.

$$V(\overline{T}, \overline{S}) \neq \overline{V(\overline{T} + T', \overline{S} + S')} \tag{2.9}$$

The signals present within the perturbation field, both natural variation and observational errors, will result in different calculated velocities. By choosing appropriate length scales most of the observational errors can be excluded from the final mean velocity field. This will also exclude some of the short length scale natural variation signal which can't be helped. With the length scales used in this thesis, the thermal wind velocity field calculated from interpolated temperature and salinity fields is compared in figure 2.1 to the thermal wind velocity field calculated from the raw temperature and velocity field before interpolation.

These two velocity sections show the same large scale signal, however, the velocity section calculated from the raw temperature and salinity fields show a lot more detail, and produce a larger net transport. For this particular section across Drake Passage, the net transport from the smoothed temperature and salinity fields was estimated to be 27% smaller than the transport calculated from the raw temperature and salinity. On average, the thermal wind transport calculated from smoothed fields was 24% smaller than the thermal wind transport calculated from the raw fields. Because of this large difference, the thermal wind velocities used in the inverse model are calculated from the raw

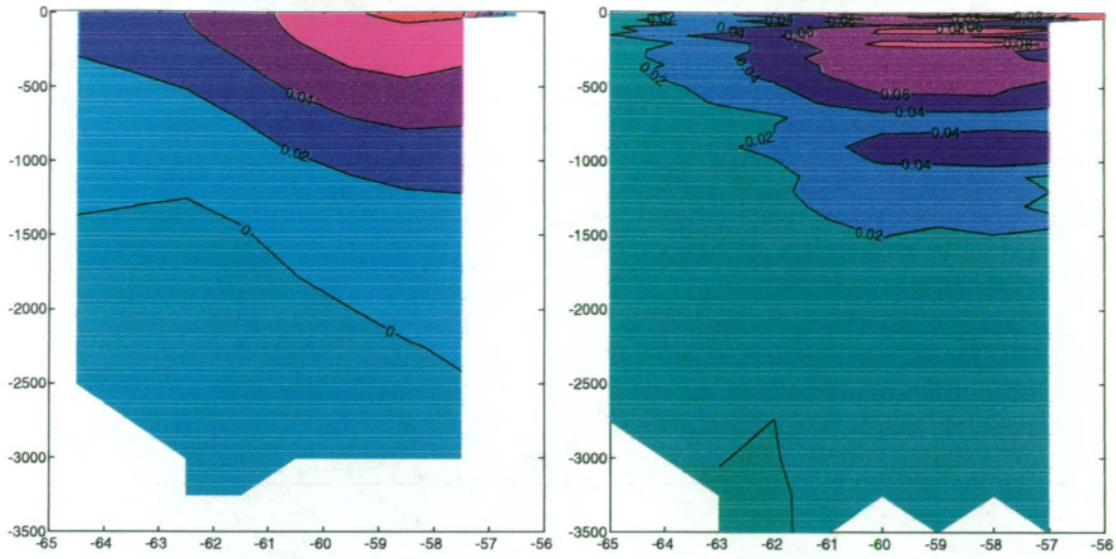


Figure 2.1: Velocity profile through Drake Passage calculated from smoothed temperature and salinity fields (left), compared to thermal wind velocity calculated from raw temperature and salinity field and then interpolated (right). m $s^{-1}$.

temperature and salinity fields, and presented in chapter 3.

# Chapter 3

# Data: Selection and Manipulation

This chapter describes, in three sections, the selection of the data and the data processing required for the inverse model. The building of a single layer model that conserves mass and linear vorticity, requires information on the total depth integrated thermal wind transport, Ekman transport, windstress curl and bottom topography.

The first section, section 3.1, compares two windstress datasets and describes how Ekman transports were calculated on the 1°× 1° grid required by the inverse model. Section 3.2 investigates two hydrographic datasets and describes how the thermal wind velocities were calculated from the raw hydrographic sections and finally, section 3.3 describes the optimal mapping procedure used to regrid the thermal wind velocities onto the 1°× 1° grid of the inverse model.

## 3.1 Windstress Datasets and Ekman Transport

For use in the inverse model, Ekman transports were calculated on the 1°× 1° grid of the model domain. Two windstress data fields were evaluated for use within this thesis by comparing data coverage and calculated transports. The two datasets were developed by Hellerman and Rosenstein [1983] and Trenberth et al. [1989].

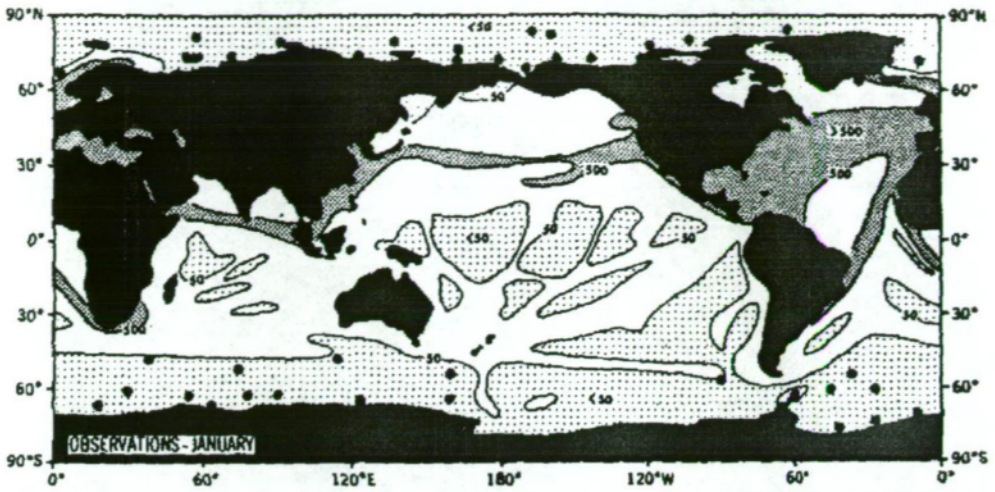


Figure 3.1a: Number of observations ($N$) per 2° × 2° box, smoothed for January; light shading for $N < 50$, no shading for $50 < N < 500$ and dark shading for $N > 500$. Heavy dots mark the locations for which data from the U.S. Navy's Atlas of the Polar Seas were used (Taken from Hellerman and Rosenstein [1983])

### 3.1.1 Hellerman and Rosenstein Windstress dataset

The Hellerman and Rosenstein dataset was compiled from over 35 million surface observations of the 10m winds that cover the world's oceans. These observations were collected by merchant ships between 1970 and 1976 along major shipping routes. As a consequence, the distribution of the observations is concentrated on the northern hemisphere trade routes. The data coverage for January and July is shown in figures 3.1a and 3.1b and shows the relatively small amount of data available south of 45°S. These observations were augmented, particularly in the Southern Ocean, by data from the U.S. Navy's Oceanographic Office's Atlas of the Polar Seas [1958 1959]. Hellerman and Rosenstein grouped the data by month into 2° × 2° boxes and calculated monthly windstress averages for each box from the grouped observations.

Yearly mean Ekman transports were calculated by averaging the 12 monthly windstress fields, linearly interpolating these values to a 1°× 1° grid and calculating the Ekman components ($T_{xEk}$, $T_{yEk}$) using the equations defined by Pond and Pickard [1983]

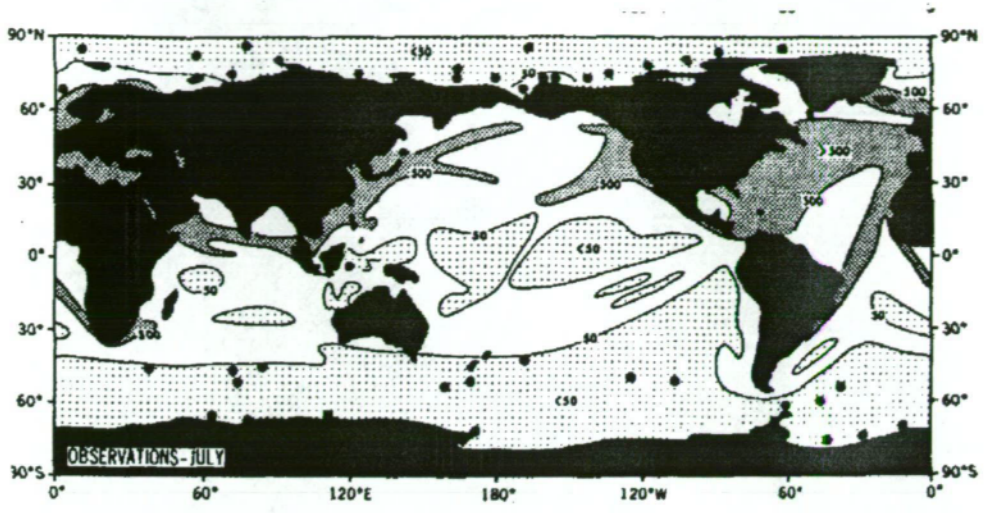


Figure 3.1b: Same as figure 3.1a except for July (Taken from Hellerman and Rosenstein [1983])

$$\begin{aligned} T_{xEk} &= \frac{f}{\rho}\tau_y \\ T_{yEk} &= -\frac{f}{\rho}\tau_x \end{aligned} \tag{3.1}$$

where $f$ is the Coriolis parameter, $\rho$ is density and $\tau_y$ and $\tau_x$ are the $x, y$ components of windstress.

The resulting Ekman transport field is shown in figure 3.3. The most striking feature of this transport field is the predominantly northward transport of water by Ekman processes in the Southern Ocean, generated by the strong westerly winds that are a feature of weather in the Southern Ocean. There is also a band of convergence between latitudes 32°S and 35°S around most of the southern hemisphere. This is a result of the easterly winds in lower latitudes, generating a southward Ekman transport, converging with the northward Ekman transport.

The Ekman transport calculated from the Hellerman and Rosenstein dataset generates a southward transport of 4 Sv across 30°S. This transport comprises 2 Sv in the Pacific, 1.5 Sv in the Indian and .5 Sv in the Atlantic. The volume of Ekman transport water entering the convergence zone can be

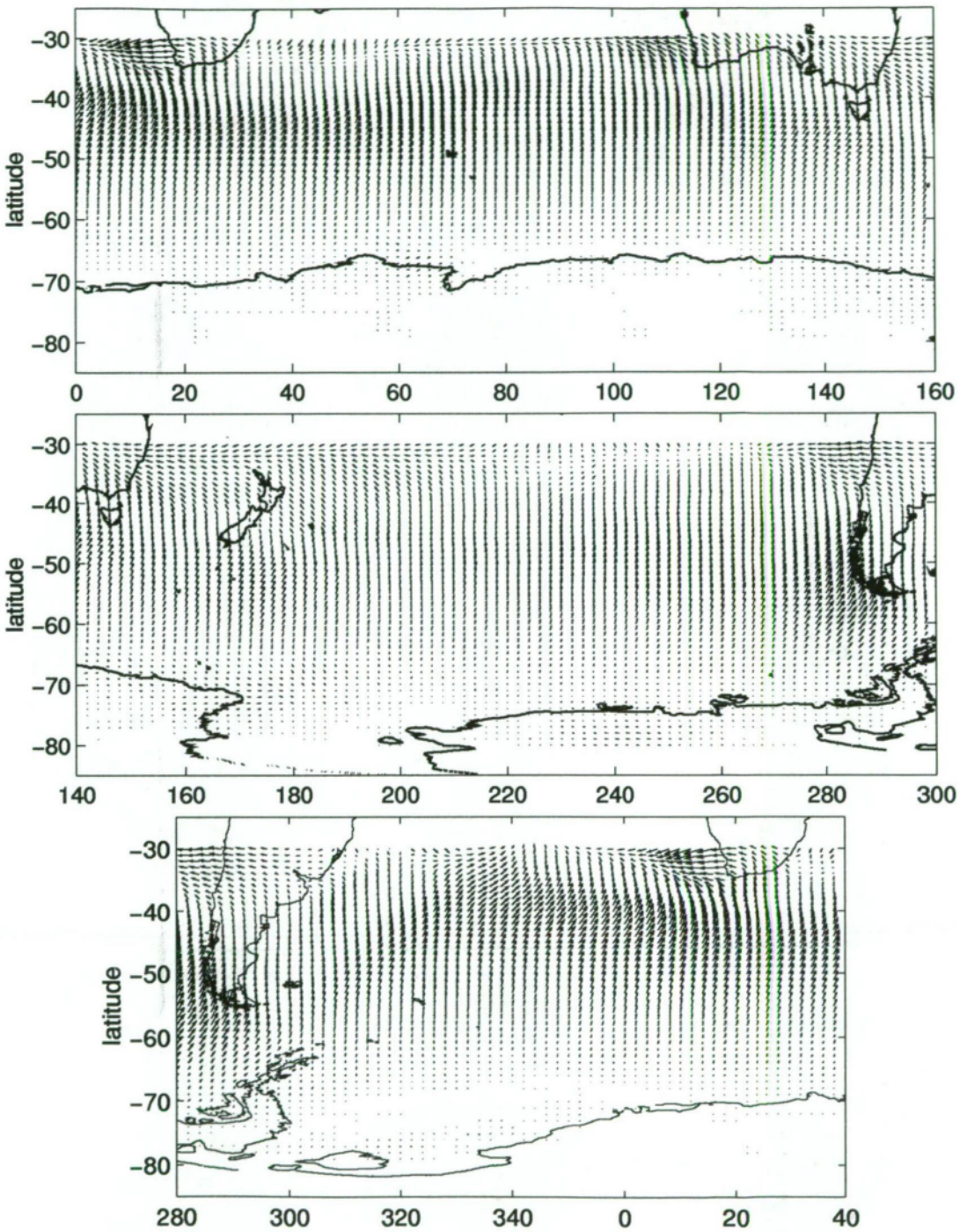


Figure 3.3: Ekman transports calculated from the interpolated 1°× 1° yearly mean Hellerman and Rosenstein windstresses. The plots are made at 1° latitude and 2° longitude resolution. (1°= 0.02 Sv in both directions).

calculated from the amount of northward transport across 40°S. This northward transport is calculated to be 26 Sv giving a total of 30 Sv of convergence in this region. The eastward Ekman transport is calculated to be <3 Sv across 20°E (south of Africa), >3 Sv across 117°E (south of Western Australia) and 1.5 Sv through Drake Passage.

The curl of the windstress, shown in figure 3.4, was calculated from the yearly mean windstress on the 1°× 1° grid using centered finite differences in zonal and meridional directions. Positive values of windstress curl represent a cyclonic regime in the horizontal windstress field, similarly negative values represent anti-cyclonic circulation. Figure 3.4 highlights the latitude band where the westerlies are most intense by the change of sign around 42°S. The effect of South America on the windstress regime manifests itself in the strong positive values through Drake Passage as the winds are forced south and then through Drake Passage. The large negative values south of Africa are a result of the windstress turning north out of the Southern Ocean to flow along the west coast of Africa. The curl of the windstress, as explained formally in section 4.2, defines the vertical component of Ekman velocity where a positive curl represents downwelling and negative values represent areas of upwelling. Upwelling and downwelling changes the length of the water column and thus changes the ratio of potential vorticity ($\frac{f}{H}$) as explained in chapter 2. Conservation of linear vorticity results in a movement of water towards or away from the equator. By inspection of figure 3.4, it is possible to determine, if linear vorticity is to be conserved and topography has a fixed depth, how water will be transported. In regions of negative curl or upwelling, the water column is stretched and so the water column will move away from the equator and vice versa for positive values of curl.

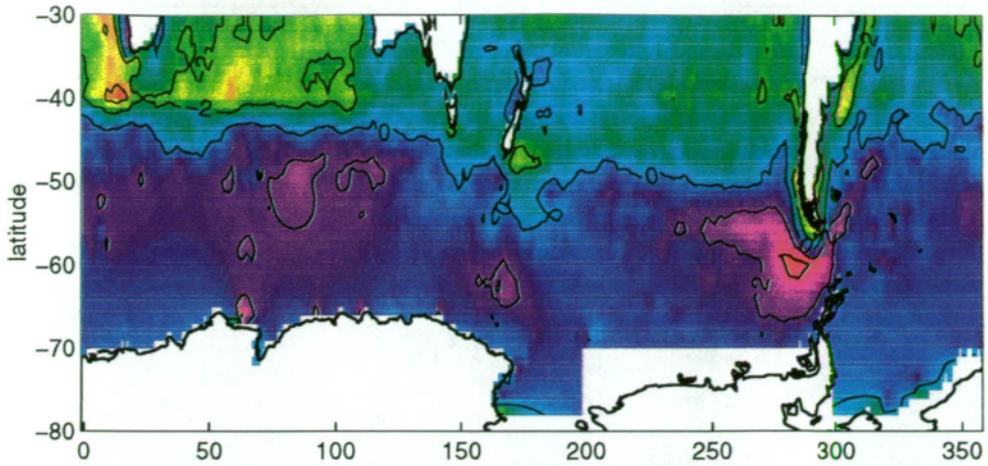


Figure 3.4: Curl of Hellerman and Rosenstein windstress. Calculated from the linearly interpolated 1°× 1° grid, yearly mean windstresses. Units = $1\times10^{-9}$ N $m^{-3}$, contour intervals $2\times10^{-9}$ N $m^{-3}$.

### 3.1.2 Trenberth, Olsen and Large (ECMWF) Windstress Dataset

The Trenberth et al. [1989] windstress fields were derived from 7-year (1980-1986) vector averages of the twice daily windstresses computed from the European Centre for Medium-Range Weather Forecasts (ECMWF) 1000mb winds on a 2.5°× 2.5°grid. The Ekman transports were calculated using equations 3.1 after linearly interpolating onto the 1°× 1° grid with the results shown in figure 3.5.

One of the most obvious features of the ECMWF dataset is the lack of data in the higher latitudes. The course resolution of 2.5°x 2.5°, combined with no available data over continental regions results in incomplete coverage at the margins of landmasses. This lack of data in the coastal regions not only affects the magnitude of the Ekman transports but introduces an artificial imbalance of mass transport in coastal regions. As explained in section 4.3, it is the mass conservation in the coastal boundary regions that is crucial to the solution of the inverse model. The Ekman transports in the 40°S to 50°S latitude range are again directed northward. However, the size of the transports are much larger

(by a factor of 5) than those generated by the Hellerman and Rosenstein windstresses.

Using equations 3.1, the ECMWF windstress dataset generates a net transport of 6 Sv into the model domain across 30°S, 2 Sv in the Pacific, 3.5 Sv in the Indian with .5 Sv out of the domain in the Atlantic. The amount of northward Ekman transport across 40°S is 31 Sv giving a total of 37 Sv of convergent Ekman transport. This is larger than the 30 Sv calculated from the Hellerman and Rosenstein dataset. The eastward Ekman transport across the three meridional sections of 20°E, 117°E, 292°E are 1 Sv, 1.5 Sv and .1 Sv respectively. These eastward transports are significantly less than the 3 Sv, 3 Sv and 1.5 Sv calculated from the Hellerman and Rosenstein data, mainly as a result of the lower spatial coverage in the ECMWF windstress field at higher latitudes.

The windstress curl of the ECMWF dataset was calculated using the same procedures as outlined for the Hellerman and Rosenstein dataset. The results are shown in figure 3.6. The curl field clearly illustrates the lack of data at higher latitudes. The values are, on average, larger than the Hellerman and Rosenstein dataset by a factor of 2, and the location of the zero contour is shifted about 5°south compared to the Hellerman and Rosenstein results. In addition, there are large values of the windstress curl near the southern boundary of the data field, particularly between 80°and 150°E, the reasons for which are unclear.

### 3.1.3 Evaluation of Windstress Datasets

The net transports generated across 30°S by the two windstress datasets are similar although the magnitudes of the pointwise transports are much larger in the ECMWF dataset. The magnitudes of the ECMWF windstress fields have

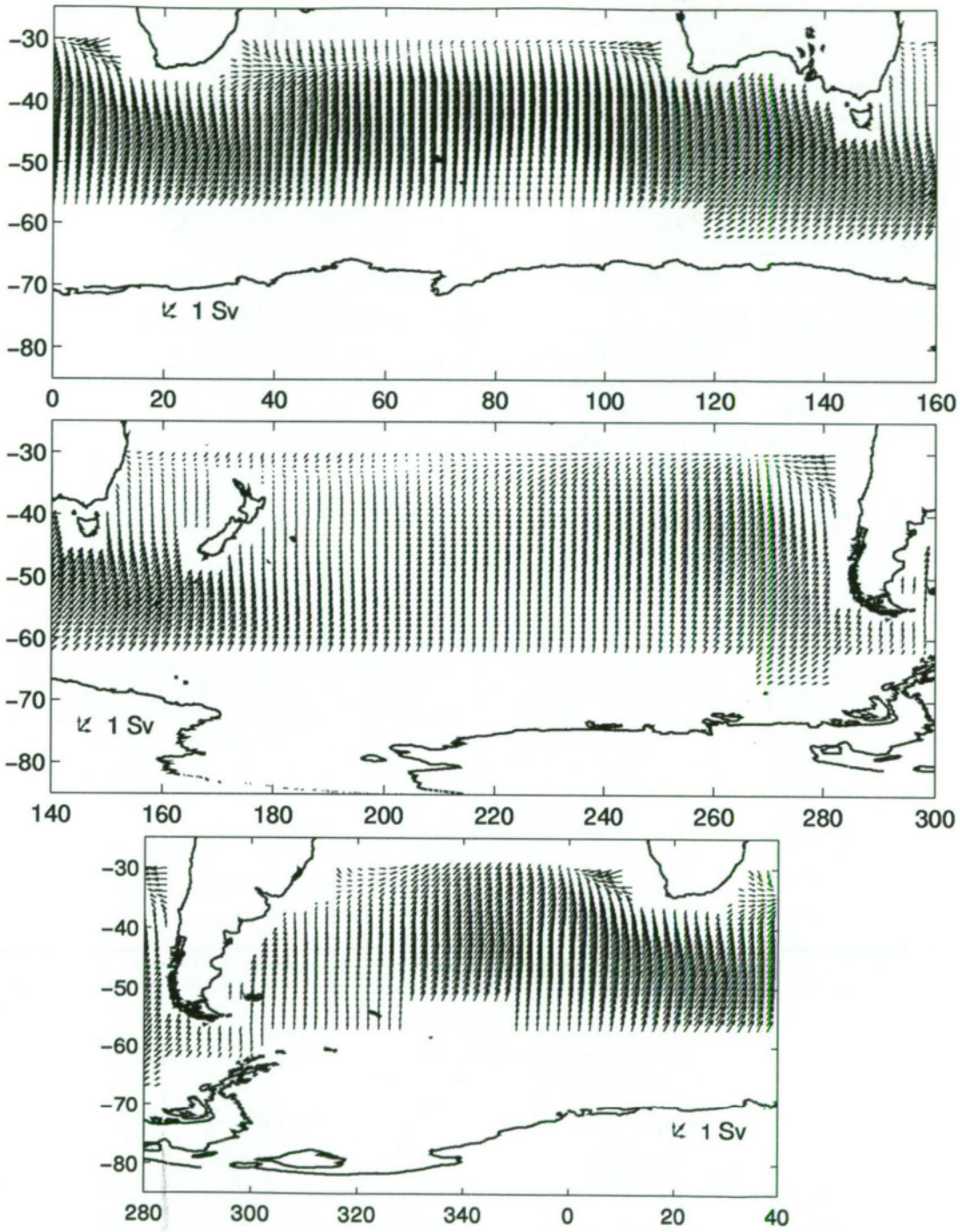


Figure 3.5: Ekman transports generated from yearly mean windstress field on 2.5°× 2.5°, linearly interpolated to 1°× 1° from Trenberth et al. [1989] windstress fields shown at 1° latitude and 2° longitude resolution (1°= .5 Sv in both directions).

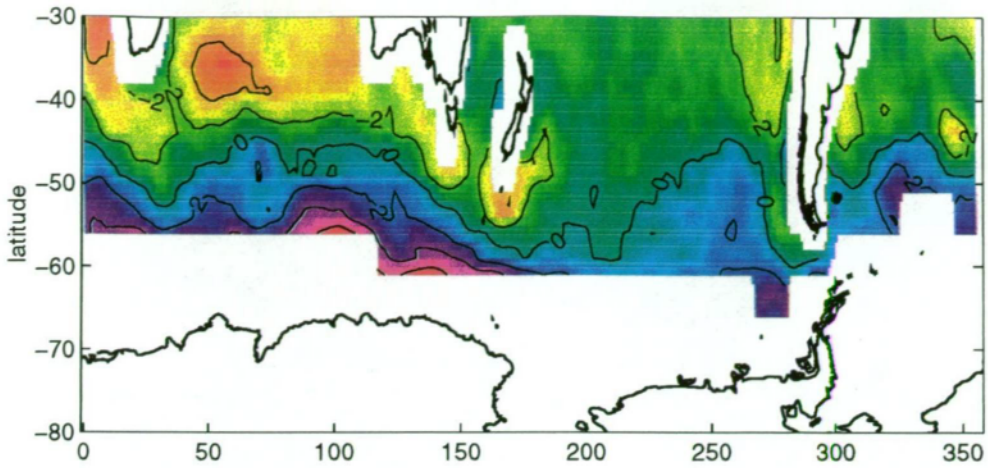


Figure 3.6: Curl of Trenberth et al. [1989] windstress. Calculated from yearly mean windstresses linearly interpolated onto 1°× 1° grid. Units = $1\times10^{-9}$ N $m^{-3}$, contour intervals $2\times10^{-9}$ N $m^{-3}$.

been compared to the windstress field derived from the Seasat-A satellite scatterometer by Mestas-Nunez et al. [1994]. They found that the ECMWF windstresses were consistently larger than the scatterometer windstresses, particularly in the Southern Ocean, by up to 50%. This was found to be mainly due to the assumption that the 1000-mb winds of the ECMWF analysis could be interpreted as 10m winds. In contrast, the Hellerman and Rosenstein dataset may be biased to lower windstresses in the polar regions when the air temperature is lower than the underlying ocean or ice [Hellerman and Rosenstein 1983]. This suggests that both windstress fields may not be reliable in the Southern Ocean making it difficult to choose a dataset on the criterion of data quality. The different magnitudes of the two windstress fields propagates to the computed windstress curl fields where, as discussed above, the magnitude of the ECMWF curl field is, on average, twice as big as the Hellerman and Rosenstein curl field.

The lack of data and data quality of the ECMWF data at higher latitudes causes most concern for the inverse model. It is desirable to have continuous data coverage in the model domain so that when conservation equations are

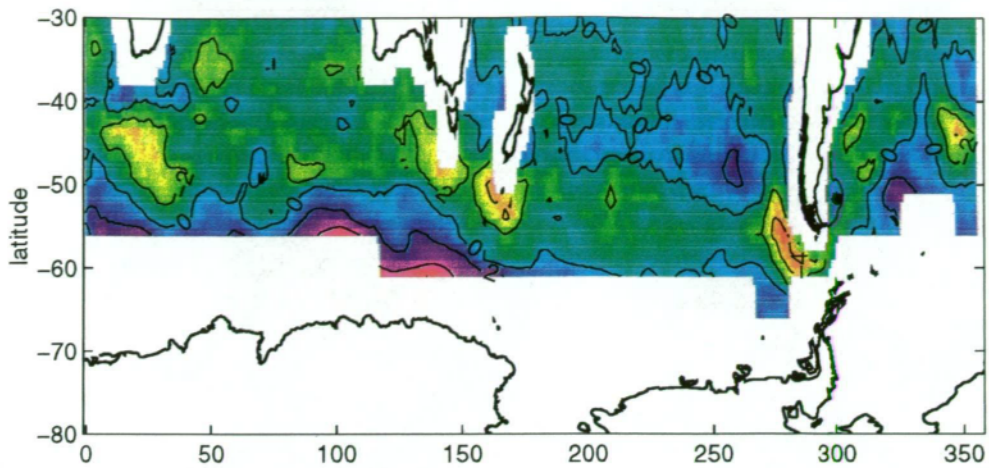


Figure 3.7: Plot of the difference between the windstress curl for the Trenberth et al. [1989] dataset and the Hellerman and Rosenstein [1982] dataset. Units = $1 \times 10^{-9}$ N m$^{-3}$.

applied over the entire domain, there are no false boundaries introduced by data dropouts. The data quality of the ECMWF data near the southern boundary of the ECMWF dataset is also questionable. Figure 3.7 shows the difference between the two windstress fields of the curl of the windstress. Away from the southern boundary of the ECMWF dataset, the difference ranges mostly between $\pm 2 \times 10^{-9}$N m$^{-3}$. In areas near the southern boundary, the difference is greater than $4 \times 10^{-9}$N m$^{-3}$. These large differences correspond to the extreme values generated by the ECMWF data discussed above. This suggests that the large values of windstress curl generated by the ECMWF near the southern boundary are unrealistic.

From the above comparison of data coverage and data quality of the ECMWF and Hellerman and Rosenstein windstress fields, it is clear that the Hellerman and Rosenstein dataset is more appropriate for use in the inverse model. The questionable quality and lack of data at higher latitudes makes the ECMWF data less desirable.

## 3.2 Hydrographic Data and Thermal Wind

This section compares two hydrographic datasets available in the Southern Ocean region and describes how the thermal wind velocities were calculated at individual cast locations. The two hydrographic datasets selected are the Southern Ocean Atlas by Gordon et al. [1982] and the Hydrographic Atlas of the Southern Ocean by Olbers et al. [1992]. To develop a mean thermal wind circulation of the Southern Ocean requires a large number of hydrographic casts distributed evenly over the Southern Ocean. The data density of the two hydrographic datasets was investigated to determine if there was sufficient data available to resolve both components of thermal wind on the 1°× 1° grid required by the inverse model.

### 3.2.1 Southern Ocean Atlas

In 1991, the main data source for raw hydrographic casts of the Southern Ocean was the Southern Ocean Atlas by Gordon et al. [1982]. This atlas contains 6313 Nansen bottle casts collected from 1906 to 1978. Each cast has different measurement depths so that interpolation was required to re-grid the data onto standard depth levels. Some simple initial data quality checking was carried out by Gordon et al. [1982]. Casts that were missing either the temperature or salinity profile were removed. Casts with more than 4 data levels missing or 3 consecutive data levels missing were also removed. Profiles with one or two missing data levels were linearly interpolated in T and S to fill in missing data. These simple data checks left 5147 casts available, distributed as shown in figure 3.8.

The South Atlantic contains most of the casts (2008), with 734 casts near Drake Passage and 231 in the Agulhas region off South Africa. The Indian and Pacific Oceans are more poorly sampled with only 1295 and 1856 casts

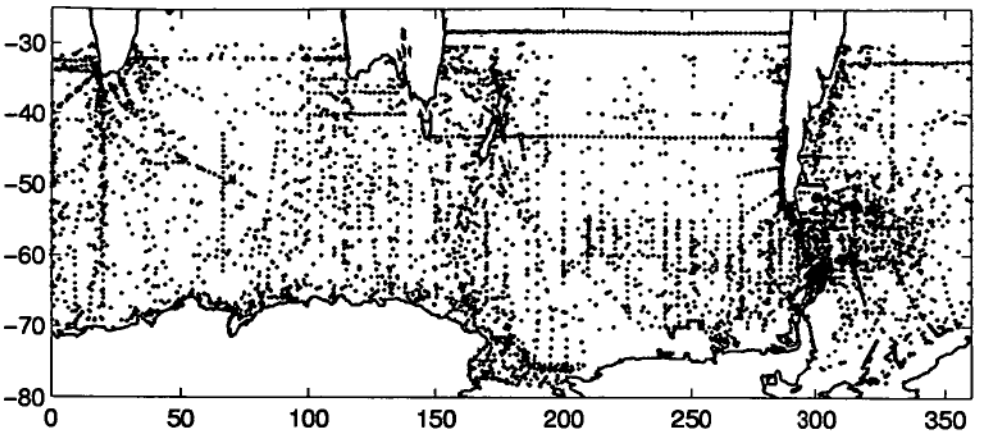


Figure 3.8: Positions of the 5147 casts available after data quality checking of the Southern Ocean Atlas [Gordon et al. 1982].

respectively. The Pacific Ocean, north of 42°S, is particularly data sparse with only 302 casts available east of New Zealand, an area of nearly 15 million square kilometres. Over the entire model domain, the Southern Ocean Atlas has only an average of 0.44 points per 1°× 1° box. Based on this data coverage, it would seem that the Southern Ocean Atlas does not have sufficient data to adequately resolve circulation of the Southern Ocean on a 1°× 1° grid.

### 3.2.2 Hydrographic Atlas of the Southern Ocean

In late 1992, Olbers *et al.* [1992] released the Hydrographic Atlas of the Southern Ocean. This atlas contains approximately 39,000 bottle and CTD casts collected during the period 1904 to 1990. Each cast has been interpolated, where possible, onto 42 standard depth levels (see Table 3.1) for the properties of temperature, salinity and oxygen. The cast locations are illustrated in figure 3.9.

Until recently, oceanographic research has focused on the Atlantic Ocean with Europe and the US acting as principal investigators. This is also true for the Southern Ocean where most measurements (over 14,000 casts) occur in the South Atlantic, especially Drake Passage (2134) and the Agulhas Current region

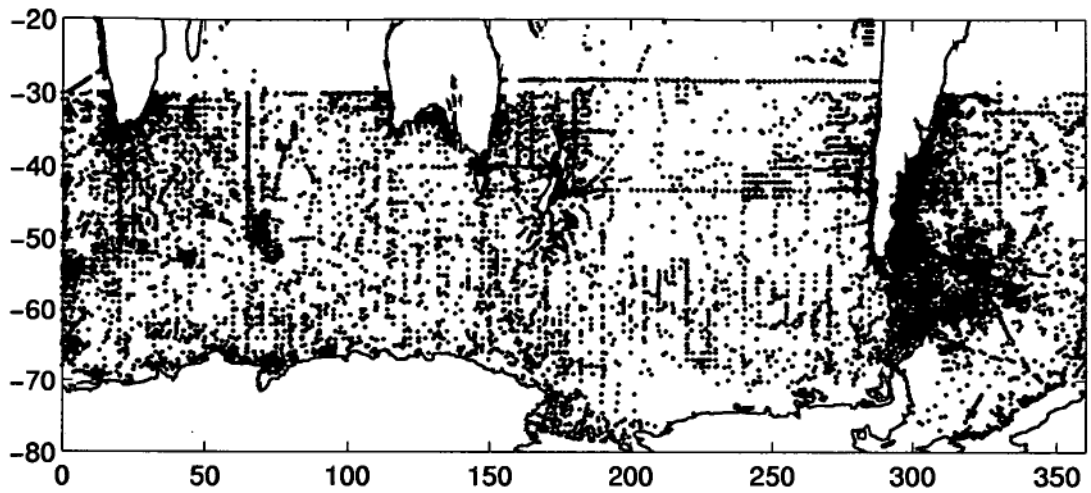


Figure 3.9: Data locations of clean casts from the Hydrographic atlas of the Southern Ocean by Olbers *et al.* [1992].

(3278). The dynamics of the South Atlantic have made it an exciting region to investigate which, combined with the proximity of seaports, has resulted in the relatively high data density seen in figure 3.9. The South Pacific and South Indian Oceans, being more remote and seemingly less exciting, although no less important, have suffered from a lack of oceanographic research. This can be easily seen in figure 3.9, where the South Indian Ocean contains only 4654 casts with 1000 of those near Kerguelen and Heard Islands, the South Pacific containing 3811 casts of which 1065 are in the Tasman Sea and with only 595 casts covering the South Pacific north of 42°S.

If the Hydrographic Atlas of the Southern Ocean data is divided into seasons, the data coverage decreases significantly with most cruises occurring in summer (10,412 good quality casts). The number of good quality casts in the austral spring (4532), autumn (6847) and especially winter (4248) leave large regions of the ocean devoid of data.

In producing the Hydrographic Atlas of the Southern Ocean, Olbers et al. [1992] applied a range of tests to ensure that the data were homogeneous and internally consistent. This involved checking for time versus position (to see if

| Level | Depth | Level | Depth | Level | Depth | Level | Depth |
|---|---|---|---|---|---|---|---|
| 1 | 0 | 11 | 250 | 22 | 1100 | 32 | 3000 |
| 2 | 10 | 12 | 300 | 23 | 1200 | 33 | 3250 |
| 3 | 20 | 13 | 350 | 24 | 1300 | 34 | 3500 |
| 4 | 30 | 14 | 400 | 25 | 1400 | 35 | 3750 |
| 5 | 50 | 15 | 500 | 26 | 1500 | 36 | 4000 |
| 6 | 75 | 16 | 600 | 27 | 1750 | 37 | 4500 |
| 7 | 100 | 17 | 700 | 28 | 2000 | 38 | 5000 |
| 8 | 125 | 18 | 750 | 29 | 2250 | 39 | 5500 |
| 9 | 150 | 19 | 800 | 30 | 2500 | 40 | 6000 |
| 10 | 200 | 20 | 900 | 31 | 2750 | 41 | 6500 |
| | | 21 | 1000 | | | 42 | 7000 |

Table 3.1: Depths, in metres, of the Standard Levels used in The Hydrographic Atlas of the Southern Ocean

consecutive stations were in a realistic location), gross range (temperatures between -2.5°C to 30°C and salinity from 34psu to 35.5psu below 1600 metres), statistical consistency (if the data were less than 3 standard deviations away from mean within a local region), static stability, vertical profile and data type (for example, comparing old, less accurate, bottle data against CTD data). Olbers et al. [1992] also inspected data reliability by flagging the entire cast if more than 50% of the cast levels were flagged. Within a section of casts, if more than 10% of the casts were flagged, the entire section data was rejected.

As with the Southern Ocean Atlas, the same additional data quality tests were performed. Casts with no temperature and salinity profiles were removed. Casts with more than 4 data levels or 3 consecutive data levels missing were removed. The remaining casts with data levels missing were linearly interpolated to fill in the missing data. By applying the data flags provided by Olbers et al. [1992] and the additional data tests described above, the number of clean casts available was reduced from 38,818 to 23,806. Assuming the data were evenly distributed, this number of casts corresponds to 1.7 casts per 1°× 1° cell. As will be shown in section 3.3.2, it is possible to resolve thermal wind

transports on the 1°× 1° grid without introducing excessive errors.

### 3.2.3 Evaluation of the Hydrographic Datasets

From the simple comparison of the data density of these two datasets, it is clear that the superior data density of the Hydrographic Atlas of the Southern Ocean [Olbers et al. 1992] makes it the most appropriate dataset for use in this thesis. As will be shown later in the presentation of optimally interpolated fields in section 3.3.2, the size of the associated interpolation errors are smaller for the Hydrographic Atlas of the Southern Ocean [Olbers et al. 1992]. However, there are a few other considerations that need to be mentioned. The Southern Ocean Atlas [Gordon et al. 1982] does not include any CTD data, of which there are many thousands in the Southern Ocean. On the other hand this does raise the question of how to integrate the CTD data with the Nansen bottle data. In their data checking, Olbers et al. [1992] compared older bottle data with newer CTD data, whenever possible, and flagged measurements that appeared dubious (both CTD and bottle). In this thesis, it was assumed that the data checking carried out by Olbers et al. [1992] detected the majority of the spurious, hydrographic data and the CTD and bottle data were considered equally. Finally, the timespan of the data collection was 14 years longer for the Hydrographic Atlas of the Southern Ocean. This longer period plus the greater number of measurements should lead to a better estimate of the mean thermal wind circulation.

### 3.2.4 Calculating components of Thermal Wind

The ability to accurately resolve the $u$ and $v$ components of thermal wind, at each cast location in the randomly distributed dataset of figure 3.9, relies simply on the ability to select appropriate casts. In data sparse regions of the Southern

Ocean, the north-south orientations of most hydrographic sections makes the selection of casts that reliably calculate the $v$ component of thermal wind difficult. In data dense regions, the difficulty is one of selecting casts where the gradient of dynamic height estimates $\frac{\partial D}{\partial x}$ and $\frac{\partial D}{\partial y}$ ($D$ = dynamic height, $x, y$ = the distance in the east-west, north-south directions respectively) reliably estimate the actual flow scales. As will be explained later, it is possible to select casts that generate unrealistic gradients in dynamic height. This was overcome by introducing a minimum cast separation distance. Ideally, only three casts, with well constructed orientation with no angles less than 30°, are required to best resolve both components of thermal wind.

Two techniques were investigated in which three selected casts from the dataset were used to resolve thermal winds. The first technique was a computationally complex technique based on Delaunay triangulation, as reported by Sloan [1986]. The second approach was a basic "look-east-look-north" technique that selected a single cast from the dataset and then chose the closest casts in an east and north direction. Both techniques failed for several reasons. With the distribution of the data, the Delaunay triangulation method tended to select three casts that represented elongated triangles in the meridional direction and therefore could not reliably calculate the gradients $\frac{\partial D}{\partial x}$ and $\frac{\partial D}{\partial y}$. Usually, with elongated triangles, the horizontal distance between casts in the $x$ direction was very small, giving rise to unstable velocities in the north-south direction. Another difficulty was that the location of the estimated velocities was shifted away from the cast locations, into a position at the mid-point between the three casts. This meant that the depth of the velocity profile was uncertain and that the coordinates of the velocities would change. Because of these difficulties both of the above techniques proved unacceptable. With the experience of these two techniques and the difficulties

encountered, a new technique was developed that utilised 13 casts from the dataset and introduced a minimum station separation in order to reliably calculate $\frac{\partial D}{\partial x}$ and $\frac{\partial D}{\partial y}$.

This new technique selects a cast from the dataset, which is termed the central cast and denoted by the open circle in the left hand side of figure 3.10. As shown in figure 3.10, the area around the central cast is divided into 12 regions outside an exclusion zone. Casts located within the exclusion zone are ignored. Thermal wind velocities, referenced to the surface, were calculated between the central cast and the closest cast in each region. No cast was chosen more than 10° away from the central cast so that some of the 12 regions could be left empty. On occasions when the region cast is shallower than the central cast, the velocity shear is set to zero and the deepest velocity used to fill in missing levels (see right hand panel of figure 3.10). For region casts deeper than the central cast, the deeper levels of the region cast are ignored (see right hand panel of figure 3.10). This results in velocity profiles to the depth of the central cast and does not introduce transports below the ocean floor. The above process was applied $N$ times ($N$ = number of casts) with each cast of the dataset acting as the central cast.

The reader may be concerned about the transport between the central cast and deeper region casts that are ignored. This transport will be calculated when the deeper region cast becomes the central cast, thus the velocity profile will apply to an appropriate depth.

The exclusion zone around the central cast was used to introduce a minimum cast separation. It was found that without this minimum separation, two casts could be chosen at almost the same location (see figure 3.10). Thus, if the two casts were separated in time by many years, the change in dynamic height, $\partial D$, could be very large, resulting in unrealistic estimates of the velocity.

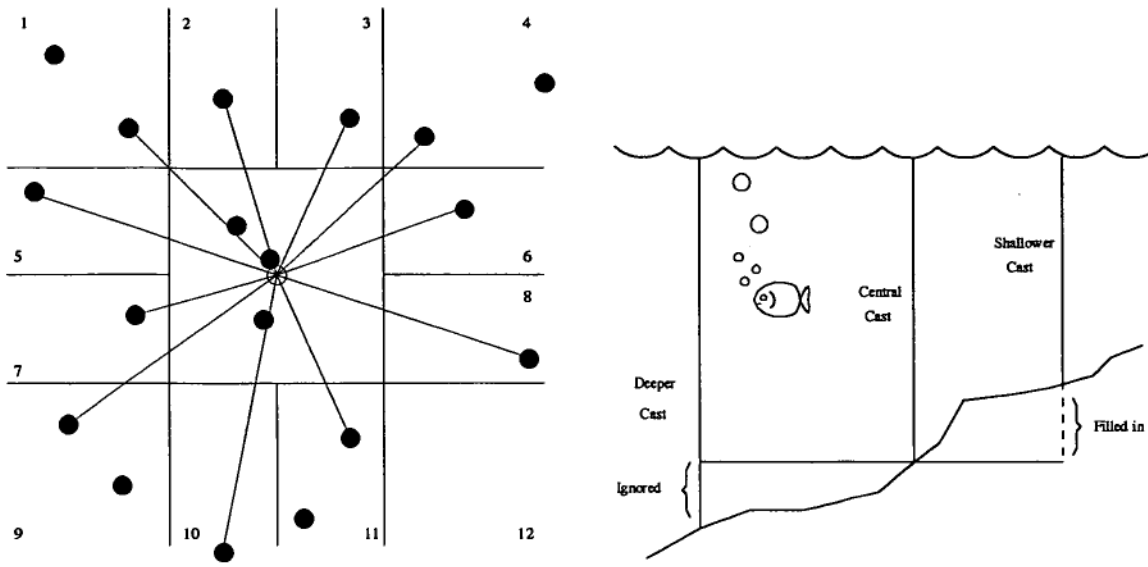


Figure 3.10: Schematic of final cast selection routine (left) and profile of selected casts (right).

To avoid this situation, any casts within the exclusion zone were ignored. The size of the exclusion zone was set to 25 km square, approximately half the normal hydrographic data spacing of between 30 nm (55 km) to 60 nm (111 km).

The thermal wind velocities ($V_\perp$), calculated between the central cast and the 12 region casts, are orientated with respect to north by an angle $\Theta$ so that, for each standard level, the $u$ and $v$ components of thermal wind velocity can be expressed by

$$\begin{aligned} u_j \cos\Theta_{(i,j)} &= V_{\perp(i,j)} \qquad (number\ of\ regions\ i = 1, \ldots, 12) \\ v_j \sin\Theta_{(i,j)} &= V_{\perp(i,j)} \qquad (number\ of\ layers\ j = 1, \ldots, 42) \end{aligned} \tag{3.2}$$

As each velocity profile between the central cast and the 12 region casts extends to the depth of the central cast, the $u$ and $v$ components of velocity can be solved on each layer simultaneously using least squares techniques. The system of equations in 3.2 are overdetermined. Singular Value Decomposition

techniques as implemented within the MATLAB® computing environment with a rank of 2, were used to estimate the $u_j$ and $v_j$ terms, although any minimisation scheme could be used.

Depth integrated velocities were calculated from the $u$ and $v$ components of thermal wind velocity by referencing the components to the bottom and integrating over the water column, giving

$$\begin{aligned} U_{therm} &= \int_{bot}^{top} u dz \\ V_{therm} &= \int_{bot}^{top} v dz \end{aligned} \tag{3.3}$$

It is these depth-integrated velocities that are optimally interpolated to a 1°× 1° grid using the interpolation scheme described in section 3.3.

## 3.3 Optimal Interpolation

Optimal Interpolation (also known as Optimal Analysis, Gauss-Markov Interpolation or Objective Mapping) has been used to re-grid the 22,481 depth-integrated, thermal wind velocities, onto the 14,240 1°× 1° grid locations required by the inverse model. Optimal interpolation is also used to re-grid the cross-correlated components of heat and salt transports as described in section 6.

Optimal interpolation was first introduced into meteorology by Gandin [1963] and is based on the Gauss-Markov theorem [Bretherton et al. 1976; McIntosh 1990; Olbers et al. 1992]. Optimal interpolation generates a smooth estimate of some measured field, in this case depth averaged velocities, where the estimation error is minimised in a best, linear, unbiased manner, but most importantly gives an estimate of the error field associated with the interpolated field [Bretherton et al. 1976; Roemmich 1983]. This section contains a brief outline of the theory of optimal interpolation and the reader is directed to

Bretherton et al. [1976] for a more complete description.

Suppose there are $N$ horizontally distributed measurements $\phi$ of zero mean, given by

$$\phi_i = \Phi_i + \varepsilon_i \tag{3.4}$$

Here, $\Phi_i$ is the true value at point $i$ and $\varepsilon_i$ is the associated measurement error. It is assumed that the errors are uncorrelated with each other and that the data have zero mean and known variance, and that the variance of the true value is known, that is

$$\begin{aligned} &< \Phi_i >= 0 \\ &< \varepsilon_i >= 0 \\ &< \varepsilon_i \varepsilon_j >= \sigma_\varepsilon^2 \delta_{ij} \qquad i,j = 1,\ldots,N \\ &< \Phi \varepsilon_i >= 0 \\ &< \Phi_i \Phi_j >= \sigma_\Phi^2 \end{aligned} \tag{3.5}$$

From Bretherton et al. [1976] , the least squares, optimum, linear estimator is defined as

$$\hat{\phi_x} = \sum_{j=1}^{N} C_{xj} \left( \sum_{i=1}^{N} A_{ji}^{-1} \phi_i \right) \tag{3.6}$$

where $A^{-1}$ is the inverse of the matrix of covariance between all pairs of observations (the data-data covariance matrix), where each element can be written as

$$\begin{aligned} A_{ji} &= < \Phi_j \Phi_i > \\ &= < \phi_j \phi_i > + \epsilon^2 \delta_{ji} \end{aligned} \tag{3.7}$$

and $C$ is the matrix of covariance between the estimated values and the observations (the model-data covariance matrix) where each element can be

written as

$$C_{ix} =< \hat{\phi}_x \phi_i > \tag{3.8}$$

It should be noted that when locations of observation points and signal variance are known in advance, the matrices $A$ and $C$ can be computed and therefore the estimate of $\hat{\phi}_x$ depends linearly on the observations $\phi_i$. Thus, equation 3.6 is a linear operator [Bretherton et al. 1976].

It is also a property of the Gauss-Markov theorem that the variance of the error in the estimate can be written in the form

$$< (\phi_x - \hat{\phi}_x)^2 >= C_{xx} - \sum_{i,j=1}^{N} C_{xi} C_{xj} A_{ij}^{-1} \tag{3.9}$$

where $C_{xx}$ is the autocovariance or diagonal element from the covariance matrix.

All optimal interpolation was carried out by applying equation 3.6 with the corresponding errors calculated from equation 3.9. The covariance matrices were calculated using a Gaussian covariance function ($\mathcal{F}$), given by

$$\mathcal{F} = \exp\left\{ -\sqrt{\left(\frac{\triangle x}{LS_x}\right)^2 + \left(\frac{\triangle y}{LS_y}\right)^2} \right\} \tag{3.10}$$

where $\triangle x$ and $\triangle y$ is the distance separating the data point from the grid point and $LS_{(x,y)}$ are the length scales in the $x$ and $y$ direction as discussed in the following section.

### 3.3.1 Implementation and Length Scales

With the available computer memory, it was not possible to interpolate all 22,481 observations onto the 14,240 grid location and estimate the a-posteriori error of the estimates in a single step, as suggested by equations 3.6 and 3.9. The limiting factor is the size of matrices $A$ and $C$ and the time taken to invert

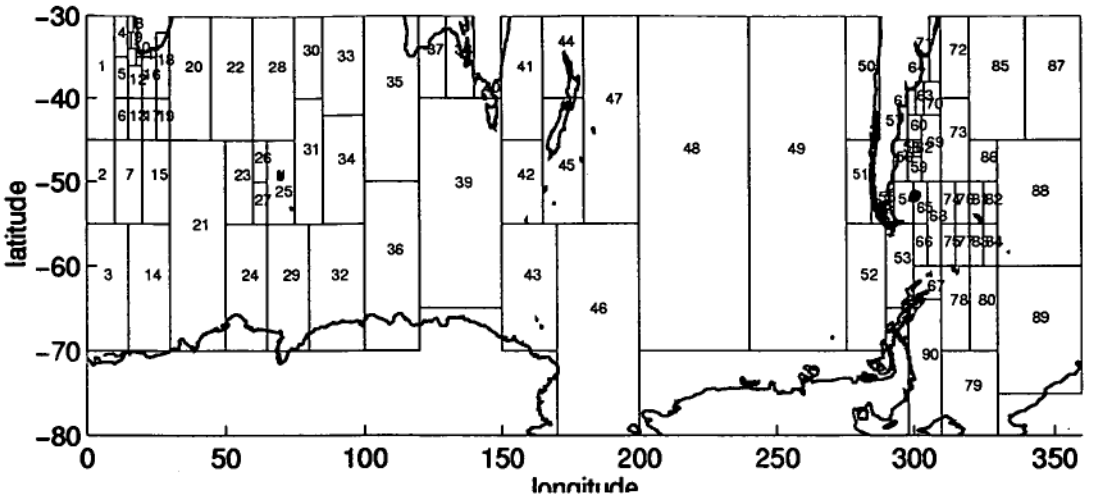


Figure 3.11: The model domain divided into the 90 regions used to optimally interpolate the thermal wind velocities.

matrix $A$. A practical size for these matrices is 1000 rows $\times$ 1000 columns (8 Mb) or for a covariance matrix of 1000 data points and 1000 grid locations. To satisfy matrices of this size, the model domain was divided into 90 regions, each of which contained roughly 1000 data points. The locations of these regions and the number of data and grid points in each region is listed in Table 3.2 and displayed in figure 3.11.

The optimal interpolation technique utilises length scales to calculate the Gaussian function (see equation 3.10) which determines at what distance observations influence the computed estimate at the grid location. To ensure that there are no discontinuities at the edge of the mapping regions, data are required to be included in the estimation process several length scales past the edge of each region. In areas of especially high data density, the computer memory limitations, resulted in many data locations being remapped onto only a few grid locations giving very small region sizes, especially around South America and Africa.

Mapping experiments with a range of length scales were conducted to determine the shortest length scales that satisfactorily resolved the hydrographic

| Optimal Mapping Region Details | | | | | | | | | |
|---|---|---|---|---|---|---|---|---|---|
| Reg. No. | Lat. Range (S) | Lon. Range (E) | No. of Data Pts | No. of Grid Pts | Reg. No. | Lat. Range (S) | Lon. Range (E) | No. of Data Pts | No. of Grid Pts |
| 1 | 30°- 45° | 0°- 10° | 289 | 150 | 46 | 55°- 80° | 170°- 200° | 416 | 1050 |
| 2 | 45°- 55° | 0°- 10° | 197 | 100 | 47 | 30°- 55° | 180°- 200° | 233 | 500 |
| 3 | 55°- 70° | 0°- 15° | 299 | 225 | 48 | 30°- 70° | 200°- 240° | 326 | 1600 |
| 4 | 30°- 35° | 10°- 15° | 1114 | 37 | 49 | 30°- 70° | 240°- 275° | 456 | 1400 |
| 5 | 35°- 40° | 10°- 15° | 40 | 25 | 50 | 30°- 45° | 275°- 288° | 347 | 195 |
| 6 | 40°- 45° | 10°- 15° | 18 | 25 | 51 | 45°- 55° | 275°- 285° | 32 | 100 |
| 7 | 45°- 55° | 10°- 20° | 138 | 100 | 52 | 55°- 70° | 275°- 290° | 122 | 225 |
| 8 | 30°- 32° | 15°- 17° | 25 | 6 | 53 | 55°- 65° | 290°- 300° | 543 | 100 |
| 9 | 32°- 34° | 15°- 16° | 16 | 4 | 54 | 50°- 55° | 293°- 300° | 331 | 35 |
| 10 | 34°- 36° | 15°- 18° | 101 | 8 | 55 | 51°- 53° | 292°- 293° | 22 | 2 |
| 11 | 35°- 36° | 18°- 20° | 117 | 8 | 56 | 45°- 50° | 293°- 298° | 242 | 35 |
| 12 | 36°- 40° | 15°- 20° | 109 | 20 | 57 | 41°- 45° | 295°- 298° | 438 | 12 |
| 13 | 40°- 45° | 15°- 20° | 52 | 25 | 58 | 45°- 47° | 298°- 300° | 656 | 4 |
| 14 | 55°- 70° | 15°- 30° | 116 | 225 | 59 | 47°- 50° | 298°- 303° | 248 | 15 |
| 15 | 45°- 55° | 20°- 30° | 219 | 100 | 60 | 42°- 45° | 298°- 303° | 362 | 15 |
| 16 | 35°- 40° | 20°- 25° | 837 | 24 | 61 | 39°- 42° | 298°- 301° | 313 | 9 |
| 17 | 40°- 45° | 20°- 25° | 57 | 25 | 62 | 45°- 47° | 300°- 303° | 242 | 6 |
| 18 | 32°- 40° | 25°- 30° | 207 | 40 | 63 | 38°- 42° | 301°- 304° | 509 | 6 |
| 19 | 40°- 45° | 25°- 30° | 41 | 25 | 64 | 35°- 38° | 303°- 306° | 271 | 6 |
| 20 | 30°- 45° | 30°- 45° | 358 | 150 | 65 | 50°- 55° | 300°- 305° | 293 | 25 |
| 21 | 45°- 70° | 30°- 50° | 588 | 500 | 66 | 55°- 60° | 300°- 305° | 333 | 25 |
| 22 | 30°- 45° | 45°- 60° | 229 | 150 | 67 | 60°- 64° | 300°- 310° | 568 | 14 |
| 23 | 45°- 55° | 50°- 60° | 78 | 100 | 68 | 50°- 60° | 305°- 310° | 227 | 50 |
| 24 | 55°- 70° | 50°- 65° | 160 | 225 | 69 | 42°- 50° | 303°- 310° | 179 | 42 |
| 25 | 45°- 55° | 65°- 75° | 774 | 100 | 70 | 38°- 42° | 304°- 310° | 264 | 24 |
| 26 | 45°- 50° | 60°- 65° | 42 | 24 | 71 | 30°- 38° | 306°- 310° | 404 | 32 |
| 27 | 50°- 55° | 60°- 65° | 11 | 24 | 72 | 30°- 40° | 310°- 320° | 213 | 100 |
| 28 | 30°- 45° | 60°- 75° | 330 | 150 | 73 | 40°- 50° | 310°- 320° | 152 | 100 |
| 29 | 55°- 70° | 65°- 80° | 228 | 225 | 74 | 50°- 55° | 310°- 315° | 84 | 25 |
| 30 | 30°- 40° | 75°- 85° | 91 | 100 | 75 | 55°- 60° | 310°- 315° | 142 | 25 |
| 31 | 40°- 55° | 75°- 85° | 92 | 100 | 76 | 50°- 55° | 315°- 320° | 321 | 25 |
| 32 | 55°- 70° | 80°- 100° | 174 | 300 | 77 | 55°- 60° | 315°- 320° | 202 | 25 |
| 33 | 30°- 42° | 85°- 100° | 88 | 125 | 78 | 60°- 70° | 310°- 320° | 379 | 100 |
| 34 | 42°- 55° | 85°- 100° | 49 | 125 | 79 | 70°- 80° | 310°- 330° | 97 | 200 |
| 35 | 30°- 50° | 100°- 120° | 480 | 400 | 80 | 60°- 70° | 320°- 330° | 74 | 100 |
| 36 | 50°- 70° | 100°- 120° | 159 | 400 | 81 | 50°- 55° | 320°- 325° | 843 | 25 |
| 37 | 30°- 40° | 120°- 130° | 217 | 200 | 82 | 50°- 55° | 325°- 330° | 153 | 25 |
| 38 | 30°- 40° | 130°- 140° | 556 | 200 | 83 | 55°- 60° | 320°- 325° | 188 | 25 |
| 39 | 40°- 65° | 120°- 150° | 388 | 750 | 84 | 55°- 60° | 325°- 330° | 138 | 25 |
| 40 | 39°- 40° | 143°- 147° | 19 | 1 | 85 | 30°- 45° | 320°- 340° | 217 | 300 |
| 41 | 30°- 45° | 150°- 165° | 610 | 225 | 86 | 45°- 50° | 320°- 330° | 92 | 50 |
| 42 | 45°- 55° | 150°- 165° | 103 | 150 | 87 | 30°- 45° | 340°- 360° | 133 | 300 |
| 43 | 55°- 70° | 150°- 170° | 212 | 300 | 88 | 45°- 60° | 330°- 360° | 358 | 450 |
| 44 | 30°- 40° | 165°- 180° | 246 | 150 | 89 | 60°- 75° | 330°- 360° | 347 | 450 |
| 45 | 40°- 55° | 165°- 180° | 410 | 225 | 90 | 64°- 80° | 298°- 310° | 306 | 192 |

Table 3.2: The position, number of data points and grid points in each of the 90 regions shown in figure 3.11 used by the optimal mapping.

data without introducing significant noise errors. The choice of length scales was primarily controlled by the distribution of the data. In data dense regions, such as the Agulhas Current region or Drake Passage, the shortest length scales could be reduced to 4°. In data sparse regions, such as the South Pacific, the shortest optimal length scale was about 9° in the east-west direction. For ease of application, and interpretation of the results, it was decided to use constant length scales for the entire model domain. Thus the final short length scales were chosen so that the errors introduced in the data sparse regions were balanced against the signals calculated in the data dense areas of the model.

The final interpolated fields were generated from the raw data in a four step process using two length scales. Initially, the raw data are interpolated back onto the data locations at long length scales to calculate residuals on the data locations. Secondly, these residuals are interpolated onto the data locations using shorter length scales to determine how well both length scales are capturing the signals present within the data. The third step interpolates the data onto the grid locations at the long length scales with the final step interpolating the residuals calculated in the first step, onto the grid locations at the shorter length scales. This allows the interpolation of the data at the shortest length scale, whilst trying to preserve the longer scale structure of the data in data sparse regions.

Because the properties of the Southern Ocean are zonal in nature [Nowlin and Klinck 1986] length scales were chosen that were longer in the E-W direction than in the N-S direction. This is also consistent with the orientation of most hydrographic sections in the Southern Ocean which are generally orientated N-S. As a result of the section orientation, the average station spacing is shorter in the N-S direction and longer in the E-W direction. Combined with the knowledge that measoscale turbulence has an upper limit of

between 150km and 250 km throughout the Southern Ocean [Nowlin and Klinck 1986] lead to the selection of long length scales of 25° E-W and 15° N-S with short length scales of 7° E-W and 5°N-S.

### 3.3.2 Interpolated fields of Thermal Wind and associated errors

Before discussing the regridded thermal wind velocities, there are several checks that are carried out to confirm that the mapped field is a good representation of the "true" field seen in the hydrographic data. Firstly, our assumption made in section 3.2.3, ie. that "more data are better", can be verified by inspecting signal variances of the two datasets. Secondly, the assumptions concerning the relationship of the noise and the data of the Hydrographic Atlas of the Southern Ocean (ie., equation 3.5), are confirmed by inspecting the correlation statistics. Finally, it must be determined that the length scales are appropriately capturing the signal of the true field.

The signal variances were calculated for each of the 90 regridded regions shown in figure 3.11, by summation of the difference between the velocity of the true value and the region mean of the true value, divided by the number of observations in the region, in the $u$ and $v$ direction, expressed as

$$VAR_i = \frac{1}{N} \sum_{n=1}^{N} \left( u_{(i,n)} - \overline{u_i} \right)^2 \tag{3.11}$$

where $i = 1, \ldots, 90$ is the region number. The less variation about the mean, the smaller will be the variance, and the more data involved in forming the variance, the less influence outliers will have on the variance.

The Signal variances for the two hydrographic datasets are presented in figures 3.12 and 3.13 and show that, on average, the signal variances for the Hydrographic Atlas of the Southern Ocean dataset are smaller than the Southern Ocean Atlas. The Southern Ocean Atlas is also more variable from

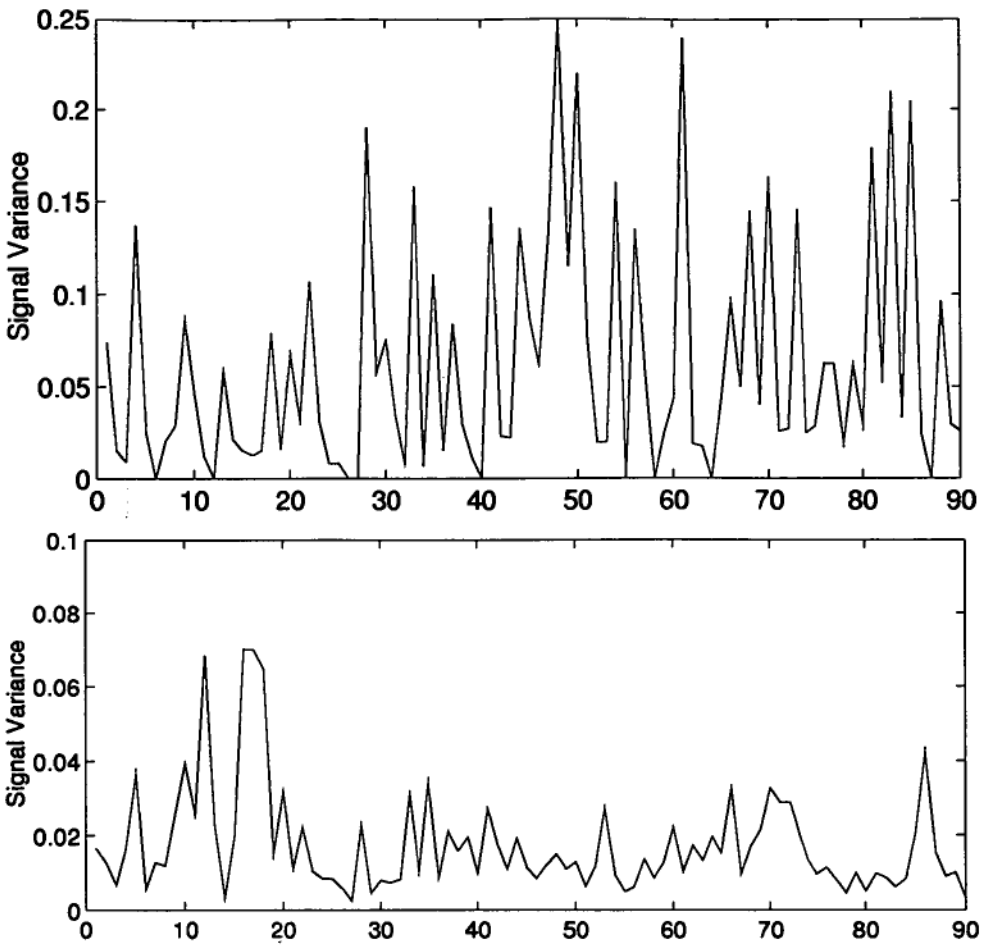


Figure 3.12: Comparison of signal variance of the u-component of thermal wind for each interpolation region between Southern Ocean Atlas (top) and Hydrographic Atlas of Southern Ocean (bottom). $(ms^{-1})$. Note the vertical scale change in the two plots.

region to region and does not show a relationship between signal variances and ocean circulation within each region. This is usually due to the low number of observations within each region allowing outliers to influence the signal variance. Several regions have a signal variance of zero because there are no valid observations within those regions.

By close inspection of the signal variances for the Hydrographic Atlas of the Southern Ocean, there is a clear relationship between the expected oceanography of the region and the signal variance of the region. Within the first 20 regions, there are several large signal variances, in particular, regions 5,

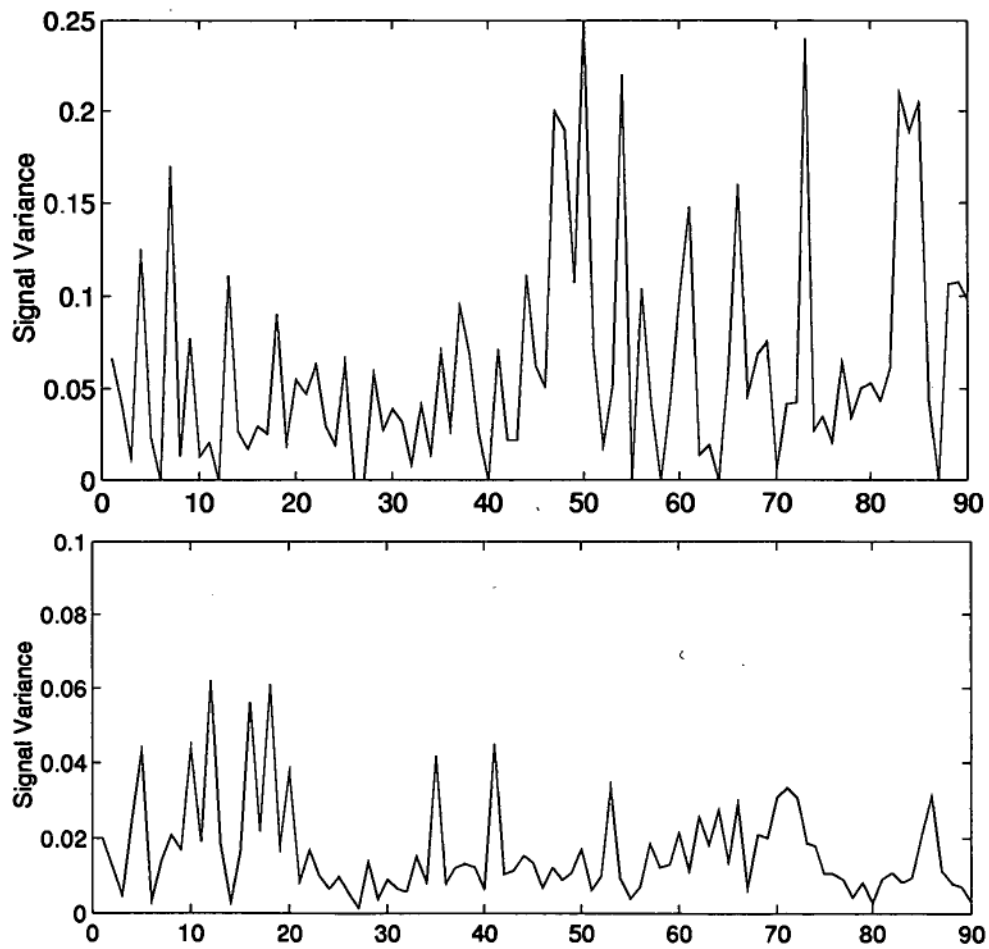


Figure 3.13: Comparison of signal variance of the v-component of thermal wind for each interpolation region between Southern Ocean Atlas (top) and Hydrographic Atlas of Southern Ocean (bottom). ($ms^{-1}$). Note the vertical scale change in the two plots.

10, 12, 16, 17 and 18. These regions are situated in the Agulhas Retroflection (see figure 3.11) where there it is expected that the calculated velocities will have a large variation. Observations in these regions suggest that there are many eddies and meanders of the mean current, so that calculated currents could have large magnitudes in any direction. Other mapping regions where there are known eddies, and so large velocity changes, occur in the Leeuwin Current (region 35), the EAC (41), Drake Passage (53) and down the east coast of South America (regions 70, 71, 72 and 86) also have relatively large signal variances. The signal variances associated with the Agulhas Current are the largest in the model domain suggesting that the Agulhas Current has the largest velocity fluctuations about the mean circulation and is therefore probably the most dynamic region of the Southern Ocean. This can be confirmed by inspection of Topex/POSIEDON satellite altimeter data, compared to the inverse solution in section 5.4, that computes the highest eddy kinetic energy values in the Agulhas Current region.

From the signal variances presented in figures 3.12 and 3.13, the optimal interpolation errors were calculated for the u and v component of thermal wind using equation 3.9 and are presented for comparison of the two datasets in figures 3.14 and 3.15. These plots show that the errors associated with the Southern Ocean Atlas are generally a factor of 10 larger than the errors associated with the Hydrographic Atlas of the Southern Ocean. The discontinuities between regions, associated with using regional signal variances, are clearly visible in all error fields. Generally, the areas associated with highest error fields are areas that correlate with the lowest data density. The northern South Pacific has the lowest data density in both datasets and is the area of highest interpolation error in both components of transport. From these figures and the above discussion, it is clear that the superior data coverage of the

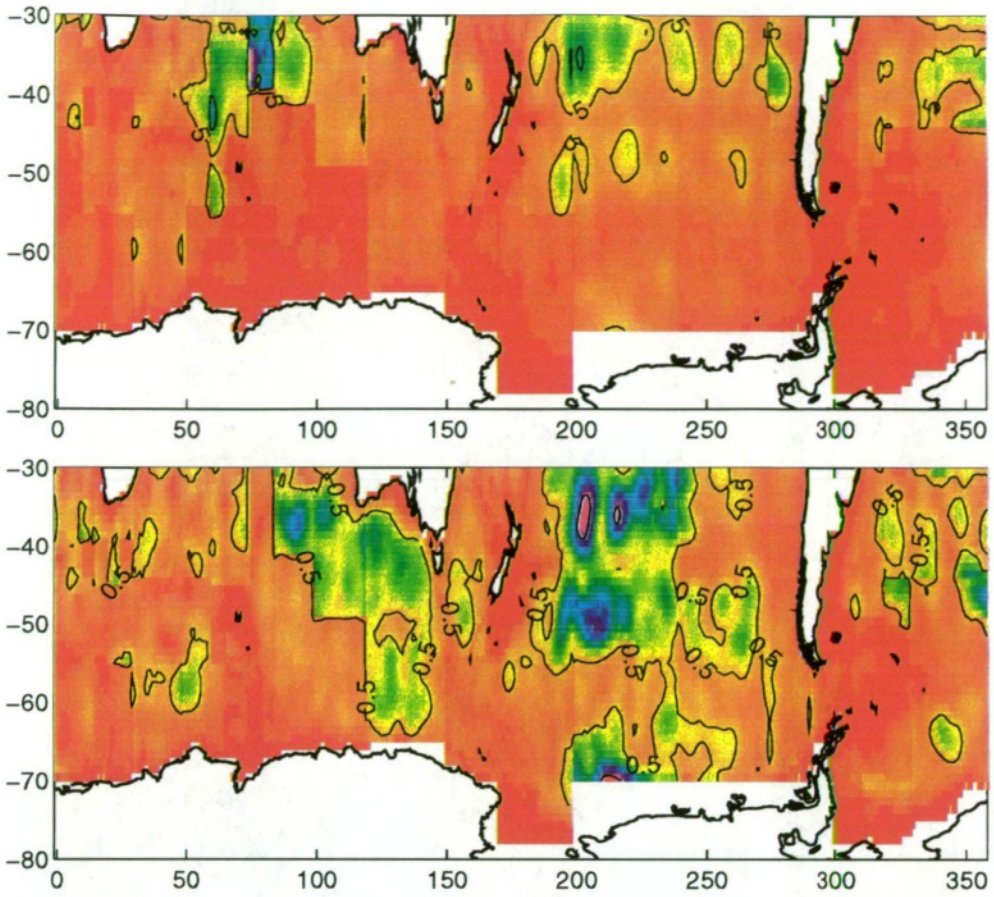


Figure 3.14: Optimal interpolation errors for the u-component of thermal wind transports (Sv/degree), generated from the Southern Ocean Atlas (top) and Hydrographic Atlas of the Southern Ocean (bottom). Note: factor of 10 Scale change between top and bottom panel.

Hydrographic Atlas of the Southern Ocean makes it the best dataset to use.

Concentrating on the error fields of Hydrographic Atlas of the Southern Ocean the majority of the Southern Ocean has been interpolated with errors less than .5 Sv. Two main regions of high error exist, in the Pacific and south of Australia. Both are primarily a result of low data density, although relatively large signal variances are partly responsible south of Australia (see regions 33 and 35 at the bottom of figure 3.12). The largest error in both the u and v-component of transport is located at 38°S, 205°E, having magnitudes of 3 Sv and 2.8 Sv respectively.

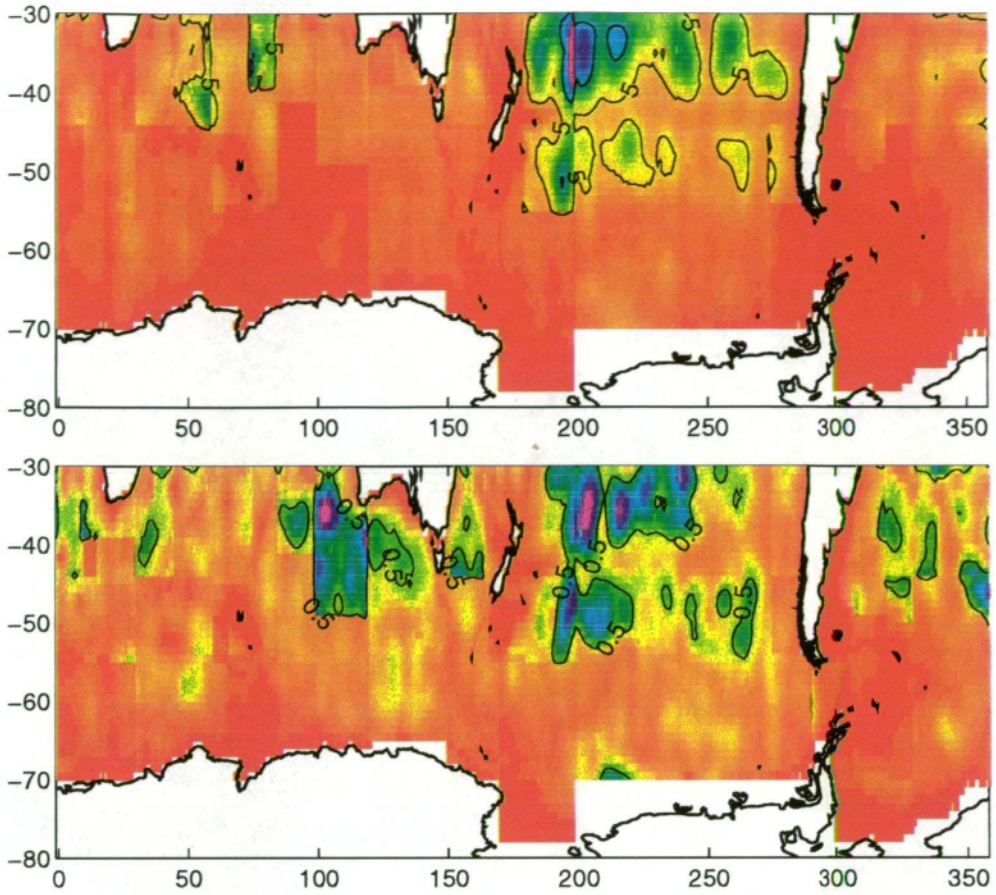


Figure 3.15: Optimal interpolation errors for the v-component of thermal wind transports (Sv/degree), generated from the Southern Ocean Atlas (top) and Hydrographic Atlas of the Southern Ocean (bottom). Note: factor of 10 Scale change between top and bottom panel.

It is interesting to note that the area of ocean where the ACC is located generally has lower errors than the ocean to the north or south. This is particularly clear in the u-component between 180° and 260°E. This is most likely due to the increased data density around the ACC. Most north-south orientated Southern Ocean cruises try to calculate an estimate for the transport of the ACC, so the sampling rate increases around the jet. This increase in data density is clearly visible in the south Pacific by inspection of the data locations in figure 3.9. Looking at the optimal interpolation errors presented in figures 3.14 and 3.15, it is clear that our assumption that "more data is better" is

correct and that the Hydrographic Atlas of the Southern Ocean is the better atlas to use in the inverse model. Further references to hydrographic data in this thesis, assume the Hydrographic Atlas of the Southern Ocean.

To confirm that the assumptions made in implementing the optimal interpolation are correct, the noise of the data within each region was calculated using closest point statistics, ie

$$NOISE_i = \frac{1}{2N} \sum_{n=1}^{N} \left( u_{(i,n)} - u_c \right)^2 \tag{3.12}$$

where $u_c$ is the closest observation to $u_{(i,n)}$. The average correlation between the data and the noise $< \Phi \varepsilon_i >$ was .02 and the correlation between the noise and itself $< \varepsilon_i \varepsilon_j >$ when $i \neq j$, was .01. The mean of the $u$ and $v$ components of velocity were .0018 m $s^{-1}$ and .0052 m $s^{-1}$ respectively, which, considering both fields range from -.3 m $s^{-1}$ to .3 m $s^{-1}$, is close to a zero mean field. Therefore, the assumptions made before applying the optimal interpolation are reasonably correct.

Before, moving on to discuss the optimally interpolated transport fields, it must be determined that the regridded field is a true representation of the data. That is, the regridding process has not introduced unwanted aliasing, and that the length scales chosen for regridding are appropriate. Some assessment of this can be achieved by inspecting the mean of the residuals after the mapping and the ratio of the variance of the residuals to the variance of the apriori noise of the data. For a successful mapping, the mean of the residuals should be close to zero and the ratio of variance of residuals to the apriori noise should be close to one. The residuals of the data are calculated by optimally interpolating the data back onto the data locations and subtracting the optimally interpolated data from the raw data. The mean of the residuals for the optimally interpolated fields shown in figure 3.17, were -.5 Sv and .9 Sv for u and v components

respectively, with a range of ±50 Sv for the original fields. More importantly, these 'biases' are smaller than the estimated error shown in figure 3.14.

When interpolating a data field, it is desirable to generate a field that simply represents the signal of the data and not the noise of the data. A relatively easy test is to inspect the ratio of the variance of the residuals of the interpolation process and the variance of the noise of the data. If the ratio is greater than 1, the mapping is not representing all of the signal and the regridded field is too smooth. The smoothness of the field is possibly a result of the length scales being too long and hence the length scales could possibly be shortened. If the ratio is less than 1, the regridded field is possibly fitting the data too well and so is likely to be introducing artificial high frequency noise. This introduction of noise into the regridded field is possibly due to the length scales being too short and so the length scales could be lengthened.

Ideally, the ratios of the variance of the residuals and the variance of the noise of the data should be close to 1. The value of the ratios for the 90 regridding regions, presented in figure 3.16, were calculated from the optimal interpolation process that used the constant length scales outlined in section 3.3.1. Most of the regions are close to 1. The regions where the ratios are not close to 1 are regions 6 and 9 in the v-component, and region 27 in the u-component. The two v-component regions have ratios greater than 1, suggesting that the regridded field is too smooth and that shorter length scales could have been used. Both regions are in the Agulhas Retroflection, a particularly active area of the ocean, with high data density. The reason for the low ratio number of region 27, near Kerguelen Island, in the u-component is unclear. From figure 3.16, it can be concluded that the optimal interpolation scheme has represented the data as accurately as possible without transferring noise of the data into the final field.

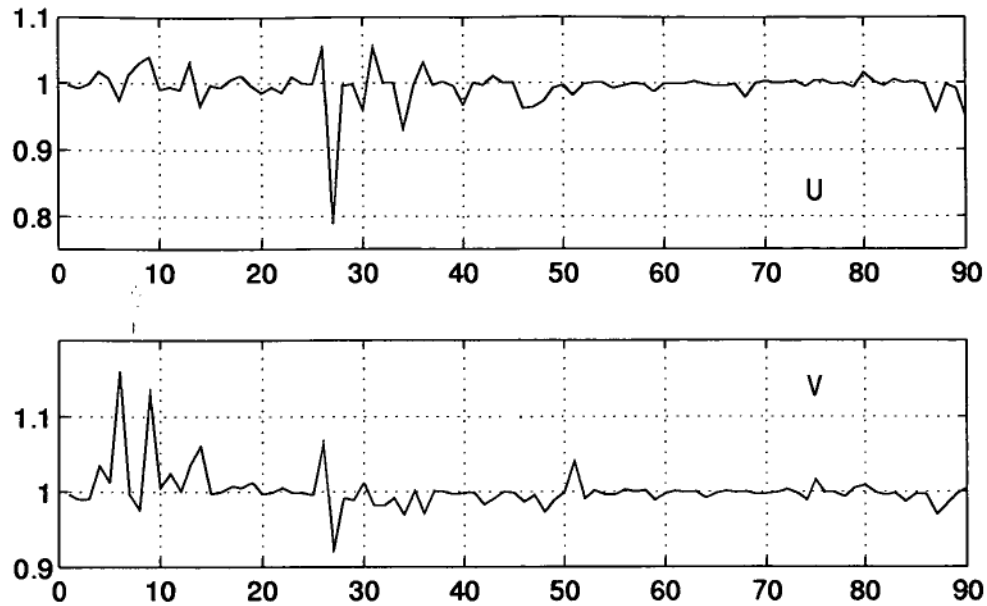


Figure 3.16: Ratios of variance of residuals to variance of noise for each of the 90 optimal interpolation regions for the u-component (top) and v-component (bot).

Another confirmation of the validity of the mapped fields can be seen in figure 3.17. It is possible to locate the main features of Southern Ocean circulation with the ACC, most boundary currents and basin scale gyres clearly discernible. However there are obvious shortcomings of this circulation that the inverse model will overcome.

The ACC is present around the globe, although in some regions the main jet associated with the ACC clearly does not conserve mass with large arrows into a region and small arrows out, or vice versa. At 50°S, 40°E a strong eastward jet (large arrows) suddenly disappears into a weak eastward flow (small arrows). Some flow turns north but not enough to conserve mass in this region. There are several regions of this nature associated with the ACC that can be distinguished by visual inspection, and several that will become apparent in section 4.1 when the divergence of mass is calculated. It also becomes clear at this stage that there is a strong relation between the location of the ACC and the underlying topography. Features like the Kerguelen Plateau,

Australian-Antarctic Ridge, Macquarie Ridge and Pacific-Antarctic Ridge all have a strong interaction with the ACC. For named topographic features see Appendix A.

Some boundary currents are present in the interpolated circulation, with the Agulhas and East Australian Current (EAC) well defined. The Agulhas sweeps around the southern tip of Africa before recirculating to join the ACC southeast of Africa. The EAC flows down the east coast of Australia before separating from the coast to flow across the Tasman Sea and around the north of New Zealand. There is a hint of a Peru-Chile boundary current although this is in the wrong direction compared to published results [Wooster and Gilmartin 1961; Silva and Neshyba 1979]. The Brazil and Malvinas Currents are mostly missing, although there seems to be a circulation associated with the Brazil-Malvinas Confluence generated at 40°S, 310°E.

Other circulation features that are present in figure 3.17 are an indication of the Weddell Sea Gyre circulating in a clockwise direction around the Weddell Sea, the southern half the South Pacific Gyre that flows into the model domain to the east of New Zealand and out of the model domain east of 240°E, and possibly an Indian Ocean gyre. The South Atlantic Ocean appears to be a very active but confused ocean with many regions of non-mass conservation.

This chapter has outlined the sources and selection of the data used in this thesis. The Hellerman and Rosenstein windstress dataset, with a more complete coverage of the model domain, has been utilised to calculate the Ekman transport and the curl of the windstress over the model domain. The raw hydrographic data from the Hydrographic Atlas of the Southern Ocean [Olbers et al. 1992] has been used to calculate the thermal wind transports. These thermal winds have been optimally interpolated onto a 1°× 1° grid over the model domain using two length scales (long: 25°E-W & 15°N-S, short: 7°E-W

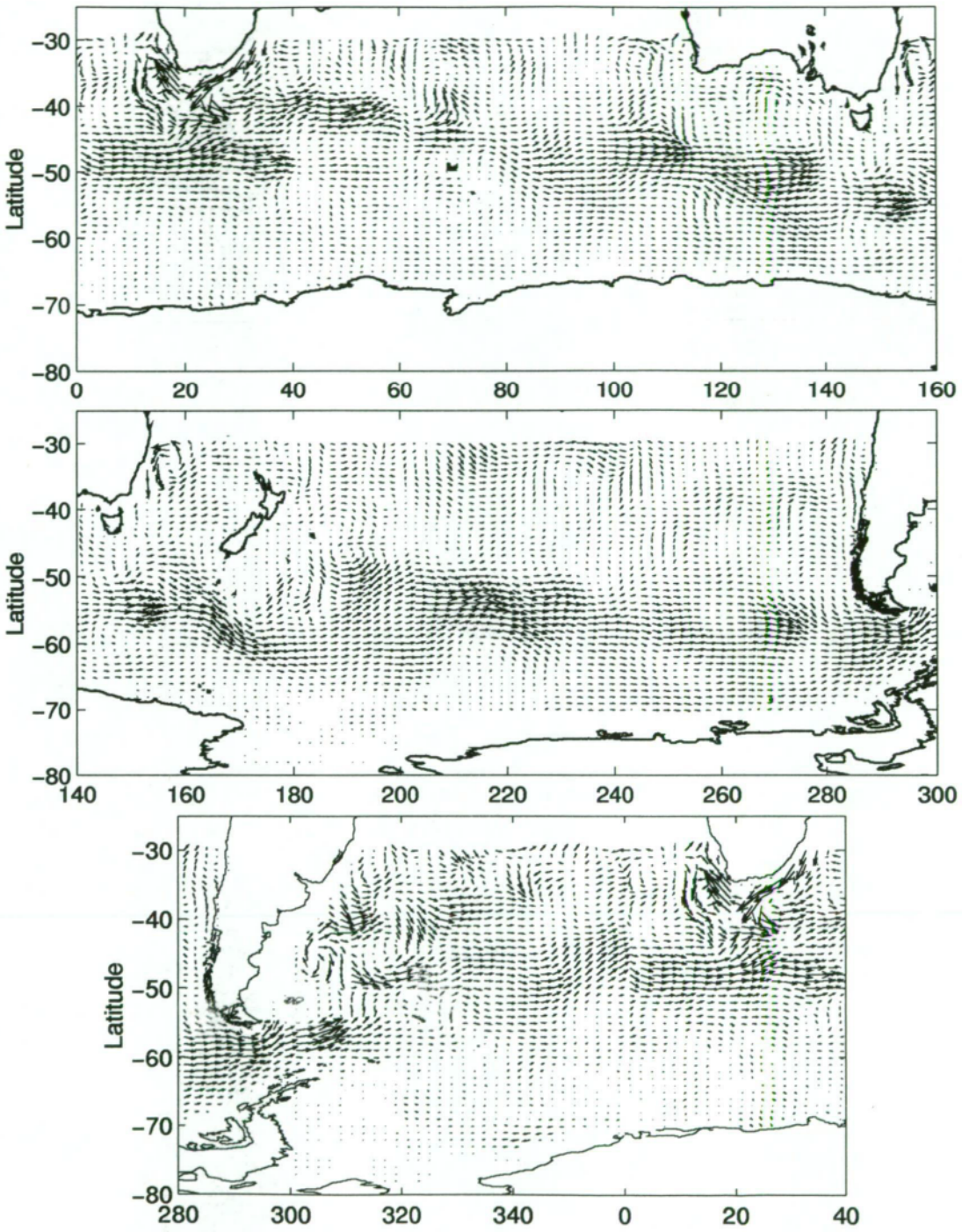


Figure 3.17: Optimally interpolated thermal wind transports on 1° latitude x 2° longitude grid (1°= 5Sv).

& 5°N-S) that, from an analysis of the ratios of the variance of the residuals and the variance of the noise of the data indicate are a satisfactory choice of length scales.

By inspection of the optimally interpolated thermal wind transports the calculated circulation does not conserve mass. The Ekman transport field, the curl of the windstress and the thermal wind transport field are passed into the inverse model described in the next chapter so that a total mass conserving, weakly vorticity conserving circulation can be calculated.

# Chapter 4

# The Model

Inverse theory, as discussed in chapter 2, has been applied to the problem of determining reference level velocities, and only once in the Southern Ocean [Olbers 1989]. The spatial resolution of inverse models are generally coarse, although recent applications have obtained resolutions of 2°× 2° in a numerical model ocean [Zhang 1995], and 3°× 3° in a densely sampled real ocean [Hogg 1987]. Previous work has divided the ocean into layers, calculated the divergence of conserved properties, and then generated reference velocities and mixing coefficients that minimised these divergences in a least squares sense. These systems are usually highly underdetermined and require many conservation constraints (i.e., mass or heat flux across a section) to generate reliable solutions.

The primary aim of this research is to understand the circulation of the Southern Ocean by developing a high resolution inverse model that was computationally tractable, yet theoretically consistent. This was done using appropriate equations with simple boundary conditions, a minimum number of constraints to determine a realistic mean circulation without the need to "artificially tune" the results. Previous inverse studies have prescribed a solution by constraining the transport through a section to be within certain bounds. For example, Rintoul [1988] in his South Atlantic model prescribed a transport of 130±13 Sv through Drake Passage. The uniqueness of the inverse model in this thesis is that it has no such constraints applied to it, resulting in a circulation derived primarily from hydrographic data.

In previous inverse models, most of the information on reference velocities

was contained in the top-to-bottom layer integrals of the continuity equations. That is, total mass conservation is the key element in determining the unknown reference velocities [Wunsch 1978; Rintoul 1988]. This suggests that the top-to-bottom integrals of the continuity equations and mass conservation constraints contain most of the information required to solve for the unknown reference velocities.

The inverse model developed in this chapter prescribes top-to-bottom layer integrals to apply the conservation of mass constraints on a 1°× 1° single layer, finite difference grid of the Southern Ocean. The 1°× 1° grid yields the highest resolution inverse model yet achieved and the length scales of the data can be interpolated onto the 1°× 1° grid without introducing excessively large mapping errors, as seen in Chapter 3. The northern boundary of the model is selected as 30°S or the continental margins of Australia, Africa, or South America. The southern boundary is the Antarctic continent, except in the Weddell Sea, where the boundary is 80°S. Between 160°W and 70°W, the model domain is set to 70°S due to lack of data. This total domain results in 14,240 grid locations on which both components of the reference velocity (or 28,480 unknowns) are calculated. There are 14,458 mass conservation equations creating an algebraic system that is approximately 50% underdetermined.

A set of independent equations, using linear vorticity based on the work by Schott and Stommel [1978], Bigg [1985] and Mellor et al. [1982], was introduced to reduce the degree to which the system is underdetermined. As explained in section 4.3, these equations are not applied to all grid location in the model and so only introduce a further 12,487 equations. The use of vorticity helps generate the large scale ocean circulation that exists in the interior of the ocean and strengthens the directional control that bathymetry has on the circulation.

This chapter describes the implementation of the conservation of mass and

linear vorticity within the inverse problem and the applied boundary conditions. In section 4.4 the method of solving the problem is presented together with a discussion of the solution.

## 4.1 Conservation of Mass

The conservation of mass, applied using steady state assumptions, can be written as

$$\nabla \cdot \mathbf{u} = 0 \tag{4.1}$$

Because of measurement and interpolation errors, the equality of equation 4.1 is only solved approximately for the total depth-integrated transport ($T_{Tot} = \int (u, v) dz$). $T_{Tot}$ has three components: the depth-integrated thermal wind transport ($T_{Th}$), the wind-driven Ekman transport ($T_{Ek}$) and the unknown reference transport ($T_{Ref}$). Writing $T_{Tot}$ in terms of equation 4.1 gives

$$\nabla \cdot T_{Tot} = \nabla \cdot T_{Th} + \nabla \cdot T_{Ek} + \nabla \cdot T_{Ref} \approx 0 \tag{4.2}$$

which can be rearranged to give the mass conservation equation constraint on the reference velocities in terms of the thermal wind and Ekman transports, as applied to the inverse model

$$\nabla \cdot T_{Ref} \approx -\left[\nabla \cdot T_{Th} + \nabla \cdot T_{Ek}\right] \tag{4.3}$$

The horizontal divergence of the depth-integrated, thermal wind and Ekman transports was calculated on a staggered grid, as shown in figures 4.1 and 4.2. The horizontal divergence operator incorporates the depth-integrated components of thermal wind and Ekman transport at the four model grid locations surrounding the divergence grid point creating a "divergence box".

The divergence box approach was utilised instead of a standard centred finite difference approach because, although the divergence estimate using the centred finite difference would estimate the divergence on the same grid as the thermal wind and Ekman transport, the grid can be aliased into two separate grids. This aliasing arises because the simplified form of centred finite difference has no component of the central grid location involved in the calculation, i.e., the central finite difference at grid points $i$ and $i+1$ is

$$\begin{aligned} \hat{u_i} &= u_{i+1} - u_{i-1} \\ \hat{u_{i+1}} &= u_{i+2} - u_i \end{aligned} \tag{4.4}$$

This results in neighbouring grid points having absolutely no influence on each other during the inversion.

The divergence box operator is first presented in cartesian co-ordinates, so that the finite difference nature of the operator is easily discernible. Using the subscript notation defined in figures 4.1 and 4.2, the cartesian co-ordinate form of the divergence box operator for $T_{Th}$ or $T_{Ek}$, where for simplicity, the subscripts $_{Th}$ and $_{Ek}$ are dropped, is given by

$$\begin{aligned} \nabla \cdot T &= \frac{\partial U}{\partial x} + \frac{\partial V}{\partial y} \\ \nabla \cdot T_{(i,j)} &= \left[ \frac{U_{(i,j+1)} - U_{(i,j)}}{2\Delta x} + \frac{U_{(i+1,j+1)} - U_{(i+1,j)}}{2\Delta x} \right] \\ &\quad + \left[ \frac{V_{(i+1,j)} - V_{(i,j)}}{2\Delta y} + \frac{V_{(i+1,j+1)} - V_{(i,j+1)}}{2\Delta y} \right] \end{aligned} \tag{4.5}$$

where $U$ and $V$ are, respectively, the north and east components of depth-integrated transport whose divergence is being calculated at latitude $i$, longitude $j$.

In the inverse model, the spherical co-ordinate form of equation 4.5 is utilised, expressed as

$$\nabla \cdot T = \frac{1}{R \sin\theta}\left(\frac{\partial U}{\partial \phi} + \frac{\partial \sin\theta V}{\partial \theta}\right)$$

$$\begin{aligned}\nabla \cdot T_{(i,j)} = {} & \frac{1}{R\sin\theta_{(i)}}\left[\frac{U_{(i,i+1)} - U_{(i,j)}}{2\Delta\phi}\right] + \frac{1}{R\sin\theta_{(i+1)}}\left[\frac{U_{(i+1,j+1)} - U_{(i+1,j)}}{2\Delta\phi}\right] \\ & + \frac{1}{R\sin\left(\frac{\theta_{(i)}+\theta_{(i+1)}}{2}\right)}\left[\frac{V_{(i+1,j)}\sin\theta_{(i+1)} - V_{(i,j)}\sin\theta_{(i)}}{2\Delta\theta}\right] \\ & + \frac{1}{R\sin\left(\frac{\theta_{(i)}+\theta_{(i+1)}}{2}\right)}\left[\frac{V_{(i+1,j+1)}\sin\theta_{(i+1)} - V_{(i,j+1)}\sin\theta_{(i)}}{2\Delta\theta}\right]\end{aligned} \tag{4.6}$$

where $R$ is the mean radius of the earth (approximately 6353.8 km), $\theta$ is the latitude and $\phi$ is the longitude.

It should be noted that equation 4.6 can be expanded so that the $V$ component is taken outside the gradient operator. i.e.,

$$\nabla \cdot T = \frac{1}{R\sin\theta}\frac{\partial u}{\partial \phi} + \frac{1}{R}\frac{\partial v}{\partial \theta} + \frac{v}{\tan\theta} \tag{4.7}$$

This manipulation makes the A matrix easier to generate but introduces a $\frac{1}{\tan\theta}$ term. This $\frac{1}{\tan\theta}$ term only operates on the $v$ component and when the finite differencing is introduced, increases the weighting of $v$. The increased weighting forces the inverse model to solve the mass imbalances by only varying $v$ and makes no change to the $u$ component because of its effective down weighting.

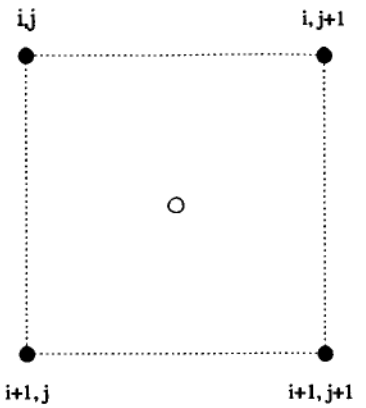


Figure 4.1: A single grid cell $(i, j)$ of the inverse model centred on latitude (i+.5)° and longitude (j+.5)° over which the properties of mass and linear vorticity are conserved. $U$ and $V$ components of transport and linear vorticity estimates are located on solid circles. Transport divergence is calculated at the open circle using the $U$ and $V$ components of transport located at the solid circles.

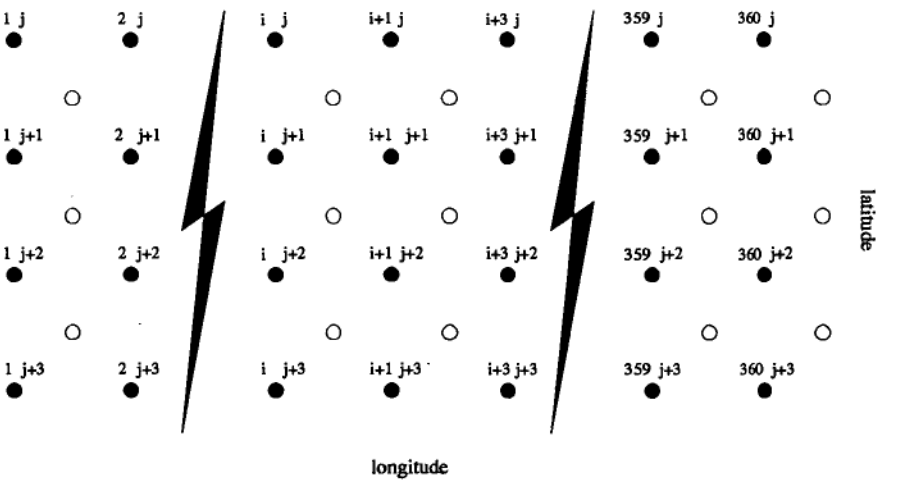


Figure 4.2: Grid numbering of the model domain. Solid and open circles represent transport and divergence grid locations as in figure 4.1. Latitude $j$ varies from 30°E to 80°E. The origin of the divergence grid is the top-leftmost divergence grid location. Note divergence grid locations on the eastern boundary (divergence grid locations [360, 30 - 80]) are used to continue circulation from east to west as described in section 4.3.

The Southern Ocean circulation derived by the model using equation 4.7 is unrealistically north-south. Hence, solutions in this thesis are generated using the unexpanded form given in equation 4.6.

The divergence field of the thermal wind and Ekman transports calculated using equation 4.6 is shown in figure 4.3. This divergence field forms the right hand side of equation 4.3. Positive values represent areas of the ocean where, over the total 1°× 1° water column, there is more mass leaving than entering the column, creating a net divergence of mass. Negative values represent convergent areas over the total water column. The most intense divergence and convergence areas are associated with the most active areas of the ocean. The most intense region of convergence is located in the Agulhas Current region with the most intense divergence occurring in Drake Passage. The ACC has many areas of convergence and divergence and the region of obvious mass convergence discussed in section 3.3.2 is visible as the area of blue at 50°S, 40°E. Other regions of mass imbalance, not obvious in figure 3.17, are visible throughout the ACC. The open ocean, away from the major current systems, has much lower mass imbalances. The model solution should explain most of the variance seen in figure 4.3 by adding mass transport to ocean circulation entering divergent areas and subtracting mass transport to ocean circulation entering convergent grid cells.

## 4.2 Conservation of Linear Vorticity

The linear vorticity equation utilised in this thesis is similar to the work by Schott and Stommel [1978], Bigg [1985] and Mellor et al. [1982]. The linearised, steady state form of linear vorticity, as described in Schott and Stommel [1978], is given as

$$\beta v = f\frac{\partial w}{\partial z} \tag{4.8}$$

where $\beta$ is $\frac{1}{R}\frac{\partial f}{\partial \theta}$, the variation of the Coriolis parameter $f$ at latitude $\theta$, and $w$ is the vertical component of velocity. $v$ is the $y$ component of total horizontal velocity minus Ekman velocity (ie., $v_{Th} + v_{Ref}$). Note, lower case $u$ and $v$ are used to signify velocity and uppercase $U$ and $V$ represent depth-integrated transport.

Using a single layer model allows two important assumptions to be included. Because vorticity is conserved on lines of constant $\frac{f}{H}$ (H = water column length), it is important to consider how circulation may change in a variable ocean depth $H$, due to forcing at the top and bottom of the water column.

The first assumption accounts for the surface forcing on $H$ by the Ekman pumping velocity $\omega_e$ . Over the total water column, $\frac{\partial \omega_e}{\partial z}$ will have a uniform value of $\frac{\omega_e}{H}$ and the Ekman velocity can be approximated in terms of the curl of the windstress and is simply the Sverdrup transport, expressed as

$$\omega_e = \frac{1}{\rho f}\left(\nabla \times \tau\right)_z \tag{4.9}$$

The second assumption involves the forcing on $H$ as the water column passes over bottom topography. This translates into a vertical bottom velocity $\omega_b$ that is driven by the gradient of $H$ times the total horizontal bottom velocity.

$$\omega_b = -\begin{bmatrix} u_{Th} + u_{Ref} \\ v_{Th} + v_{Ref} \end{bmatrix} \cdot \nabla H \tag{4.10}$$

However, remember that the thermal wind is referenced to the bottom (ie. $u_{Th} = v_{Th} = 0$), simplifying $w_b$ to be a function of the unknown reference velocity and the gradient of H. Again, over the total water column, $\frac{\partial \omega_b}{\partial z}$ has a

constant value of $\frac{\omega_b}{H}$.

Using equations 4.9 and 4.10 and taking the vertical integral, equation 4.8 can now be expressed as

$$\beta(V_{Th} + V_{Ref}) = \frac{1}{\rho}(\nabla \times \tau)_z - \frac{f}{H}\begin{bmatrix} U_{Th} \\ (V_{Th} + V_{Ref}) \end{bmatrix} \cdot \nabla H \qquad (4.11)$$

where $U$ and $V$ are the depth-integrated transports. The minus sign accounts for a positive (downward) velocity compressing the water column at the surface, $\omega_e$, but stretching the water column at the ocean floor. $\omega_b$

Rearranging equation 4.11 for the unknown reference velocities gives the form of the conservation of linear vorticity equation used in this thesis,

$$U_{Ref}\left(\frac{f}{\beta H R \sin\theta}\frac{\partial H}{\partial \phi}\right) + V_{Ref}\left(\frac{f}{\beta H R}\frac{\partial H}{\partial \theta} + 1\right) = \frac{1}{\beta\rho}(\nabla \times \tau)_z - V_{Th} \qquad (4.12)$$

where $\frac{1}{R\sin\theta}\frac{\partial H}{\partial \phi}$ and $\frac{1}{R}\frac{\partial H}{\partial \theta}$ are the $x$ and $y$ components of $\nabla H$ written in spherical coordinates.

Equation 4.12 was implemented using centred finite differences to calculate $\nabla \times \tau$ and $\nabla H$ on the transport grid locations shown in figures 4.1 and 4.2.

## 4.3 Boundary Conditions

There are three types of boundary situations in the model; continuity of flow across the Greenwich meridian, open boundaries and closed boundary conditions. The eastern most point of the model domain is 360°E [U(360,j)], and the western most point is 0°E [U(1,j)]. The continuity of flow from the eastern boundary at 360° to the western boundary at 0° represents the continuous Southern Ocean. That is, flow out of the models eastern boundary is

equal to flow into the model's western boundary. For the conservation of mass equations, the continuity of total transport across the Greenwich meridian was achieved by calculating the divergence of mass between the eastern-most grid points $[u(360, j)]$ and the western-most grid points $[u(1, j)]$ (see figure 4.2). For linear vorticity, the centred finite differences of $\nabla \times \tau$ utilised the windstresses on either side of the Greenwich meridian.

At the open northern boundary (30°S), the model solves for the boundary transports and there are no boundary conditions applied. This is unlike previous inverse models where flux constraints of mass and/or other conservative properties are applied to impose a circulation solution on the model [Rintoul 1988]. It is also unlike general circulation models that need to have boundary conditions to be well posed. This formulation of the boundary explicitly avoids the problems associated with the application of open boundary conditions in forward models. Explicitly solving for the boundary conditions results in a circulation into and out of the model domain that is generated by the data, and not by assumptions about what the modeller thinks should be flowing across the northern boundary.

At closed boundaries, the total transport cannot pass through land margins, and normal flow is explicitly set to zero. The resulting mass imbalance around closed land boundaries is the dominant signal in the inverse model. Figure 4.4 illustrates the model grid near a continental boundary. The thermal wind and Ekman transport values are explicitly set to zero on the land grid points ($U_{1,4}$, $V_{1,4}$). Therefore, the source of the mass imbalance is the thermal wind and Ekman transports on the ocean grid points. This results in the divergence operator as exactly

$$\nabla \cdot T = (U_2 - \not{U}_1^0) + (U_3 - \not{U}_4^0) + (V_3 - V_2) + (\not{V}_4^0 - \not{V}_1^0) \qquad (4.13)$$

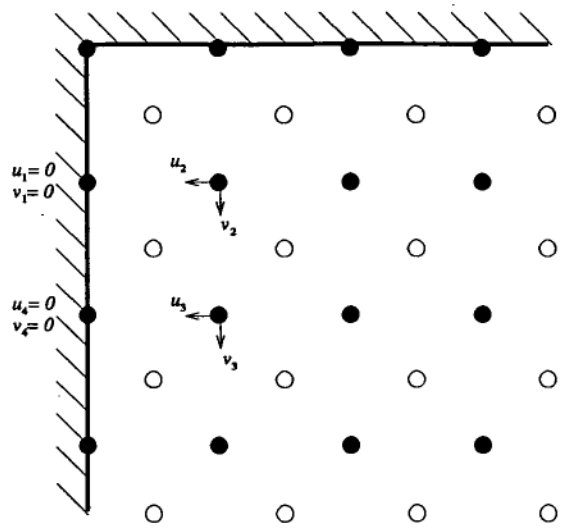


Figure 4.4: Velocity and divergence grid (as specified in figure 4.1 ) near a continental boundary (shaded). $U_{2,3}$ and $V_{2,3}$ are the optimally interpolated, depth-integrated, thermal wind and Ekman transports.

with $U$ representing normal flow (thermal wind + Ekman transport), and $V$ representing parallel flow to the western boundary.

The only location that mass adjustment can occur is through reference transports of the ocean grid points. The simplest solution of this situation would be for the reference transports to equal the negative of the thermal wind and Ekman transports, however this establishes large mass imbalances in neighbouring boxes. Thus, a local solution is not feasible and a global solution involving all grid points is required. The least squares solution over the global domain turns some of the normal transport ($U$) into parallel transport ($V$) along the boundary reducing the signal propagated back into the interior of the ocean. From figure 4.4, one can see how the different boundary orientations will affect the divergence calculation of equation 4.13.

In most models of circulation, vorticity is destroyed in western boundary currents [Rhines and Young 1982; Rhines 1983; Gill 1982]. It therefore does not make sense to try to conserve vorticity in these regions. As most boundary currents do not extend further than 2° from the coast [Boland and Church 1981;

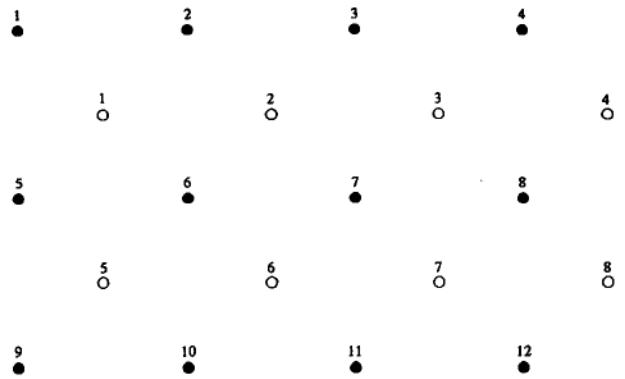


Figure 4.5: Example grid locations for a 3×4 area, $i = 1 \ldots 3$, $j = 1 \ldots 4$. Solid and open circles are as defined in figure 4.2.

| | U | | | | | | | | | | | | V | | | | | | | | | | | |
|---|---|---|---|---|---|---|---|---|---|---|---|---|---|---|---|---|---|---|---|---|---|---|---|---|
| | 1 | 2 | 3 | 4 | 5 | 6 | 7 | 8 | 9 | 10 | 11 | 12 | 1 | 2 | 3 | 4 | 5 | 6 | 7 | 8 | 9 | 10 | 11 | 12 |
| 1 | -1 | 1 | 0 | 0 | -1 | 1 | 0 | 0 | 0 | 0 | 0 | 0 | -1 | -1 | 0 | 0 | 1 | 1 | 0 | 0 | 0 | 0 | 0 | 0 |
| 2 | 0 | -1 | 1 | 0 | 0 | -1 | 1 | 0 | 0 | 0 | 0 | 0 | 0 | -1 | -1 | 0 | 0 | 1 | 1 | 0 | 0 | 0 | 0 | 0 |
| 3 | 0 | 0 | -1 | 1 | 0 | 0 | -1 | 1 | 0 | 0 | 0 | 0 | 0 | 0 | -1 | -1 | 0 | 0 | 1 | 1 | 0 | 0 | 0 | 0 |
| 4 | 1 | 0 | 0 | -1 | 1 | 0 | 0 | -1 | 0 | 0 | 0 | 0 | -1 | 0 | 0 | -1 | 1 | 0 | 0 | 1 | 0 | 0 | 0 | 0 |
| 5 | 0 | 0 | 0 | 0 | -1 | 1 | 0 | 0 | -1 | 1 | 0 | 0 | 0 | 0 | 0 | 0 | -1 | -1 | 0 | 0 | 1 | 1 | 0 | 0 |
| 6 | 0 | 0 | 0 | 0 | 0 | -1 | 1 | 0 | 0 | -1 | 1 | 0 | 0 | 0 | 0 | 0 | 0 | -1 | -1 | 0 | 0 | 1 | 1 | 0 |
| 7 | 0 | 0 | 0 | 0 | 0 | 0 | -1 | 1 | 0 | 0 | -1 | 1 | 0 | 0 | 0 | 0 | 0 | 0 | -1 | -1 | 0 | 0 | 1 | 1 |
| 8 | 0 | 0 | 0 | 0 | 1 | 0 | 0 | -1 | 1 | 0 | 0 | -1 | 0 | 0 | 0 | 0 | -1 | 0 | 0 | -1 | 1 | 0 | 0 | 1 |

Table 4.1: The structure of the divergence part of Matrix A for the example grid shown in figure 4.5. Rows correspond to divergence grid locations, columns correspond to transport grid locations for $U$ and $V$ components respectively. Note: The above matrix is written in full notation, in sparse form all of the zero elements are removed.

Evans et al. 1983; Toole and Warren 1993], vorticity was only conserved on interior grid points further than 2° away from the coast. Although excluding coastal gridpoints from the conservation of linear vorticity slightly reduces the number of equations, it is physically more rigorous.

### 4.3.1 Building the Inverse Model

Using the example grid illustrated in figure 4.5 and equation 4.5 (cartesian co-ordinates), the $A$ matrix takes the form outlined by Table 4.1. This is generated by moving from grid cell to grid cell, from west to east, and from north to south.

Looking at row 1 of Table 4.1, the divergence equation 4.5 assuming

$\Delta x = \Delta y = .5$, is written as $-U_1 + U_2 - U_5 + U_6 - V_1 - V_2 + V_5 + V_6$. Moving from grid cell to grid cell, one can see how matrix $A$ is constructed. Several points need to be highlighted about Table 4.1. The matrix positions (row,col), U(4,1), U(4,5), V(4,1), V(4,5), U(8,5), U(8,9), V(8,5), V(8,9) represent the divergence calculation that continues the circulation from east to west, i.e. divergences 4 and 8 in figure 4.5. Under the spherical coordinate system, the position of the elements does not change, but there is a factor of $\frac{1}{Rsin\theta}$ introduced. This matrix has a good diagonal shape, which increases the ease the problem can be solved, because the inversion is non-singular.

Following the same procedure for linear vorticity with equation 4.12 generates two diagonal sub-matrices. One with $\frac{f}{\beta HR\sin\theta}\frac{\partial H}{\partial \phi}$ as the diagonal elements for the $U$ component matrix and $(\frac{f}{\beta HR}\frac{\partial H}{\partial \theta} + 1)$ as the diagonal elements for the $V$ component matrix.

The full $A$ matrix is generated by combining the four sub-matrices discussed above as outlined in equation 4.14

$$A = \left[\begin{array}{c|c} \frac{\partial u}{\partial x} & \frac{\partial v}{\partial y} \\ \hline \frac{f}{\beta HR\sin\theta}\frac{\partial H}{\partial \phi} & \frac{f}{\beta HR}\frac{\partial H}{\partial \theta} + 1 \end{array}\right] \tag{4.14}$$

The final shape of matrix A, with land grid points removed, is illustrated in figure 4.6.

From figure 4.6, the $U$ and $V$ components of the matrix are easily distinguished. The divergence equations occupy the top two sub-matrices, and the vorticity equations generate the lower sub-matrices. In the top part of the matrix, the grid locations involved in recirculating the transport from east to west are visible as the line of 50 dots on the lower diagonal in the two upper sub-matrices. The solid lines in each half of the matrix have width 2 separated by 358 columns. In the vorticity component part of the matrix, the elements are

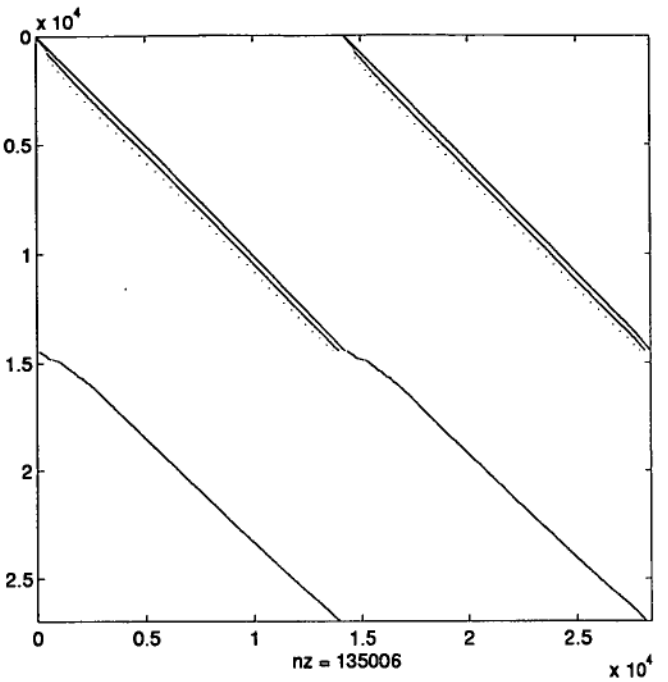


Figure 4.6: Location of non-zero elements in matrix A (26,945 rows, 28,480 cols).

diagonal with rows and columns associated with land removed.

The total size of this matrix is 26,945 x 28,480. The first 14,458 rows are associated with the divergence equations, and the remaining 12,487 rows represent the vorticity equations. The number of columns is divided evenly between the $u$ and $v$ components of unknown reference transport, with 14,240 columns associated with each component. The equations are written from the south-eastern corner of the model domain, moving eastward across the model domain before moving north across the model domain. The discontinuities, for example near the top of the matrix are caused by removing rows (equations) and columns (unknown reference transports) that are associated with model grid points that are over the Antarctic land mass. All rows and columns associated with land masses are removed from the matrix. It is clear that matrix $A$ is indeed sparse with only 135,006 non-zero elements, requiring only 1Mb of storage using sparse matrix techniques.

## 4.4 The Inverse Solution

"Inverse theory is simply the set of methods used to extract useful inferences about the world from physical measurements" [Menke 1984]. There are many inverse techniques available, each with their strengths and limitations in analysing data. In this section, a brief review is given of the inverse technique relevant to this thesis and no attempt is made to review all inverse techniques.

Solution of the inverse problem requires the determination of the $U$ and $V$ components of the unknown reference transport using the dynamical constraints of conservation of mass and linear vorticity, given the divergence of thermal wind transport, Ekman transport and windstress curl. In matrix notation equations 4.3 and 4.12 are written as

$$Ax \approx B \tag{4.15}$$

where $x = [U_{r:1}, \ldots, U_{r:N}, V_{r:1}, \ldots, V_{r:N}]^T$ is a column vector of the unknown reference transports.

$B = [div_1, \ldots, div_N, curl_1, \ldots, curl_N]^T$ is a column vector of the known data field

$A = M \times N$ matrix representation of equations 4.3 and 4.12.

By having fewer equations than unknown reference transports, the matrix system shown in equation 4.15 is singular and does not provide enough information to uniquely determine a solution, i.e. an underdetermined problem. Therefore, there are an infinite number of solutions to equation 4.15. The key task is to choose the "best" solution from the infinite number of available solutions.

To select a unique solution, the model parameters are statistically constrained to the solution that generates the smallest model norm, $||x^T x||$, while solving the equations to within the required noise level, i.e., the smallest residual norm $||(B - Ax)^T(B - Ax)||$ . The smallest model norm solution is also the simplest solution. The initial guess of the reference transports was set to zero ($U_{Ref} = V_{Ref} = 0$) so the smallest model norm is the solution that generates the smallest reference transports. As a consequence, the reference level must be carefully chosen. It has been generally accepted that the ACC in the Southern Ocean extends throughout the water column, so the bottom reference assumption is likely to be acceptable [Savchenko et al. 1978; Callahan 1971]. In other regions of the world's oceans, such as subtropical regions, the bottom reference assumption may not be acceptable [Wunsch et al. 1983].

Equation 4.15 can be solved using singular value decomposition (SVD) of the matrix A. Any matrix can be written as $A = \mathcal{U}\Lambda\mathcal{V}$ where $\mathcal{U}$ is the matrix of eigenvectors that span the data space and $\mathcal{U}\mathcal{U}^T = I$ (the identity matrix). Similarly, $\mathcal{V}$ is a matrix of eigenvectors that span the model parameter space and $\mathcal{V}^T\mathcal{V} = I$. The matrix $\Lambda$ is a diagonal eigenvalue matrix whose diagonal elements are non-negative and are called singular values Menke [1984]. Using SVD, the solution to equation 4.15 can be written

$$x = \mathcal{V}\Lambda^{-1}\mathcal{U}^T b \tag{4.16}$$

In the underdetermined problem, the number of non-zero eigenvalues cannot exceed the number of equations. Usually, some of the equations are dependent, so the number of non-zero eigenvalues is less than the number of equations. The problem of determining how many eigenvalues to include is the problem of determining the rank of $A$. As additional eigenvalues are added to the solution, the norm of the residuals decreases, but the model norm

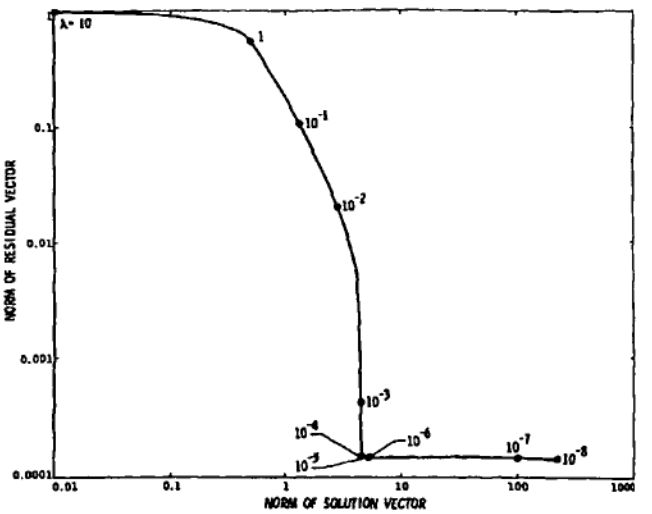


Figure 4.7: Residual Norm versus Solution Norm for varying rank (from Lawson and Hanson [1974])

increases-this later norm is not the desired solution. The chosen solution for the inverse model is the one that minimises both the residual norm and the model norm.

The trade-off between the residual norm and the model norm is illustrated by plotting them against each other as each additional eigenvalue is included, as shown by Figure 4.7. The optimal solution is near the knee of the curve ($10^{-4}$ in figure 4.7), where the residual norm has been reduced to an acceptable level without generating an excessively large model norm. This is known as the Levenberg-Marquardt stabilisation method [Lawson and Hanson 1974; Rintoul 1988].

However, to solve equation 4.15 using SVD, matrix $A$ must be manipulated as a full matrix. In this thesis, the full form of matrix $A$ would require over 6 Gbytes of memory and is beyond the capabilities of our current computer systems. There are several approaches available that reduce matrix $A$ to a manageable size. The total inverse problem can be broken into several smaller sub-matrices, each of which is solved separately using SVD.

Alternatively, sparse matrix methods can be implemented. If the system was broken into smaller sub-matrices, the global mass conserving properties of the system over all regions could be lost. To maintain the global mass conservation of the system, without having to resort to iterative procedures, sparse matrix techniques were used.

Sparse matrix algebra allows the manipulation of matrix problems where most of the matrix elements are zero. Using sparse procedures, a diagonal matrix 28,000 × 28,000 uses only 224 kbytes of memory compared to over 6 Gbytes needed for storage of the full matrix. Unfortunately, there are limitations on the types of problems that can be solved. For example, the direct inversion of a sparse matrix usually results in a full matrix.

Using the criterion of minimised residual and model norm allows the definition of a cost function which is a measure of the goodness of fit of the model to the data. The cost function is defined as

$$L = e^T e + \epsilon^2 x^T x \tag{4.17}$$

where $e$ = the residuals $(B - Ax)$,
so $e^T e$ is the norm of the residuals to be minimised.
$x^T x$ = the model norm
$\epsilon$ = damping factor.

By minimising $L$ with respect to $x$ (i.e., minimising $\frac{\partial L}{\partial x}$), the least squares estimator of $x$ is

$$x = [A^T A + \epsilon^2 I]^{-1} A^T B \tag{4.18}$$

This solution is known as the damped least squares solution of equation 4.15

[Menke 1984]. The different solutions generated by varying $\epsilon$ in equation 4.18 is broadly analogous to choosing the rank of the SVD solution. The damping factor $\epsilon$ controls the relative importance of the residual norm to the model norm. If $\epsilon$ is small, the solution minimises the residual norm at the cost of large model norm, conversely, a large $\epsilon$ solution generates small model norm at the expense of a large residual norm. Determining the appropriate $\epsilon$ that results in the best solution, consistent with errors, is achieved by solving the system of equations many times, varying $\epsilon$ for each solution and plotting the resulting model norm against the residual norm. This generates a similar plot to the Levenberg-Marquardt method outlined above, and the "best" solution is near the knee of the plot.

### Weighting

Before solving the inverse problem, the equations are usually scaled by a weighting matrix $W$, to give each equation its correct relative importance and to remove the effects of units [Wunsch 1978; Rintoul 1988]. This can be carried out while determining the solution by using the weighted damped least squares solution to equation 4.15 [Menke 1984], written as

$$x = [A^T W A + \epsilon^2 I]^{-1} A^T W B \tag{4.19}$$

In matrix $A$, the units of the divergence of transport are m $s^{-1}$, while the units of vorticity are $m^2$ $s^{-1}$. These difference of units are removed by normalising the equations using the weighting matrix $W$, where $W$ is a diagonal matrix with the top half of the diagonal matrix using the variance of the divergence field ($\sigma_d^2$) and the bottom half diagonal using the variance of the vorticity field ($\sigma_v^2$). The weight matrix can be written as

$$W = \begin{bmatrix} \frac{1}{\sigma_d^2} & 0 \\ 0 & \frac{1}{\sigma_v^2} \end{bmatrix} \tag{4.20}$$

The relative importance of each equation can also be controlled by $W$. As discussed above, it is required to solve the conservation of mass constraints to a higher degree of accuracy than the vorticity constraint so the mass constraint has more influence on the solution. The relative importance of the conservation of mass and vorticity constraints can be controlled by the introduction of a scaling factor $\alpha$ into the weighting matrix $W$.

$$W = \begin{bmatrix} \frac{1}{\sigma_d^2} & 0 \\ 0 & \frac{1}{\alpha\sigma_v^2} \end{bmatrix} \tag{4.21}$$

By increasing $\alpha$, the relative importance of the vorticity equations decrease and vice versa.

Using sparse matrix manipulation as implemented in the Matlab®computing environment, equation 4.19 is solved using Gaussian elimination with pivoting, which, for the full inverse problem, takes approximately 30 minutes to compute.

**Errors**

The covariance matrix of the solution gives an estimate of the precision associated with the solution. The covariance matrix of the weighted, damped least squares solution is expressed as

$$[covx] = \left[[A^T W_e A + \epsilon^2 I_1]^{-1} A^T W_e\right] \sigma_{data}^2 I_2 \left[[A^T W_e A + \epsilon^2 I_1]^{-1} A^T W_e\right]^T \tag{4.22}$$

where $\sigma_{data}^2$ is the variance of the divergence and vorticity fields and $I_1$ and $I_2$

are identity matrices of different dimensions having the same dimensions only when matrix $A$ is square. This involves the calculation of the inverse of the $[A^T W_e A + \epsilon^2 I]$ matrix. Because the inverse of a sparse matrix is a full matrix, the calculation of covariance results in a full matrix (28,480 x 28,480 elements), requiring 6,488 Mb to store. As the covariance matrix is symmetric, iterative procedures exist that allow the generation of the top half of the covariance matrix. However as this still requires 3,244 Mb of storage, it is still beyond available computer resources.

The covariance matrix is also very sensitive to the choice of $\epsilon$ with small changes in $\epsilon$ giving large changes to the covariance matrix and hence the precisions. This makes the computation of the error field unstable and with the computer resources required, this covariance matrix was not calculated. Therefore, unfortunately there are no precision estimates available from the inverse solution, which is the trade off to solving the entire system simultaneously and maintaining the global mass conservation of the model.

### Choosing the solution

As explained above, the "best" solution to the inverse problem using equation 4.19 is determined by plotting the model norm against the residual norm for varying $\epsilon$, as shown in figure 4.8, similar to the Levenberg-Marquardt stabilisation method. As $\epsilon$ increases, the cost function (equation 4.17) increases the weighting of the model norm and the solution gets smaller while the residual norm increases (top left of solid line in figure 4.8 with $\epsilon = \frac{max(A)}{1}$). As $\epsilon$ decreases, the cost function downweights the model norm and the solution size increases as the residual size decreases (bottom right of solid line in figure 4.8, $\epsilon = \frac{max(A)}{100{,}000}$). The "best" solution is near the "knee" of the solid line of figure 4.8 (where the two curves intersect $\epsilon = \frac{max(A)}{1000} = 6.3$), where the residual norm has

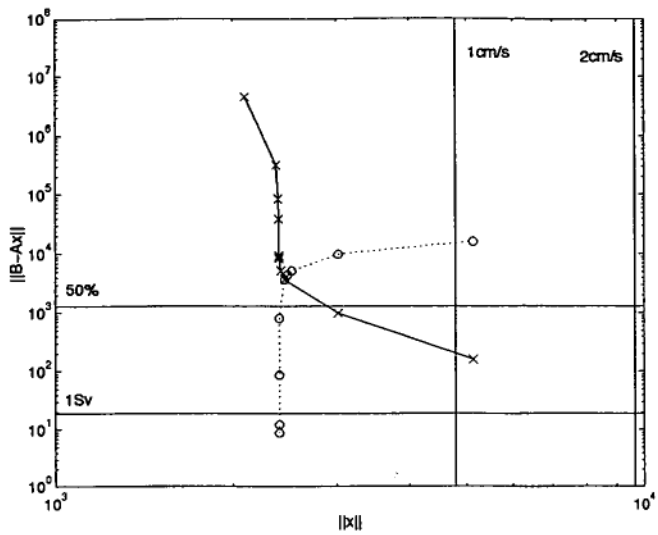


Figure 4.8: Plot of residual norm ($||Ax - B||$) vs model norm ($||x||$). Solid line illustrates the effect of varying $\epsilon$. The dashed line illustrates the effect of changing weighting of the vorticity equations. The two vertical lines are solution norms for solution velocities of 1 and 2 cm $s^{-1}$. Horizontal lines are residual norms of mass conservation of 1 Sv for the pure mass problem and 50% of the variance of vorticity.

been minimised without allowing the model norm to grow excessively large.

The other part to choosing the "best" solution to the inverse problem is selecting the correct weighting matrix. As explained above, the weighting matrix, $W$, in equation 4.19, has two parts. A weighting for units and a weighting for relative importance of the equations. The weighting of the units is standard and $\sigma_d$ and $\sigma_v$ do not change (see Table 4.4). The weighting of the relative importance of the equations can change by varying $\alpha$. The dotted line in figure 4.8 shows the effect of changing $\alpha$ with constant $\epsilon$ set to $\frac{max(A)}{1000}$. As $\alpha$ increases the vorticity equations are downweighted and the solution tends to the simple mass conservation equation (bottom left of dotted curve, $\alpha = 1000$). As $\alpha$ decreases the vorticity equations have more impact on the solution (top right of dotted curve, $\alpha = .01$).

The full suite of curves for varying both $\alpha$ and $\epsilon$ can been imagined by sliding the solid curve along the dotted curve, and vice versa which gives some

| | | |
|---|---|---|
| $\epsilon$ | $\frac{max(A)}{1000}$ | 6.3 |
| $\sigma_d$ | variance of divergence field | $3.3\times10^{12}$ m $s^{-1}$ |
| $\sigma_v$ | variance of vorticity field | 110 $m^2$ $s^{-1}$ |
| $\alpha$ | | 1.8 |

Table 4.2: Damping and equation weightings used to generate the final solution.

indication of the number of solutions available. The values used for the damping and equation weightings used to calculate the presented solution is summarised in Table 4.4. To have confidence in this solution, it is possible to set an upper limit on the model norm and a lower limit on the residual norm.

The upper limit of the model norm estimates that the solution is broadly consistent with the ocean circulation and that the transports generated by the solution give realistic reference velocities. Bryden and Pillsbury [1977] estimated that in Drake Passage, possibly the location of the strongest currents in the Southern Ocean, the mean velocity at 2700 metres was $1.56\pm1.44$ cm $s^{-1}$. Solution reference velocities, that were on average 1 - 2cm $s^{-1}$, would translate to a model norm between $4.8\times10^3$ and $9.6\times10^3$ (see the vertical lines at the right hand edge of Figure 4.8). The model norm of the final solution, shown at the crossover of the two plots in Figure 4.8, generates velocities that are, on average, .5 cm $s^{-1}$, a realistic bottom velocity given the measurements from Drake Passage.

The lower limit of the residual norm is a guide to indicate when the solution is close to solving the system of equations to an expected accuracy. The expected accuracy depends on the noise of the data and the degree to which mass and vorticity are to be conserved. Further reducing the size of the residuals only serves to introduce the effects of data noise into the solution velocity fields. The horizontal line labeled 1 Sv in Figure 4.8, illustrates the size of the residual norm when mass was conserved to 1 Sv within each grid cell for a purely mass

conserving model. Given that the optimal mapping errors of the hydrographic data (see Figures 3.12 and 3.13) were generally less than 0.5 Sv it was felt that a 1 Sv imbalance within each grid box was a realistic lower limit. The 50% line shows the residual norm when 50% of the vorticity variance is explained by the mass and vorticity conserving model, that is, only half the variation in the vorticity field is being solved for. This meant that the mass conservation equations were roughly twice as important to the solution as the vorticity equations. As will be explained when discussing the solution, it was felt that when the importance of the vorticity equations was increased, unrealistic small scale circulation due to bottom topography began to dominate the solution.

**The solution**

Figure 4.9 shows the combined transport due to thermal wind and Ekman transport (input, top panel), the inverse solution which represents the reference transports (middle panel), and the total combined transports (bottom panel) for the South Atlantic Ocean. The three transport pictures illustrate the relatively small changes that are necessary to make the input transport field conserve mass and weakly conserve vorticity.

Most striking is how continuous the ACC appears in the total transport field. Also how the circulation on the continental shelf now obviously balances the circulation off the shelf. For example, at 40°S, 310°E in the input circulation (top panel), the outflow from the Brazil-Malvinas confluence is obviously missing the inflow of the Brazil and Malvinas currents to balance mass. The total circulation now has a mass circulation on the continental shelf that balances a slightly reduced outflow. Regions in the open ocean with obvious convergence or divergence of mass, i.e., 40°S, 322°E, the area of strong divergence of mass now appears smooth and continuous. The above examples

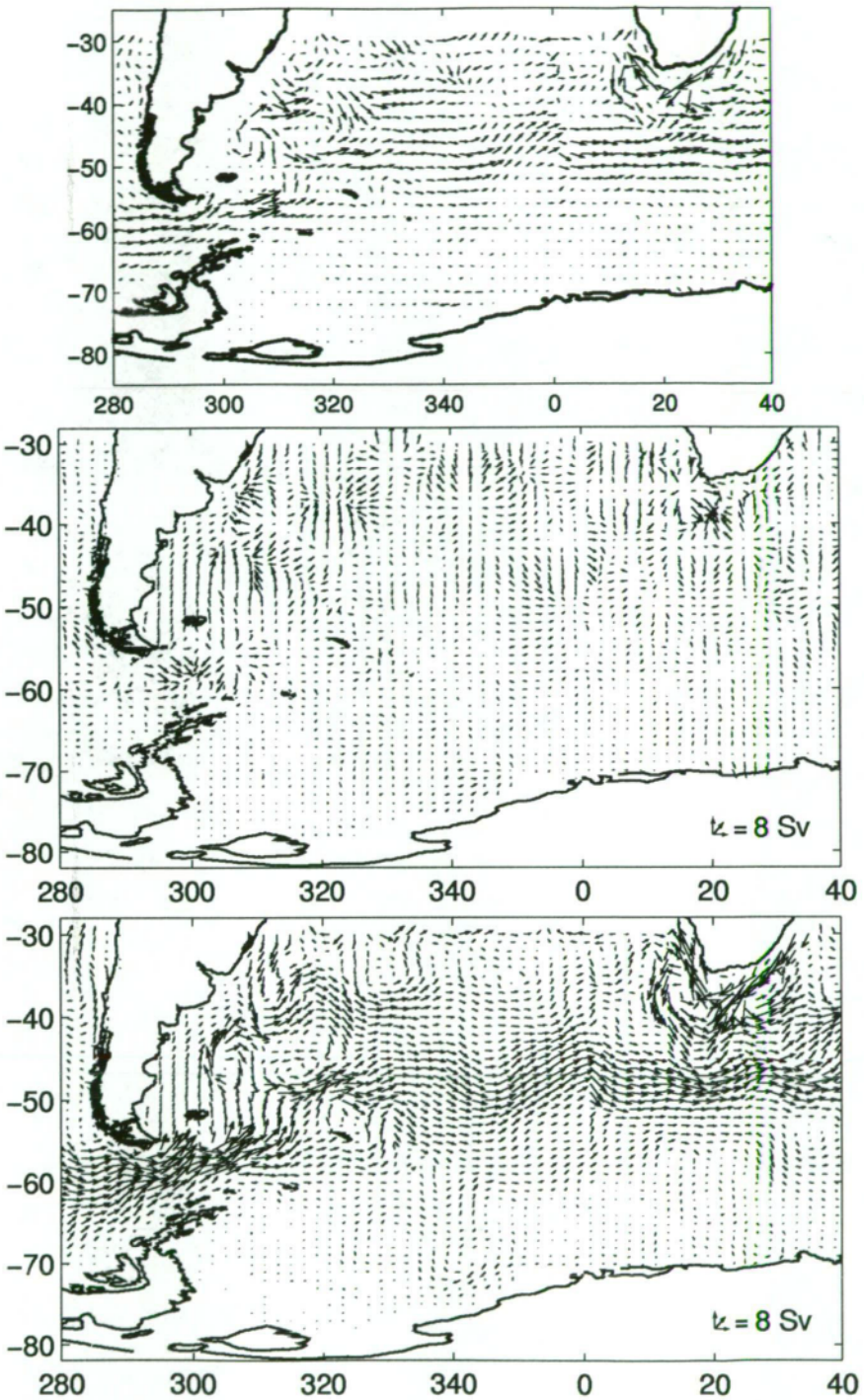


Figure 4.9: Atlantic sector of the model domain showing input thermal wind and Ekman transports (top), reference transports from the inverse model (middle), combined total transport (bottom) at 1° latitude × 2° longitude (Arrow lengths of 1° represent 4Sv).

are strong indications that the model is working well and is consistent with expected oceanography. A full description of the oceanographic implications is carried out in chapter 5.

A further inspection of the quality of the solution can be made by comparing the divergence of the input thermal wind and Ekman transports to the divergence of the total transport (input transports plus inverse solution transports) as shown in figure 4.10. This shows that the model solution has explained the variance of the divergence field to within working accuracy. The size of the solution divergence field is a factor of $10^{-5}$ smaller than the input divergence field. Also, how much of the variability of the input field has been explained by the solution can be inspected by calculating the $\mathcal{R}^2$ value, defined as

$$\mathcal{R}^2 = \frac{||Ax||}{||B||} \tag{4.23}$$

The $\mathcal{R}^2$ value of the inverse solution of Figure 4.9-4.10 is 1 to within working precision, indicating that the solution is explaining most of the input divergence field variability.

A further test of the quality of the solution can be carried out by examining the global conservation of mass in the model. The northern boundary at 30°S is the only location at which the model can gain and lose mass as the model is bounded to the south by Antarctica. Therefore, the total integrated transport across 30°S should be close to zero if global mass is conserved. Figure 4.11 presents the integrated total transport across 30°S around the globe starting from 0°E, that is, the mass transported into and out of the model domain across 30°S. A full discussion of the implications this has on the oceanography is presented in chapter 5 with a brief discussion given below. Moving east, mass is transported out of the model domain by a

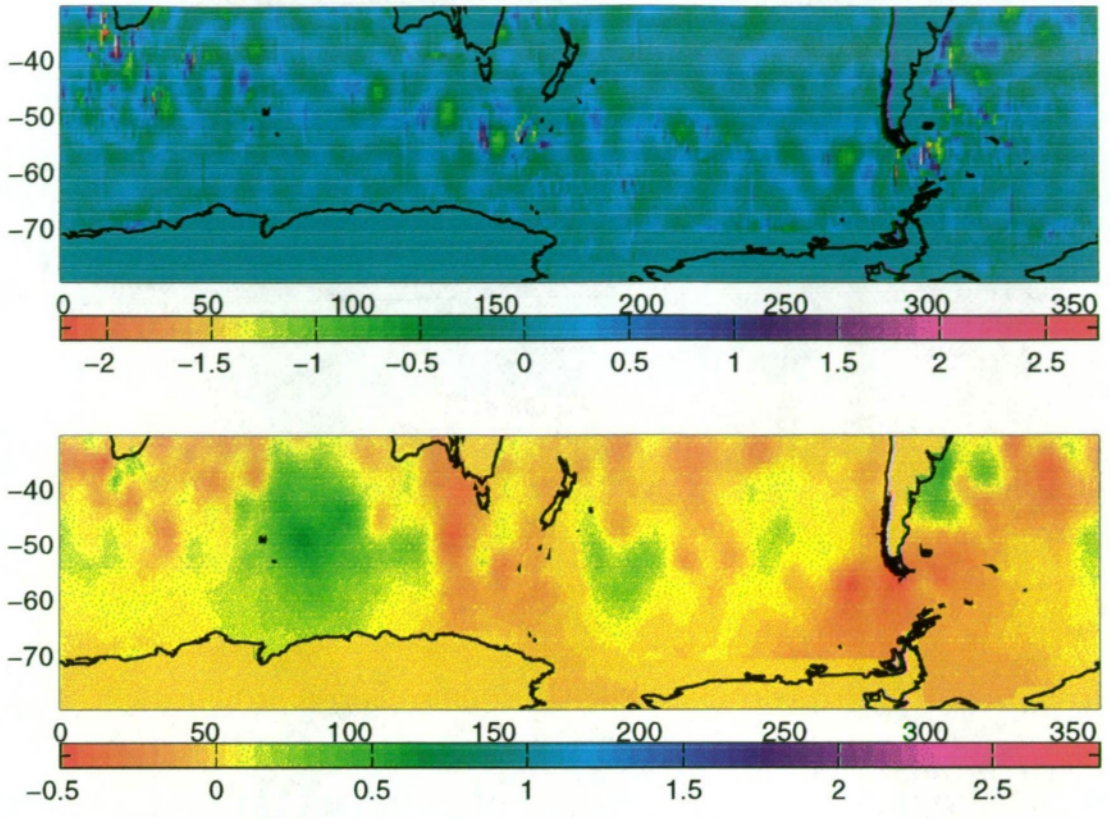


Figure 4.10: Divergence of the thermal wind + Ekman transport (top, $10^{-5}$ ms$^{-1}$) and the divergence of the total transport field (bottom, $10^{-11}$ ms$^{-1}$)

northward transport of water on the west coast of Africa. On the east coast of Africa, the Agulhas current transports mass south into the model domain. Further east, the Indian Ocean transports mass northward and then southward before the Leeuwin boundary current system transports mass north and then south. Similar boundary currents and subtropical gyre circulations can be identified in the Pacific and Atlantic Ocean and closely represent observed circulations for those regions. From figure 4.11 it is clear that mass is conserved over the model domain. The degree to which global mass is conserved depends on how accurately the mass conservation equations have been solved. When the mass conservation equations are solved more accurately (smaller $\epsilon$), the individual cell mass conservation approaches zero and is typically less than 2 Sv in the final solution. Because the solution has been solved to this rms residual

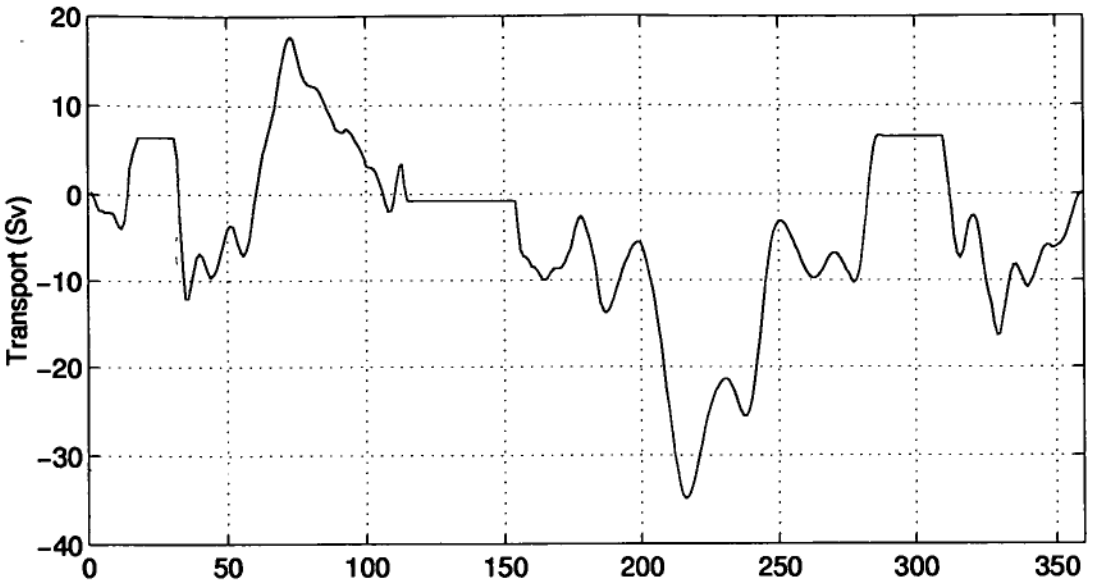


Figure 4.11: Integrated total transport (thermal + Ekman + reference, Sv) across the northern boundary of the model domain. Positive values = northward transport.

for mass, the divergence in the individual cells is randomly distributed, so that over the model domain, the sum of the divergence imbalances, hence the global mass conservation, is also close to zero. In the inverse model solution, the global mass imbalance across 30°E is less than 1 Sv.

Figure 4.12 presents the total circulation for the inverse model that only conserves mass (top), conserves mass and weakly conserves vorticity (middle) and the difference between the two (bottom). At first inspection, there appears to be very little difference. However, there is a slight rotation of the large scale eddy circulations such as the Agulhas Current. A greater difference between the two circulations could have been achieved by increasing the importance of the vorticity equations. Unfortunately, because of the roughness of the topography, the short length scale topographic gradients started to introduce unrealistic small scale circulations, by trying to conserve vorticity on contours of $\frac{f}{H}$. By including the vorticity equations, although the difference between the two solution is small, the inverse problem approached being evenly determined, and

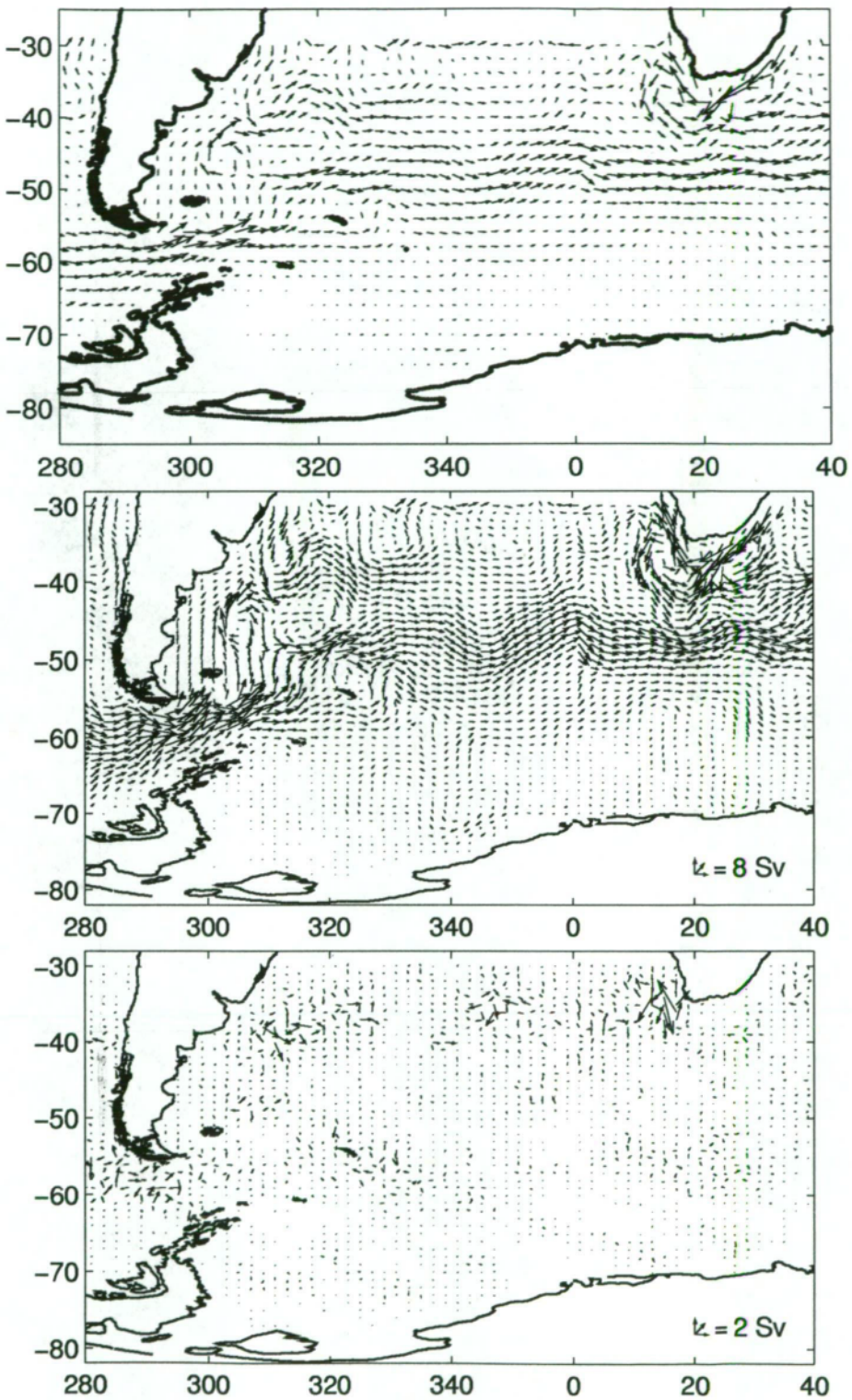


Figure 4.12: Comparison between an inverse model that conserves mass only (top) and both mass and vorticity conservation (middle) and the difference between the two (bottom).

so was not as ill-posed as with just the mass conservation equations.

Several problems are encountered when the transports are converted into velocities. At grid locations bordering land, several of the velocities are calculated to be in excess of 10 m $s^{-1}$. Several strong boundary currents have surface velocities in excess of 2 m $s^{-1}$ (EAC [Boland and Church 1981], Agulhas current [Grundlingh 1980]), suggesting that velocities greater than 10 m $s^{-1}$ is unrealistic. These excessive velocities are mainly a result of shallow topography. By solving the inverse model for depth-integrated transports, the model has no information about the topography. Therefore, the depth-integrated transports associated with continental shelf regions will be smaller than open ocean transports due to the depth of the water column. Because the inverse model is trying to find a solution that minimises the model norm, the model makes small changes to small coastal transports rather than large changes to large transports. With coastal depth often less than 20 metres, a relatively small transport ch ange of 1 Sv generates velocities of 1 m $s^{-1}$.

Another contributing factor to generating transport changes in coastal regions is the land boundary condition. At grid cells adjacent to land cells, normal circulation is either rotated into parallel or return flow as explained in section 4.3. This divergence mass at adjacent cells is the largest adjustment made by the inverse solution, often generating relatively large transport changes at coastal regions where the ocean depths are shallow.

The excessive reference velocities generated by the processes outlined above usually only occur at grid points directly adjacent to land and the transports associated with these velocities have little effect on the overall transport calculations. However, velocities larger than 2 m $s^{-1}$ are removed from subsequent presentations of model results.

This chapter has outlined an inverse model of the Southern Ocean that

conserves mass and weakly conserves vorticity. The inverse model uses finite difference techniques to conserve mass for the Southern Ocean given a divergence of mass field, calculated from the thermal wind and Ekman transports calculated in chapter 3. The inverse model also conserves linear vorticity given the curl of the windstress and the gradient of the topography over the model domain. The inverse model has very simple boundary conditions and has no circulation constraints applied to it.

In order to maintain the global mass conservation property of the model, the entire model domain is solved simultaneously using weighted damped least squares. While maintaining the global mass conservation of the model, it is difficult to compute associated errors of the circulation. The presented solution was determined by solving the model many times, each time varying the weighting of the equations ($\alpha$), or the damping factor ($\epsilon$). The final solution was the solution that minimised the residual norm and the solution norm.

By inspection of the total circulation of the Southern Ocean, the inverse model appears to have generated a reference circulation that gives a realistic total circulation. Just how accurate this circulation is, will be discussed in chapter 5.

# Chapter 5

## Southern Ocean Circulation

This chapter describes the implications the inverse solution, calculated in the previous chapter using the weightings outlined in table 4.4, has on the integrated mass transport of the Southern Ocean. The solution is compared with in-situ observations, previous inverse studies and a high resolution numerical model. These comparisons show that while the pointwise velocities are smaller than observed velocities, there is a high qualitative agreement between the observations and Southern Ocean inverse model (SOINV). The location of the ACC, western boundary currents such as the Agulhas, Brazil and EAC, and subtropical gyres in the SOINV are in strong agreement with observed locations of these circulation features.

Section 5.1 conducts a qualitative analysis between the SOINV circulation and insitu observations. A quantitative comparison is conducted in sections 5.2 and 5.3 by comparing vertical sections to in-situ observations across 30°S, Drake Passage and south of Africa and Australia. These comparisons show that the SOINV eastward mass transport is approximately 70% of the accepted eastward transport estimate and that the SOINV estimate of transport across 30°S falls within the range of estimates for transport across 30°S in the three ocean basins.

Using the reference transports generated by the SOINV, a three dimensional velocity field can be generated, that is consistent with the observations and conserves mass over the total water column. Using this three dimensional velocity field, the surface velocities and dynamic height of the Southern Ocean are compared to observations. The velocity field also allows for the investigation of the existence of the Deacon Cell, something not usually

possible from observational data.

## 5.1 Depth Integrated Circulation

The mass conserving, depth-integrated transport (thermal wind + Ekman + reference) is shown in figure 5.1. This figure could be compared to figure 1 in Nowlin and Klinck [1986], in reality figure 1 of Nowlin and Klinck [1986] only depicts the surface velocities relative to 1000 dbar. A comparison between the SOINV surface velocities and Nowlin and Klinck [1986] is carried out in section 5.7.

The circulation depicted in figure 5.1 has all the major components of Southern Ocean circulation. The ACC can be seen circulating around the globe, strongly controlled by topography. Boundary currents, both eastern and western, are present entering and leaving the model domain in all three ocean basins. It is also possible to see basin-scale, subtropical gyres entering and leaving the model domain in the three ocean basins.

The main feature within the Indian Ocean sector (top panel figure 5.1) is the ACC and Agulhas current systems. The ACC enters from the west, is directed north by the south-west Indian Ridge before dividing into two streams around the Crozet Plateau. The southern jet is smaller in magnitude and rejoins the main jet by flowing around and over the Kerguelen Plateau at 49°S, 60°E, 51°S, 72°E, 58°S,79°E and 66°E, 82°E, which coincides with the north and south extent of the plateau and two channels through the plateau. The northern jet of the ACC merges with the outflow of the Agulhas current system and flows across the Crozet Basin at approximately 42°S. Across the basin there are several small offshoots that turn north and flow out of the model domain. It is thought that these offshoots form the southern branch of the Indian subtropical gyre which closes outside the model domain, of which the Agulhas is

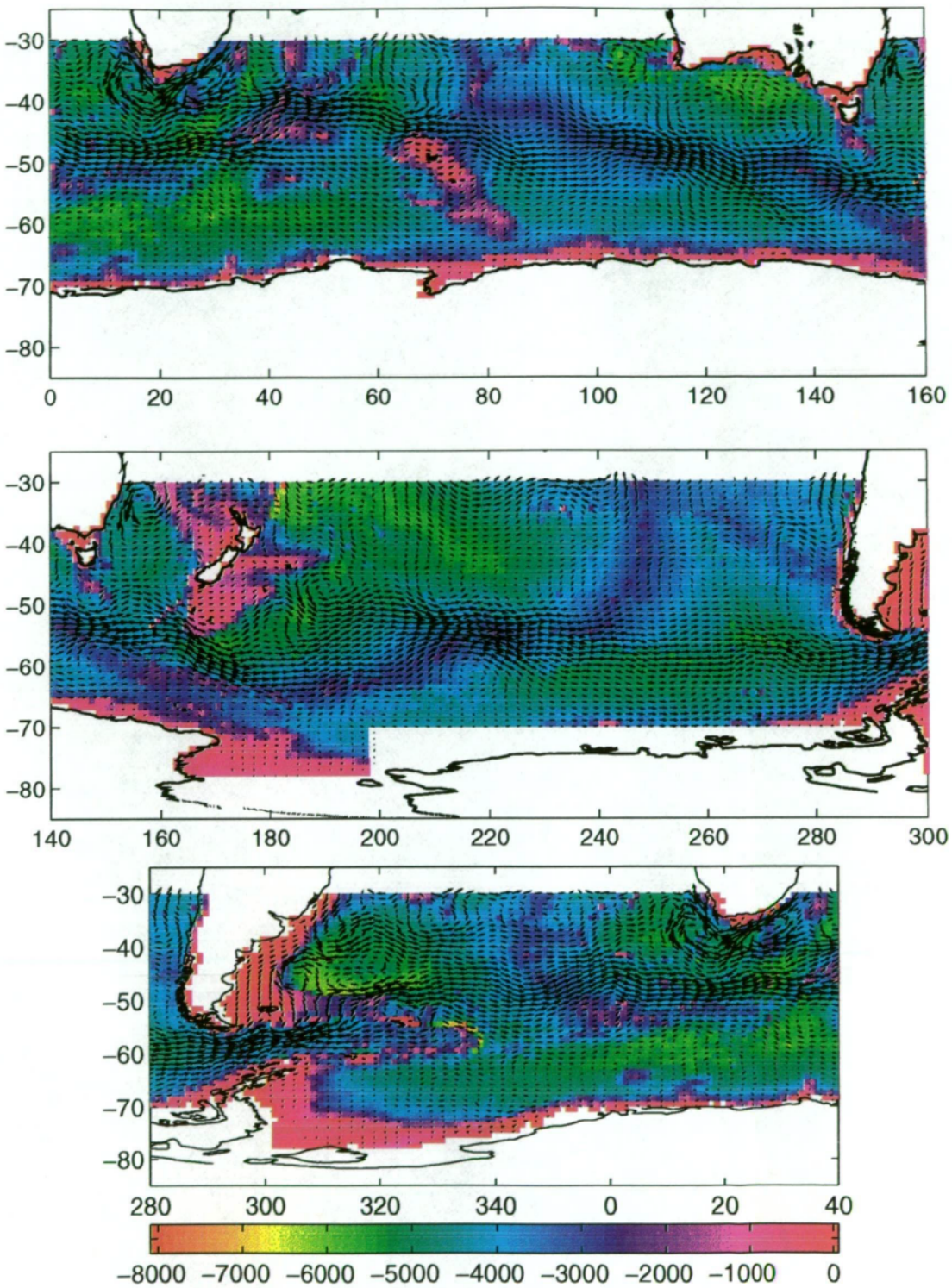


Figure 5.1: Total depth-integrated transport (Thermal wind + Ekman + Reference Transport) at a resolution of 1° lat × 2° long, 1°in = 4 Sv ) for model domain plotted over model bathymetry (metres).

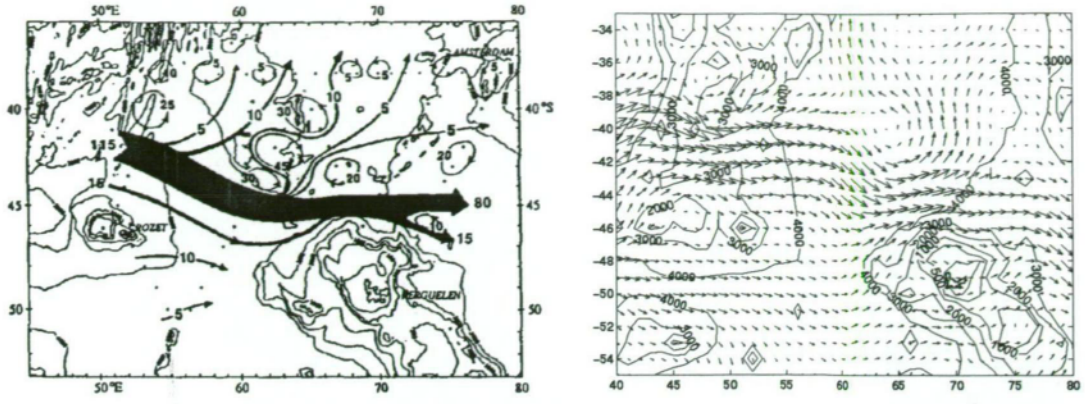


Figure 5.2: Schematic representation of the size and direction of the circulation through Crozet Basin (from Park et al. [1993]) compared to the SOINV circulation.

the western boundary current. This northward movement of water away from the ACC has been reported by Park et al. [1993] and Fine [1994] among others. Park et al. [1993] investigated the circulation of the Crozet Basin and developed a schematic representation for the resultant circulation, which is compared to the SOINV circulation of the same area in figure 5.2. The location of the main jet of the ACC is almost identical with several smaller streams to the south of the main jet. Park et al. [1993] resolved five small offshoots, four which enter the Indian Ocean, and a fifth crossing the Mid-Indian Ridge north of Amsterdam Island. By the small scale eddies drawn into the schematic by Park et al. [1993], it appears that they had difficulty resolving the circulation north of the ACC, which suggests that the region is eddy rich. Because of these eddies, the schematic and the SOINV circulation cannot be expected to exactly match. However, the SOINV circulation, which uses all observations within the region, confirms that Park et al. [1993] extracted the key elements of the circulation in the Crozet Basin with the limited amount of data available to them. From the SOINV circulation, in figure 5.2 it appears that the 4000 metre contour between Amsterdam and Kerguelen Islands is responsible for the deflection of most of the northward moving water away from the ACC.

The main jet of the ACC crosses the ridge between Amsterdam and Kerguelen Islands at 45°S and continues southeast, directed by the Southeast Indian Ridge, before entering the Australian-Antarctic Basin at 48°S, 80°E (see figure 5.2). In the Australian-Antarctic Basin, the main ACC jet is less concentrated with several small jets joining the main jet. Between 100°E and 130°E, the ACC is a concentrated jet controlled very strongly by the Indian-Antarctic Ridge. At approximately 130°E, the main current breaks into two jets, north and south of the ridge, possibly influenced by the Australian-Antarctic Discordance between 125°and 130°E. The ACC re-intensifies east of 140°E as the southern jet is forced north over the Australian-Antarctic Ridge at 142°E and rejoins the northern jet that is forced south by the Tasman Plateau. This intensification of the ACC is somewhat curious, as the southern jet has been forced back over the Austra lian-Antarctic Ridge for no apparent reason. One possible explanation is the desire of the circulation to flow along contours of $\frac{f}{H}$. As the southern jet flows south, east of the Australian-Antarctic Discordance, the Coriolis parameter is decreasing. Combined with the increased depth $H$ of the basin, both serve to decrease $\frac{f}{H}$. The only way to conserve vorticity is for the circulation to flow north, or over shallower topography, so the circulation turns north west, crosses the Australian-Antarctic Ridge, and rejoins the northern branch of the ACC. The intense jet continues east, spreading out across the southern extent of the Tasman Basin before encountering the Macquarie Ridge.

The Agulhas Current is depicted as a very intense circulation that enters the model domain very close to the African coastline and continues to remain very close to the shelf break. This association with the shelf break is consistent with the work by Toole and Raymer [1985] and Toole and Warren [1993] who found that there is a strong correlation between the location of the main

Agulhas jet and the shelf break. The main jet continues to follow the continental shelf around Cape Agulhas and Cape of Good Hope before breaking away from the continent and returning as a strong counter current. There are two major regions where the Agulhas separates from the coast, at 33°S, 18°E and 36°S, 22°E, the eastern separation being the most intense. This separation of the Agulhas forms two large eddy like circulations, known as the Agulhas Retroflection. The region of these eddies is very dynamic and most in-situ measurements usually depict more than two eddies in this region.

Gordon [1985] presents the results of a cruise through the Agulhas Retroflection in December 1983, which shows three main eddies in this region. Figure 5.3 compares the depth of the 10°C isotherm measured during the cruise to the SOINV circulation. The 10° isotherm is a strong indication of circulation of the region. The location of the eastern eddy is almost identical in both the SOINV and the data with the jet leaving the continental shelf break at 21°E. It is thought that this is the main separation path of the Agulhas, a hypothesis confirmed by the SOINV circulation which shows the most intense separation of the Agulhas in this region.

In the location of the SOINV's western eddy, the in-situ data shows two eddies that are not as intense as the eastern eddy suggesting that they are spinoffs from the main retroflection at 22°E [Gordon 1985]. The difference between the two circulations is most likely due to the number of observations. The data presented by Gordon [1985] presents a snap shot of the circulation, the SOINV circulation includes all the data of the region and represents the mean circulation. The western eddy in the SOINV circulation is probably a result of combining all observations of spinoff eddies that break away from the main Agulhas current. Once they have broken off, the eddies only travel slowly westward, remaining in the area of the SOINV's western eddy for a reasonable

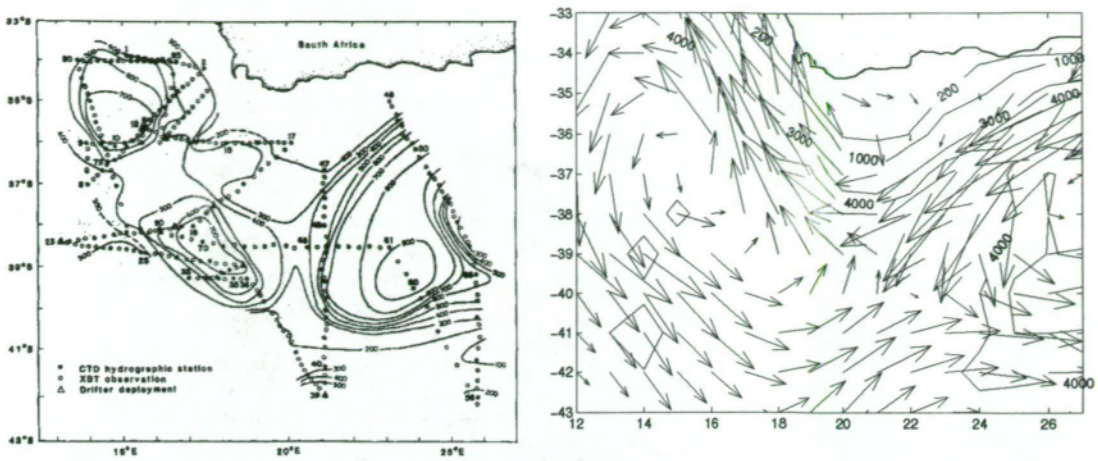


Figure 5.3: Results from December 1983 cruise reported by Gordon [1985] showing depth in metres of 10°C surface compared to the SOINV circulation for the same region. The 10°C surface bears a linear relation with sea-surface dynamic topography, relative to 1500 dbar [Gordon 1985].

amount of time (it would be impossible from this study to estimate how long). Then, the eddies either break out of the region and travel further to the west relatively quickly, making their observation by in-situ data more rare, or they dissipate and are lost to the surrounding ocean somehow. If this is the case, then the western eddy generated in the SOINV circulation is a mean circulation of spinoff eddies that have been observed in the area.

On the eastern boundary of the Indian Ocean, the Leeuwin Current generated by the SOINV appears as the cyclonic eddy off the coast of Western Australia. The Leeuwin Current was, until recently, thought to be a seasonal current possibly changing direction throughout the year. Recent work by Smith et al. [1991] has shown that there is seasonal variation superimposed on a continuously poleward flowing current with an average transport of 5 Sv. The Leeuwin Current is a very shallow, saline, surface current, with an equatorward flowing undercurrent. The Leeuwin Current's origin is much further north of the SOINV's northern boundary somewhere near the north west coast of Australia [Godfrey and Ridgway 1985; Cresswell 1991; Smith et al. 1991].

In the Pacific sector (middle panel of figure 5.1), the location of the ACC continues to be controlled by the underlying topography. The ACC spills over the Macquarie Ridge at 54°S, 160°E as a narrow, concentrated jet before spreading out into the southwest Pacific Basin. At 175°E, the ACC splits into two distinct cores. The southern and strongest jet, continues along the northern flank of the Pacific-Antarctic Ridge being forced north as it travels east. The northern jet flows along the eastern edge of the Campbell Plateau until 49°S, where it meets southward moving water and turns east to rejoin the main jet between 190°- 200°E. Heath [1981] measured a similar flow pattern when investigating the circulation around southern New Zealand. Figure 5.4 shows the comparison between the dynamic heights measured by Heath [1981] and the SOINV circulation for the same region. The ACC is seen entering in the southwest with dynamic height ranging from 0.6-1.1 dynamic metres. The main jet of the ACC then moves south and out of Heath's area of research before reappearing in the southeast. The breakaway jet is depicted by the 1.0 to 1.1 dm contours moving north around the Campbell Plateau before turning east to meet with the main jet further east.

The location of the northward flowing SOINV circulation is nearly identical to the results presented by Heath [1981]. Interestingly, the SOINV circulation developed a region of almost no flow centred at 54°S, 181°E which coincides with the region in Heath [1981] results where the gradient of dynamic height is also very small. Also the SOINV circulation has generated an anti-cyclonic circulation centred at 47°S, 190°E that does not appear explicitly in the dynamic height contour. Heath [1981] does show a hint of the circulation with the curvature of the dotted contour in this region, however, he does not have sufficient data to resolve the circulation adequately.

Slightly east of 200°E, the ACC intensifies and crosses the

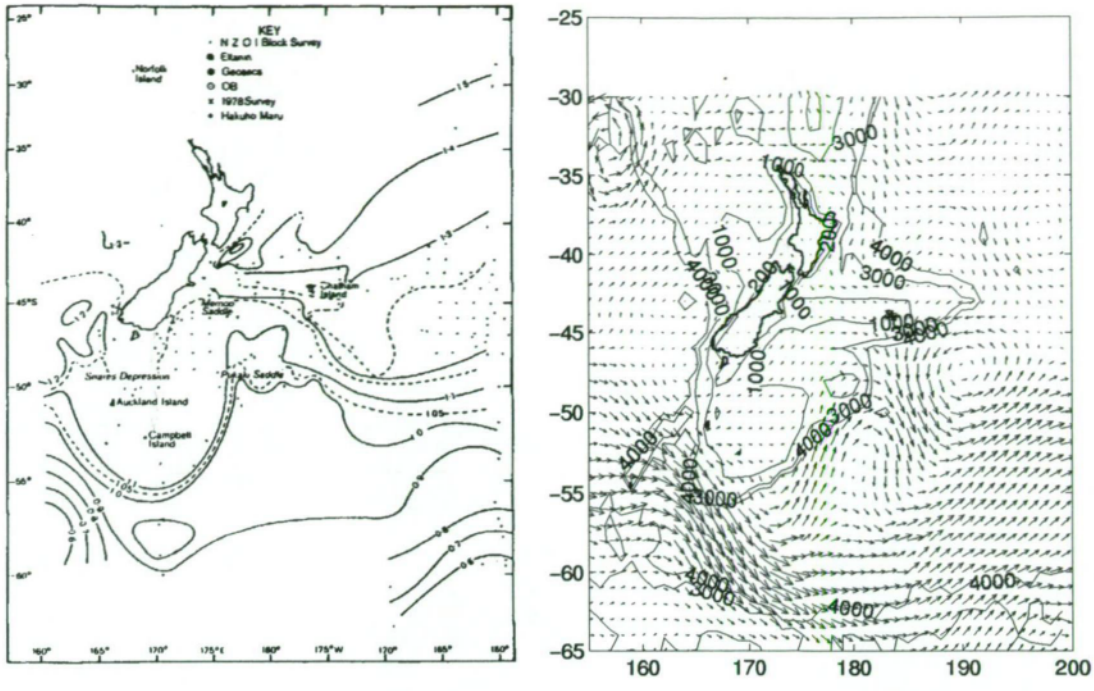


Figure 5.4: Contours of dynamic height (dynamic metres) of the sea surface relative to 1000 dbars [Heath 1981] compared to SOINV circulation around New Zealand.

Pacific-Antarctic Ridge through the Eltanin and Udintsev Fracture Zones. After crossing the ridge, the ACC continues to flow zonally across the southeast Pacific Basin before converging to flow through Drake Passage. While crossing the Pacific Antarctic Ridge, it seems likely that topographic effects steer some of the circulation northward away from the ACC. Flow on the western side of the ridge continues northward and joins with the Pacific Subtropical gyre that flows out of the model domain between 220°E and 260°E. Circulation on the eastern side of the Pacific-Antarctic Ridge continues north but crosses the Challenger Fracture zone to form a northward flowing Chile-Peru Current. This is consistent with reported observations [Reid 1973; Toole et al. 1995], although it has been reported that there is a strong subsurface counter current [Wooster and Gilmartin 1961; Silva and Neshyba 1979], which moves high salinity, low oxygen water poleward. How this and other subsurface currents move mass,

heat, salt and freshwater around the oceans is discussed in the next chapter.

The SOINV generated, Tasman Sea circulation contains a large eddy and boundary current representation of the EAC. The EAC is the western boundary current of the Pacific Subtropical gyre [Hamon 1970] originating north of 25°S. The EAC flows south down the coast of Australia, separating from the coast between 31°S and 33°S, the exact location of separation changing with time [Mulhearn 1987]. Boland and Church [1981] investigated the EAC in 1978 and found that of the water that separates from the coast, some flowed north to recirculate back into the EAC, while the remainder continued east across the Tasman Sea to flow north of New Zealand. Stramma et al. [1995] in their investigation of South Pacific circulation developed the schematic shown at the top panel of figure 5.5, which shows the main jet of the EAC separating from the coast and then meandering across the Tasman Sea to flow north of New Zealand. The SOINV circulation (bottom-right panel figure 5.5) has generated a recirculation cell that is too strong, possibly the result of being close to the boundary of the model domain. However, from the work by Boland and Church [1981] it is not uncommon to have a well developed recirculation cell in this region, as shown by the bottom left panel of figure 5.5. It is worth noting that the SOINV circulation generates a weak northward flowing current very close to the Australian coast south of 32°S. This northward flowing current has been observed in raw hydrographic data [Boland and Church 1981; Cresswell and Legeckis 1986] and is hinted at in the bottom left panel of figure 5.5 with the 170 - 200 dynamic height contours originating from further south before entering the main eddy.

The circulation pattern shown in the bottom-right panel of figure 5.5 also shows an approximate location of the Tasman Front. In the SOINV circulation, a line can be drawn from the northern tip of Tasmania, to the northern tip of

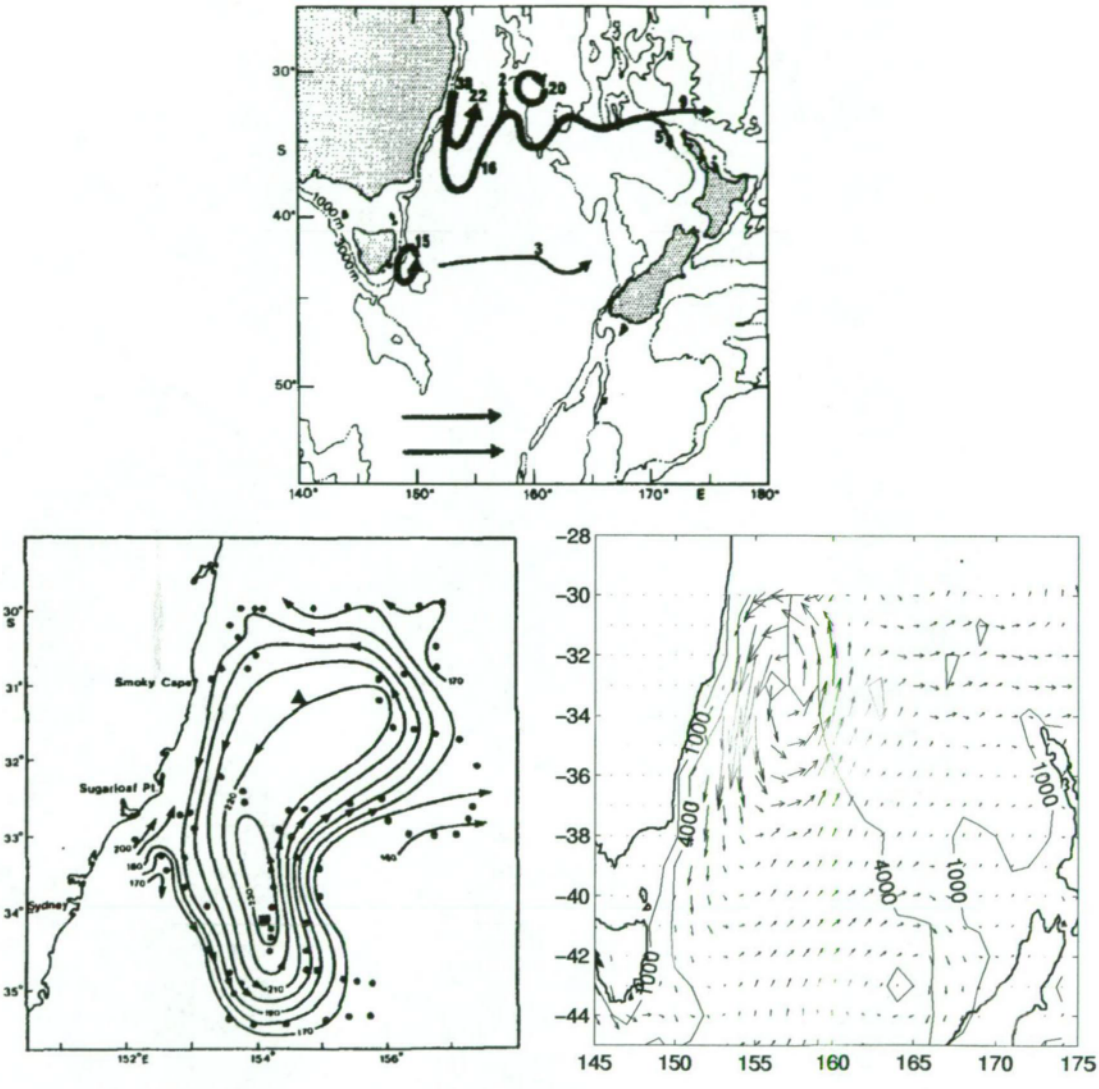


Figure 5.5: Schematic representation of the circulation of the EAC across the Tasman Sea (top) compared to the dynamic height contours (dynamic centimetres) near the separation point of the EAC from Boland and Church [1981] and SOINV circulation for the Tasman Sea.

New Zealand, where water to the north flows north around New Zealand, and water to the south flows around the southern tip of New Zealand, with a weak circulation cell centred at 43°S, 164°E. The location of this front is further south than the frontal location depicted by Reid [1986] and Mulhearn [1987], however, they defined the front from the sudden change in surface temperature and not by direction of flow.

As the outflow of the EAC flows across the Tasman Sea and north of New Zealand, some of the circulation turns north and out of the model domain. This northward flowing water is thought to recirculate back into the EAC as proposed by Ridgway and Godfrey [1994]. The remaining EAC outflow continues down the eastern side of New Zealand, around the Chatham Rise to join either the northward arm of the ACC that has circulated north around the Campbell Plateau, as discussed above, or the South Pacific gyre (see figure 5.4). The South Pacific gyre is discussed in detail by Reid [1986], who notes that the centre of the gyre moves south down through the water column. At the surface, the centre is located well north of the model domain at 18°S, 195°E but moves to the edge of the model domain at 3000 db to 30°S, 200°E. This means the model domain only contains the southern part of the gyre, which appears to enter the model domain between 180°E to 218°E and leaves between 220°E and 260°E, consistent with the description given by Reid [1986].

Peterson and Stramma [1991] produced a schematic representation of the circulation, shown in figure 5.6, which can be used to compare the SOINV's circulation (bottom panel of figure 5.1). The ACC enters the South Atlantic through Drake Passage, is forced north by the Scotia Ridge where, at 50°S, it turns east and flows zonally before entering the Indian sector of the Southern Ocean at 48°S. A little surprisingly, the topography of the Mid-Atlantic Ridge does not seem to affect the ACC as dramatically as the Pacific-Antarctic Ridge.

The Malvinas (Falkland) Current flows north over the shallow South American Continental Shelf around the Falkland Islands until 40°S, where it meets the southward flowing Brazil Current and forms the region of ocean known as the Brazil-Malvinas Confluence. The circulation of the Brazil-Malvinas confluence is complex and highly variable [Gordon and Greengrove 1986; Nowlin and Klinck 1986; Peterson and Stramma 1991; Bianchi et al. 1993; Garzoli 1993]. The Brazil Current is the western boundary current for the South Atlantic subtropical gyre and originates near 15°S [Peterson and Stramma 1991]. Some observations of the circulation associated with the Brazil-Malvinas confluence are compared to the SOINV circulation in figure 5.7. These features all show a northward flowing Malvinas current meeting the southward flowing Brazil current on the continental shelf between 40°S and 34°S. The combined jet moves offshore at 38°S out into the Atlantic. There are two recirculation cells north and south of the outflow. The southern cell, centred at 46°S, 305°E, appears to be confined by the bathymetry of the Argentine Basin. The northern cell centred at 37°S, 311°E is formed by the Brazil-Malvinas outflow moving north to 35°S before turning east to cross the Atlantic Ocean.

The eastern South Atlantic circulation is dominated by circulation associated with the Agulhas, the Agulhas Retroflection and Benguela Current around South Africa. The SOINV circulation shows an Agulhas Current that follows the continental shelf break around South Africa before returning as a counter current as discussed above. The Benguela Current is thought to be the eastern boundary current of the south Atlantic subtropical gyre and originates off the Cape of Good Hope [Peterson and Stramma 1991]. It appears that the SOINV circulation is some mean mixture of the Benguela Current, the Agulhas Current and many eddies that pinch off from the Agulhas current, a result of smoothing over all observations of the region. The southern South Atlantic

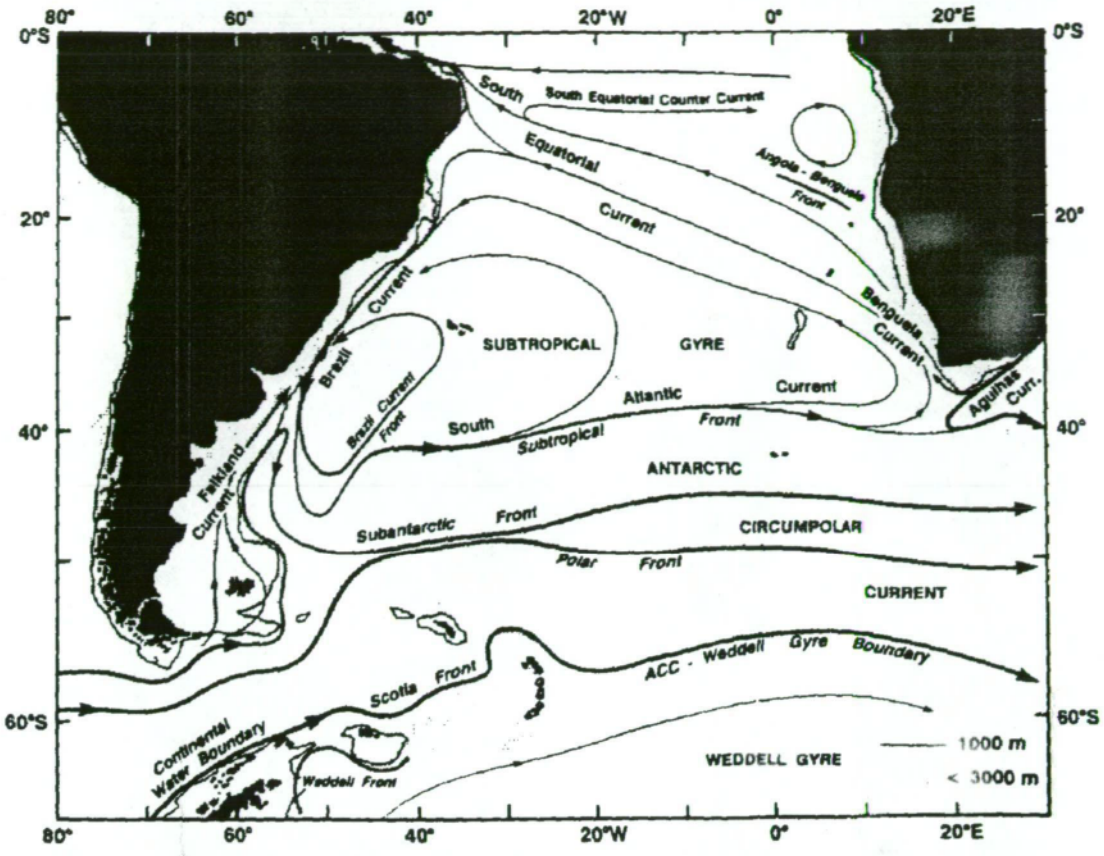


Figure 5.6: A schematic of the circulation of the South Atlantic developed by Peterson and Stramma [1991].

contains a weak Weddell Sea Gyre which circulates in a cyclonic direction south of 60°S. The Weddell Sea is the main site of bottom water production that flows down the continental slope where it moves north along the eastern side of the Antarctic Peninsula, before spreading east and north over the ocean floor [Gill 1973; Carmack and Foster 1975; Foster and Carmack 1976; Georgi 1981; Warren and Speer 1991] . The SOINV's Weddell Sea gyre is a cyclonic circulation that circulates around the Weddell Sea extending as far as 10°E along the Antarctic coastline [Orsi et al. 1993]. The SOINV circulation appears as a weaker circulation than the one described above, that is poorly resolved, mainly the result of sparse data.

The above discussion shows that qualitatively the SOINV circulation has all the major features of the Southern Ocean that have been observed

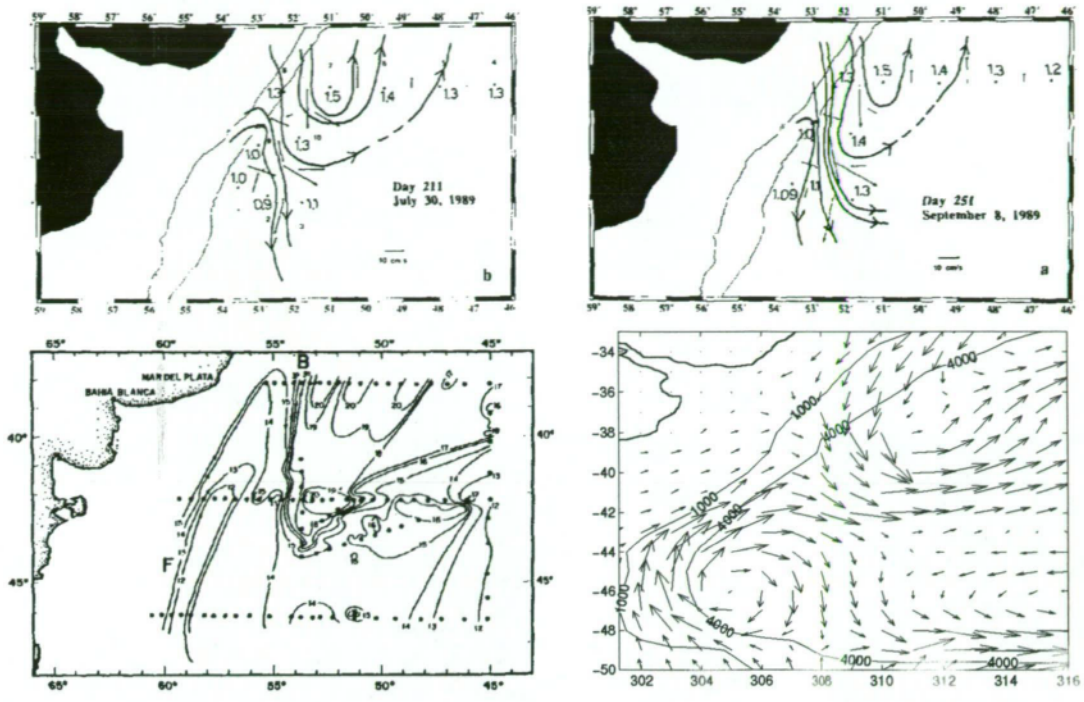


Figure 5.7: Measured circulation of the Brazil-Malvinas confluence from Garzoli [1993] (top) and Gordon and Greengrove [1986] (bottom-left) compared to SOINV circulation of the same region (bottom-right).

previously. It is clear that bottom topography has a major effect on Southern Ocean circulation, particularly the path taken by the ACC. The location of the SOINV's ACC closely matches observed circulations. The SOINV also appears to be resolving most of the boundary currents that have been observed within the Southern Ocean, particularly the Agulhas, EAC and Brazil-Malvinas current systems. The following sections compare the SOINV circulation in a quantitative manner across the northern boundary of the model domain and at three "choke points" across the Southern Ocean to Antarctica from Africa (30°E), Australia (140°E) and South America (290°E).

## 5.2 Mass Transport across 30°S

This section compares the mass transport across the northern boundary of the SOINV in a quantitative sense to previous observations. The comparisons with

the observations was carried out in two ways. Initially, the total depth-integrated transport across 30°S was compared to published results, looking closely at each ocean basin (figure 4.11 presents the transport across the entire model domain). Finally, vertical sections of velocity were compared to in-situ sections across the Indian, Pacific and Atlantic Oceans. These comparisons of transport into and out of the three ocean basins then allow us to discuss the implied transport between the ocean basins, in particular the transport through Indonesian and the Bering Strait.

The vertical sections of horizontal velocity presented in this, and following chapters were constructed as follows. The thermal winds at each cast location were calculated on the 42 standard levels of the Atlas (See Table 3.1). On each standard level, the thermal wind velocities were optimally interpolated in the horizontal onto the model grid, independent of the layer above, or below. This generates a three dimensional thermal wind field, to which the results from the SOINV can be added. From this three dimensional field of velocity, the presented vertical sections of horizontal velocity were extracted.

### 5.2.1 Indian Ocean

Figure 5.8 presents the transport across 30°S for the Indian Ocean sector. This shows that across 30°S, there is approximately 14.5 Sv transported south, into the model domain. A southward transport of 14.5 Sv compares favorably to published estimates of the transport, that vary from 2-14 Sv [Piola and Gordon 1984; Fine 1985; Fu 1986; Murray and Arief 1988; Toole and Warren 1993]. The southward transport is dominated by the Agulhas Current down the east coast of Africa, a surface subtropical gyre west of 75°E, that transports mass north, and a deep southward circulation east of 75°E that moves mass south.

From figure 5.8, the SOINV's Agulhas current transports 38 Sv southward

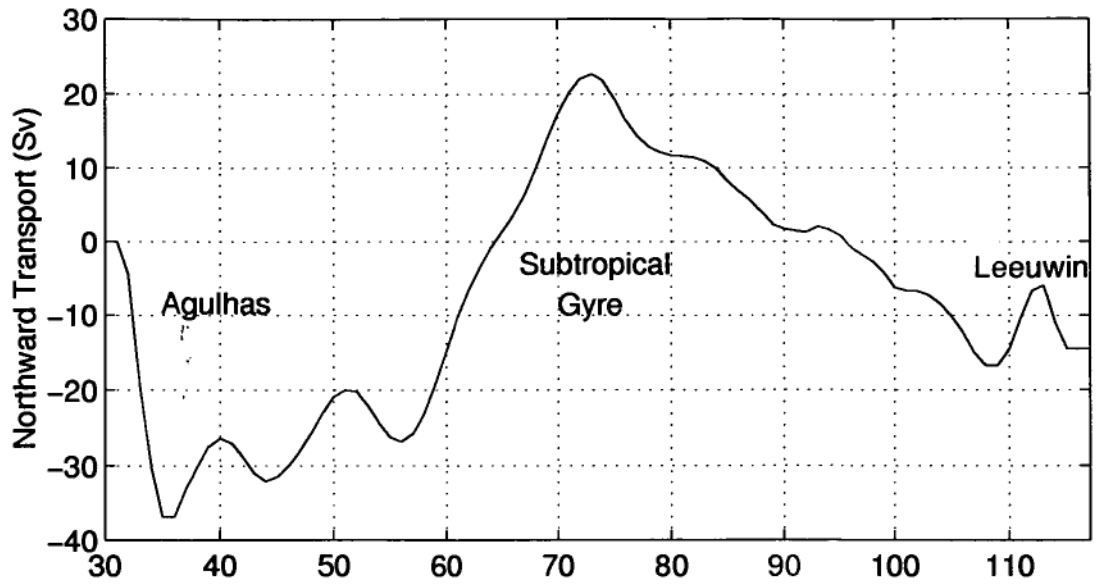


Figure 5.8: Northward transport (Sv) across 30°S in the Indian Ocean.

into the model domain. This is slightly lower than the published estimates of 44 Sv by Toole and Raymer [1985] or 60 Sv reported by Grundlingh [1980], Toole and Warren [1993] and Read and Pollard [1993]. The Subtropical gyre is estimated to transport 60 Sv northward out of the model domain, mainly between 55°E and 75°E. As will be shown shortly, the subtropical gyre circulation is mostly surface mass transport, while the general southward transport into the model domain east of 75°E is due to deep water transport. Close to the coast of Australia, the SOINV estimates a Leeuwin Current transporting 8 Sv southward, which is slightly larger than the estimated 5 Sv calculated by Smith et al. [1991] and Godfrey and Ridgway [1985].

The trans-Indian velocity (thermal wind + reference) section across 30°S is presented in figure 5.9 with the associated optimal mapping error field. The velocity field shows that the surface waters (above 800 metres) are generally moving north, and that the deeper water flows south. There is a core of northward flowing water centred on 70°S that extends through the water column. This northward flowing water matches the location of the main

offshoot from the ACC, that is defected north by the 4000 metre contour between Amsterdam and Kerguelen Islands. The location of this main offshoot has been observed to be fairly constant. Fine [1994], while investigating the circulation of the South Indian Ocean using chloroflourocarbons, observed a compact anticyclonic gyre which was located west of 72°E, so that the northward flowing arm of the gyre was centred on 70°E. As the circulation of the SOINV, that includes all observations in the area, depicts a northward transport at the same location, suggests that it is a stable feature. Most of the deep waters, east of 72°E, are flowing southward, with a strong core located on the eastern flank of the Mid-Indian Ridge.

The largest velocities of the SOINV section are associated with the Agulhas and Leeuwin currents. Figure 5.10 presents enlarged sections of the Agulhas and Leeuwin currents. The enlarged sections show that the maximum velocities of the Agulhas Current are only 5 cm $s^{-1}$, and 12 cm $s^{-1}$ for the Leeuwin Current. These are considerably smaller than observed velocities, such as 120 cm $s^{-1}$ [Toole and Raymer 1985] or 200 cm $s^{-1}$[Grundlingh 1980] for the Agulhas Current, and 150 cm $s^{-1}$ [Cresswell 1991] or 180 cm $s^{-1}$ [Church et al. ] for the Leeuwin Current. These comparisons are somewhat meaningless because the SOINV circulation has undergone an amount of smoothing and been calculated on a relatively course grid when compared to the width of these boundary currents. It is also somewhat difficult to compare a mean transport circulation to extreme velocity circulations. However, although the SOINV's velocities are much smaller than the observed velocities, the estimates of transport across the section are comparable.

It is possible to compare the shape of the vertical circulation. From figures 5.9 and 5.10, the SOINV's Agulhas current extends to the bottom which is consistent with the work of Grundlingh [1980] and Toole and Raymer [1985].

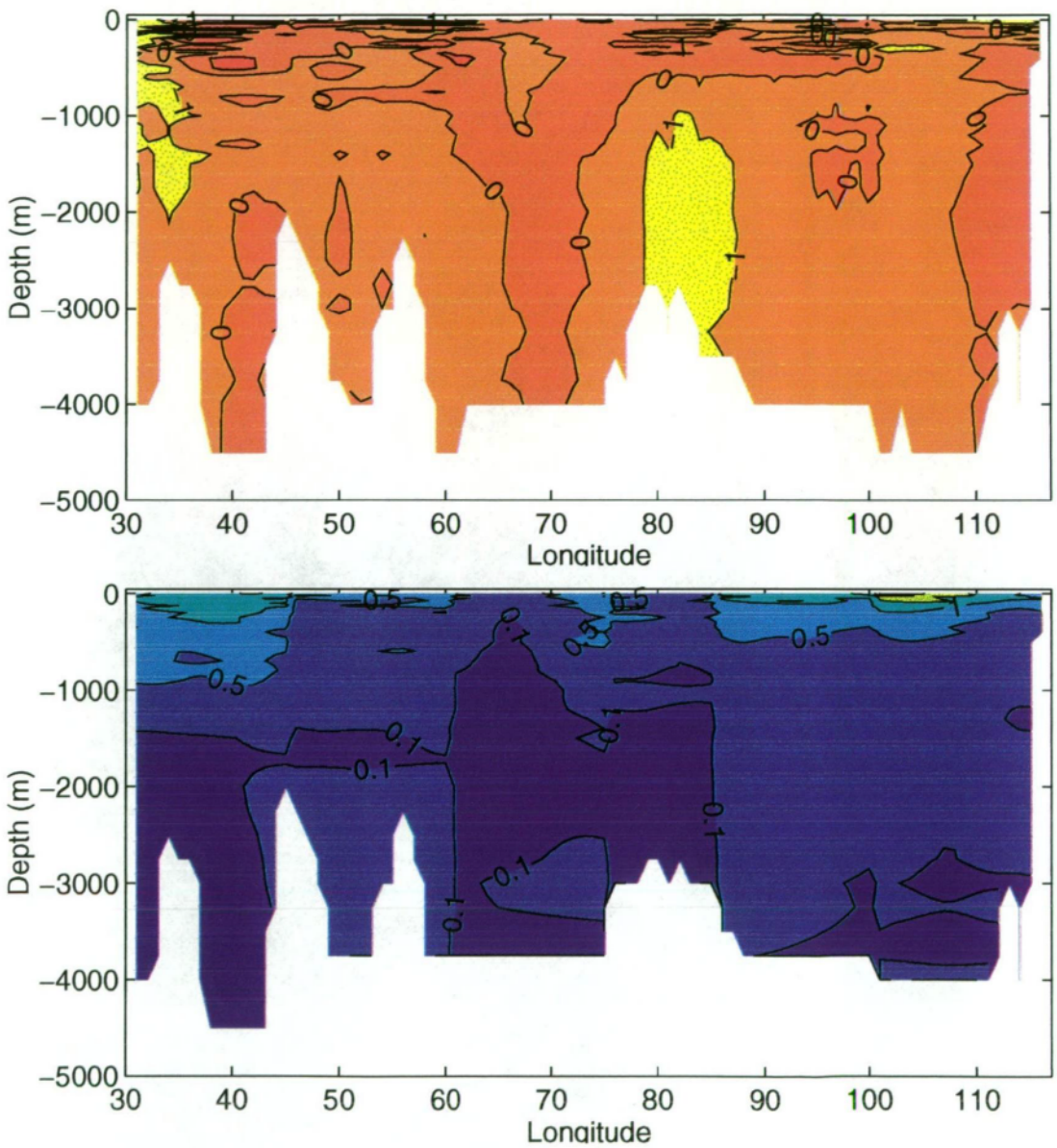


Figure 5.9: Velocity section (Thermal + Reference, cm $s^{-1}$) across the Indian Ocean at 30°S and associated optimal interpolation error field.

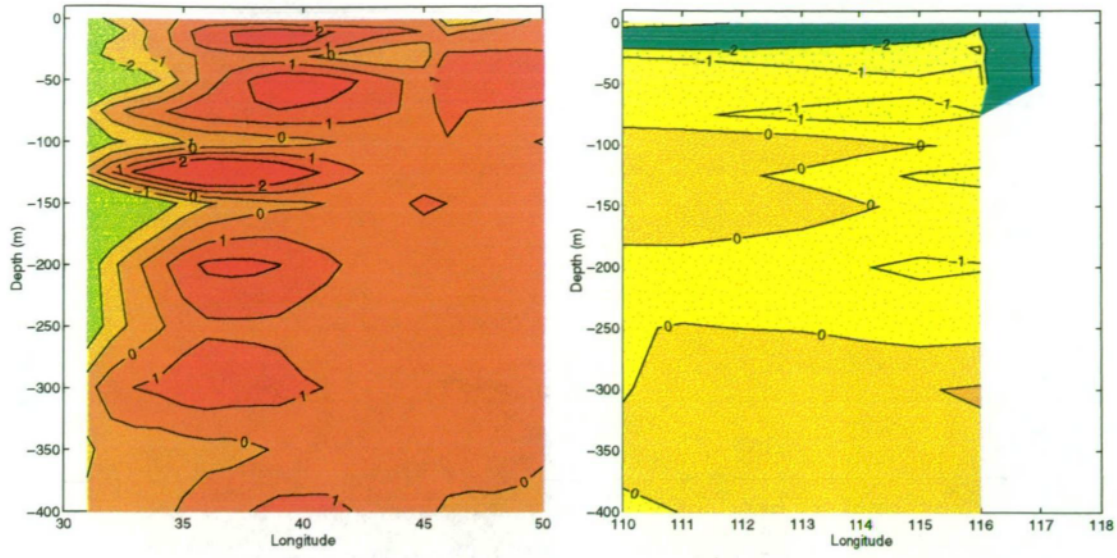


Figure 5.10: Expanded velocity sections for the Agulhas (left) and Leeuwin (right) Boundary Currents.

There is a significant, relatively shallow (above 500 metres), return current that extends across the Indian basin as far as 80°E and appears to continue subsurface until 100°E. The Leeuwin Current is a shallow, intense southward current on the continental shelf with a deeper (down to 250 metres) southward current extending off the shelf. Below 250 metres, there is a weak return current as observed by Godfrey and Ridgway [1985] and Smith et al. [1991].

The errors presented in figure 5.9 are the errors from the optimal interpolation process. As outlined in section 4.4, error estimates from the inverse solution are not available and cannot be included. The errors show the effect of using different signal variances in the different regions with apparent, sudden jumps in error estimation associated with the edges of the remapping regions shown in figure 3.11. These errors give some feel for the confidence of the estimated velocities. Surface velocities generally have higher interpolation errors, because of the higher signal variances. As depth increases, the number of observations decrease, causing an associated decrease in signal variance, thus reducing the error estimate. However, at depths where there are only a few

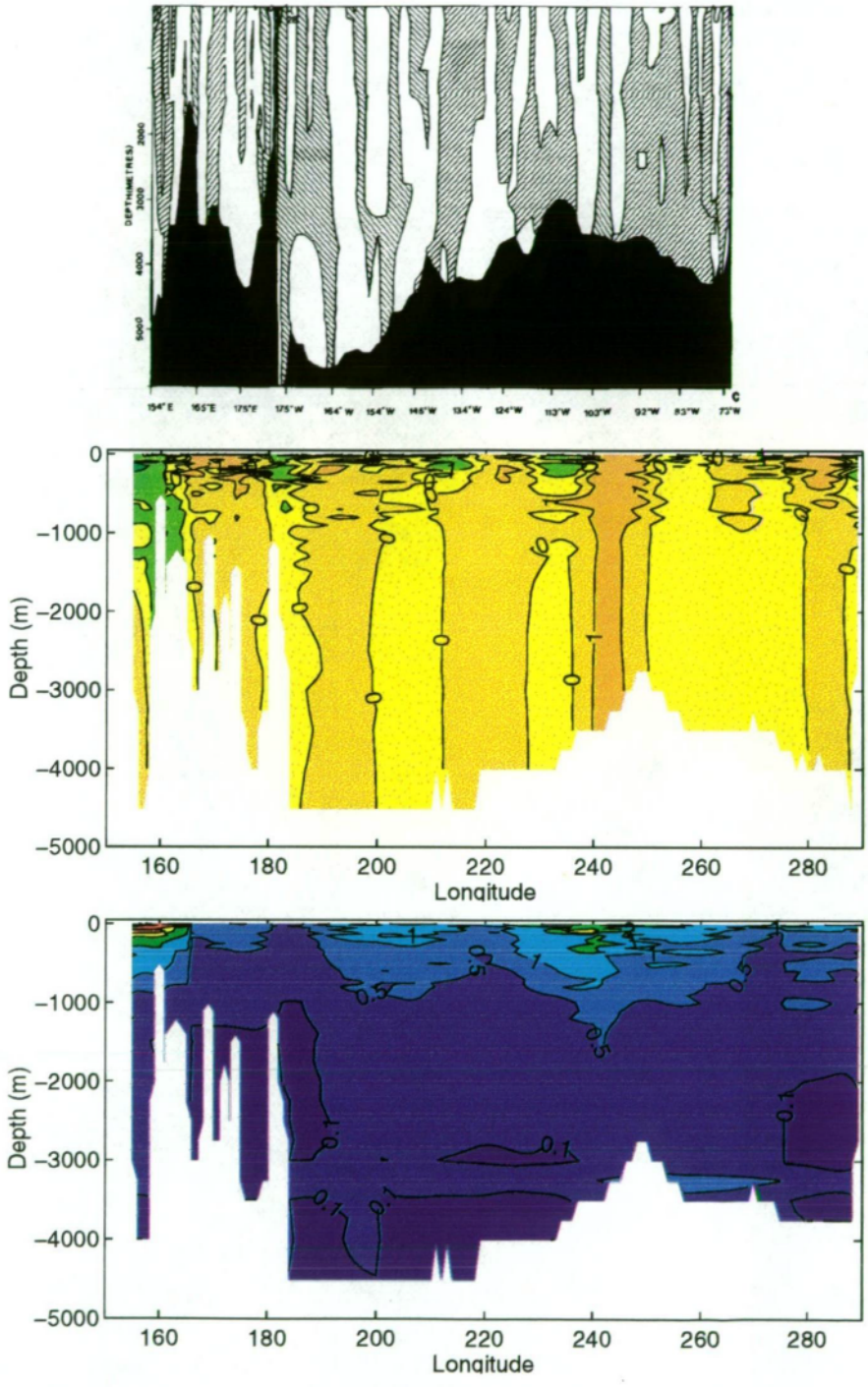


Figure 5.12: Velocity section across 28°S from Wunsch et al. [1983] (top panel) compared to the SOINV circulation (Thermal wind + Reference velocity, cm $s^{-1}$) across the Pacific Ocean at 30°S (middle) and associated optimal interpolation errors (bottom).

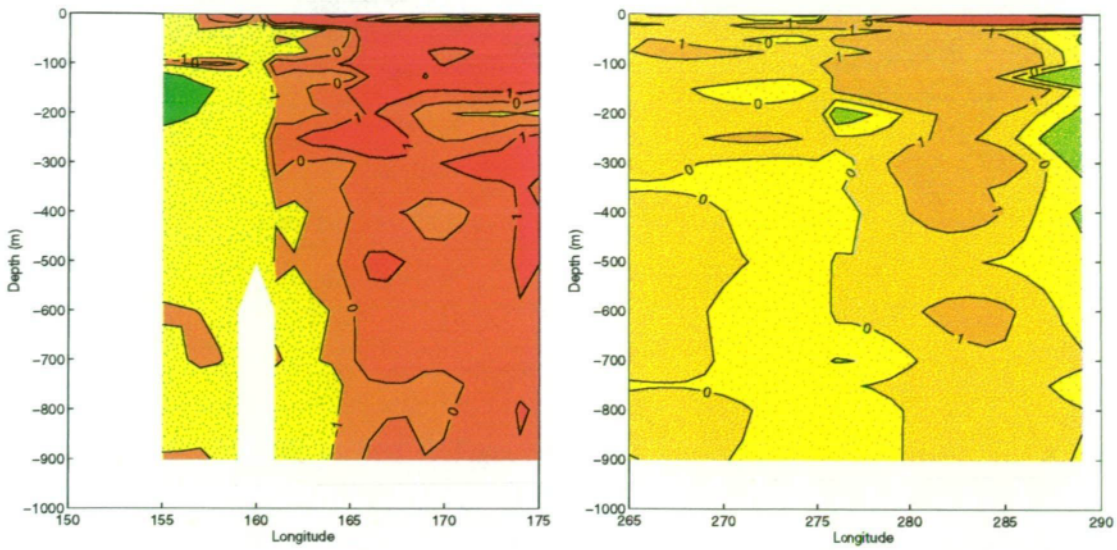


Figure 5.13: Expanded velocity sections (cm $s^{-1}$) for the EAC (left) and Chile-Peru (right) Boundary Currents of the Pacific Ocean. (In right panel: Unmarked contours close to South America, below 100 metres depth are all -1 cm $s^{-1}$.)

and comparing to the inverse results of Wunsch et al. [1983], it is clear that there is a strong vertical structure to the section, particularly in the deeper layers. This is consistent with the sections from the SCORPIO cruises [Warren 1973]. Warren [1973] referenced his velocities to 2000 metres and as a result developed some bottom velocities in excess of 20 cm $s^{-1}$ on the eastern side of Campbell Plateau. The SOINV circulation does not generate any large velocities at depth, consistent with the circulation developed by Wunsch et al. [1983] as shown in the top panel of figure 5.12. Both model results show the vertical banding across the entire section, although these results are more noisy than those presented by Wunsch et al. [1983] in the surface layers, but tend to be smoother in the deeper layers. Both models show their largest velocities in the two boundary currents, although the Wunsch et al. [1983] model shows a poleward transport associated with the Chile-Peru Current while these results show a equatorward transport consistent with the velocity sections discussed by Warren [1973] and Reid [1973]. Wunsch et al. [1983] discuss their discrepancy to the observations and note that they did not use the two shallowest casts at the

eastern end of the SCORPIO sections which contain the Chile-Peru Current signal. They justified this by stating that the integrated results were insensitive to the inclusion of the two casts.

The SOINV's depiction of the Chile-Peru Current, presented in figure 5.13, shows a strong, equatorward surface current close to the continent. This overlies a weak poleward return current that extends to the bottom, very close to the South American continent, matching the observations reported by Wooster and Gilmartin [1961] and Silva and Neshyba [1979]. This subsurface counter current forces the surface equatorward current away from the continent as it extends through the water column, also to the bottom. It is felt that the model by Wunsch et al. [1983] has possible over emphasised the strength of this subsurface current.

In the western boundary current, the circulation of the two models compares extremely closely. Both show an intense, poleward surface current that extends through the water column. At depth, below approximately 2000 metres, both show an equatorward flow up the east coast of Australia. Offshore, both models show an equatorward return current, also extending through the water column. These are consistent with the work by Boland and Hamon [1970].

By comparing figures 5.11 and 5.12, it appears that the deep ocean is having the most influence on the total transport across 30°S. The strong southward and northward transport of water, previously associated with the subtropical gyre, coincides with the coherent vertical sections of horizontal velocity, suggesting that the subtropical gyre extends throughout the water column. This is somewhat contradictory to the idea that the subtropical gyres are wind-driven surface circulations and so the previous statement needs clarification. What appears to be happening is that the northward transport on the western flank of the East-Pacific Rise, coincides with the northward

transport of the subtropical gyre and that the Southwest Pacific Basin is acting as a sub-basin within the Pacific Ocean for large scale circulation with both western and eastern boundary currents. The eastern boundary current is the northward circulation discussed above. The western boundary current is only weakly present in the SOINV results as the weak southward transport at 185°E on the eastern flank of the ridge that extends north of New Zealand to the Fijian Islands.

The results of the Pacific sections are slightly less reliable than the Indian section. This can be seen by comparing the optimal interpolation errors of the Pacific (bottom panel of figure 5.12) to the optimal interpolation errors for the Indian section (figure 5.9). This comparison shows that the error contours in the Pacific are generally deeper than the Indian section with some regions having errors as large as 2 cm $s^{-1}$. This increase in interpolation errors is primarily due to the lack of data in the region. As discussed in chapter 3, the Pacific ocean is data sparse, particularly east of New Zealand, which corresponds to the region of highest interpolation errors seen in figure 5.12.

### 5.2.3 Atlantic Ocean

The Atlantic Ocean is estimated to have a total southward transport of <1 Sv (see figure 5.14). The Atlantic is generally considered not to have a net transport associated with it across 30°S [Rintoul 1988], although a small transport (<1 Sv) from the Pacific to the Atlantic through the Arctic Ocean has been measured in the Bering Strait by Coachman and Aagaard [1988]. From figure 5.14 it can be seen that 28 Sv of water is transported into the model domain between the coast and 315°E by the Brazil Current mainly as a deep boundary current (see figure 5.15). There is a small return current of 8 Sv until a large inflow of water (25 Sv) that extends through the water column between

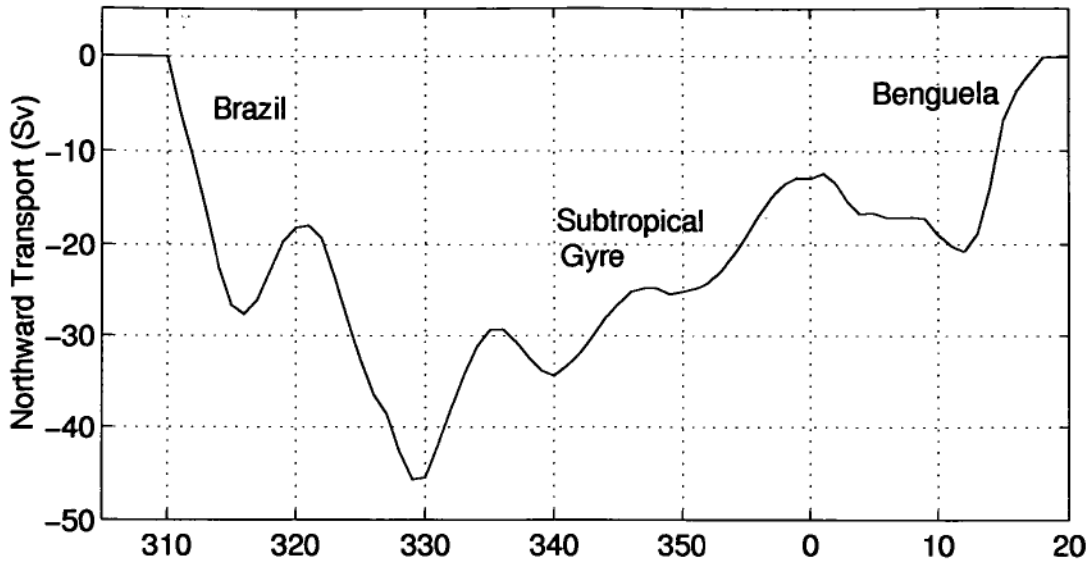


Figure 5.14: Integrated northward transport (Sv) across 30°S in the Atlantic Ocean.

320°and 329°E. Between 330°E and 360°E the subtropical gyre transports 30 Sv northward out of the model domain. East of 0°E there is a weak southward flow that is thought to be mainly a southern excursion of the eastern subtropical gyre. Close to the African coast, east of 12°E there is a strong northward flowing boundary current transporting 21 Sv. This northward current is a mixture of the Benguela and Agulhas Currents .

Estimates for the total transport associated with the Brazil current vary widely from less than 1 Sv [Stramma et al. 1990] to greater than 70 Sv [McCartney and Zemba 1988; Zemba and McCartney 1988; Peterson 1990]. However, the estimates by McCartney and Zemba [1988], Zemba and McCartney [1988] and Peterson [1990] are the only estimates to consider the contribution of the deeper waters, suggesting the SOINV's estimate of 28 Sv is low for the Brazil Current. The expanded view of the Brazil Current is shown in the left hand panel of figure 5.16. Maximum velocities associated with the Brazil Current exceed 8 cm $s^{-1}$. It is closely associated with the continental shelf and bounded by a relatively strong return current.

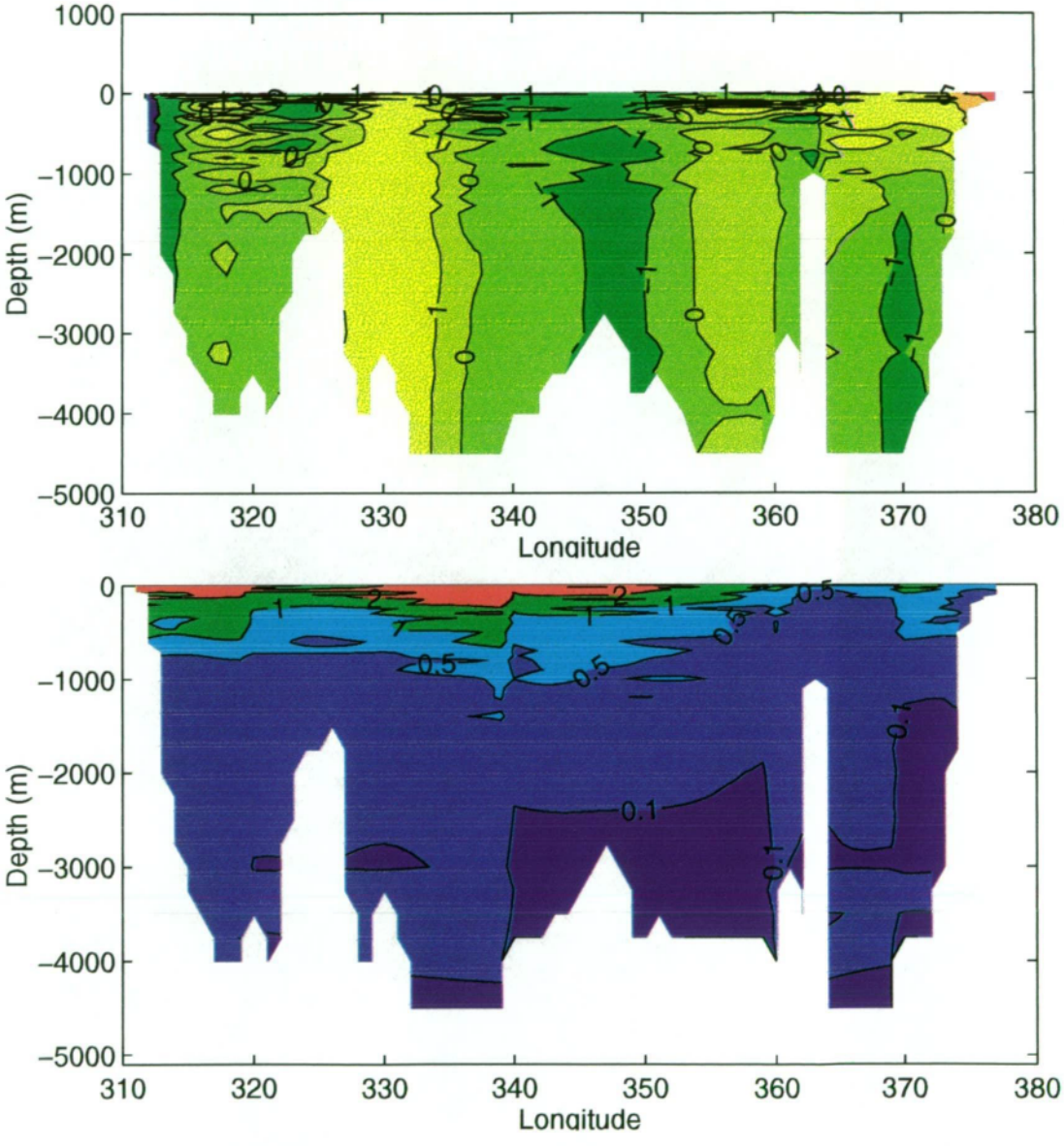


Figure 5.15: Velocity profile (Thermal + Reference, cm $s^{-1}$) across the Atlantic Ocean at 30°S and associated optimal interpolation error field.

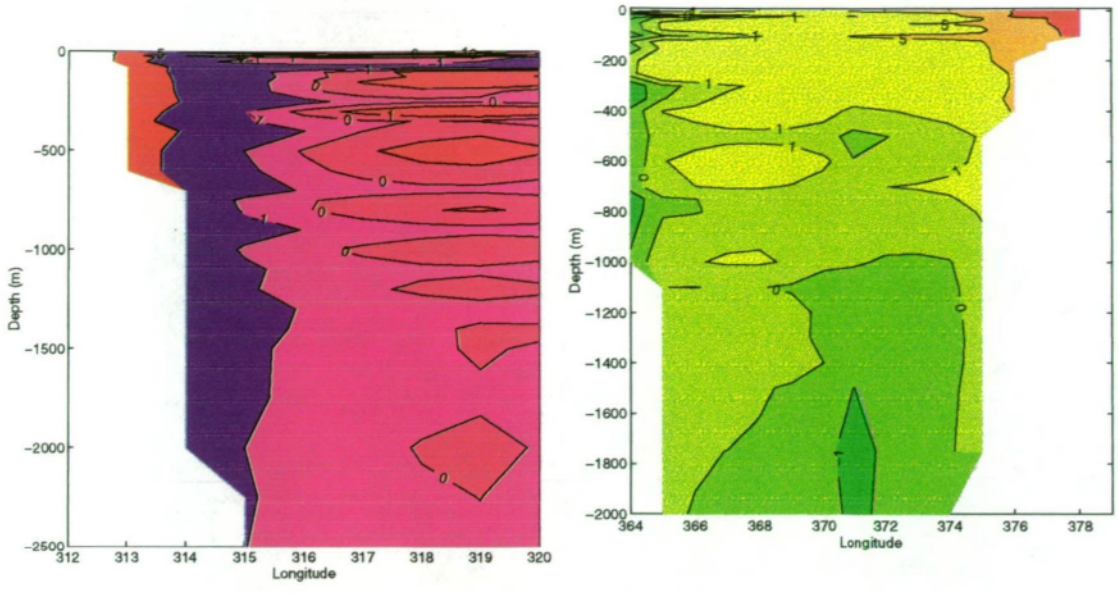


Figure 5.16: Expanded velocity profiles for the Brazil (left) and Benguela (right) Boundary Currents.

The SOINV representation of the Benguela Current that transports 21 Sv north is, by inspection of figure 5.1 a complex mixture of Agulhas transport continuing into the Atlantic, and the Benguela current. Thus, it is difficult to compare directly to previous studies. Peterson and Stramma [1991] compiled a table of estimates for Agulhas transport into the Atlantic which vary from 3-15 Sv [Stramma et al. 1990]. The Benguela Current is reported to be the eastern current of the south Atlantic Subtropical gyre, originating off the Cape of Good Hope and flowing north along the coast of Africa before separating from the coast at approximately 30°S. Estimates of the volume transport of the Benguela Current vary from 15 Sv, relative to 1500m by Wooster and Reid Jr [1963], to 21 Sv in the upper layer by Stramma and Peterson [1989]. The right hand panel of figure 5.16 shows the intense surface current on the continental shelf that continues over the edge of the continental shelf down to a depth of 1000 metres. Below the sill depth of the Walvis Ridge, at 30°S, 4°E, there is a southward flowing counter current that extends to the bottom as observed by Reid [1986].

### 5.2.4 Inter-basin exchange outside model domain. Implications for Indonesian Throughflow and Bearing Strait transport.

From the above discussions on mass transport across the northern boundary of the SOINV, some conclusions can be drawn about the ocean circulation on basin scales outside the model domain. As noted above, 14.5 Sv enters the model domain from the Indian Ocean, 14.7 Sv leaves in the Pacific and the balance of the flow enters from the Atlantic. These basin scale transports are generated by the SOINV without any constraints prescribing mass transport across the sections and without any knowledge of the global geography outside the model domain. It appears that the SOINV generates basin transports that recognise a route of connection between the Pacific and Indian Oceans and a minimal connection between the Pacific and Atlantic Oceans outside the model domain. It also implies that the only route of connection between the Atlantic and Indian Oceans is within the model domain, and that the net exchange between the Indian and Atlantic Ocean balances. This result of implied circulation outside the model domain gives us a great deal of confidence in the skill of the SOINV to adjust the boundary circulation to make a consistent estimate of the transport of mass.

From the presented transports it can be concluded that there is a transport of 14.5 Sv associated with Indonesian throughflow. By comparison to estimates of Indonesian throughflow by direct methods, that include 2 Sv [Wyrtki 1961], 5 Sv [Godfrey and Ridgeway 1984; Fine 1985], 10 Sv [Godfrey and Golding 1981], 12 Sv [Meyers et al. 1995] and 14 Sv [Piola and Gordon 1984], it appears that the total throughflow is larger than most studies estimate. The Indonesian group of Islands divide the region into many channels, providing many paths for water to move from the Pacific into the Indian Ocean. Attempting to measure all of these channels is difficult, with most investigations

concentrating on particular regions [Godfrey and Golding 1981; Murray and Arief 1988; Meyers et al. 1995]. It is therefore probable that most estimates of Indonesian throughflow, except those who use basin scale methods, are missing some part of the transport.

Using a similar argument it could be concluded that there is an exchange of mass between the Pacific and Atlantic Oceans through the Bering Strait. Coachman and Aagaard [1988] estimated the net transport through the Bering Strait by the combined use of hydrographic data and current meter moorings to be less than 1 Sv. This is of comparable size to the less than 1 Sv estimated to circulate from the Pacific to the Atlantic outside the model domain.

## 5.3 Eastward Mass Transport

In this section the eastward mass transport through the three main choke points of the Southern Ocean, namely Drake Passage and south of Africa and Australia. The integrated transport across each choke point is presented with the vertical sections of horizontal, compiled as described in the previous section, and compared to observations within the region.

### 5.3.1 65°W, Drake Passage

The ocean around Drake Passage is the most intensely measured area of the Southern Ocean and an obvious choice to compare measurements to SOINV results. In the 1970's the International Southern Ocean Studies program carried out several hydrographic sections from Cape Horn to Livingston Island in the South Shetland Islands [Sievers and Nowlin 1984]. Later in 1990, the World Ocean Circulation Program (WOCE) carried out a section across Drake Passage along a track slightly westward of the ISOS program sections [Roether et al. 1993]. Two hydrographic sections, one from each program, are compared to the

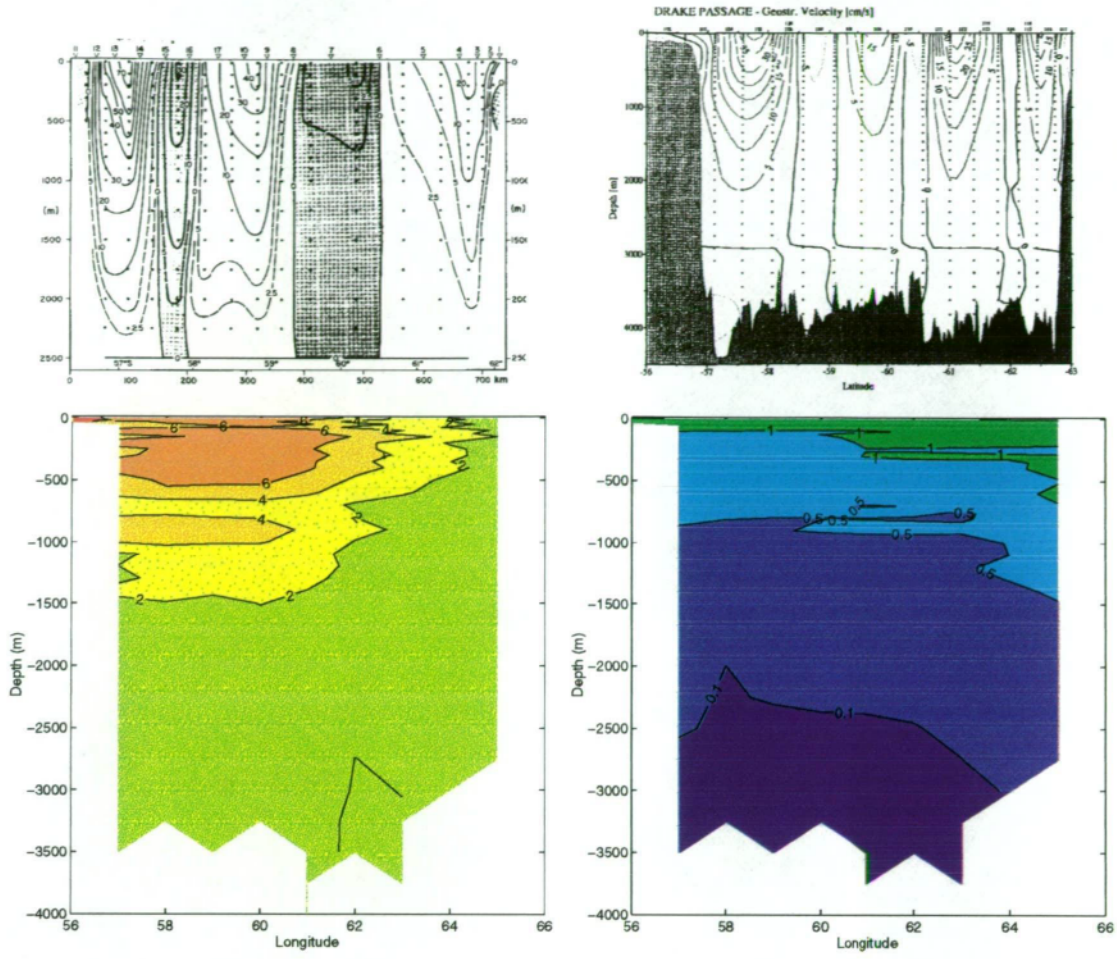


Figure 5.17: Velocity sections for the ISOS (top-left) and WOCE (top-right) transects of Drake Passage compared to SOINV velocity section (thermal wind + reference) (bottom left) and associated optimal interpolation errors (bottom right) (cm $s^{-1}$).

SOINV results in this part of the thesis. The section carried out during ISOS was conducted aboard the R/V Melville from 26 February to March 7 1975 and reported by Sievers and Nowlin [1984], while the WOCE section was conducted aboard the R/V Meteor from January 23 to March 8 1990 and reported by Roether et al. [1993].

Across Drake Passage, the ISOS results show 5 current cores and the WOCE section presents 7 current cores, see figure 5.17. The ISOS velocity section (top left panel), calculated relative to 2500 metres, shows three strong

eastward moving current cores associated with the Sub-Antarctic Front, the Polar Front and the Continental Water Boundary [Sievers and Nowlin 1984]. There are two weak westward flowing coutercurrents at 58°and 60°S represented by the shaded regions in figure 5.17. The WOCE velocity section (top right panel), calculated relative to 3000 metres, shows four eastward flowing current cores separated by weak westward coutercurrents. Roether et al. [1993] identifies the two central cores as Polar Frontal cores caused by bifurcation of the Polar Front west of the ISOS section. In both sections, the current cores extend to the bottom.

The major feature of the SOINV velocity section is the dramatic smoothing that has occurred. There is no hint of the many current cores that exist in this region. The smoothing and time averaging has smeared all the current cores into one large core centred at 62°S that extends through the water column to the bottom. There is an order of magnitude difference between the maximum SOINV velocities and the maximum observed velocities, yet the SOINV generates a net mass transport of 92 Sv through Drake Passage. This transport through Drake Passage is estimated from the SOINV with no constraints applied. Rintoul [1988] estimated a transport of 129 Sv, but only after constraining the model to have a transport through Drake Passage of 130±13 Sv based on the estimate calculated by Nowlin and Klinck [1986]. Rintoul [1988] did run an unconstrained model of the South Atlantic using a reference level of 3500 db, which generated a transport of only 113 Sv. Other observational estimates for the transport through Drake Passage range from 70-80 Sv [Whitworth 1980] to greater than 250 Sv [Bryden and Pillsbury 1977], but the most accepted value is the estimate by Nowlin and Klinck [1986] of 130±13 Sv.

### 5.3.2 30°E, South of Africa

To investigate the volume fluxes south of Africa, the SOINV section was located at 30°E to allow the section to be closed at both the northern and southern end. In 1983-84, along 0°E, the AJAX section was occupied in two stages and is used to compare volume fluxes. A closer section along 40°E is used to compare temperature and salinity sections in the following chapter, but the 40°E section did not have a published velocity profile. The two stages of the AJAX section were joined at 45°S and taken several months apart with the northern section observed in October, November 1993 and the southern section observed in January 1984. The southern section of AJAX is reported by Whitworth and Nowlin [1987].

The velocity sections for AJAX and the SOINV are compared in figure 5.18. The velocity profiles are remarkably similar, much more so than in Drake Passage, unfortunately the similarity is artificial. Because the AJAX section is comprised of two hydrographic sections, taken several months apart and joined at 45°S, there are differences in temperature and salinity that are due solely to the time difference. These temperature and salinity differences generate an artificial jump in dynamic height at 45°S that generates the corresponding current core located at 45°S in top panel of figure 5.18 and thus it should be ignored. The more southern velocity core located at 49°S on the northern edge of the Mid Atlantic Ridge is real. The SOINV section also has two main velocity cores, however the northern jet at 39°S is associated with the Agulhas Return Current and the southern core at 46°S is the ACC, again on the northern side of the South-West Indian Ridge. So by ignoring the northern velocity core in the AJAX section, and acknowledging that the Agulhas-Return Current core will not be in the AJAX section, the two sections are still very similar. It should also be noted that in both sections, there is a weak westward

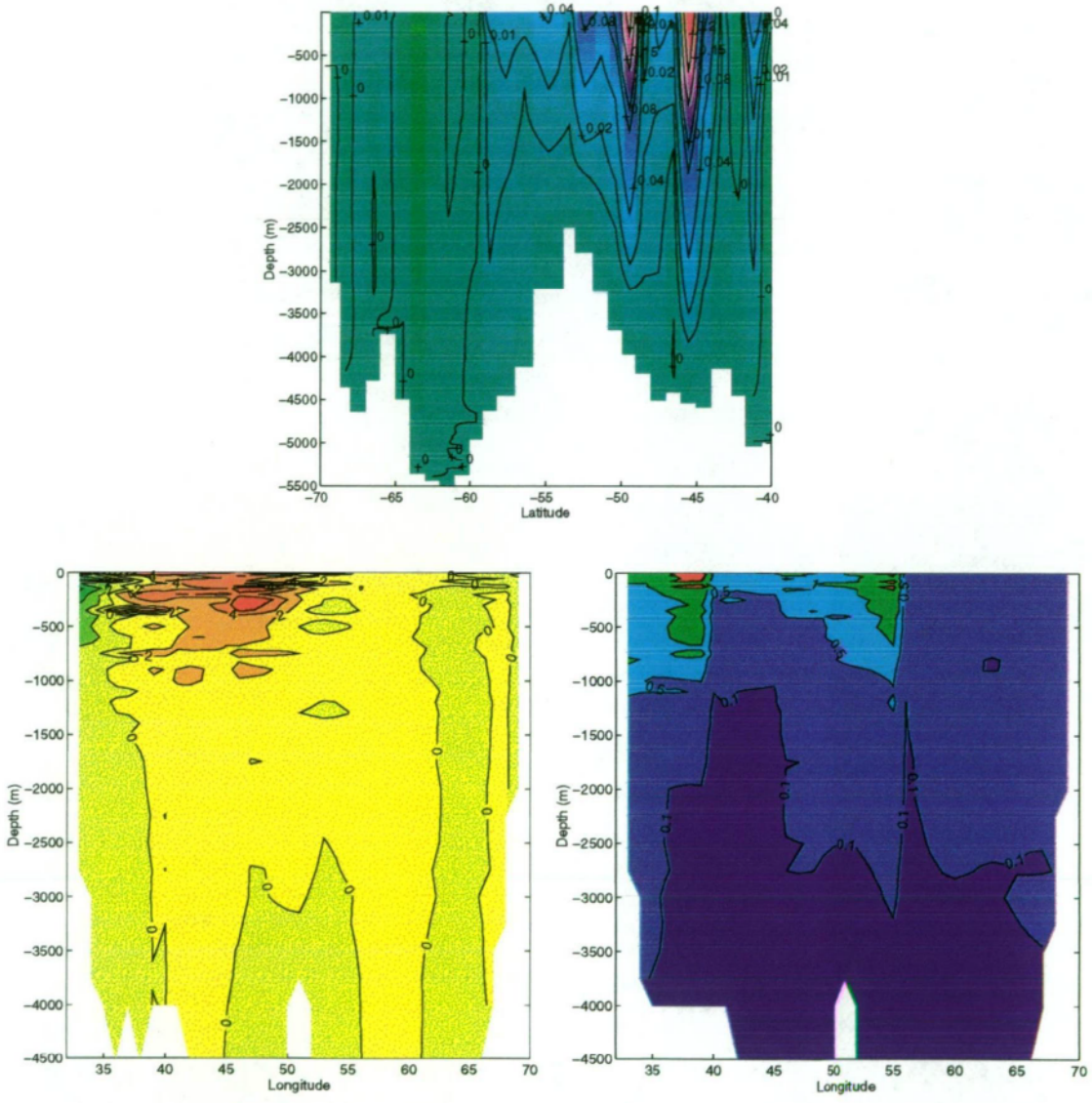


Figure 5.18: Velocity (cm $s^{-1}$) section for AJAX (top) compared to SOINV velocities (bottom left) and associated errors (bottom right).

velocity core located at approximately 65°S, that is characteristic of the eastern limb of the Weddell Sea Gyre [Carmack and Foster 1975; Foster and Carmack 1976]. Both of the SOINV current cores extend to the bottom as does the Agulhas Current Core that can be seen close to the African continent at 34°S.

Because there is so little net southward transport entering the model domain from the Atlantic Ocean, the transport south of Africa is virtually the same as through Drake Passage, i.e., 92.5 Sv. This transport is small compared to current estimates of 130±13 Sv [Nowlin and Klinck 1986; Rintoul 1988]. By inspection of figure 5.19, it is possible to see that most of the mass is being transported to the east by the ACC, located at 48°S, and to the west by the Agulhas Current at 39°S. Moving north from Antarctica, the first significant feature in figure 5.19 is a weak westward current located at 69°S, close to the Antarctic Continent. North of this westward current, the Southern Ocean is very weakly eastward until 53°S, where the effect of the ACC begins. The ACC extends from 53°S to 43°S with a maximum transport of approximately 14 Sv per degree of latitude. North of the ACC, and south of 36°S, is the Agulhas Return Current transporting 10 Sv per degree to the east. The intense westward boundary Current is, as explained above, the Agulhas Current that has continued down the east coast of Africa and about to enter the Atlantic Ocean.

From figure 5.19, it is possible to estimate how much mass transported by the Agulhas Current, is leaving the Agulhas to continue into the Atlantic Ocean. The estimate is subject to the assumption that mass transported westward by the Agulhas Current is transported eastward by the Agulhas Return Current. As defined above, the Agulhas Return Current ranges from 43°S to 36°S and the main Agulhas Current from 36°S to the African continent. From the bottom panel of figure 5.19, there is an integrated mass imbalance between 43°S and the African continent of approximately 2 Sv to the west. This

suggests that nearly all of the circulation of the Agulhas Current returns to the east, which is at odds to the conclusions made by Gordon [1985] that there was a significant transport by the Agulhas Current into the Atlantic Ocean of 14 Sv.

### 5.3.3 145°E, South of Tasmania

The ocean south of Australia is unique in that it is the largest continuous section of the Southern Ocean that is land locked to the north. It is also a relatively poorly sampled section of the Southern Ocean, with few measurements away from coastal Australia (see figure 3.9). As part of the WOCE initiative, there have been 5 repeat occupations of the SR3 section between Tasmania and Antarctica which lies mainly along 140°E. The data presented here are for the 1994 occupation which occurred between January 3rd to January 28th 1994 [pers. comm. S. Rintoul]. As means of comparing to some historical data, the zonal velocity from the USNS Eltanin cruise 36 during October 22 to November 3 1968 as reported by Callahan [1971] is also presented (see figure 5.20).

The velocities produced by the SOINV are an order of magnitude smaller than both the SR3 and Eltanin results. The main jet associated with the ACC is situated on the northern side of the Australian Antarctic Ridge in all three sections with the SR3 and Eltanin jet more concentrated than the SOINV data suggesting that the ACC, while remaining close to its central position, does wander over several degrees north and south. Both the SR3 and Eltanin sections have a small westward countercurrent on the southern side of the ridge. Although the SOINV does not have this feature, by inspection of the circulation in plan view (see figure 5.1), at 140°E the ACC turns north giving a weak zonal component but a large meridional component. Interestingly the SOINV section has developed a permanent recirculation cell to the north of the ACC at 46°S, which is present in the SR3 data but not observed in the Eltanin data further to

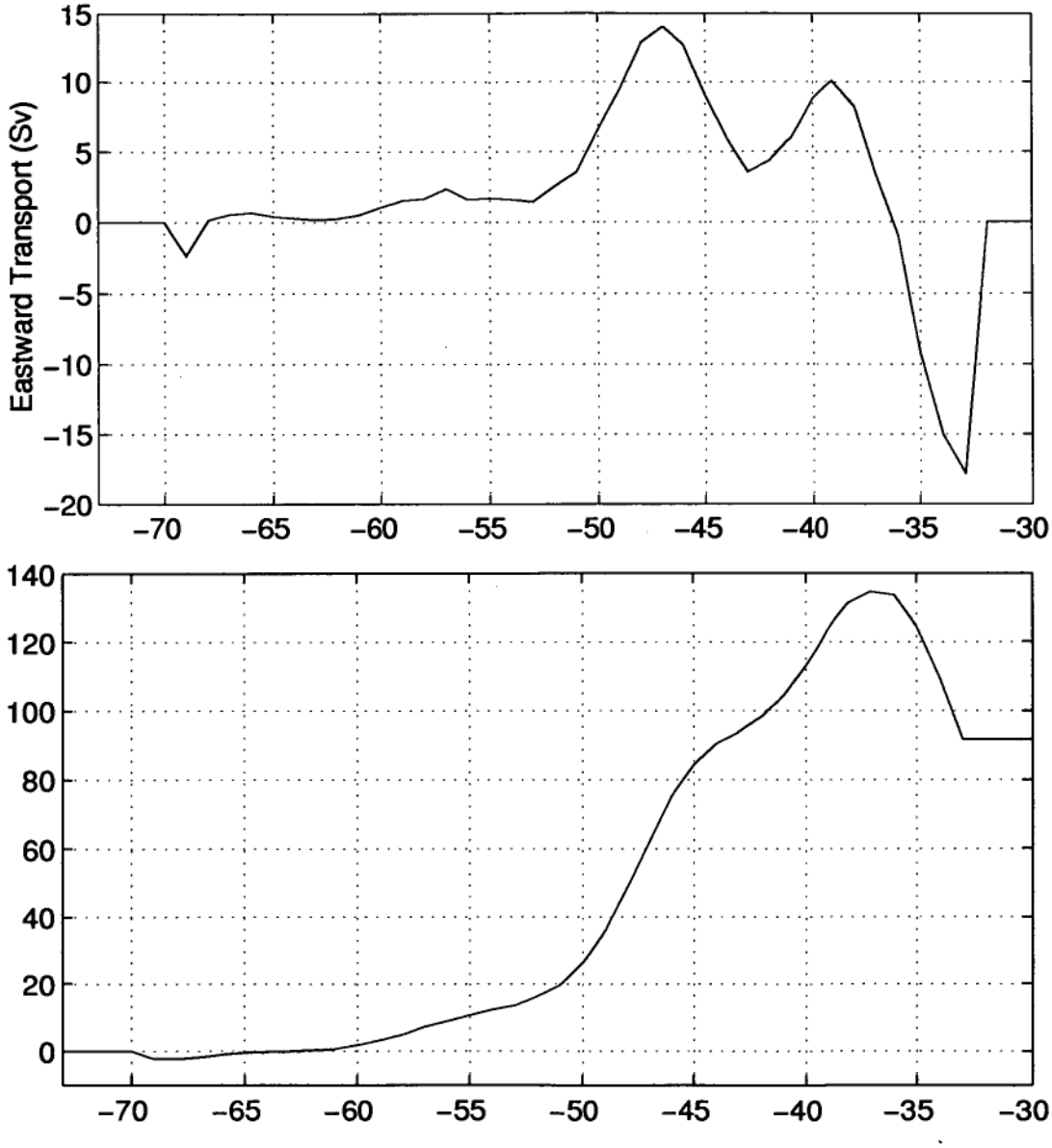


Figure 5.19: Eastward transport (Sv) per degree latitude (top) and integrated transport (Sv) (bottom) across 30°E (South of Africa) from the SOINV.

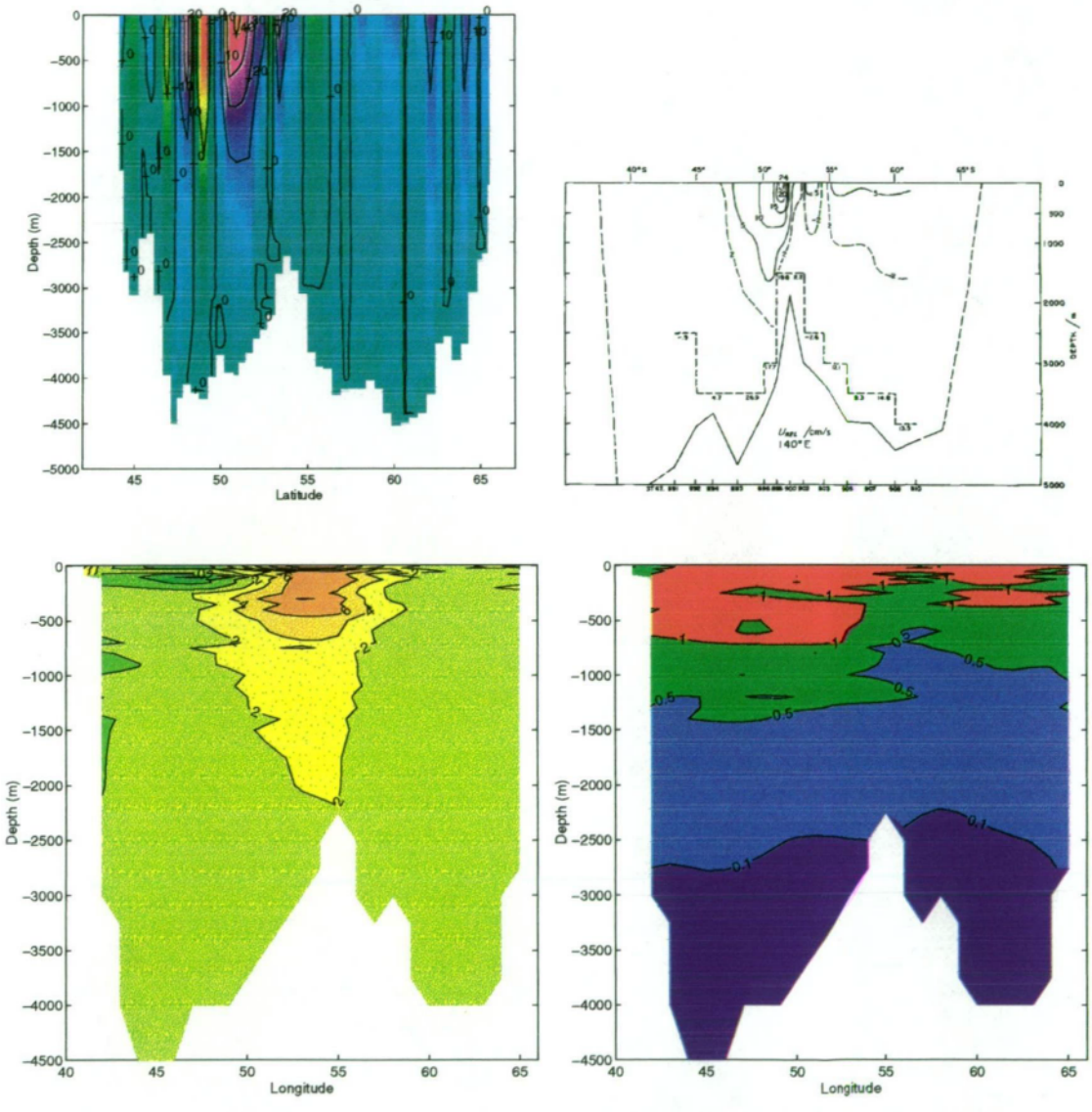


Figure 5.20: Velocity (cm $s^{-1}$) section for SR3 (top-left), Eltanin (top-right) compared to SOINV velocities (bottom left) and associated errors (bottom right).

the west. This westward current is much smaller than the ACC in both the SR3 and SOINV results.

Because of the circulation from the Pacific Ocean into the Indian Ocean through Indonesia, the transport south of Australia is larger than the transport south of Africa and South America. The total transport south of Australia is estimated to be 104 Sv with the north-south structure shown in figure 5.21. This is less than the transport calculated from the WOCE SR3 hydrography section of 146 Sv. Most of the mass is transported by the ACC that extends between 60°S and 45°S. The apparent width of the ACC, by inspection of figure 5.1, is a result of the ACC dividing around the Australian Antarctic Ridge at the Australian Antarctic Discordance, which is slightly upstream of the section. North of the ACC, the weak westward transport is observed at 43°S. The magnitude of the transports per degree, associated with the ACC is much smaller in the SR3 section than those in the 30°E section, again the result of the dividing of the ACC upstream.

## 5.4 Model circulation and Eddy Kinetic Energy (EKE)

Eddy Kinetic Energy (EKE) is a measure of the variability of the ocean currents. The geographical distribution of EKE can reveal important information about the dynamics of the Southern Ocean circulation [Morrow 1992; Morrow et al. 1994]. Increased EKE values can result from instabilities in the mean current, from topographical interactions, boundary effects and current interactions [Nowlin and Klinck 1986]. Areas of high EKE may act as sources or sinks of energy from the mean flow, although EKE maps alone cannot distinguish between these processes [Morrow 1992; Morrow et al. 1994]. It is believed that eddies play a significant role in the poleward transport of heat across the ACC [Bryden 1979; Bryden and Heath 1985]. The development of

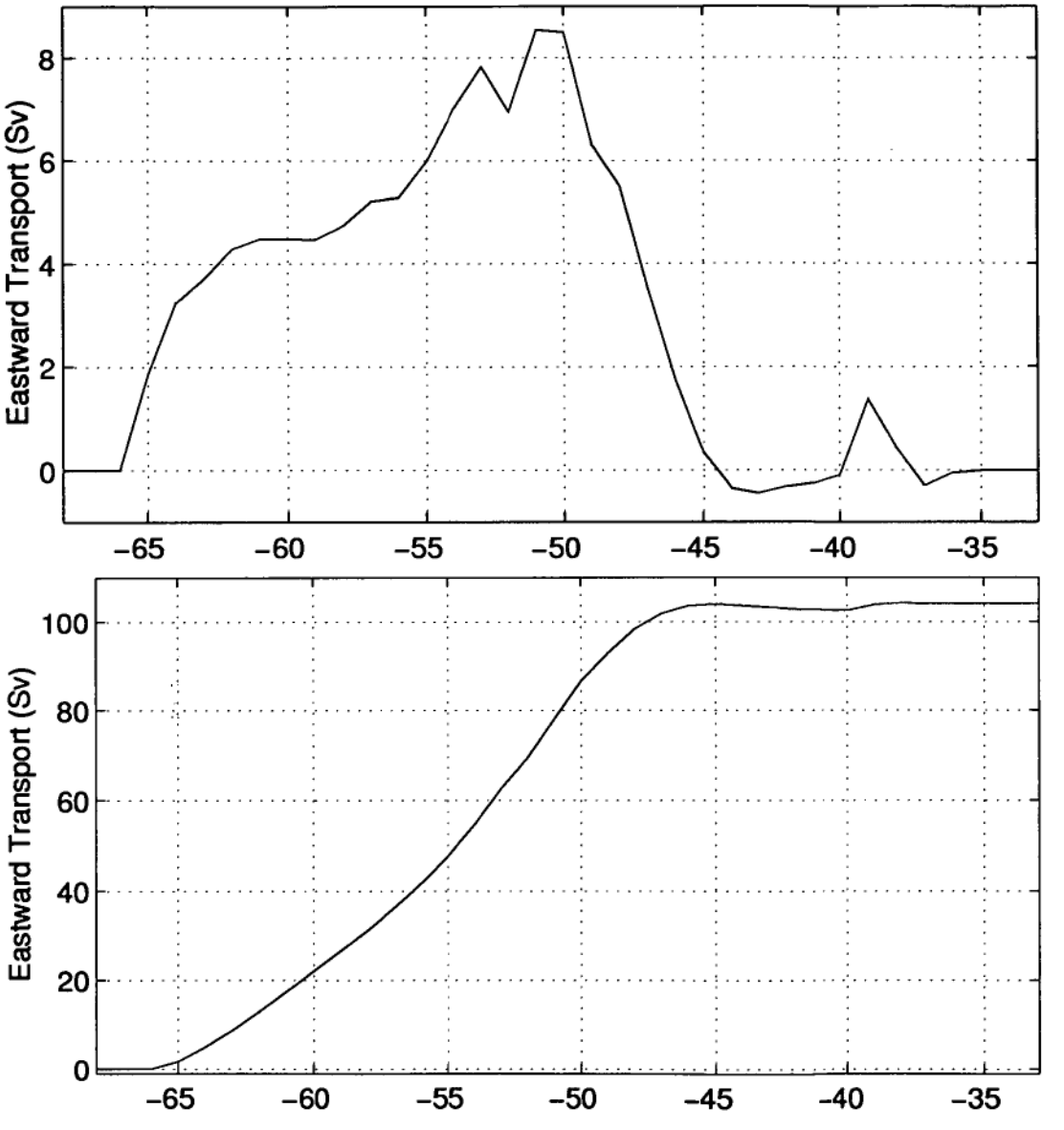


Figure 5.21: Eastward transport (Sv) per degree (top-panel) and transport integrated from Antarctica (Sv, bottom-panel) across 140°E, south of Australia.

satellite altimeters has allowed for basin scale investigations of circulation variability, and hence the calculation of EKE [Cheney et al. 1983; Colton and Chase 1983; Shum et al. 1990; Morrow 1992]. EKE is not limited to distinct eddies, as the name suggests, but also to small time scale meanders in the local currents. This section compares the SOINV results to an EKE field calculated from the Topex/POSEIDON altimeter data to determine if there is any relationship between the mean circulation field calculated by the SOINV and the EKE field determined from the satellite data.

The EKE field presented here was calculated from Topex/POSEIDON data acquired between 1992 and 1994. Residual sea surface velocities were calculated and kindly made available by Neil White (CSIRO, Division of Oceanography, Hobart) and Richard Coleman (Department of Surveying, University of Tasmania). A brief summary of how residual sea surface velocities and EKE values are calculated is outlined below and the reader is directed to Morrow et al. [1994] and Morrow [1992] for a thorough presentation.

After the mean sea surface height and orbit errors have been removed to give the residual sea surface height, $h$, the residual sea surface velocities ,$V$, are calculated from the smoothed alongtrack sea surface slope using the geostrophic relation,

$$V_{(a',d')} = \frac{g}{f}\frac{dh}{dx} \tag{5.1}$$

where $g$ is the acceleration due to gravity, $f$ is the Coriolis parameter and $x$ is the along track direction. The subscripts $a$ and $d$ denote ascending and descending satellite passes. The sea surface slope is calculated using a 25-point linear regression to the along track residual heights. Filtering is necessary because of measurement noise in the altimeter data, and any eddy variability at shorter space scales than the noise cannot be resolved [Morrow et al. 1994].

The magnitude and direction of the residual velocity can only be resolved at satellite groundtrack crossover points by a simple geometric transformation expressed as

$$u' = \frac{V_{a'} + V_{d'}}{2\cos\theta}$$
$$v' = \frac{V_{a'} - V_{d'}}{2\sin\theta} \tag{5.2}$$

where $u', v'$ are the east and north components of residual velocity and $\theta$ is the known angle between the satellite ground track and the north meridian. As defined by Stevens and Killworth [1992], EKE can be calculated from the east/north components of residual sea surface velocities using

$$EKE = \frac{1}{2}\overline{(u'^2 + v'^2)} \tag{5.3}$$

Comparisons of the altimeter derived EKE and the SOINV circulation are given in figure 5.22.

Figure 5.22 shows the strong correlation between the distribution of EKE, large SOINV transports and bottom topography. Around South Africa there are high EKE values associated with the Agulhas Current, the Agulhas Retroflection and outflow from the Retroflection into the south Indian Ocean. In this region, the maximum EKE (1050 $cm^2\ s^2$) is associated with the retro-flecting current, located between the two stationary eddies at 39°S, 20°E. From the discussion in section 5.1 and inspection of figure 5.3, observations suggest that this is the main formation site for eddies that pinch off from the Agulhas Current, before moving westward into the Atlantic Ocean. These high EKE values extend in both the east and west direction, highly correlated to the

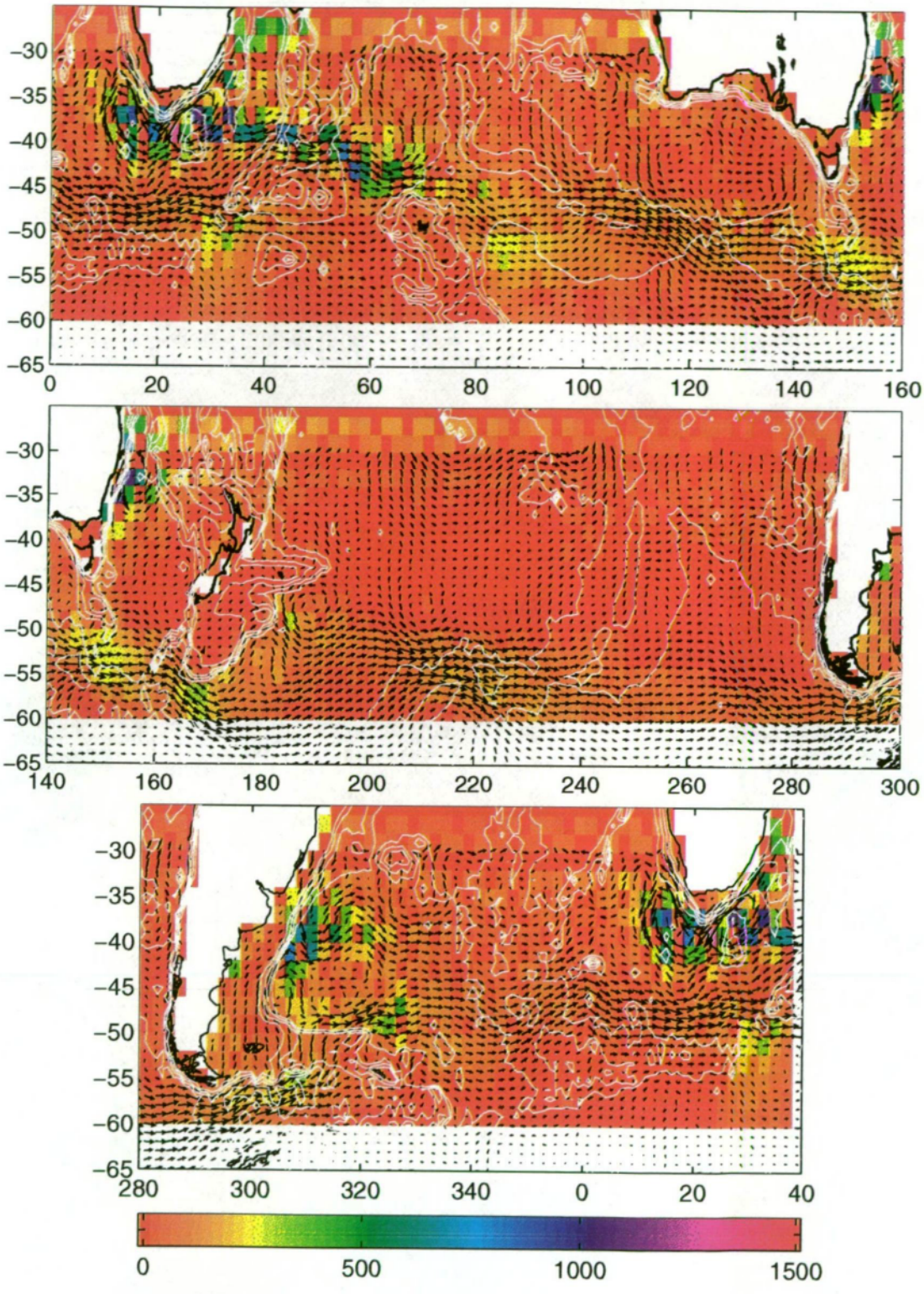


Figure 5.22: Total SOINV Transport Circulation plotted over Eddy Kinetic Energy ($cm^2.s^{-2}$) from Topex/POSEIDON and contoured bathymetry (contour interval 1000 metres). Missing latitude bands between 32°S - 30°S and 26°S to 25°S are due to the absence of satellite crossover points from which to calculate EKE between these latitudes.

mean Agulhas circulation. Interestingly, EKE values associated with the western eddy show strong correlation between the extent of the eddy and the extent of the high EKE values. There is a dramatic decrease in EKE values outside the influence of the western eddy's circulation. This is a strong indication that the SOINV's western eddy is a realistic depiction of the mean circulation in this region.

East of 20°E, the high EKE values closely follow the position of the Agulhas Retroflection outflow as it extends into the Indian Ocean. There are high EKE values in excess of 500 $cm^2$ $s^2$ associated with the outflow until the circulation reaches the topographic ridge that extends northward between Kerguelen and Amsterdam Islands. East of this ridge, the EKE are less than 250 $cm^2$ $s^2$.

To the north of the outflow, there are increased values of EKE associated with the Agulhas return current in the Mozambique Basin, and the northward turning of the circulation in the Crozet Basin. In the schematic representation of the circulation of the Crozet by Park et al. [1993], shown in figure 5.2, page 93, there are several eddies depicted to the north of the main current. The depiction of these eddies is supported by the increased EKE values to the north of the SOINV's main current.

South of the Agulhas Current system at 50°S, 34°E there is a region of increased EKE where the ACC turns north before meeting the Agulhas outflow current. The northward turning of the ACC appears to be influenced by bottom topography, as the Atlantic-Indian Ridge turns north to join the Crozet Plateau. However, there is a slight saddle in the topography, known as the Prince Edward Fracture Zone, that allows some of the ACC to continue eastward, south of the Crozet Plateau. The highest EKE values are on the eastern flank of the fracture zone and it is unclear as to the exact cause of these high EKE values. Most

investigations are focused on the Agulhas Current when investigating the EKE of this region. The Prince Edward Fracture Zone is the deepest crossing point in the Atlantic-Indian Ridge. From the SOINV circulation, it appears that most of the circulation that enters the Atlantic-Indian-Antarctic Basin, enters over this fracture zone. As it crosses the fracture zone, the topography seems to make the circulation unstable, generating the high EKE values observed by the satellite.

As discussed above, there is a sudden decrease in EKE values downstream of where the ACC crosses the ridge between Kerguelen and Amsterdam Islands. There is a slight increase in EKE values as the ACC spills into the Australian-Antarctic Basin at 61°S, 84°E before turning north to focus on the Indian-Antarctic Ridge. Here the ACC intensifies and enters a region of low EKE values between 110°E and 140°E. There are small values of EKE located on the ridge, but away from the ACC, EKE values are extremely low, despite several currents that join and leave the ACC in this region at 45°S 110°E, 47°S 140°E and 53°S 120°E. These low EKE values appear to be the complete opposite to the situation that is occurring east of South Africa, associated with the Agulhas Retroflection outflow.

This contrast in EKE values is obviously saying something about the circulation of the two regions. In the case of the Agulhas Current, there is an intense mixing of two different water masses from the Indian and South Atlantic [Fine et al. 1988]. It appears that this mixing may be causing instability in the water column, either baroclinic or barotropic or a combination of both leading to the increased EKE values in the Agulhas region. In contrast, the relatively well mixed ACC south of Australia does not become as unstable, even from the influence of the Australian-Antarctic Ridge.

South of Tasmania, the ACC enters a region of uniform depth, west of the Macquarie Ridge that coincides with an increase in EKE values. Wilkin and

Morrow [1994] propose that the lack of topographic control enables the ACC to generate transient eddies, leading to the increased EKE values. The SOINV circulation associated with these increased EKE values is spreading out across the basin before concentrating again over the Macquarie Ridge at 160°E. The spreading of the SOINV circulation is consistent with averaging of an active eddy field depicted by the EKE values. At the point of crossing the Macquarie Ridge, the ACC is very concentrated with low EKE values. This is a little surprising as one expects a topographic influence on the main current. It is hypothesised that the strong topographic influence of the ridge system is constraining the flow, and decreasing EKE values.

East of the Macquarie Ridge, at 168°E, with the topographic influence removed, the EKE values increase. This is also the location where the ACC divides to either continue along the Pacific-Antarctic Ridge, or to follow $\frac{f}{H}$ contours along the Campbell Plateau. The location of where the ACC divides, associated with the increased EKE values suggests that there is an active eddy regime associated with the dividing of the ACC. The ACC south of the Campbell Plateau and across to the Eltanin Fracture zone has two modes. A southward mode that continues south along the Pacific-Antarctic Ridge, and a northern mode flowing north along the Campbell Plateau before turning east to cross the south west Pacific Basin to the Eltanin Fracture zone. What proportion of the total flow follows each mode is variable. On the time scales of the satellite repeat period (10 days), the region of the highest EKE values will be where the circulation is switching between modes, or dividing into the two modes, creating meanders and eddies in the process. This location is depicted by the high EKE values seen at 58°S, 168°E.

Away from the ACC in the Pacific Ocean, the EKE values are extremely low. Even in the ACC, except at the Eltanin Fracture Zone, the ACC is

relatively clear of EKE. The EAC, however, shows extremely high values of EKE, exceeding 1000 $cm^2$ $s^2$. These highest values are associated with the region where the EAC separates from the coast before heading into the Tasman Sea. The location of this separation migrates up and down the coast over time [Boland and Hamon 1970; Boland and Church 1981; Coleman 1984; Cresswell and Legeckis 1986] on time scales short enough to be detected by the altimeter [Coleman 1984]. The increased EKE field down the east coast of Australia, south of the EAC, are a result of eddies pinching off from the EAC as it turns east, and spinning down the east coast of Australia [Wilkin and Morrow 1994].

In Drake Passage, the highest EKE values are again associated with the main jet. As the ACC turns north to cross the North Scotia Ridge EKE decrease, as at the Macquarie Ridge, before increasing again as the ACC spills into the deep Argentine Basin. The Argentine Basin has very high EKE values throughout, strongly associated with the large SOINV currents of the area. As the ACC enters the basin from the south the topographic control is lost. As the circulation turns east, the current becomes unstable and generates meanders and transient eddies that decrease to the east.

To the north, the Brazil Current generates high EKE values as it flows down the east coast of South America and into the Argentine Basin. The Current has been observed to be very active with many meanders and eddies observed in observational data [Gordon and Greengrove 1986; Bianchi et al. 1993; Garzoli 1993]. The band of high EKE values associated with the Brazil Current continues south as the southward flowing Brazil Current mixes with the northward flowing Malvinas Current and moves east into the Argentine Basin. The high EKE values present within the Argentine Basin continue to follow the SOINV circulation but decrease rapidly on leaving the basin. This is somewhat unexpected as it could be reasonable to assume that the mid-Atlantic Ridge

would have an influence of the circulation, which is not apparent in the maps of EKE.

There is a strong relationship between EKE values and the SOINV circulation and there is a strong influence on both by the bottom topography. There are obviously many different processes at work in different regions of the ocean that create instabilities, and thus high EKE values such as the Agulhas and EAC current systems. As well, there are very stable systems that have low EKE values such as the ACC over the Australian-Antarctic Ridge and the mid Atlantic Ridge systems. These processes may include mixing of water masses and the effect of topography on baroclinic and barotropic instabilities, but a full investigation is beyond the scope of this thesis.

## 5.5 Comparison to OGCM.

In this section, a comparison is made between the SOINV results and the mean depth-integrated barotropic speed from a primitive equation model. The numerical model used for comparison has been developed by Semtner and Chervin [1988] with the results presented here kindly made available by Braccio [1995]. A discussion of the details of the numerical model can be found in papers by Semtner and Chervin [1988], Cox [1984] and Bryan [1969]. The model has $\frac{1}{6}$ ° horizontal resolution over 20 layers, has been initialised with a 33 year run before being forced with atmospheric conditions from 1985 to 1994 [Smith et al. 1996]. Robust diagnostics are applied to the deep ocean to stop long-term climatological drift. The data used to relax the model below 710 metres is from Levitus [1982], relaxed on a time scale of 3 years. The surface layers, above 710 metres are unconstrained and reach equilibrium in the order of decades [Semtner and Chervin 1988]. At $\frac{1}{6}^{\circ}$ resolution, the models are now close to resolving the deformation radius of the eddies, and so becoming truly eddy

resolving [Semtner 1995].

Figure 5.23 shows the SOINV transports (arrows) compared to the mean barotropic velocity of the numerical model (background) taken from 1985 to 1994. The barotropic velocity field only shows current magnitudes, integrated over depth. However, the location of the largest magnitude circulation should be similar. From figure 5.23, it can be seen that this is generally the case although there are some significant exceptions.

The broad areas where there are high velocities in both the SOINV and numerical model results are the same. The band associated with the ACC, the Agulhas, the EAC, and the Argentine Basin all show increased velocities in both the numerical model and SOINV. However, on close inspection of these regions, there are subtle differences that highlight the different physics of the models and possible inconsistencies between the numerical model results and the observational data.

The first major feature is the deep boundary currents that exist in the numerical results that follow deep topographic slopes. The numerical model applies the vorticity conservation constraint along contours of $\frac{f}{H}$ more strictly than the SOINV. These currents are particularly noticeable on the continental shelf edge of Antarctica, and on several topographic features of the Southern Ocean, i.e., 55°S, 5°E, and around the Campbell Plateau.

Concentrating on regions that show the most discrepancy between the two circulations, the Agulhas and the Agulhas Retroflection show significant differences, particularly in the apparent shape of the western eddy. The SOINV circulation associated with the eddy, located at 38°S, 18°E, shows the circulation following the coast of Africa into the Atlantic much further than depicted by the numerical results. The numerical model shows the Agulhas apparently heading due west from the southern tip of Africa instead of curling

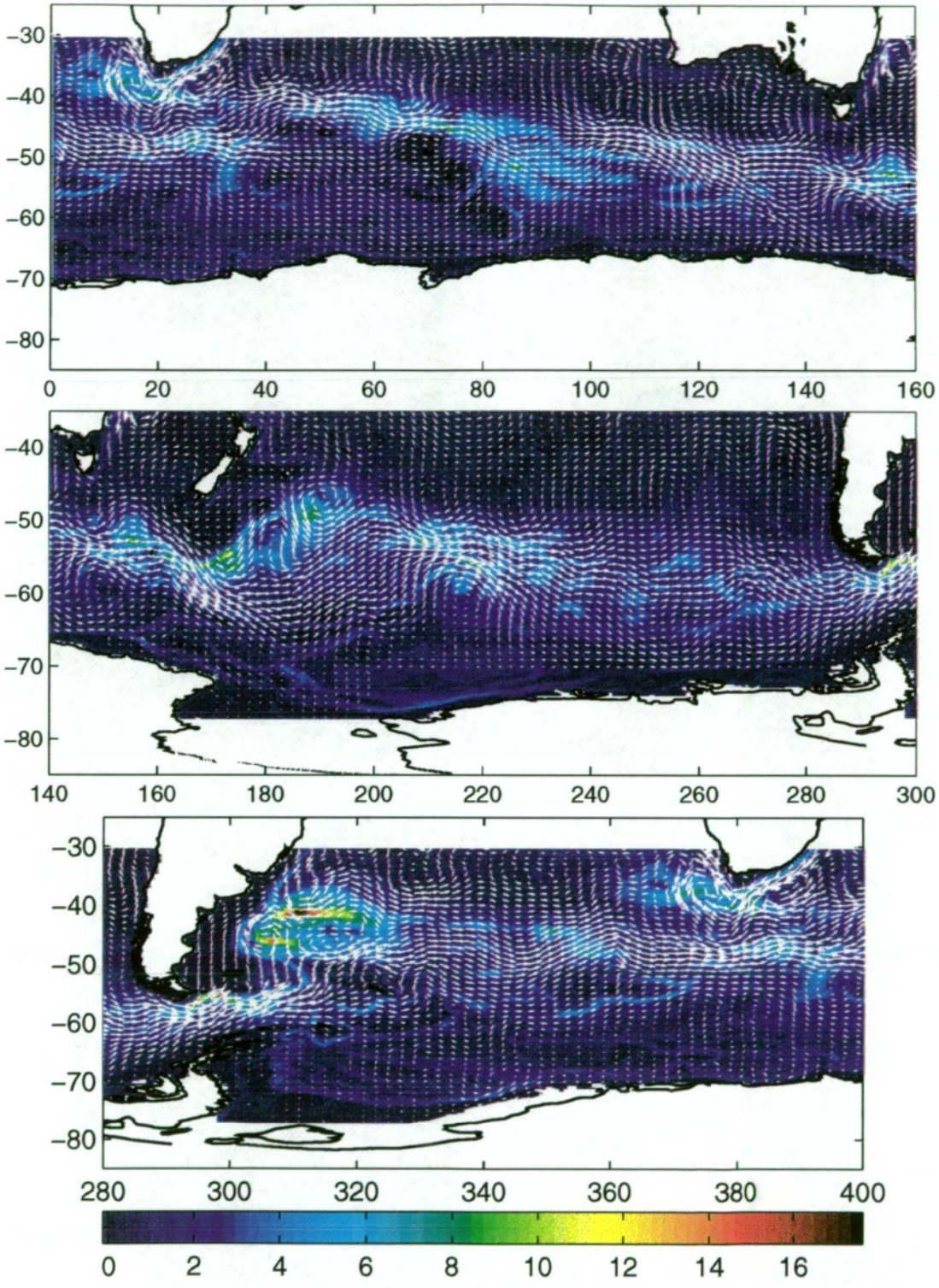


Figure 5.23: Inverse model transport results (arrows) compared to mean barotropic speed from numerical model (background). Inverse model results, shown at 1° latitude × 2° longitude resolution, are scaled 1°= 4 Sv in both latitude and longitude. Numerical model units are $cm^2\ s^{-1}$.

round to continue into the south Atlantic. The numerical model's Retroflection current is also depicted to be a more zonal circulation than the SOINV suggests. North of Kerguelen Island, the two circulations agree very closely, however slightly down stream the two circulations show a different location for the centre of the ACC. The SOINV suggests that the mean location of the ACC continues in a south easterly direction, entering the Australian-Antarctic Basin before turning north to focus on the Australian-Antarctic Ridge. The numerical model depicts the main jet tending to follow the ridge-line more closely, with several distinct jets of current. Once the ACC has focused, there is a 3°difference in latitude between the inverse ACC and the numerical ACC.

Probably the biggest difference between the two circulations is downstream of the Macquarie Ridge, south of the Campbell Plateau. Both circulations show strong, well focused currents across the Macquarie Ridge. The SOINV circulation shows that most of the ACC continues along the Pacific-Antarctic Ridge, before crossing the ridge at the Eltanin Fracture Zone, with a smaller amount of the circulation flowing up the southern edge of the Campbell Plateau. In contrast, the numerical model's circulation depicts most of the ACC moving north along the Campbell Plateau, with very little continuing along the Pacific-Antarctic Ridge. This difference illustrates the differences between how the numerical model deals with vorticity compared to what the data is showing.

In the Atlantic Ocean, the circulation in the Argentine Basin agrees quite closely, although the numerical model's circulation appears to be too zonal. The outflow of the Brazil-Malvinas confluence is at the same location in both circulations, however the SOINV circulation meanders north and south more than the numerical model's circulation. The Argentine Basin is a relatively flat basin with very little change in $H$ so that lines of constant $\frac{f}{H}$ are zonal.

Differences in the two circulations, apparently due to contours of planetary

vorticity, show that there are several regions of the Southern Ocean where the numerical model's circulation is not accurately representing the circulation that is being depicted in the observations. These differences in circulation patterns will obviously include differences in location of temperature and salinities with corresponding differences in transports of these properties. From this comparison, it is clear that while the higher resolution numerical model shows circulation features not usually observable with observational data, it is not clear that the numerical model is consistent with the observational data.

## 5.6 Is there a Deacon Cell?

Numerical models have allowed oceanographers to investigate ocean circulation in ways not usually possible with observational data [Doos and Webb 1993]. One of the features that have been highlighted by numerical models is a series of apparent circulation cells generated when the meridional velocity field is integrated zonally to give a meridional streamfunction [Doos and Webb 1993] expressed as,

$$\psi(\theta, z) = \int_z^0 \int_o^{2\pi} v(\phi, \theta, z') R \cos\theta d\phi dz' \tag{5.4}$$

The apparent circulation cell that develops in the Southern Ocean has been termed the Deacon cell, which, from the Fine Resolution Antarctic Model (FRAM), gives a meridional cell circulation as described in the left hand panel of figure 5.24. With the three dimensional velocity field generated in this thesis, a similar calculation can be carried out on the SOINV results. The resultant circulation is presented in the right hand panel of figure 5.24. In the SOINV circulation of figure 5.24, positive values generate a clockwise circulation about the cell, and negative values generate anti-clockwise circulation.

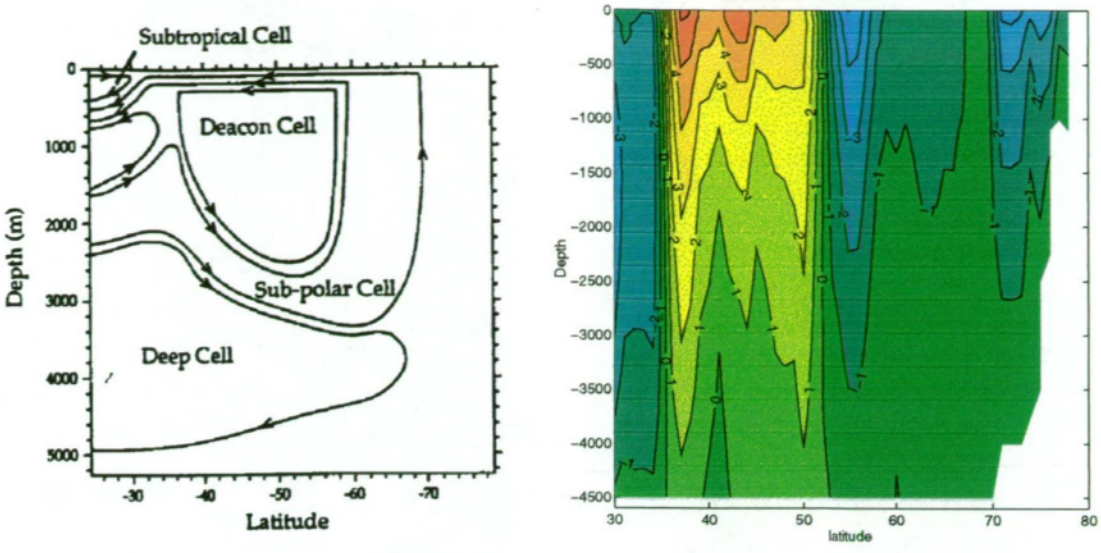


Figure 5.24: Meridional stream functions as calculated from the FRAM numerical model (left) and from SOINV (right). Contour interval is 1 Sv. Positive values generate clockwise circulation about the cell.

The SOINV streamfunctions suggest that there are three complete circulation cells, and the southern edge of a fourth cell, south of 30°S. This is in contrast to the single Deacon Cell described above. It appears that the boundaries between the cells are coincident to the mean location of the major fronts in the Southern Ocean. The boundary at 36°S seems to coincide with the mean position of the sub-tropical Front. The boundary at 52°S coincides with the mean location of the Antarctic Convergence. The two most southern cells circulate in an anti-clockwise direction and together move water from the Antarctic Convergence down to a depth of between 500 and 4000 metres and then south upwelling along the Antarctic Continent. Together these form what has been labeled the Sub-polar Cell by previous investigators, which encompasses the Deacon Cell [Manabe et al. 1990; Doos and Webb 1993]. North of these two cells and south of the Subtropical Front, there is a deep intense clockwise cell that downwells water at the Antarctic Convergence to depths between 500 and 4000 metres before moving the water north until 35°S where upwelling takes place at the Sub-tropical Front. This cell was not generated by

the FRAM results [Doos and Webb 1993] and was only weakly generated by Manabe et al. [1990] above 1200 metres. North of 35°S, the inverse results generates another anti-clockwise cell, rotating in the same direction as the Deacon Cell and is part of the Subtropical Cell as labeled in the left hand panel of figure 5.24.

The meridional streamfunctions illustrate that there is a strong correlation between meridional circulation cells and frontal features of the Southern Ocean. This correlation has not been established before and is an interesting result. Also, the two circulation cells south of 53°S, in the region usually defined by the Deacon Cell in numerical models, is unexpected. The most southern circulation cell appears to downwell water south of 68°S and upwell along the Antarctic Continent. However, the only part of the SOINV's Southern Ocean that is south of 68°S is the Weddell and Ross Seas. Thus, this southern Deacon cell is simply the extension of the northern Deacon cell into the Weddell and Ross Seas, but because of the zonal integration, appears to be pinched off from the northern cell at 70°E. Therefore, interpretation of figure 5.24 should only include a Southern Deacon cell, a Sub-Antarctic Cell and a Subtropical Cell.

The SOINV's Deacon Cell is consistent with Circumpolar Deep Water upwelling south of the Antarctic Convergence, however the depth of the clockwise rotating Sub-Antarctic Cell, north of the Antarctic convergence, appears to preclude the Circumpolar Deep water crossing the Antarctic Convergence. By close inspection of the right hand panel of figure 5.24, it is possible to discern a very weak anti clockwise circulation cell under the strong Sub-Antarctic Cell. This suggests that there is a weak southward transport of mass, at depth, under the Sub-Antarctic Cell, into the region of upwelling described by the SOINV's Deacon Cell.

The calculated transports associated with the inverse cells are only about

10% of those presented by Manabe et al. [1990] and Doos and Webb [1993]. This is a large difference, which is mostly due to differences in the models. Because the SOINV conserves mass on a single layer, it tends to emphasise the horizontal circulation, rather than vertical exchanges, therefore generating a weak Deacon cell. The numerical model explicitly solves for the vertical velocities and vertical diffusions, sometimes creating large vertical exchanges, that create large Deacon Cells. The inverse circulation has been generated so that it is consistent with the observational data, leading to meridional streamfunctions that are consistent with the data. It is not clear that the numerical model's circulation is consistent with observations, leading to an uncertainty about the meridional streamfunction cells derived from numerical results.

## 5.7 Surface Velocities

Here the SOINV generated surface velocities are compared to in-situ observations of surface velocities. The SOINV surface velocities were generated by summation of the reference velocities, the thermal wind velocities and the Ekman velocities. The reference velocities were generated by dividing the reference transports by the model bathymetry. The thermal wind velocities were calculated by optimally interpolating the thermal wind velocities, referenced to the bottom, for layer 1 of the dataset as described in section 5.2. The Ekman velocities were calculated by assuming an Ekman depth of 50 metres. The SOINV's total surface velocities are shown in figure 5.25 that can be compared to figure 1 of Nowlin and Klinck [1986], shown in figure 5.26. It must be remembered that the velocities depicted by Nowlin and Klinck [1986] are referenced to 1000 db.

South of Africa, Nowlin and Klinck [1986] have difficulty in depicting the

Agulhas and Agulhas Retroflection because of lack of data and depth of the ocean. This is a limitation with all boundary currents in the results published by Nowlin and Klinck [1986]. However, the outflow of the Agulhas Retroflection at 42°S, 40°E depicts surface velocities in excess of 20 cm $s^{-1}$. The SOINV circulation shows surface velocities of the order of 10 cm $s^{-1}$. As the ACC moves east, the location of the strongest surface velocities are in close agreement, although a bifurcation of ACC at 90°E in Nowlin and Klinck [1986] is depicted as a broadening of the ACC in the SOINV circulation. Continuing east, there is an intensification of the ACC south of Australia in both datasets. Maximum velocities are 20 cm $s^{-1}$ (Nowlin and Klinck [1986]) and 13 cm $s^{-1}$ (SOINV). The location of the ACC is again associated very strongly with the Australian-Antarctic Ridge.

Over the Macquarie Ridge, Nowlin and Klinck [1986] show large surface velocities of the order of 30 cm $s^{-1}$. These large velocities are not shown in the SOINV circulation with surface velocities decreasing over the ridge, the reasons for which are not clear. East of the Macquarie Ridge, Nowlin and Klinck [1986] shows the bifurcation of the ACC at 175°E that is also seen strongly in the transport figures of the SOINV circulation (figure 5.4). However, in the SOINV surface velocities, the northern branch is much weaker with only a suggestion of the northward flowing transport around the Campbell Plateau. This difference between the surface velocities and the depth-integrated transports is due to the deep flow moving north around the plateau, under the influence of vorticity. The ACC is seen to intensify over the Pacific-Antarctic Ridge in both datasets with Nowlin and Klinck [1986] showing velocities close to 25 cm $s^{-1}$ and the SOINV circulation indicating velocities of 12 cm $s^{-1}$. East of the Pacific-Antarctic Ridge, both datasets indicate the ACC spreads out across the Pacific-Antarctic Basin to flow zonally towards Drake Passage with surface

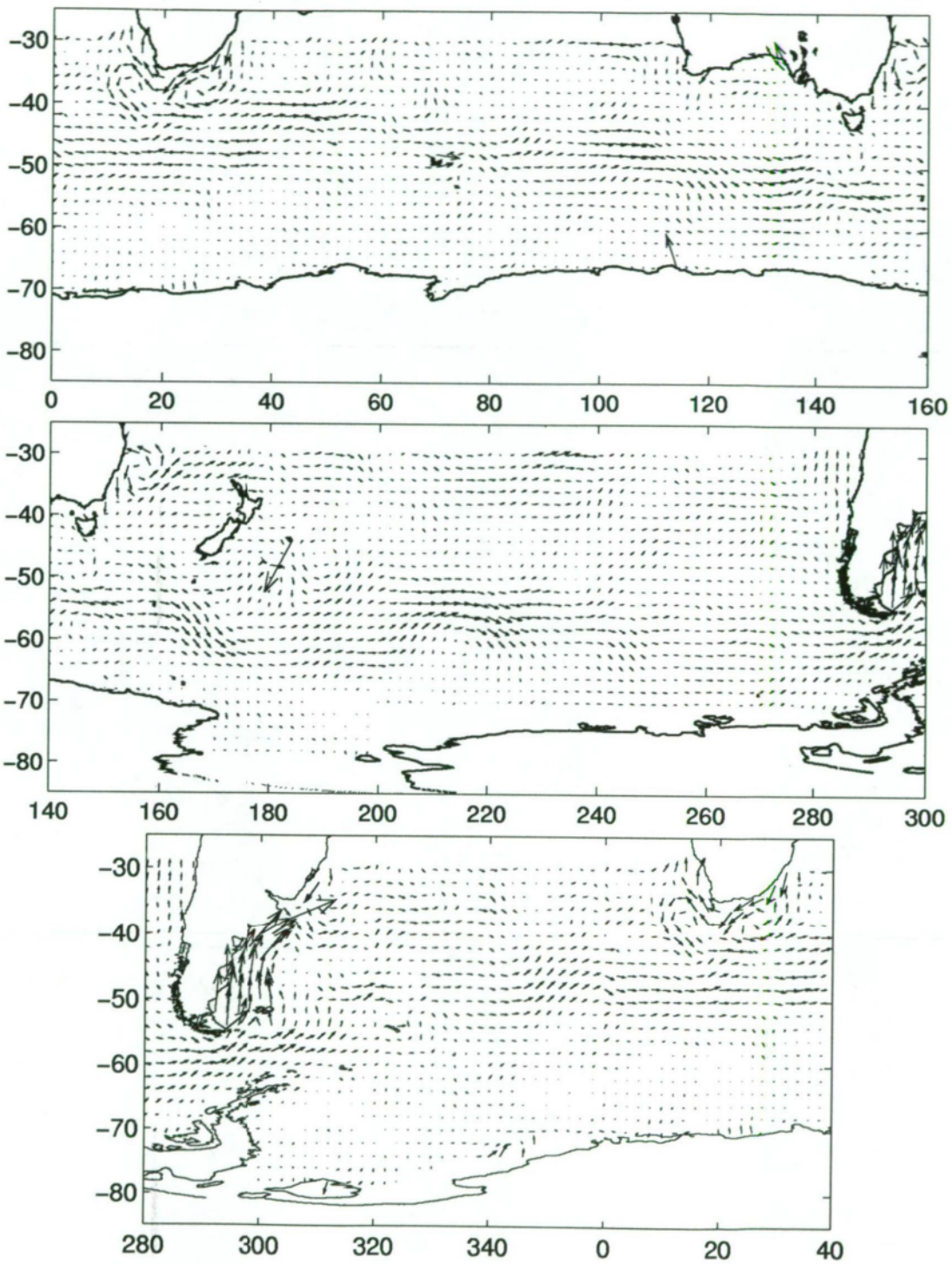


Figure 5.25: Total Surface velocities for the Southern Ocean shown every $2° \times 2°$. ($2° = 10$ cm.s$^{-1}$)

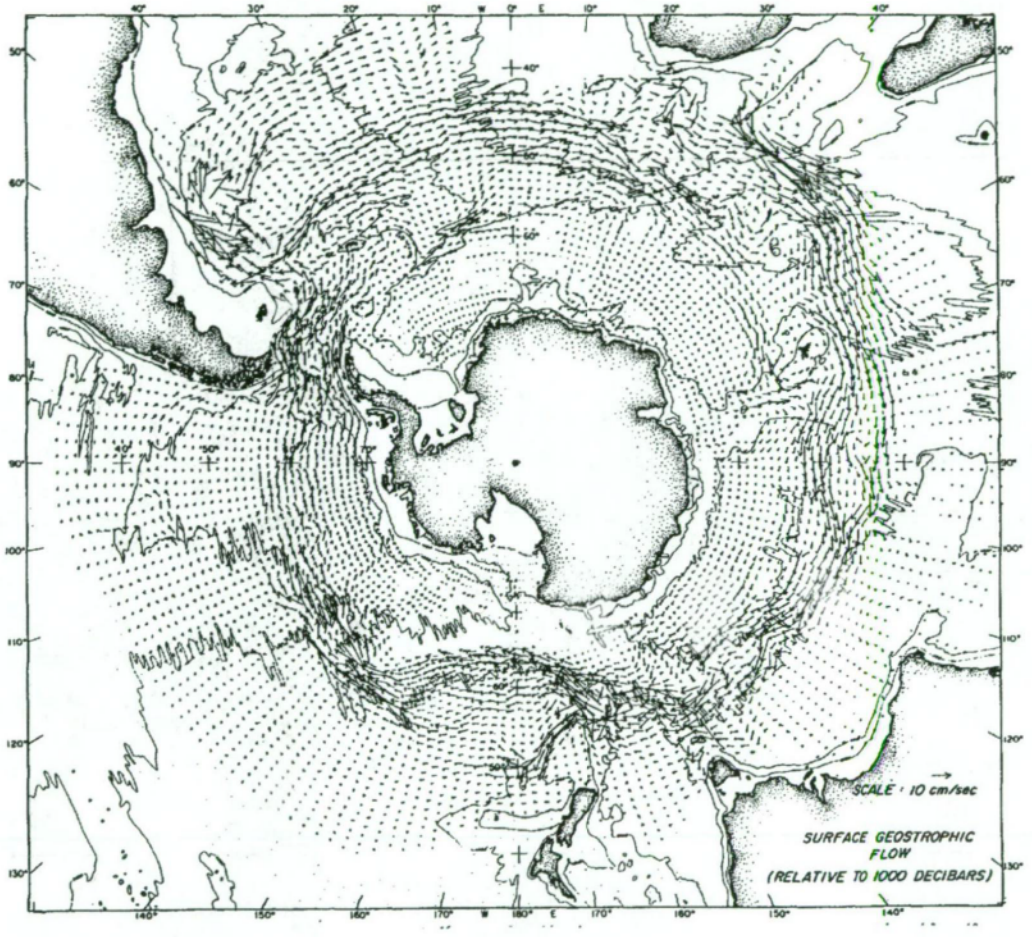


Figure 5.26: Geostrophic current at the sea surface relative to 1000 dbar shown in figure 1 of Nowlin and Klinck [1986].

velocities less than 5 cm $s^{-1}$.

Through Drake Passage, surface velocities increase to 10 cm $s^{-1}$ in both circulations before decreasing as they turn north across the Scotia Ridge. The SOINV circulation shows extremely fast surface velocities on the continental shelf around the Falkland Islands which are not shown by Nowlin and Klinck [1986]. These large surface velocities are mainly a result of relatively large transports being divided by the shallow bathymetry resulting in large reference velocities. Nowlin and Klinck [1986] indicate extremely large surface velocities (>30 cm $s^{-1}$) for the Brazil-Malvinas Confluence outflow with the direction of the mean flow uncertain. A similar flow is present in the SOINV circulation although occurring closer to the coast with much smaller surface velocities at the location depicted by Nowlin and Klinck [1986]. Across the Atlantic, the surface velocities of both datasets agree that the ACC is a broad current with surface velocities of the order of 5-10 cm $s^{-1}$.

## 5.8 Dynamic Height of the Southern Ocean

Using the full circulation derived from the inverse solution, it is possible to investigate the mean dynamic height of the Southern Ocean. The dynamic height of the Southern Ocean was calculated from the eastward component of the SOINV velocities using

$$h = \frac{1}{g} \int_{Ant.}^{30°S} f(u_{Th} + u_{Ref})\ dy \tag{5.5}$$

which is simply the integrated form of equation 5.1 on page 128, used to calculate velocity from altimeter measurements. The integration is carried out northward from the Antarctic coastline, with the results shown in the top panel of figure 5.27.

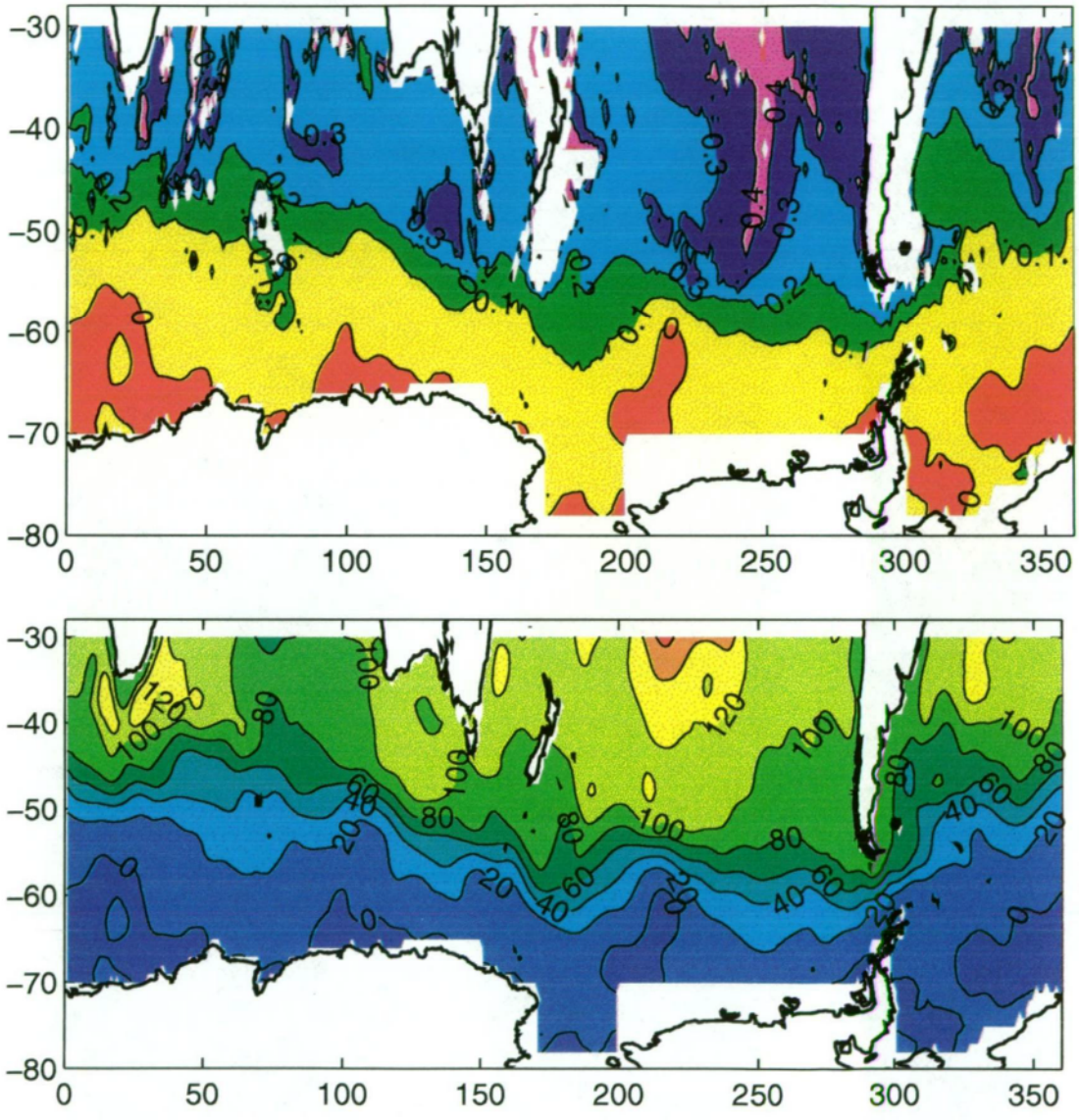


Figure 5.27: Dynamic height ($m^2\ s^{-2}$) of the Southern Ocean, integrated from the Antarctic Coastline (top panel) and integrated eastward transport (Sv) of the Southern Ocean circulation (lower panel).

The dynamic heights range from -.02 $m^2\ s^{-2}$ to greater than 1 $m^2\ s^{-2}$, however the values greater than .55 $m^2\ s^{-2}$ are due to excessively high velocities over shallow bathymetry and have been removed. This bathymetric effect is also apparent in the northern part of the model domain where mid oceanic ridges become apparent, particularly along the Mid-Pacific Ridge at 250°E, the Indian-Antarctic Ridge at 45°E and the shallow bathymetry around New Zealand.

Starting near the Antarctic continent, the four negative regions close to the continent represents cyclonic gyres close to Antarctica. It is possible to see the Weddell Sea Gyre extending as far as 50°E, although it does break up at 325°E in the Weddell Sea, while observations suggest that the two circulations in the Weddell Sea should be joined into one continuous gyre [Orsi et al. 1993; Fahrbach et al. 1996]. The Ross SeA circulation is also smaller than observations suggest.

Moving north, the .1 $m^2\ s^{-2}$ and .2 $m^2\ s^{-2}$ contour can be thought of as representing the southern and northern extent of the ACC. The contours follow very closely the circulation location presented in figure 5.1. Where the two contours are close together, the mean circulation of figure 5.1 is relatively strong, and vice versa. East of South America, the .2 $m^2\ s^{-2}$ contour sweeps north around the Argentine Basin. This is the location that the Sub-Antarctic Front as reported by Peterson and Stramma [1991]. East of the Macquarie Ridge, the two contours divide with the .1 $m^2\ s^{-2}$ moving south to follow the Pacific-Antarctic Ridge and the .2 $m^2\ s^{-2}$ contour moving north around the Campbell Plateau.

North of the .2 $m^2\ s^{-2}$ contour, bathymetry becomes very noticeable particularly the mid oceanic ridges in the three ocean basins, the Lord Howe Rise and Campbell Plateau and the continental shelf around South America.

These bathymetric effects actually mask out most of the signal present in the circulation.

An alternative inspection is the integration of transport north from Antarctica to give a streamfunction of transport with the topographic influence removed. This depiction allows for a more detailed analysis of the northern half of the model domain. Immediately the Subtropical gyre of the Pacific Ocean becomes apparent as the transport streamlines enter and leave the Pacific Ocean between 180°E and 280°E. A similar, although smaller, transport circulation is present in the Atlantic Ocean between 320°E and 10°E. This depiction also allows an inspection on the transport of water between the three ocean basins.

On the east coast of South America water flows into the model domain and turns east as depicted by the 100 Sv contour. The 100 Sv contour continues east and moves south of South Africa, south of the Agulhas Retroflection and finally turns north into the Indian Ocean at 60°E. The 100 Sv contour then re-enters the Atlantic from the Indian Ocean close to the South African continent north of the Agulhas Retroflection. This suggests that water flows down the western side of the Atlantic, turns east at approximately 40°S and moves into the Indian sector of the Southern Ocean where it turns north into the Indian Ocean. This Atlantic origin water is surmised to then recirculate back into the Atlantic Ocean via the Agulhas Current, establishing a constant exchange of mass between the Atlantic and Indian Oceans. As discussed in section 5.2.4, there is a zero net exchange of mass between the Atlantic and Indian Ocean so the eastward transport south of the Agulhas Retroflection is balanced by the westward transport into the Atlantic by the Agulhas Current.

Again following the 100 Sv contour, a similar exchange can be traced from the Indian to the Pacific, although the closure of the loop is surmised to occur outside the model domain via the Indonesian throughflow that was discussed in

section 5.2.4. The 100 Sv contour moves south out of the Indian Ocean at 110°E down to nearly 50°S before returning to 40°S in the Tasman Sea. This seems to indicate that there is some water branching off the ACC and turning north into the Tasman Sea west of the Macquarie Ridge. The 100 Sv water returns to 50°S west of the Pacific Antarctic Ridge before moving north to leave the model domain near the west coast of South America. It is thought that outside the model domain this contour would then move towards the equator before travelling east on the northern side of the Subtropical Gyre, then north of Australia and through Indonesia and down the west coast of Australia to close the loop.

It is also possible that outside the model domain in the Indian Ocean, that the water originating from the Atlantic Ocean continues east to flow south of Australia. This would indicate that the Indonesian throughflow closure moves west in the northern Indian Ocean before flowing south down the African continent and back into the Atlantic Ocean to close the loop. This is precisely the circulation imagined by the ocean conveyer belt logo depicted by Gordon [1985] and discussed by Schmitz [1995].

This chapter has compared the circulation from the SOINV to observations and numerical model results. It has been shown that with the results of the SOINV, many investigations not usually possible with inverse models can be undertaken.

The two dimensional depth-integrated circulation shows a high degree of agreement with in-situ observations. The shape and relative size of the circulation is comparable to observed flows, as demonstrated in many direct comparisons. The depth-integrated circulation can also be compared to satellite measurements, as presented in the comparison to EKE maps. These show that such a comparison is possible, and that the SOINV circulation is in close

agreement with the Topex/POSEIDON observations.

At 1°× 1° grid spacing the SOINV can start to be compared to high resolution forward differencing numerical models. Again, this is usually only possible at the edges of inverse models. The comparisons have shown that they are in close agreement, although there are differences in the physics of the models. These difference lead to some inconsistencies between the numerical model circulation and the in-situ observations.

The three dimensional circulation of the SOINV can be compared to many hydrographic sections, not just at the boundary of the model, as is the case with previous inverse models, but anywhere within the model domain. The comparisons illustrated that as a result of the optimal interpolation, the SOINV velocities were usually too small, particularly in boundary currents. However, these comparisons also showed that the mass transport across the sections was comparable to the observations.

The advantage of developing a high resolution circulation that is consistent with the observations was illustrated in the investigation of the existence of a Deacon Cell. The Deacon Cell has only been observed in numerical model circulations. While this comparison suggested that the vertical exchanges of the Deacon Cell derived in the FRAM model were over estimated, it did illustrate the type of investigations that can be carried out using this form of inverse model.

This chapter has demonstrated that global scale, 1°× 1° grid spacing inverse model is possible. The circulation has been demonstrated to closely agree with hydrographic observations and satellite measurements. Developing a high resolution inverse model allows for the investigation of many circulation features not usually possible with inverse techniques, or observations by themselves. The following chapter now utilises this circulation to diagnose

implied heat and freshwater transports to inspect the heat and freshwater budget of the Southern Ocean.

# Chapter 6

## Heat and Freshwater Circulation

In the previous chapter, the implications of the inverse solution on mass circulation around the Southern Ocean were presented and discussed. It was found that the circulation was consistent with the observations and that the new three dimensional velocity field could be used to investigate mass circulation features not possible with standard observational datasets. In this chapter, the mass circulation discussed in chapter 5 is used to diagnose the movement of heat and freshwater around the Southern Ocean. An understanding of the movement of heat and freshwater around the oceans is crucial to understanding the global thermohaline circulation [Gordon et al. 1992; van Ballegooyen et al. 1994] and global climate [Macdonald 1993]. The calculated fluxes of heat and freshwater are totally unconstrained by the inverse solution. Thus, in this chapter the focus is on the skill of the inverse technique in estimating the transports of heat and freshwater.

This chapter is organised by first defining the heat and freshwater transports used in this thesis and are calculated using similar methods to Bryden et al. [1991]. With these definitions, the transport of heat and freshwater across 35°S are presented and compared to previous investigations. Following this discussion, the total depth-integrated circulation of heat and freshwater are outlined. Finally, with the divergence of heat and freshwater used to estimate surface fluxes, the implied movement of heat and freshwater around the Southern Ocean is discussed.

## 6.1 Definition of Heat and Freshwater Transport

The definitions of heat and freshwater transport used in this thesis are the same as those defined by Roemmich and McCallister [1989] and Bryden et al. [1991]. Bryden et al. [1991] define heat flux (HF) as

$$\begin{bmatrix} HF_u \\ HF_v \end{bmatrix} = \int\int \rho C_p (T - T_0) \begin{bmatrix} udy \\ vdx \end{bmatrix} dz \tag{6.1}$$

where $C_p$ is the specific heat of sea water and $\rho$ is the density of sea water and $T_0$ is the volume averaged temperature calculated by summing over volume $\times$ local temperature and then dividing by total volume.

As there are no significant sources or sinks of salt in the global ocean [Roemmich and McCallister 1989], the net salt flux into a region of the ocean is zero. The effect on the mass transport of an imbalance between evaporation and precipitation is negligible, but the salinity contrast between the ocean and water vapour magnifies the freshwater imbalance, and significantly influences the salt budget [Roemmich and McCallister 1989]. The volume transport of water presented in chapter 5 includes these imbalances of evaporation and precipitation. By multiplying the volume transport by a mean salinity, and subtracting the salt transport defines the time-averaged freshwater budget as

$$\begin{bmatrix} FW_u \\ FW_v \end{bmatrix} = \int\int \rho (S_0 - S) \begin{bmatrix} udy \\ vdx \end{bmatrix} dz \tag{6.2}$$

The results of these equations, like the thermal wind equations discussed in chapter 2 (page 15), will be different due to the cross correlation between the velocity and the salinity or temperature field and the length scales of the interpolation process. The inclusion of the perturbation fields of temperature, $T'$, and salinity, $S'$, makes a significant difference to the net transports of heat

and freshwater. Figure 6.1 shows the difference between the optimally remapped heat transport and the heat transport calculated from the remapped velocity and temperature fields for the Indian Ocean. This shows that there are significant differences in the top 500 metres of the section associated with the inclusion of the perturbation fields. The positive regions of difference between 35°E to 50°E and 60°E to 90°E indicate where the interpolated heat transport is larger than the heat transport calculated from the interpolated fields of velocity and temperature. The southward flowing Agulhas Current shows a negative difference, as it will be shown in section 6.2.1, this is a region of negative heat transport across 35°S. Therefore, a negative difference, indicates that the interpolated heat transport is larger and more negative than the heat transport calculated from the interpolated temperature and velocity fields. Both of these results show that the heat transport estimated from the interpolated heat transport is larger than the heat transport estimated from the interpolated velocity and temperature fields.

The thermal wind components of heat and freshwater are computed in the same manner as thermal wind in section 3.2.4. A cast is selected from the dataset, and the surrounding area divided into 12 regions (see figure 3.10, page 36). The heat and freshwater transport between the central cast and each of the twelve region casts and calculated and orientated to north on the 42 levels of the dataset. On each level of the dataset, the $x$ and $y$ components of heat and freshwater transport are calculated (see equation 3.2) using singular value decomposition as presented on page 36. The $x$ and $y$ components of heat and freshwater transport are then optimally interpolated on each of the 42 levels of the dataset.

The heat and freshwater transported by the reference velocity calculated by the inverse model, is estimated by multiplying the reference velocity by the

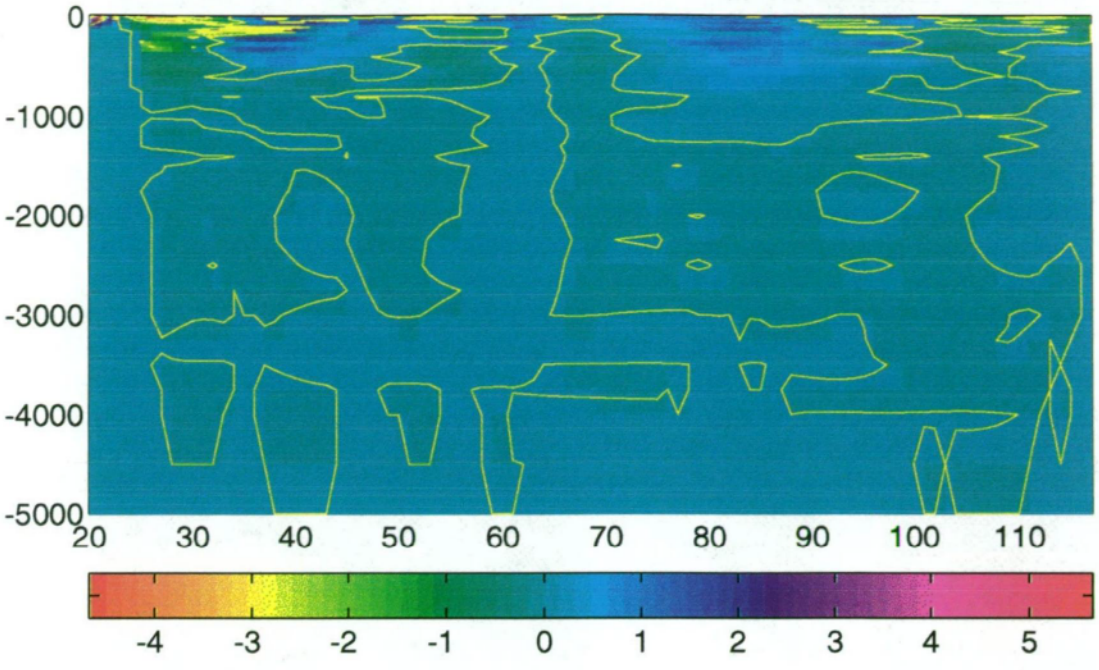


Figure 6.1: Difference between optimally interpolated heat transport and heat transport calculated from interpolated velocity and temperature fields ($10^{10}$ W) across the Indian Ocean at 35°S. Zero difference contoured.

interpolated temperature and salinity fields at each depth level. These reference transports are then added to the thermal wind transports to generate the presented vertical sections of heat and freshwater transport. This approach of generating heat and freshwater transports does not include the $T'$ and $S'$ perturbations associated with reference transport. However, this barotropic component cannot be calculated at this stage from the density field data.

The Ekman component of heat and freshwater transport was added to the thermal wind and reference transports by assuming that the Ekman layer extends to a depth of 50 metres, and includes the top 5 layers of the dataset. This is the depth used by Bryden et al. [1991] to estimate Ekman transport. The Ekman transport was divided equally over the top 5 layers and multiplied by the layer temperature and salinity to try and estimate the Ekman components of heat and freshwater on each layer. These Ekman transports were then added to the thermal wind and reference transports of heat and freshwater.

As the depth of each layer increases with depth, the Ekman velocity decreases with depth. Following the procedure outlined by Bryden et al. [1991], the mean temperature and salinity of the five Ekman layers was used to calculate the Ekman heat and freshwater transport instead of the full ocean mean.

Using the heat and freshwater transports calculated in the manner outlined above, the three dimensional field of heat and freshwater transports can be constructed and analysed. In the following sections, the heat and freshwater transports across 35°S are compared to observational estimates. The total depth-integrated transport of heat and freshwater are presented before investigating the divergence of heat and freshwater throughout the model domain.

## 6.2 Heat and Freshwater flux across 35°S.

This section inspects the heat and freshwater transport calculated to cross 35°S. Initially, the interpolated temperature and salinity fields are compared to nearby observations along the sections to confirm that the optimal interpolation of the data is consistent with the observations and to assist in defining water masses across the section. Using these remapped fields to estimate the transport due to the reference velocity and combining the thermal wind and Ekman transports, the sections of heat and freshwater transport are presented and interpreted.

### 6.2.1 Indian Ocean

As discussed in chapter 5, the Indian Ocean transports 14 Sv into the model domain. This transport must originate from the Pacific Ocean via the Indonesian throughflow and is likely to be associated with a significant heat and freshwater transport. The heat and freshwater transport of the Indian Ocean has been estimated many times [Bennett 1978; Toole and Raymer 1985; Fu

1986; Murray and Arief 1988; Meyers et al. 1995; Toole and Warren 1993; Nof 1995] and these results are compared to the SOINV results. The optimally interpolated temperature field across the Indian Ocean at 35°S is presented in figure 6.3 and is compared to the results of a trans-Indian section occupied by the RRS Charles Darwin in November-December 1987 as reported by Toole and Warren [1993]. The Darwin section is broken into two depth ranges. The top layer is an expanded view of the top 1000 metres, while the bottom section covers the full depth range. The isotherms generally slope upwards to the east, towards Australia with a small depression of the isotherms near the continent of Australia. Surface temperatures exceed 20°C near the coast of Africa, associated with the Agulhas Current, and at longitudes 54°E, 80°E and near the Australian continent. Deep layer temperatures reach a minimum less than 1.5°C, with a small region less than 0.5°C at 60°E. There are several differences between the observed field and the interpolated field. As expected, the fine scale structure present in the observations is not present in the smoothed temperature field. For example, the rise in the isotherms close to the African continent (less than 1° of longitude wide) is smoothed out, except in the top 1000 metres of the smoothed field. The depth of the isotherms are generally in close agreement.

The bottom panel of figure 6.2 presents the optimal interpolation errors associated with the temperature field. These errors give an estimate to how well the interpolation procedure is performing. Large errors indicate regions where the signal variance of the data is large, ie., there is a lot of variation in the observations, or that the optimal interpolation length scales are too short. In the region west of 60°E, above 1000 metres, the large errors are in the Agulhas Current region which is known to be extremely variable [Read and Pollard 1993] and hence the signal variances are large, leading to the large observed errors. Below 1000 metres, the fluctuations in temperature decrease, resulting in

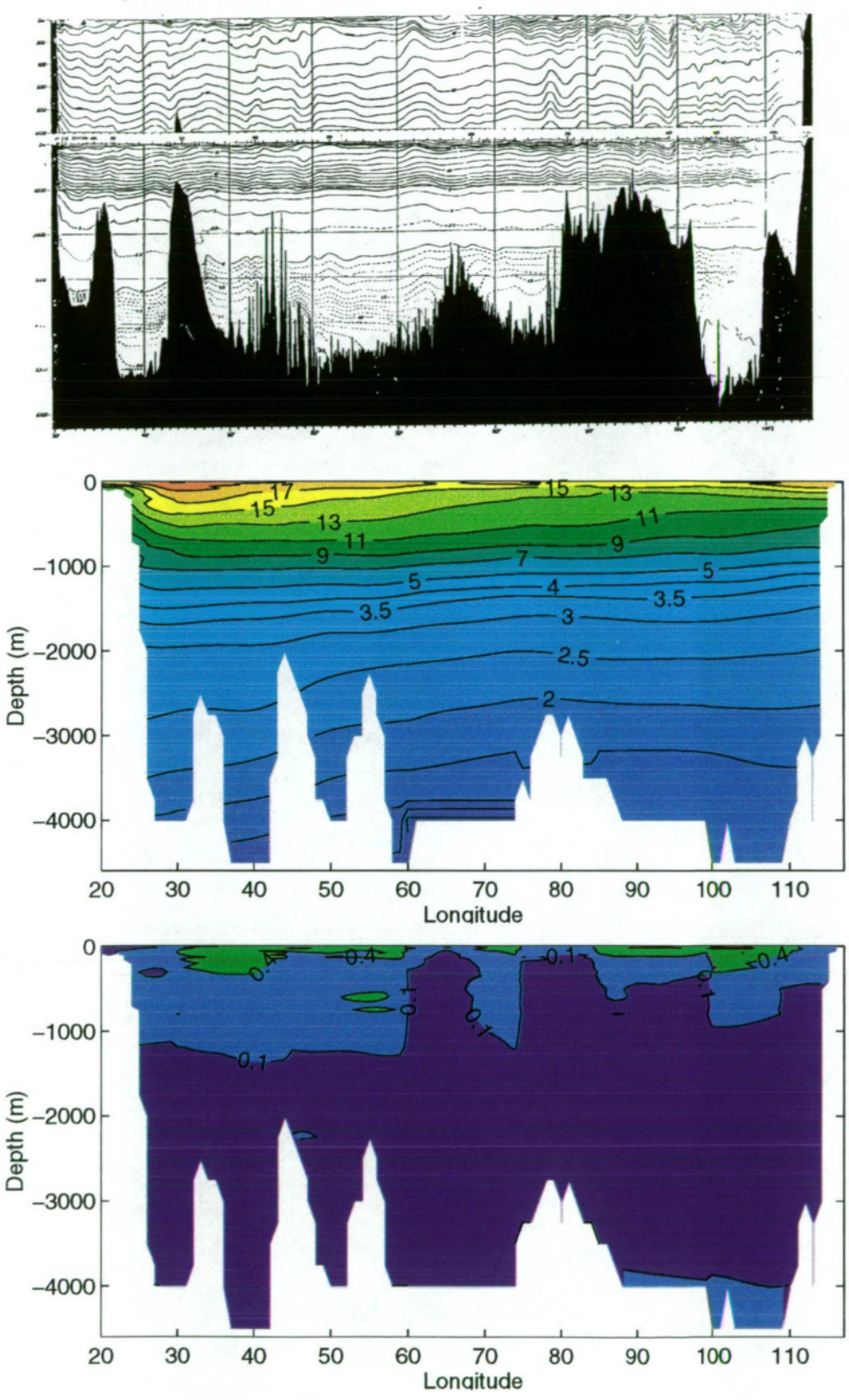


Figure 6.2: Potential temperature (°C) sections for Darwin section (top) [Toole and Warren 1994], the remapped temperature (middle) and associated error field from optimal mapping (bottom) for the Indian Ocean.

smaller signal variances, and hence smaller errors. The slight increase in the error field at 4000 metres between 86° and 109°E is due to a decrease in the number of observations. As the number of observations decreases with depth, the horizontal distance between observations increases to the extent that it exceeds the optimal interpolation short length scales, and thus the optimal interpolation introduces some artificial signals. However, as the optimal interpolation procedure utilises two length scales, long and short, the size of the introduced artificial signals will be small because even if the data separation exceeds the short length scales, the interpolation process will utilise the long length scale estimates.

It must also be noted that, as discussed in section 4.4, the errors due to the inverse solution are not calculated. As the smoothed temperature profile is multiplied by the reference velocities generated by the SOINV to estimate the heat transported by the reference velocities, the optimal interpolation errors of temperature show where the modeller can have confidence in the remapped temperature field but not necessarily the reference heat transport. In the following sections, similar error profiles are presented. It must be remembered that they only represent the optimal interpolation error field of temperature, and do not give the combined estimate of the errors for the reference fluxes or thermal wind transport.

Figure 6.3 compares the salinity section measured by the Darwin, to the optimally interpolated salinity section. The salinity contours generally rise towards the east. Surface values range from approximately 35.6 psu near the coast of Africa to greater than 35.9 psu near the coast of Australia. At depth, there is a salinity minimum layer rising from 1200 metres in the west to 1000 metres in the east associated with Antarctic Intermediate Water. At 3000 metres, there is a tongue of high salinity water extending eastward from the

African continent, which is also coincident to a spreading of the isotherms in figure 6.2. These are characteristic of North Atlantic Deep Water that has moved northward into the Indian Ocean basin from around the southern tip of Africa [Toole and Warren 1993]. Given that there is a salinity minimum, it is clear that there is some bottom water, although at the vertical resolution of the hydrographic dataset below 3000 metres, it is not clear to the extent Antarctic Bottom Water is present.

Now that the different water masses across the Indian Basin have been identified, and using the three dimensional field developed from the SOINV, it is possible to investigate which water masses are responsible for heat, and freshwater transport across 35°S in the Indian Ocean. By multiplying the reference velocities generated by the inverse model by the interpolated temperature field, and adding them to the interpolated thermal wind and Ekman heat transports, estimates of the heat transport can be calculated using equation 6.1. These heat fluxes are presented in figure 6.4 and generate a net southward transport of .52 PW across the Indian Ocean basin. This compares favourably to published estimates of Indian Ocean heat transport by Toole and Raymer [1985] (.6 PW southward at 32°S) and Fu [1986] (.69 PW southward at 18°S and .25 PW southward at 32°S). An advantage of this approach to constructing heat and freshwater transports is that the contribution by the different components, can also be inspected. Across the Indian Ocean, the thermal wind heat transport is estimated to be .84 PW northward. This northward transport by the thermal wind, is in the opposite direction to most published estimates, but does compare to Bennett's [1978] estimate of .88 PW northward. The Ekman component of heat transport across the Indian Ocean contributes a northward transport of .25 PW. The reference transport creates the net southward transport by transporting 1.61 PW southward. So the

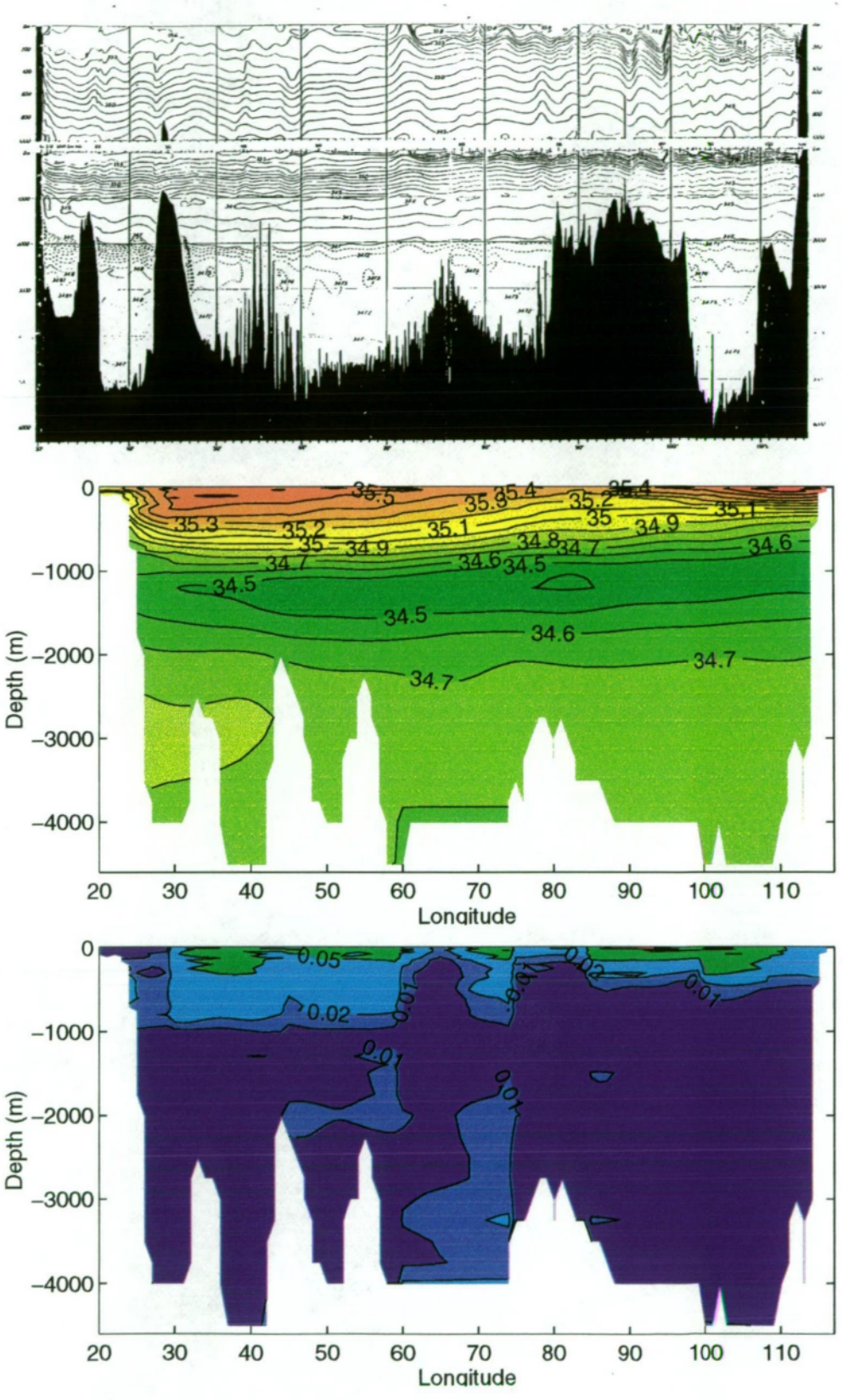


Figure 6.3: Salinity (psu) sections for Darwin cruise (top) [Toole and Warren 1994], the remapped salinity (middle) and associated error field from optimal mapping (bottom) for the Indian Ocean.

reference velocities make a dominant contribution to the net heat transport in the Indian Ocean.

By inspection of figure 6.4, it can be seen that most of the heat is being carried southward by the Agulhas Current. The Agulhas extends to a depth of 800 metres and to 38°E between 500 and 850 metres. There is a layer of strong southward transport at approximately 700 metres depth, extending from the Agulhas Current, east to 60°E. This water is above the salinity minimum Antarctic Intermediate Water and is associated with SubAntarctic Mode Water. Most of the surface waters above 700 metres are transporting heat northward, as is the deep bottom layer. Generally the Antarctic Intermediate Water is transporting heat southward, with an intense core at 80°E, associated with the southward velocity core of figure 5.9. This velocity core has a strong influence on the heat transported by the Circumpolar Deep Water. East of the Mid-Indian Ridge, heat transport closely matches the velocity profile. West of the Mid-Indian Ridge, the heat transport is both north an d south, with a northward core at 55°E.

The bottom panel of figure 6.4 depicts the optimal interpolation errors of only the thermal wind component of heat transport.

By integrating the heat flux across 35°S (figure 6.4) on each depth layer, the layer contribution to the heat transport across the Indian Ocean can be investigated and is shown in figure 6.5. It is also possible to investigate the contribution each of the three components make to heat transport. Above 300 metres the reference transport of heat is balancing the thermal wind transport of heat. However, the total heat transport is generally northward. At 500 metres, the reference heat transport is very strongly southward, which because of the weakening, northward, thermal wind transport gives a strong southward transport of heat for this layer. Below 700 metres, the thermal wind

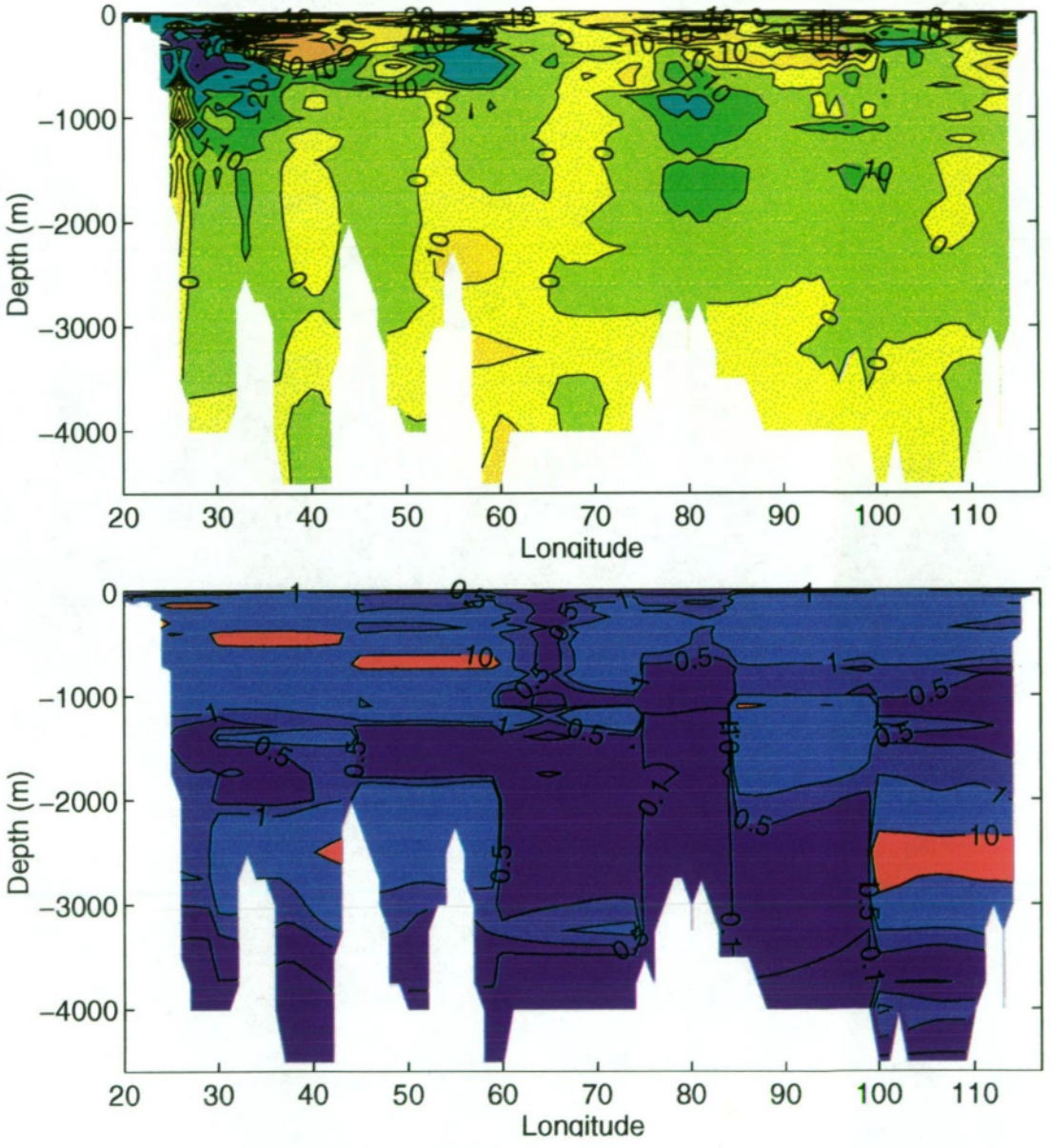


Figure 6.4: Heat flux, $HF$ $(10^{11}W)$, across 35°S in the Indian after inverse solution with associated optimal mapping errors.

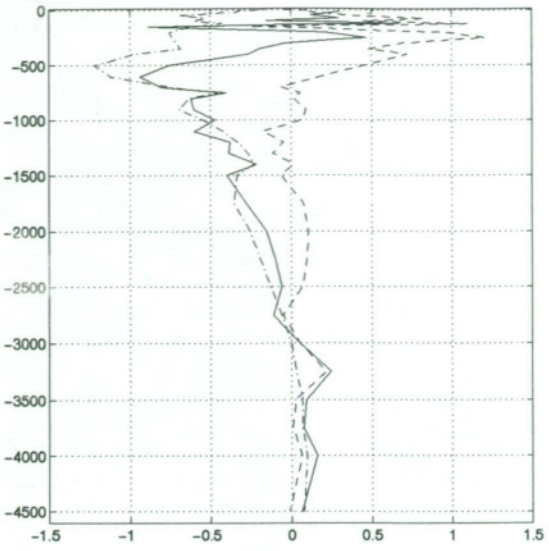


Figure 6.5: Heat transport on each layer ($10^{14}$ W, +ve is northward), integrated across the Indian Ocean. (Solid = Total, Dashed = Thermal wind, Dashed-dot = Reference, Dotted = Ekman).

contribution decreases to be close to zero, and the reference transport of heat dominates the total heat transport.

The freshwater transport, calculated using equation 6.2, is presented in figure 6.6. It is estimated that there is a net southward transport of freshwater of $2.5\times10^{8}$ Kg $s^{-1}$. Most of the southward transport occurs in two cores located at 2200 metres and 3200 metres at 60°E. There is also significant southward transport associated with the deep Agulhas Current. The surface waters are slightly southward, overlying a general northward transport. The Subantarctic Mode Waters are also responsible for a strong northward transport of freshwater at 60°E. As mentioned above, the Antarctic Circumpolar Deep Water is transporting most of the freshwater south at 60°E. East of the Mid-Indian Ridge, the freshwater transport is weakly northward. But there seems to be little structure within each water mass.

In summation, the Indian Ocean has several distinct sections. The Agulhas Current which is transporting heat and freshwater southward. The Agulhas return current which transports heat northward, freshwater weakly

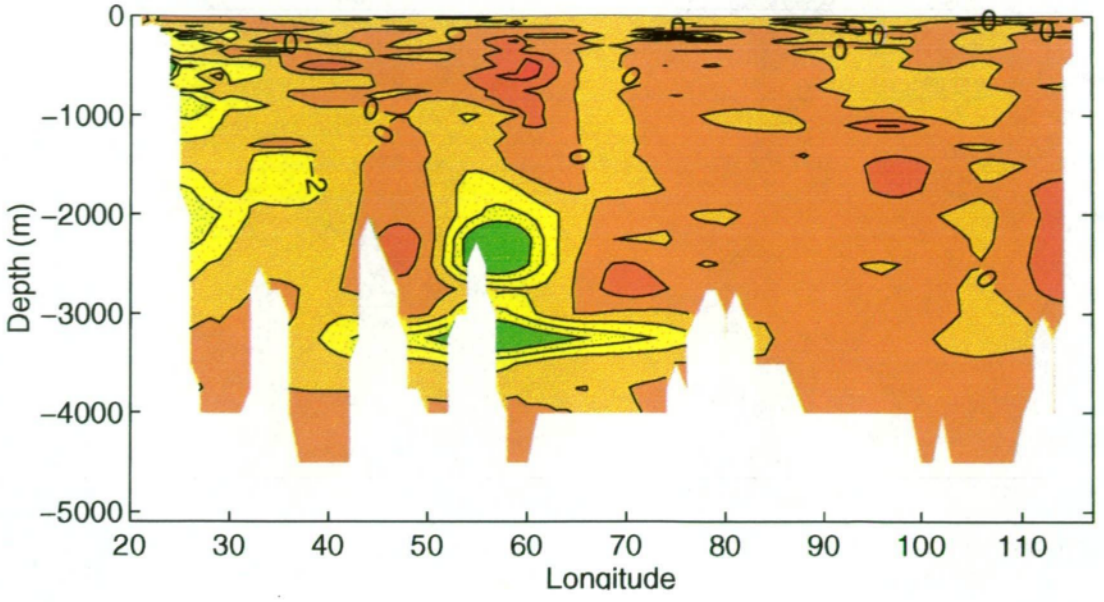


Figure 6.6: Freshwater transport across 35°S in the Indian Basin calculated using velocity and salinity fields ($10^6$ Kg $s^{-1}$).

northward. The Sub-Antarctic Mode Water transporting heat southward and freshwater northward. East of the Mid-Indian Ridge, the Circumpolar Deep Water is transporting heat northward and freshwater southward. West of the Mid-Indian Ridge, Circumpolar Deep Water is transporting heat southward and freshwater northward.

### 6.2.2 Pacific Ocean

The smoothed temperature profile for the Pacific Ocean is presented in figure 6.7 and compared to the temperature profiles measured along the WOCE P6 section presented by Toole et al. [1995]. Generally, the isotherms shoal towards the east, except close to the Australian continent west of 170°E. This shoaling is most apparent in the top 1000 metres. Below 1000 metres in the smoothed field, and below 2000 metres in the P6 section, the isotherms tend to deepen again east of 260°E. Surface temperatures exceed 20°C for nearly the entire section. In comparison to the Indian Ocean temperatures of figure 6.2, the Pacific Ocean

is cooler than the Indian Ocean, with the 2.5°C isotherm nearly 1000 metres shallower in the west Pacific. Near South America, the difference is approximately 100 metres.

In the salinity profiles, shown in figure 6.8, there is once again the characteristic salinity minimum associated with Antarctic Intermediate Water. It is slightly shallower than in the Indian Ocean, ranging from 1000 metres in the west to 750 metres in the east in both the P6 and smoothed sections. Surface salinities exceed 35.7 psu near Australia but freshen considerably across the Pacific until a minimum of less than 34.5 psu off the South American Coast as the salinity minimum shoals towards the surface. Below the salinity minimum layer, there is a broad depth range with the 34.7 psu contour at a nearly identical depth in both the P6 and smoothed fields. Together with the slight spreading of the temperature contours in figure 6.7, the salinities are characteristic of Circumpolar Deep Water. The deep 34.7 psu contour also suggests that there is some NADW entering the Pacific basin south of Australia and New Zealand.

In both the salinity and temperature fields, the associated optimal interpolation errors were larger than those produced in the Indian Ocean. Unlike the Indian Ocean errors, the increased errors are a result of a decrease in data density. As explained in the discussion of the Indian Ocean errors, if data density exceeds the length scales of the optimal interpolation, the interpolation procedure can add artificial signals. The South Pacific Ocean has the lowest data density of the model domain, which leads to the relatively high observed interpolation errors.

Figure 6.9 depicts the calculated heat transport across the Pacific Ocean. The total transport of heat is estimated to be 1.2 PW northward. The individual contributions to this transport are .29 PW northward by reference

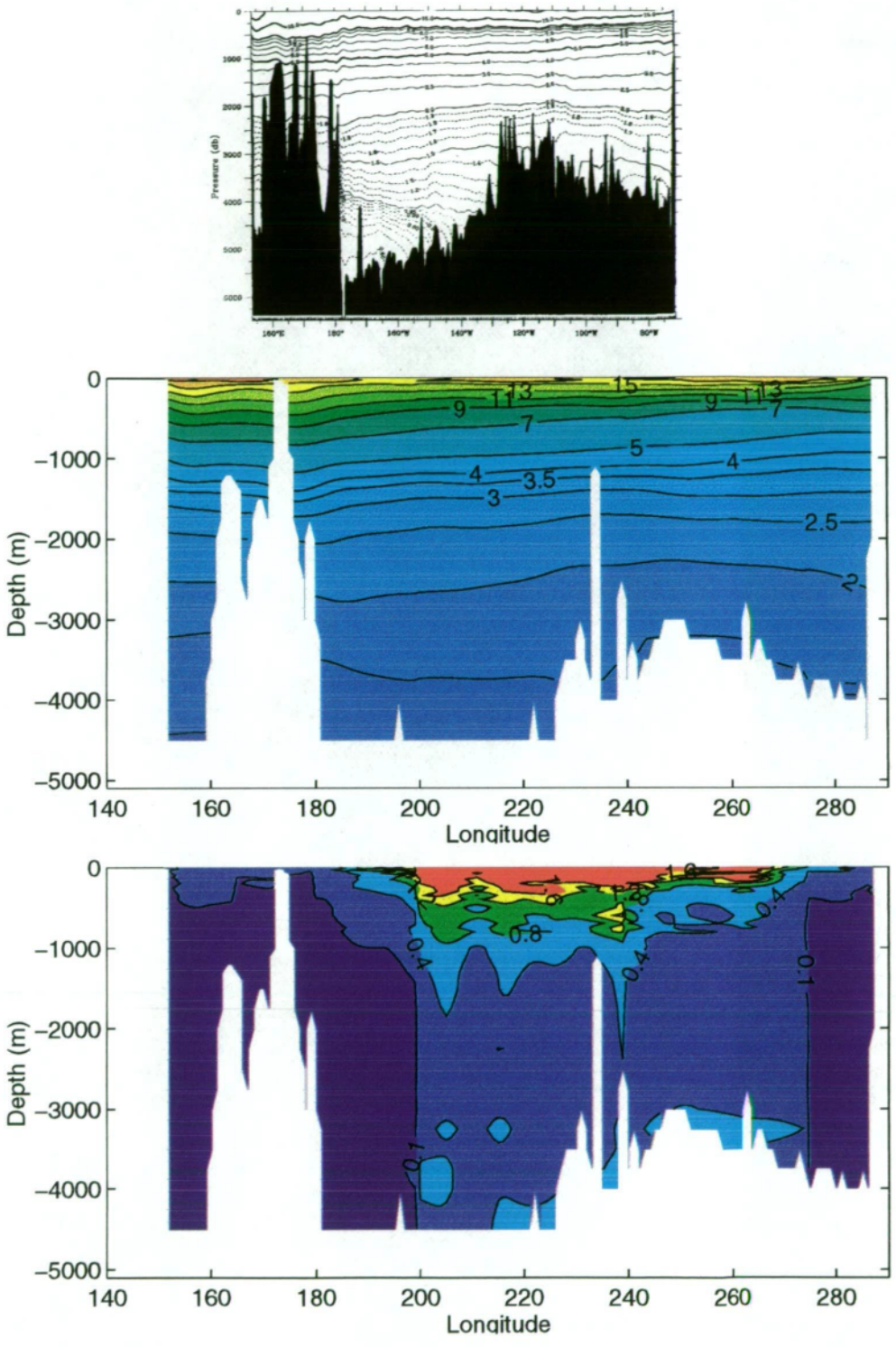


Figure 6.7: Potential temperature (°C) sections for the P6 section (top) [Toole et al. 1995], the remapped temperature (middle) and associated error field from optimal mapping (bottom) for the Pacific Ocean.

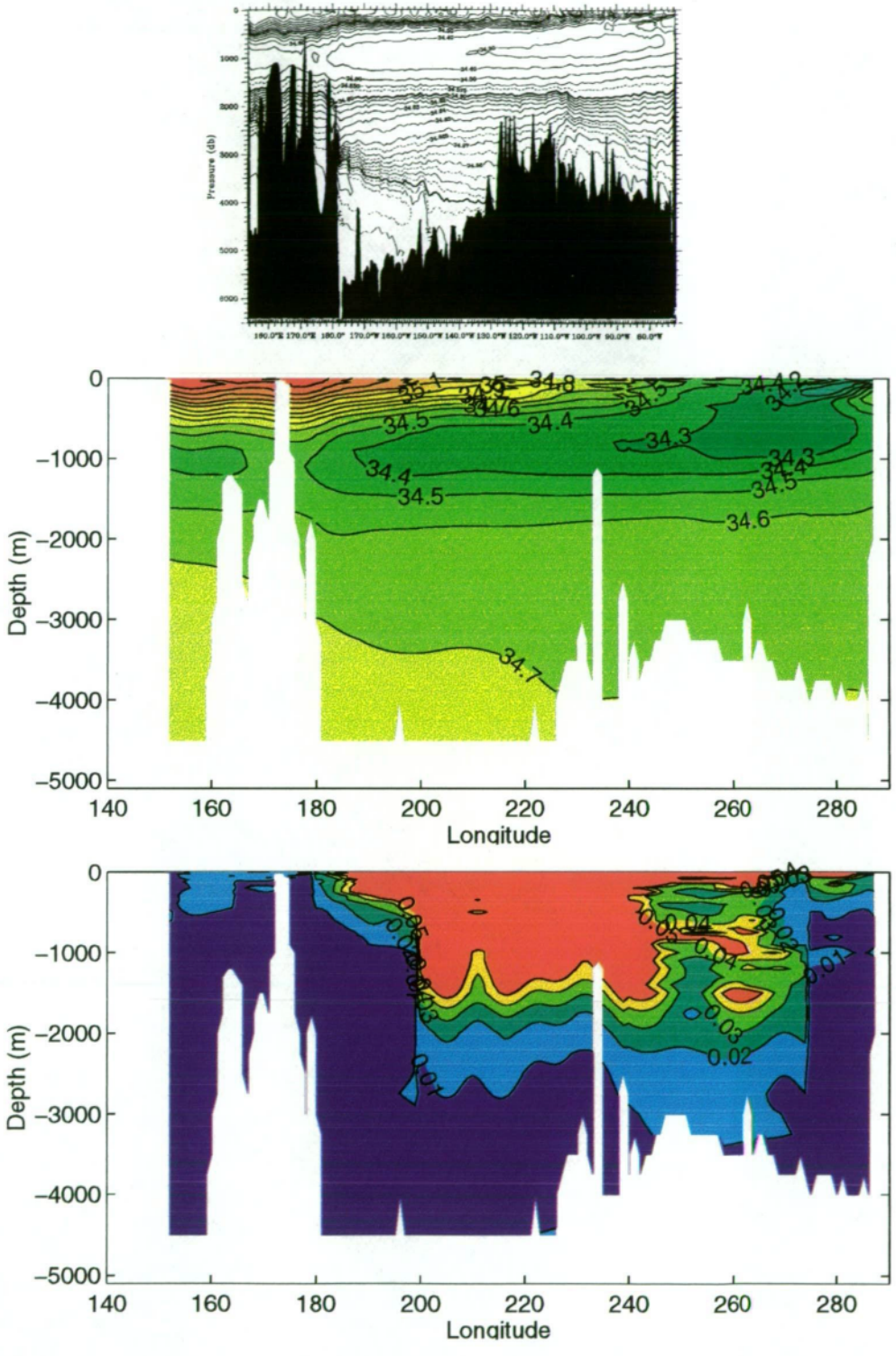


Figure 6.8: Salinity (psu) sections for P6 (top) [Toole et al. 1995], the remapped salinity (middle) and associated error field from optimal mapping (bottom) for the Pacific Ocean.

transport, .76 PW northward by thermal wind transport and .15 PW northward by the Ekman layer transport. This is unexpected as it is generally accepted that the Pacific Ocean has a net southward transport of heat [Macdonald 1993]. Previous estimates of Pacific Ocean heat transport range from .15 PW northwards [Macdonald 1993], to 2.2 PW southward [Macdonald 1993]. Thus the SOINV is estimating a heat transport that is more northward than previous observations.

From the section shown in figure 6.9, most of the heat transport in the Pacific occurs in the top 1000 metres of the ocean, above the Antarctic Intermediate Water. The Chile-Peru Current, the eastern arm of the Subtropical Gyre, and the EAC return Current are the major conduits of northward heat transport. There is a southward transport of heat associated with the western arm of the Subtropical Gyre. Below 1000 metres, the magnitudes of the heat transport are much smaller than the surface layer values. Most of the surface features do extend down through the water column, but with significantly smaller heat transports at depth. This weak vertical profile is consistent with the results of Wunsch et al. [1983].

The contribution each component makes to the transport of heat across the Pacific Basin is presented in figure 6.10. From figure 6.10 it is clear that, unlike the Indian Ocean, the thermal wind velocities are the dominant component. The heat transported by the reference velocities is very small compared to the thermal wind. Both components are relatively small below 1000 metres, but near the surface layers the reference transport of heat does not vary as greatly as it does in the Indian Ocean. It is possible to see the Sub-Antarctic Mode Water transporting heat north, overlying the weaker northward transport associated with the Antarctic Intermediate Water.

The freshwater profile presented in figure 6.11 is in some respects in

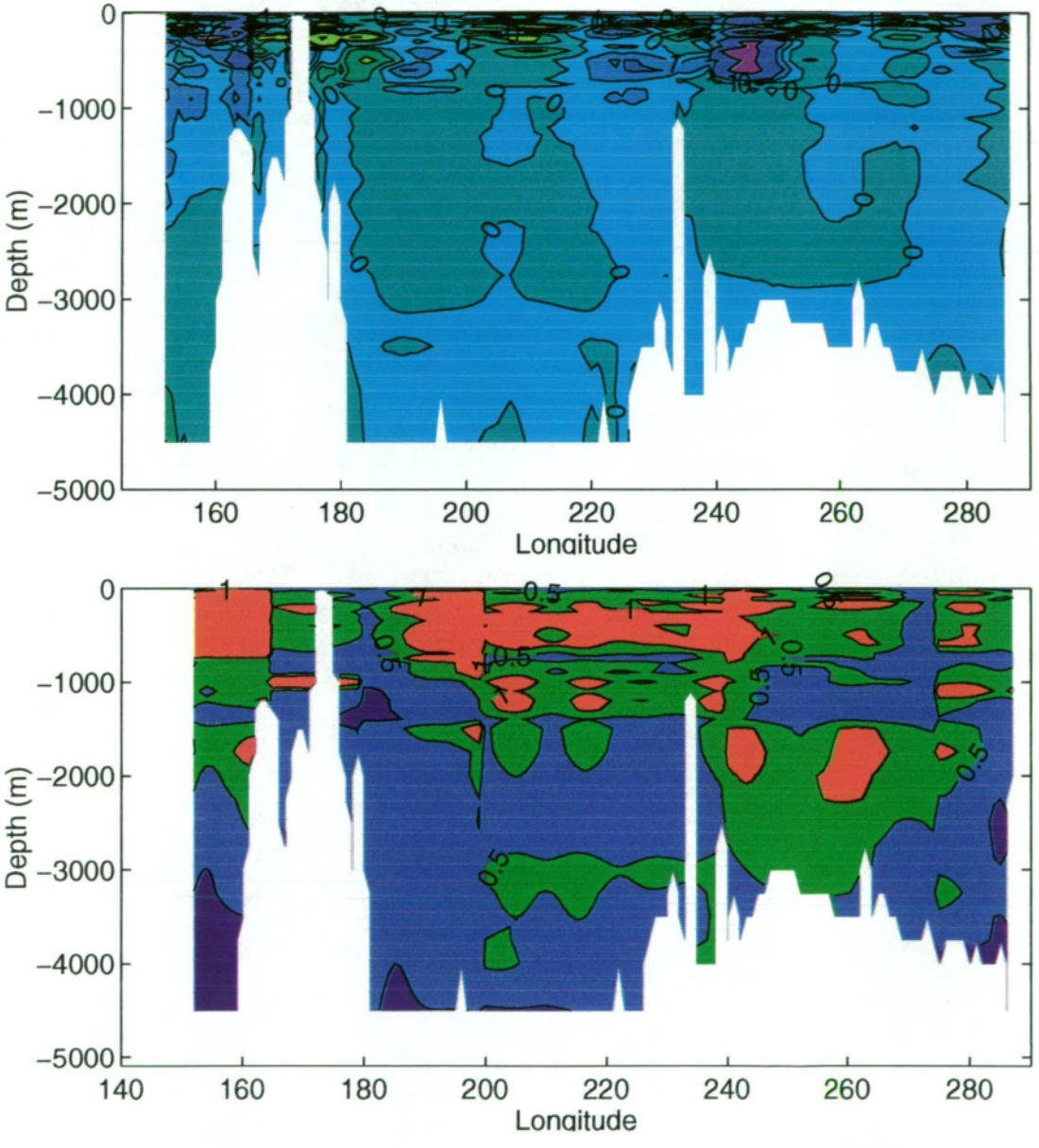


Figure 6.9: Heat flux, $HF$ ($10^{12}W$), across 35°S in the Pacific after inverse solution with associated optimal mapping error for the Pacific Ocean.

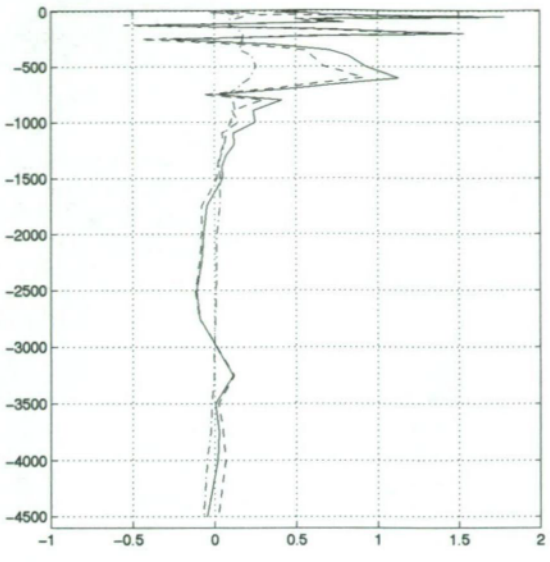


Figure 6.10: Heat transport on each layer ($10^{14}$ W, +ve is northward), integrated across the Pacific Ocean. (Solid = Total, Dashed = Thermal wind, Dashed-dot = Reference, Dotted = Ekman).

complete contrast to the Pacific heat transport. It is estimated that the net southward transport is $4.2\times10^{7}$ Kg $s^{-1}$. Most of this transport occurs in the deeper ocean, in particular the Circumpolar Deep Water. The surface layers show generally weak transports of freshwater above approximately 1000 metres. The exception to this is the southward transport associated with the EAC on the east coast of Australia. This southward transport extends to a depth of 2000 metres and overlies an intense core of northward freshwater transport. On the eastern side of the New Zealand Ridge, there is a strong northward transport of freshwater that extends between 1000 and 3000 metres. Over the East Pacific Ridge, at 3500 metres depth, there is a strong core of southward transport, that continues eastward and joins a general southward transport of freshwater east of the East Pacific Ridge.

From the profiles discussed above, it appears that the surface waters of the Pacific, above 1000 metres, are the most influential in the heat transport, while the deeper interior of the ocean, below 1000 metres, is important to the

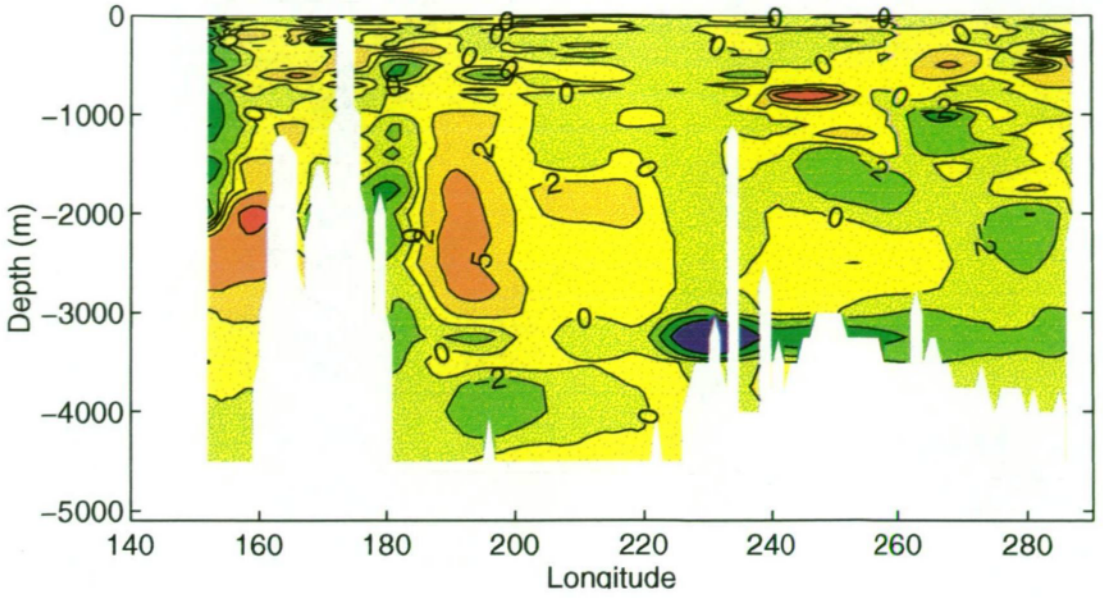


Figure 6.11: Freshwater flux across 35°S in the Pacific Basin calculated using velocity and salinity fields for the Pacific Ocean. ($10^6 kg.s^{-1}$)

freshwater transport. The Chile-Peru Current is transporting both heat and freshwater northward, whilst the EAC is transporting freshwater southward but only weak southward heat transport. The net transport of heat is northward, which as noted, does not agree with published results listed in MacDonald's [1993] paper. This apparent inconsistency with the observed heat transport is investigated and discussed in detail in section 6.4.

### 6.2.3 Atlantic Ocean

From chapter 5, it was shown that the net transport across 30°S in the Atlantic Ocean was close to zero. Therefore, any net transport of heat or freshwater in the Atlantic will be due to the difference in properties of the transported water masses. The temperature profile across the Atlantic is shown in figure 6.12. Surface temperatures are fairly uniform at approximately 20°C across the basin. Down to a depth of 1000 metres, the vertical gradient of temperature is almost uniform with isotherms sloping upwards towards the east. Below 1000 metres,

the isotherms spread over depth, consistent with CDW. On the western boundary, the 3° isotherm is depressed from 1400 metres to nearly 3000 metres. This depression of the isotherm is a signature of North Atlantic Deep Water flowing south down the western boundary of the Atlantic Basin. Below the Circumpolar Deep Water, the 2° isotherm indicates the presence of Antarctic Bottom Water, particularly west of t he Mid-Atlantic Ridge.

The salinity section shown in figure 6.13 highlights the different water masses that are present within the Atlantic basin more clearly. The surface waters, down to a depth of 800 metres, show salinities greater than 35psu. The salinity minimum layer, <34.4 psu, indicative of Antarctic Intermediate Water is clearly seen at a depth of 850 to 1100 metres. Below the salinity minimum the steady increase in salinity with depth, together with the temperature gradient, indicates the presence of Circumpolar Deep Water and North Atlantic Deep Water on the western boundary of the basin. There is the presence of Antarctic Bottom Water underlying the Circumpolar Deep Water across the section.

The heat transport across 35°S in the Atlantic, shown in figure 6.14, is estimated to be .37 PW northward. The reference velocities and Ekman component are calculated to contribute a northward transport of .83 PW and .16 PW respectively while the thermal wind component is estimated to transport .61 PW southward. It is generally considered that the Atlantic Ocean has a net northward transport of heat associated with it, with published results varying from .04 PW to .83 PW northward [Macdonald 1993]. In the Atlantic, the transport of heat appears to be evenly distributed over the water column. The southward flowing Brazil current generates a net southward transport of heat down the east coast of South America. This southward transport extends eastward, throughout the water column to 333°E. Over the Mid-Atlantic Ridge, there is a strong northward transport of heat through the water column, except

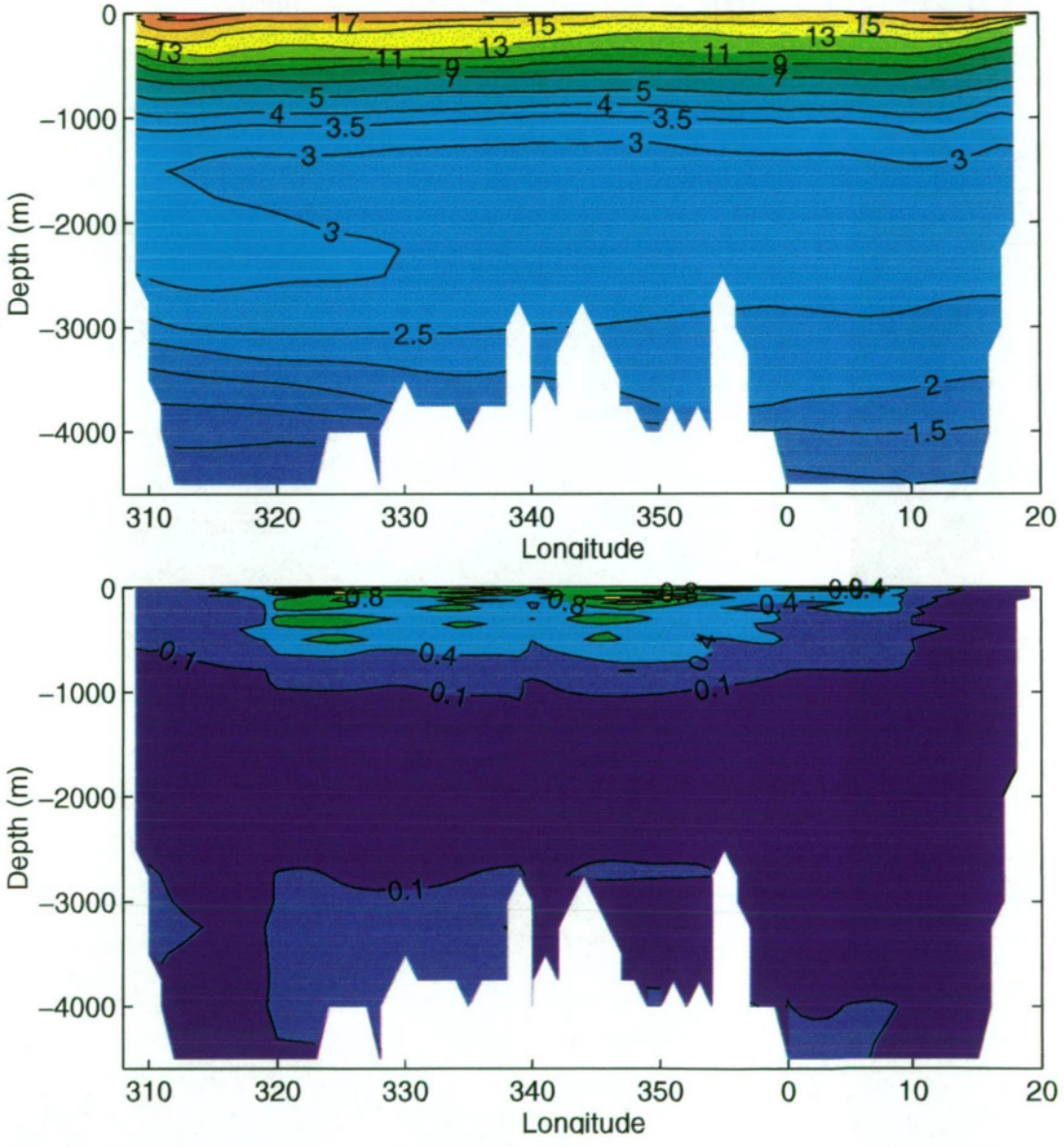


Figure 6.12: Potential temperature (°C) sections for remapped temperature (top) and associated error field from optimal mapping (bottom) for the Atlantic Ocean.

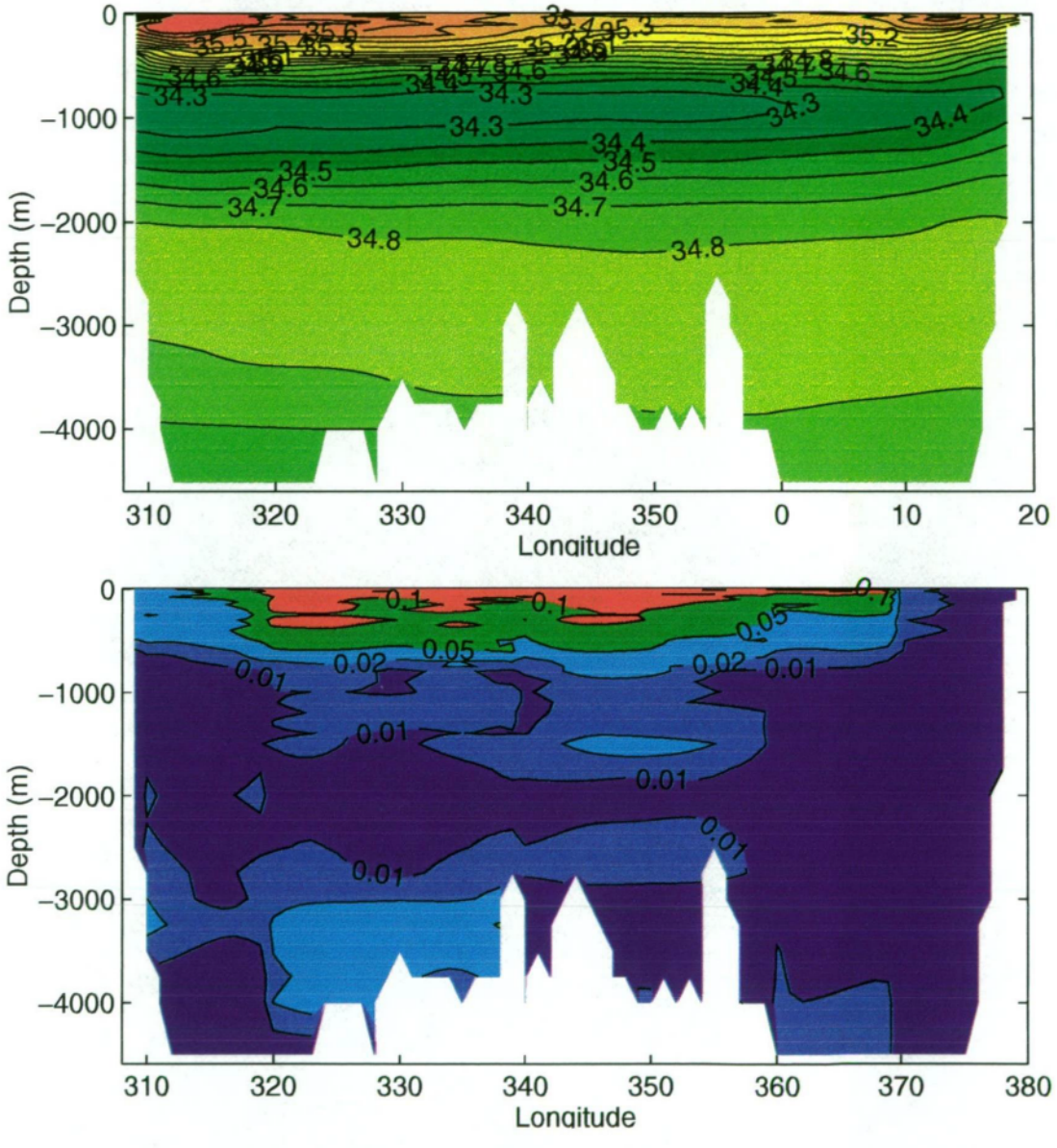


Figure 6.13: Salinity (psu) sections for remapped salinity (top) and associated error field from optimal mapping (bottom) for the Atlantic Ocean.

for the top 200 metres. This northward transport of heat extends eastward, decreasing and then increasing again, reaching a maximum in the Benguela Current on the west coast of Africa. There is a surface return current between 0°and 10°E, mostly associated with the western eddy of the Agulhas Return circulation. There is also a southward transport of heat below 3500 metres associated with Antarctic Bottom Water, that extends across the Atlantic, across the Mid-Atlantic Ridge, and reaching a maximum at 15°E, at the base of the continental shelf of Africa.

Figure 6.15 depicts the zonal integration on depth layers of heat transport across the Atlantic Ocean. Like the Indian Ocean, the reference circulation is counteracting the thermal wind transport, particularly at depth, to generate the net northward transport. In the surface layers, the thermal wind transport is relatively large and negative. However the reference heat transport is opposite in sign, reducing the southward transport of heat. Below 800 metres, the reference heat transport becomes the dominant circulation leading to net northward transports of heat at depth.

The freshwater transport depicted in figure 6.16 shows that the $1.7\times10^8$ Kg $s^{-1}$ of northward flowing freshwater is transported mostly in the deeper layers of the Ocean. The total freshwater transport is consistent with previous estimates, such as $3\times10^8$ Kg $s^{-1}$across 32°S by Macdonald [1993]. The North Atlantic Deep water generates relatively large cores of northward freshwater current on the western side of the basin, between 3800 metres and 1500 metres. Above the North Atlantic Deep Water, the Brazil Current transports freshwater southward close to the South American Continent and then northward as the return current moves north again. East of 340°E, between 800 metres and 3250 metres, there are several cores transporting freshwater both north and south.

Unlike the Indian and the Pacific, it is the deep interior of the Atlantic

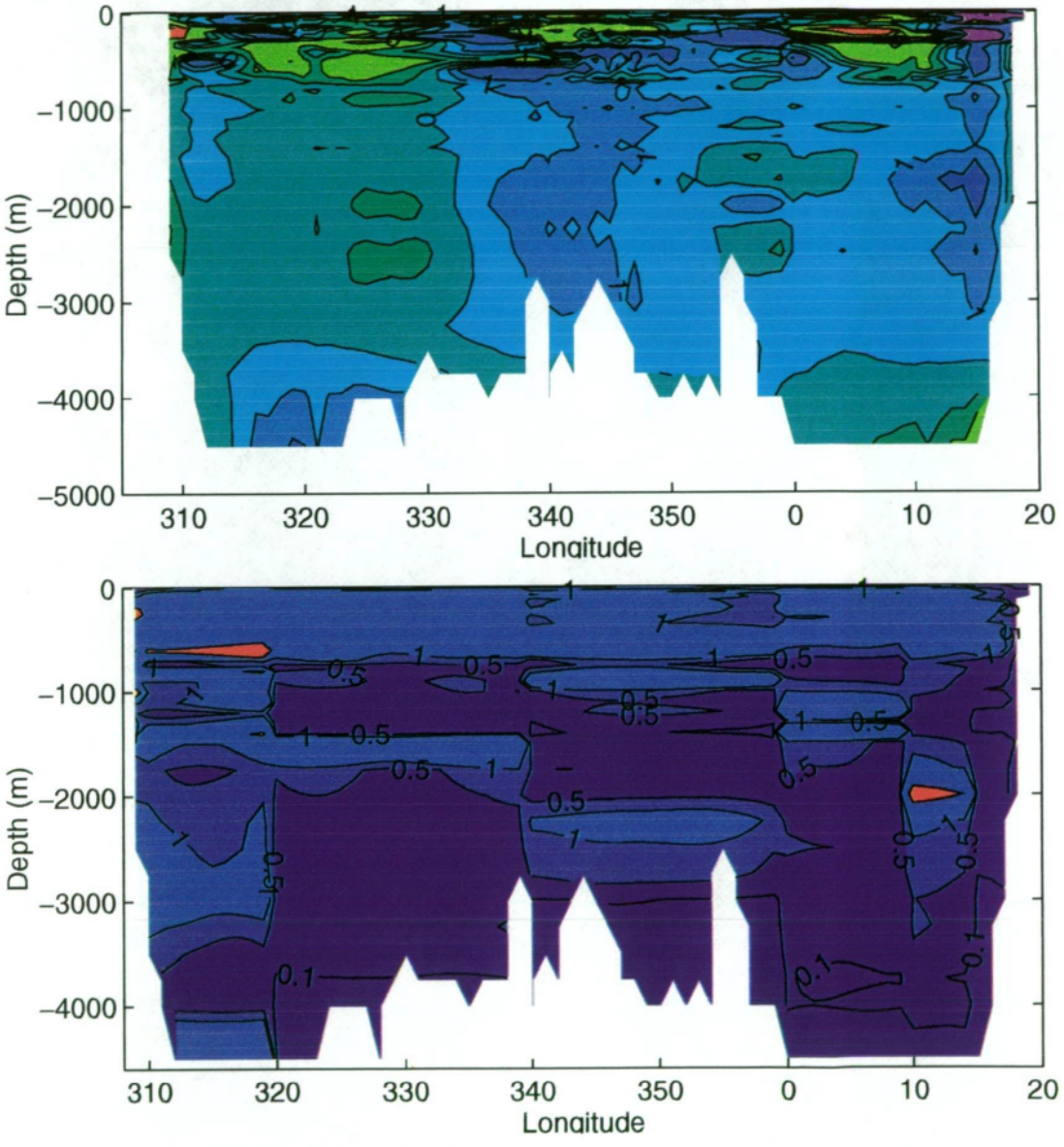


Figure 6.14: Heat flux, $HF$ ($10^{12}$ W), across 35°S in the Atlantic after inverse solution with associated optimal mapping error for the Atlantic Ocean.

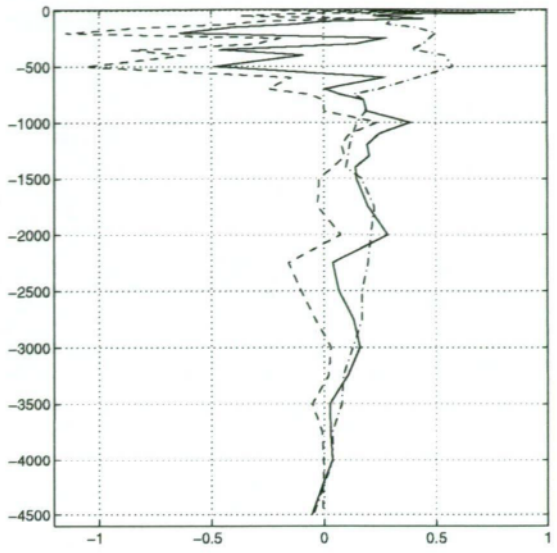


Figure 6.15: Heat transport on each layer ($10^{14}$ W, +ve is northward), integrated across the Atlantic Ocean. (Solid = Total, Dashed = Thermal wind, Dashed-dot = Reference, Dotted = Ekman).

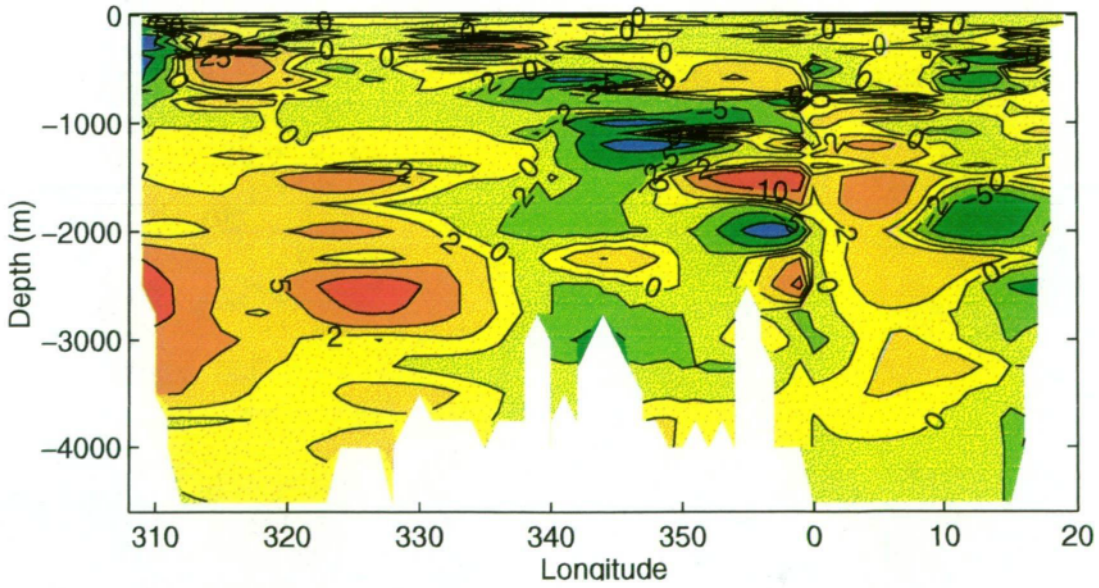


Figure 6.16: Freshwater flux across 35°S in the Atlantic Basin calculated using velocity and salinity fields for the Atlantic Ocean. ($10^6$ Kg $s^{-1}$)

that is having the most influence on the heat and salt transport across 35°S. The western boundary current is having an effect, but not nearly to the same degree as in the other ocean basins. Surface heat transport is, as with the other two basins, significant across the basin with little salt flux in the surface layers. Freshwater is generally transported northward across the basin except for two intense cores associated with the Brazil Current and AAIW over the Mid-Atlantic Ridge.

## 6.3 Depth-Integrated Transport and Divergence

With the three dimensional field of heat and freshwater transport that has been created in the previous section, the depth-integrated horizontal transport of heat and freshwater can be calculated on the 1°× 1° grid of the model domain. This is at much higher grid spacing than previous inverse or observational studies. The transport figures presented in the following pages were created by calculating the transport of heat and freshwater using equations 6.1 and 6.2 for the thermal wind, reference and Ekman transports using the global average of temperature and salinity. The divergence fields were calculated from the depth-integrated transport fields in the same manner as the divergence of mass, calculated in section 4.1.

The two dimensional transport flow fields give an indication of how heat and freshwater is moved around the Southern Ocean by the mean circulation. Taking the divergence of these flow fields represents the areas of heat and freshwater imbalance over the total water column. These imbalances can be used to represent heat and freshwater exchanges at the surface of the ocean, into the atmosphere, and so can be thought of as surface fluxes of heat and freshwater.

### 6.3.1 Heat

The total heat transport field shown in figure 6.17 depicts the depth integrated movement of heat around the Southern Ocean by the mass conserving circulation presented in chapter 5.

From figure 6.17, it is clear that, while most heat is being transported by the ACC, there is significant heat transport associated with the subtropical gyres. In the Indian Ocean (top panel of figure 6.17), heat is being transferred in an easterly direction by the ACC north of 50°S. North of the ACC, heat is being transferred northward away from the ACC. It appears that most of this heat is being re-circulated back south through the Agulhas Current, with a westerly heat transport along 30°S, west of 90°E. East of 90°E, the heat is circulated back south through the Leeuwin Current. South of Australia, heat is transported in a large anti-cyclonic gyre located in the Great Australian Bight. South of the ACC, the size of the heat transports are generally smaller, and northward into the ACC.

On the east coast of Africa, the Agulhas Current system is transporting heat south into the ACC. On the west coast of Africa, there appears to be heat transferred from the ACC into the boundary current. The boundary transport of heat continues north up the west coast of Africa and into the Atlantic Ocean.

In the Tasman Sea (middle panel of figure 6.17), there is a northward transport of heat away from the ACC, some of which recirculates south of New Zealand before meeting an eastward transport of heat over the Campbell Plateau. The remainder continues north to join southward-moving heat associated with the EAC return current. The southward transport of heat expected to be associated with the EAC is not present. This is because some of the boundary grid points had excessively large heat transports and were excluded from the estimates.

The Pacific Subtropical Gyre transports heat predominately eastward, west of 240°E and north, east of 240°E. The Chile-Peru Current has an associated northward transport of heat out of the model domain. The ACC continues to transport heat eastward, following closely the mass circulation path across the Pacific. South of the ACC, the magnitudes of the heat transport are smaller and not as well defined, but generally show a westward transport of heat.

In the Atlantic sector (bottom panel of figure 6.17), the heat transport associated with the ACC is much smaller than expected. Through Drake Passage, there is a weak westward transport of heat depicted. It is not until the ACC flows south of Africa that the ACC generates a strong eastward transport of heat. The region north of 50°S and west of 250°E shows strong eastward heat flow. This is the area of the Brazil-Malvinas Confluence outflow and it appears that heat is being transported south by the Brazil Current (not shown because of unrealistic reference velocities) and then across the Atlantic to join the ACC south of South Africa.

The two dimensional heat transport field shown in figure 6.17 represents the depth integrated heat transport at that location. Calculating the divergence of heat, $\nabla \cdot (u, v)T$, estimates the imbalance of heat within each cell can be diagnosed. Since there is a negligible gain of heat at the bottom of the ocean, the surface flux of heat can be defined as

$$\rho C_p \nabla \cdot \begin{bmatrix} u \\ v \end{bmatrix} T = HF_{surface} \tag{6.3}$$

Using equation 6.3, the surface heat flux around the Southern Ocean is presented in figure 6.18. Grid cells with unrealistic surface fluxes (>200 W $m^{-2}$) have been removed. Positive values of the divergence operator represents heat

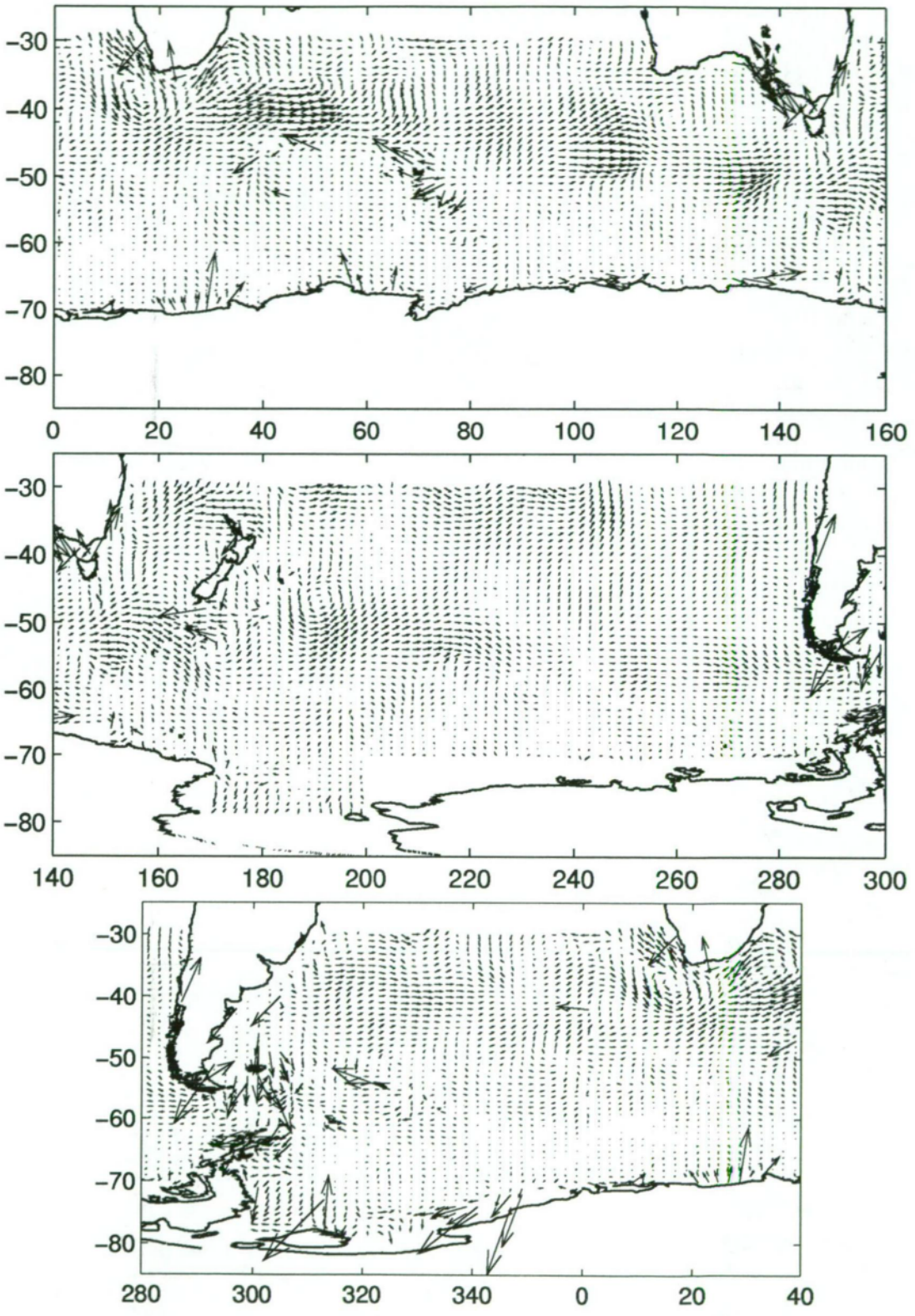


Figure 6.17: Depth-integrated transport circulation of heat around the Southern Ocean shown at 1° lat. × 2° long. grid spacing (1°= $2\times10^{14}$ W).

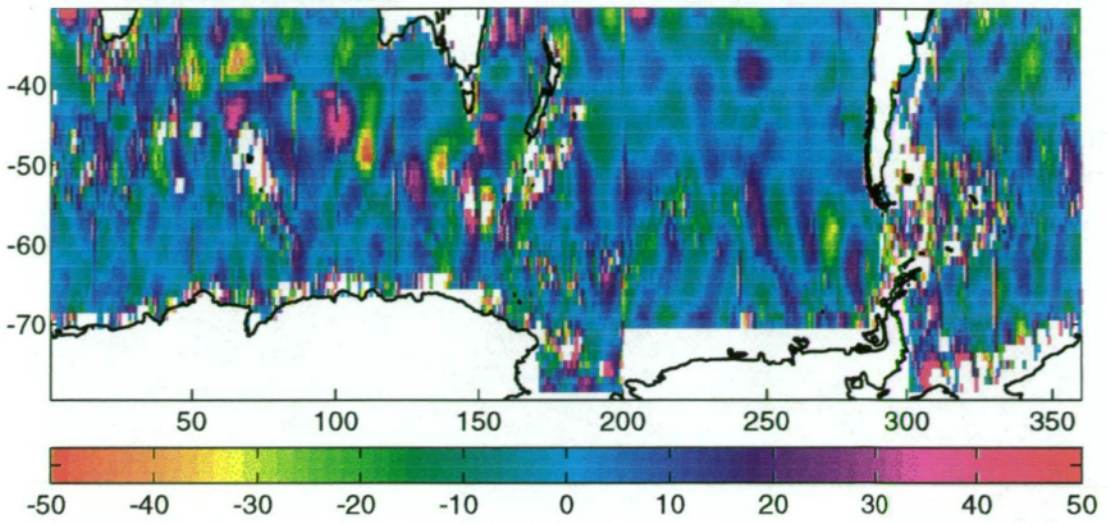


Figure 6.18: Divergence of heat (W $m^{-2}$) in the Southern Ocean from the transport field shown in figure 6.17.

being transferred into the ocean and negative values represent a transfer of heat out of the ocean.

Figure 6.18 shows that the largest imbalances of heat, and thus the largest surface fluxes of heat, are associated with the ACC. The Agulhas and Agulhas Retroflection Currents have large values of heat flux, both positive and negative, associated with them. In the Indian Basin, the largest surface fluxes are $\pm 30$ $Wm^{-2}$. At 37°S, 60°E, the large negative flux is associated with the northward turning of some of the circulation away from the ACC in the Crozet Basin. North and south of the ACC, the size of the divergence field decreases away from the ACC.

In the Pacific Basin, the size of the surface fluxes associated with the ACC are smaller than those presented in the Indian basin. South of New Zealand, the surface fluxes are more confused, sometimes changing sign in neighbouring grid cells. In the north of the Tasman Sea there is a large positive divergence suggesting heat is being transferred into the ocean in this regions. This is the opposite of what is expected, as the EAC is a warm current that gives off heat to the atmosphere [Ridgway and Godfrey 1994]. East of New Zealand, the

surface heat fluxes are generally smaller than the rest of the Pacific Basin.

Through Drake Passage and along the east coast of South America, the surface fluxes are poorly resolved. This is a combination of the bathymetry of the region leading to unrealistic reference transports, and the circulation of heat through Drake Passage being poorly determined. In the interior of the Atlantic Basin, the surface fluxes are smaller than the other two basins. The Atlantic surface fluxes also appear not to be as well defined, particularly in the ACC. This is consistent with the heat circulation shown in figure 6.17, that depicts a slightly confused heat circulation associated with the ACC.

From these two presentations of heat transport of the Southern Ocean, zonal integrations of the meridional component of heat transport and zonal integration of the divergence of heat transport can be calculated. These zonally integrated values estimate the net northward transport of heat and the net exchange of heat between the ocean and the atmosphere as a function of latitude (figure 6.19).

Concentrating on the meridional transport, the meridional net transport of heat is depicted by the solid curve in the top panel of figure 6.19. This shows that, contrary to most published work [Hsiung 1985; Rintoul 1988; Toole et al. 1995], the net transport of heat is calculated to be northward, mainly a result of the Ekman (dotted curve) and thermal wind transport (dashed curve). South of 55°S the heat transport is generally southward as a result of the Ekman transport. North of 55°S, the net transport generally increases reaching a peak of 2.3 PW at 39°S. North of 39°S the net transport decreases to .9 PW then increasing again to 2.1 PW at 33°S before decreasing to 1.6 PW at 30°S.

Inspecting the structure of the components of heat transport shows that the Ekman transport of heat is northward, between 50°S and 31°S peaking at 2.1 PW at 41°S. South of 50°S the Ekman component of heat transport is

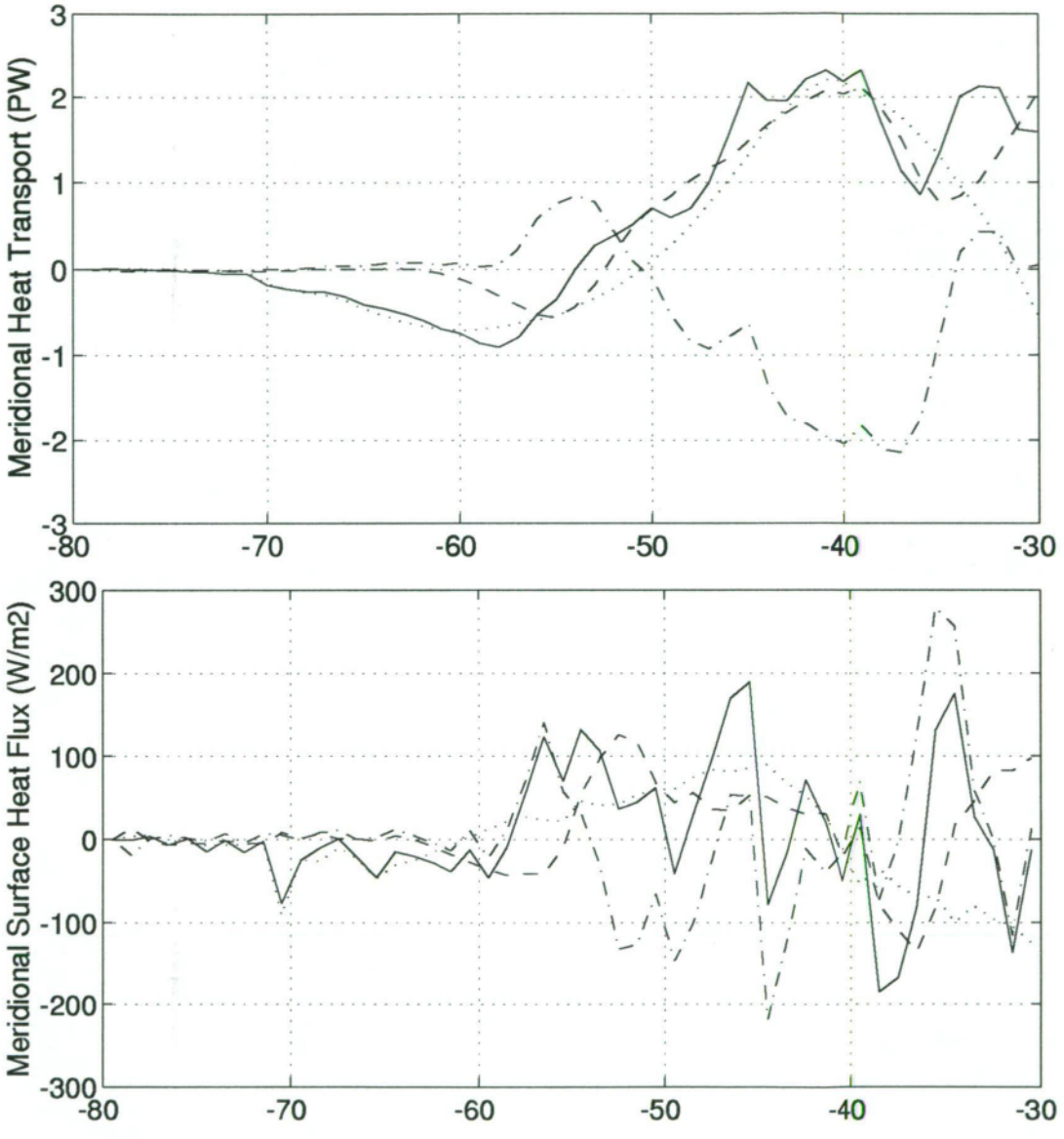


Figure 6.19: Meridional heat transport (top, PW) and meridional surface heat flux (bottom, W $m^{-2}$) for the Southern Ocean. Positive is northward transport and heat lost to the atmosphere. (Solid line = Total, Dashed = Thermal Wind, Dash-dot = Reference transport, Dotted = Ekman).

southward reaching a minimum of -.8 PW at 60°S. The thermal wind component is generally northward except between 53°S and 61°S. The maximum northward transport is slightly greater than 2 PW at 40°S and the minimum northward transport is -.5 PW at 55°S. South of 61°S the thermal wind component is negligible.

Interestingly the reference heat transport is almost balancing the thermal wind component. Between 34°S and 51°S the reference heat transport is strongly negative, reaching a maximum southward transport of -2.1 PW at 37°S. The reference heat transport is then positive between 50°S and 59°S, opposite to the thermal wind component.

The top panel of figure 6.19 can be directly compared to the work by Hsiung [1985] who estimated ocean heat transport using bulk formulas (see figure 6.20). The comparison indicates that the estimated transports of the SOINV are possibly slightly overestimated, but of the right order of magnitude. However, the transports are in the opposite direction.

Turning to the meridional divergence of heat in the Southern Ocean (bottom panel of figure 6.19) represents the heat exchange at the surface of the Southern Ocean. Positive values represent heat lost from the ocean to the atmosphere. Again, the three components are also plotted. This shows maximum exchanges between the ocean and the atmosphere of $\pm 200$ W m$^{-2}$ with an average exchange of 8.5 W m$^{-2}$. The exchanges are larger north of 58°S with the reference transport component developing most of the variation. The Ekman and thermal wind components are relatively smooth, consistent with the zonal integral plots in the top panel of figure 6.19.

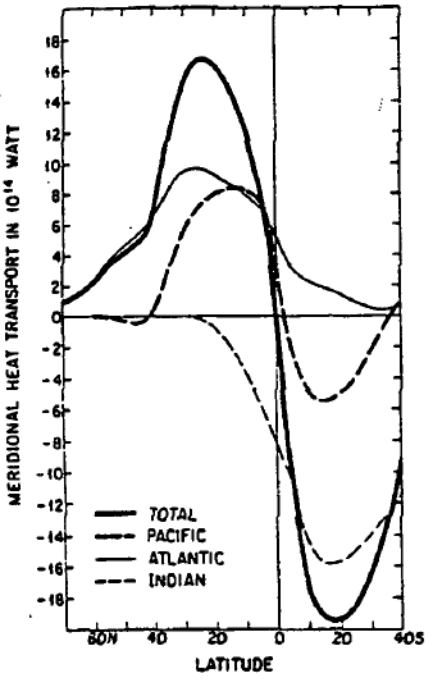


Figure 6.20: Meridional heat transport calculated by Hsiung [1985].

### 6.3.2 Freshwater

The transport of freshwater presented in figure 6.21 was estimated by first calculating the total freshwater transport on each layer using equation 6.2, and then integrating over depth. The freshwater transport field is much smoother than the heat transport field and reflects the mass conserving transport field presented in chapter 5 more closely. Near the Antarctic continent, over the Kerguelen Plateau and in the Great Australian Bight, there are several very large freshwater transports. These large transports are erroneous from the result of converting transports to velocities over shallow bathymetry.

The ACC is responsible for most of the freshwater transport around the Southern Ocean. North of the ACC, the freshwater transport is significantly weaker than the transport of the ACC. The Agulhas Current has a weak southward transport which joins the ACC south of South Africa. West of 70°E there is a northward flow associated with the Subtropical Gyre which is

balanced by a southward flow east of 70°E.

In the Pacific there is a weak southward transport of freshwater entering the Tasman Sea from the north. This southward transport turns east and flows north of New Zealand and north out of the model domain. There is a northward transport away from the ACC into the Tasman Sea from the south that joins the southward transport of freshwater discussed above, or recirculates south of New Zealand to flow over the Campbell Plateau. The transports reported over the Campbell Plateau are relatively large and could be a result of converting transports to velocities over shallow bathymetry. However, the transports presented in this region in the previous chapter were small and the coherence of the transports suggest that they are realistic. The subtropical Gyre transports freshwater south, west of 220°E and north east of 220°E bounded by the Pacific Antarctic Ridge. The Chile-Peru Current is also transporting freshwater north.

Turning to the Atlantic, the ACC is again the dominant transport feature. Away from the ACC the transport of freshwater is significantly smaller. The lack of data on the continental shelf of South America is a result of generating unrealistic transports by converting transports to velocities over shallow bathymetry. It is possible to gain some idea of the transport associated with the Brazil and Malvinas currents with the transport of freshwater depicted in the first and second deep water grid points. The strong southward transport of freshwater north of 40°S is associated with the Brazil Current, which turns east at 40°S to flow across the Argentine Basin before joining the ACC.

The divergence of freshwater is shown in figure 6.22. Again, the problem of converting transports to velocities has required the removal of many shallow water results. In the deep ocean the divergence field does not show any large areas that are uniformly gaining or losing freshwater suggesting that the net freshwater budget of the Southern Ocean is poorly resolved. This is somewhat

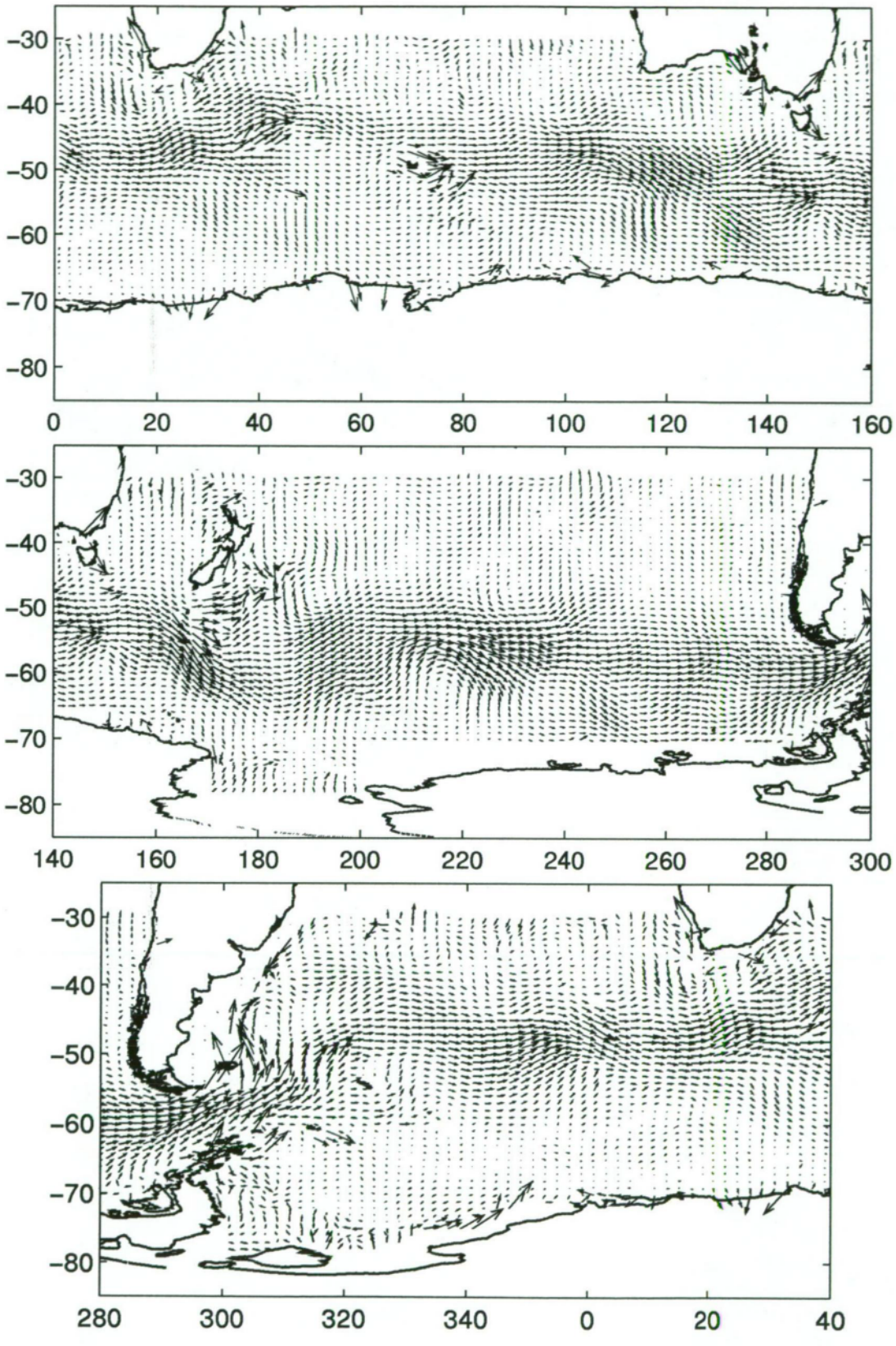


Figure 6.21: Depth-integrated transport circulation of freshwater around the Southern Ocean shown at 1°lat. × 2°long. (1°= $2\times10^5$ Kg m$^3$ s$^{-1}$).

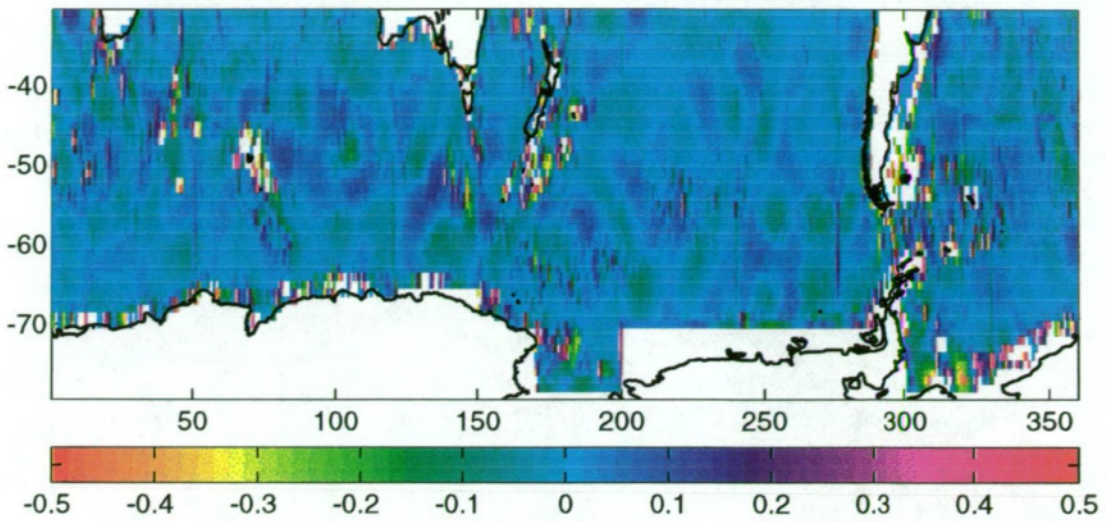


Figure 6.22: Divergence of freshwater ($10^3$ Kg m$^{-}$2 s$^{-1}$) in the Southern Ocean from the transport field shown in figure 6.21.

confirmed by inspection of the zonally integrated meridional transport and surface freshwater flux, figure 6.23. The meridional transport ranges over $\pm 4 \times 10^9$ Kg s$^{-1}$, mainly a result of the variation of the reference freshwater transport generated by the SOINV. The influence the reference transport is having on the freshwater circulation is confirmed when inspecting the Surface flux of freshwater. The range of surface freshwater flux is -15 to 24 m/yr with an average of 47 cm/yr mostly generated by reference surface exchange. The Ekman and thermal wind exchanges are rarely larger than 4 m/yr. This suggests that the SOINV results are making large changes to the freshwater transport, which may not be realistic.

## 6.4 Discussion of Heat and Freshwater Transports

As highlighted in the above discussions, there are some inconsistencies between the heat and freshwater transport generated by the SOINV and the observed transports of heat and freshwater. The estimates of heat and freshwater transport generated by the SOINV are compared to observed estimates in table

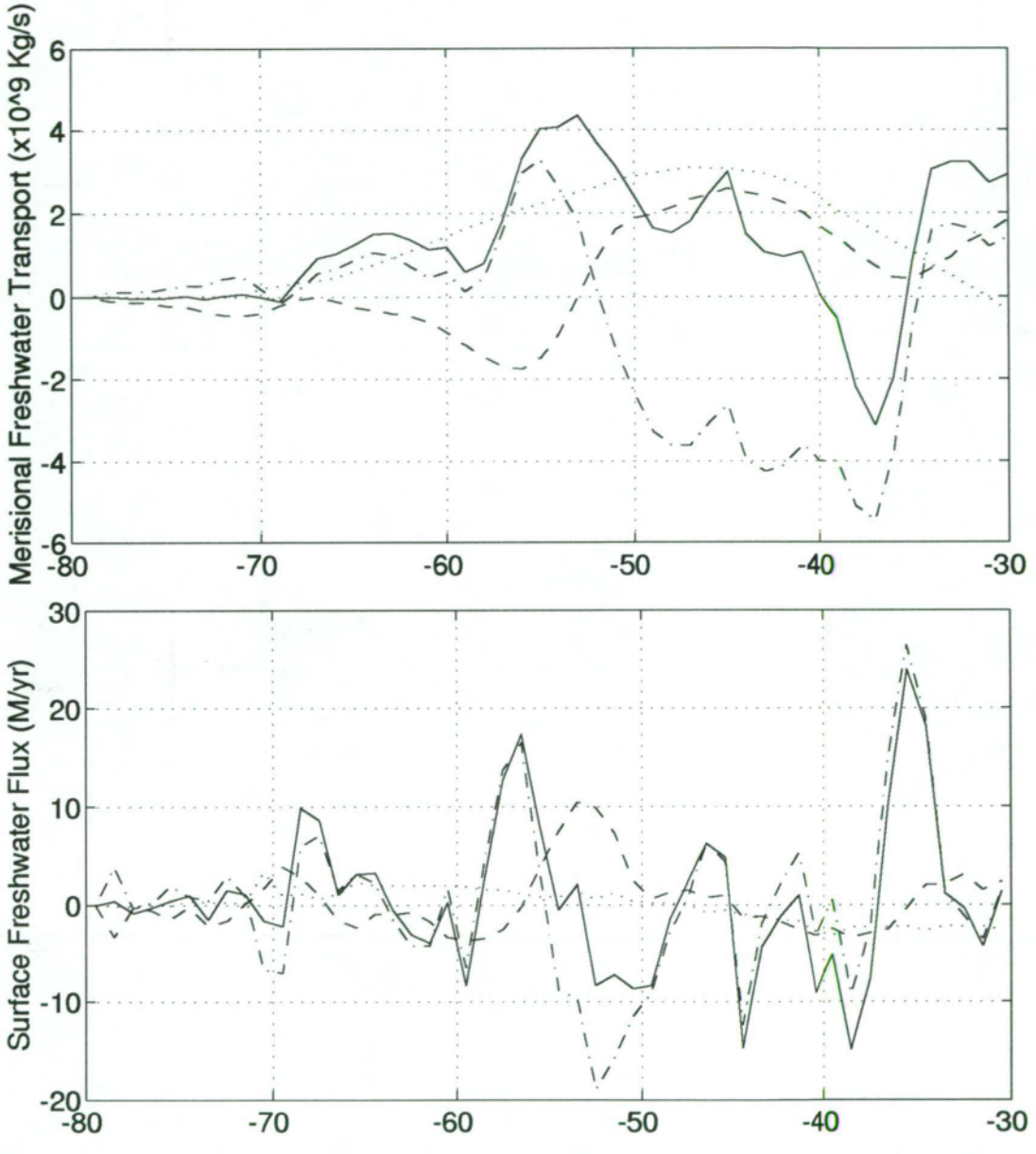


Figure 6.23: Zonally integrated meridional freshwater transport (top, $10^9$ Kg $s^{-1}$) and zonally surface freshwater flux converted to annual rainfall (metres/year). (Solid line = Total, Dashed = Thermal Wind, Dash-dot = Reference transport, Dotted = Ekman).

| Location | Heat PW | Range of Estimates PW | Freshwater $10^8$ Kg $s^{-1}$ | Estimates $10^8$ Kg $s^{-1}$ |
|---|---|---|---|---|
| Indian | -.52 | -.6 [Toole and Raymer 1985] to -.25 [Fu 1986] | -2.5 | 6.5 [Wijffels et al. 1992] |
| Pacific | 1.2 | .15 to -2.2 [Macdonald 1993] | -.42 | 3.5 [Wijffels et al. 1992] |
| Atlantic | .37 | .04 to .83 [Macdonald 1993] | 1.7 | -2 [Wijffels et al. 1992] |

Table 6.1: Implied heat and freshwater transports from the model circulation across 35°S compared to observed estimates. Positive = north.

6.1. As can be seen the main discrepancy is the heat transport associated with the Pacific Ocean, and the direction of freshwater transport.

When combined with the Indian and Atlantic Oceans, the Pacific Ocean generates a net northward transport of approximately 1 PW. This northward transport is inconsistent with the requirement that the oceans must transport heat away from the equator in order to maintain global climate [Toole and Raymer 1985]. The question must be asked as to why is the heat transport in the Pacific acting in the wrong direction.

An indication of the reason can be highlighted by inspecting the integrated heat transport across 35°S. Figure 6.24 shows the zonally-integrated, top-to-bottom heat transport across 35°S. Observations by Evans et al. [1983], Toole and Raymer [1985] and Ridgway and Godfrey [1994] have shown that the western boundary currents of the three ocean basins transport warm water southward. A southward transport of warm water would lead to a southward transport of heat in the boundary currents of figure 6.24. On the east coast of Africa, at 30°E, there is a strong negative movement of heat, suggesting that the Agulhas Boundary Current is transporting heat southward. On the East coast of South America, at 310°E, there is a strong negative transport of heat associated with the Brazil Current. On the East coast of Australia, at 160°E,

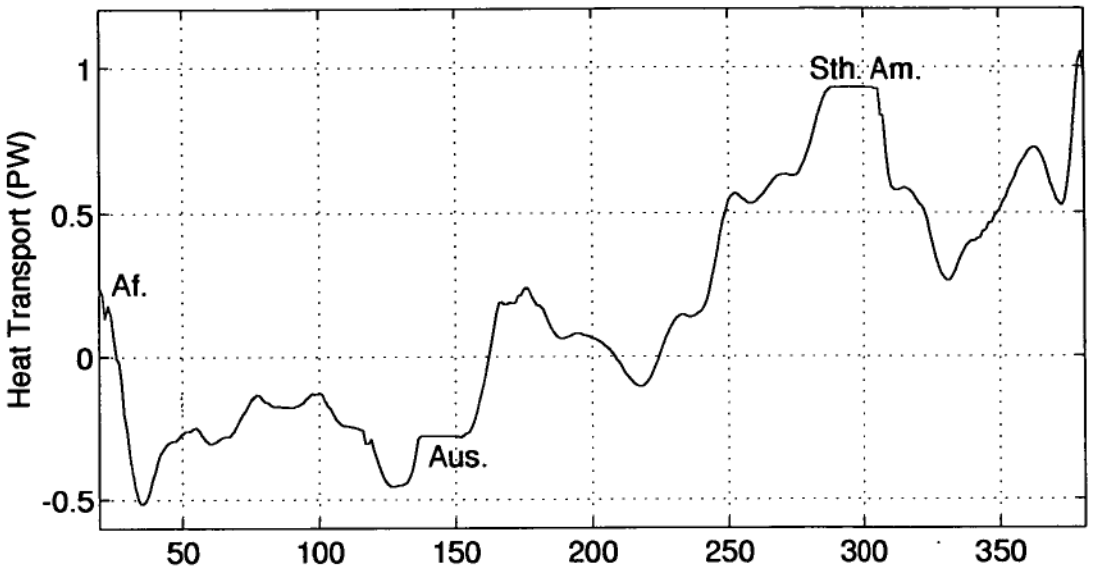


Figure 6.24: Integrated heat transport (PW) across 35°S.

there is an absence of negative heat transport associated with the EAC.

The absence of the southward EAC heat transport is a contributing factor to the northward heat flux. However, to generate a net southward Pacific Ocean heat transport, the EAC heat transport would have to be very large. So there are other contributing factors. Another possible factor is the weak southward transport of heat between 180°E and 215°E, associated with the gyre circulation. The reasons for the weak southward transport of heat in the western Pacific are unclear even when inspecting the two dimensional flow field of heat shown in figure 6.17. However, when comparing the two dimensional flow fields of both heat and freshwater to the mass circulation field in chapter 5, there is an interesting feature that may reveal some of the physics that is missing from the inverse model.

When comparing the heat circulation field (figure 6.17) to the mass circulation field (figure 5.1), the heat circulation can be roughly divided into two. To the north of the ACC, and including some of the ACC itself, the heat transport field looks very much like the mass circulation field, and appears to

conserve heat. The Agulhas Circulation in particular is very similar. In contrast, to the south of the ACC, the heat circulation appears to be completely independent of the mass circulation.

The freshwater circulation can be divided in roughly the same manner as the heat circulation, except in the opposite way. To the south of the ACC, the freshwater transport is very similar to the mass circulation and appears to conserve freshwater. To the north of the ACC, the freshwater transport bears little resemblance to the mass circulation, particularly the Agulhas Circulation. So it seems as though the heat and freshwater are changing from active to passive tracers of the mass circulation, as a function of latitude. This can possibly be traced back to the varying effect temperature and salinity have on the equation of state as temperatures decrease with increasing latitude, with the largest change occurring at the ACC. If this is the case, and the influence temperature and salinity are having on the mass circulation significantly changes in space, then it will be very difficult to accurately diagnose the heat and freshwater circulation throughout the model domain without introducing explicit constraints on the heat and freshwater circulation within the model.

This chapter has attempted to resolve the heat and freshwater transports associated with the mass circulation presented in chapter 5. It has been shown that the resulting transports of heat and freshwater are inconsistent with present knowledge of the circulation of heat and freshwater. These inconsistencies suggest that there are some components of the circulation presented in chapter 5 that are missing, or inadequately resolved. In this section, it was shown that it is necessary to introduce explicit constraints on heat and freshwater circulation in order to accurately look at the thermohaline circulation.

# Chapter 7

## Discussion and Conclusions

In this thesis, a single layer inverse model that conserves mass and vorticity on a 1°× 1° grid of the Southern Ocean has been developed. Using the circulation generated by this inverse model, several aspects of Southern Ocean circulation have been explored.

The SOINV utilises all suitable hydrographic data measured between 1904 and 1990. Optimal interpolation was used to interpolate the observations onto the final 1°× 1° grid carried out using long (25°E-W, 15°N-S) and short (7°E-W, 5°N-S) length scales. At these length scales, the interpolation process showed that there are still regions of the Southern Ocean (ie. South Pacific) that are data sparse and do not satisfactorily resolve ocean circulation. These length scales smooth the observations in boundary regions leading to an underestimate of most boundary currents in the model domain.

By utilising all the observational data, the circulation presented in this thesis represents a circulation that has been averaged over time. This is in contrast with the synoptic approach of previous inverse studies [Wunsch 1978; Rintoul 1988; Martel and Wunsch 1993; Wunsch 1994]. The time averaging approach eliminates some of the effects of natural variability of the Southern Ocean currents and develops a mean circulation that can be compared to synoptic observations.

Although interpolating all the suitable observational data onto the model's 1°× 1° grid involves a high degree of smoothing, it does reduce the degree that the inverse problem is underdetermined. By conserving mass and vorticity, and solving for both $u$ and $v$ components of reference transports on the 1°× 1° grid,

the problem is reduced to solving 28,480 unknowns from 26,945 equations. This means the SOINV is more well determined than typical inverse box models.

By interpolating the observations onto, and solving reference transports on the 1°× 1° grid, the SOINV achieves the highest horizontal spatial resolution of present inverse studies. Inverse box models, although having a higher resolution along the edge of each box (30 Nm, 55 km), do not have any data between sections with which to resolve transports. In contrast, beta-spiral inverse techniques, while having a similar resolution do not conserve mass over the model domain [Olbers et al. 1985].

In this study, there are no additional circulation constraints applied to the model. Previous inverse studies required transport or flux constraints to reduce the under-determinacy of the model to generate a realistic model circulation [Rintoul 1988]. Because the SOINV is closer to being evenly determined than previous studies, the mass circulation problem could be solved without using any such constraints. It can be argued that not constraining the solution, is not using all the available information that we know about the Southern Ocean circulation. This may be true, and constraints could be included in revised versions of the model. However, there are two important points that support the development of the unconstrained model. Firstly, this is the first inverse model developed to use all available data and it is important to clearly show how it performs. Secondly, constraining the solution assumes that the information used to constrain the solution, and hence our knowledge about the Southern Ocean circ ulation, is accurate.

In the absence of circulation constraints, the dominant signals of the inverse model were the mass conservation boundary conditions. These relatively simple boundary conditions rotated circulation that was normal to a land boundary, into parallel circulation. By solving all equations simultaneously, the

rotation of the flow at boundaries was carried out, so that the signal propagated through the inverse solution, generating the globally mass conserving circulation presented in this thesis. At open boundaries, the velocities were explicitly solved for.

In chapter 5, it was shown that qualitatively, the mass conserving circulation generated by the SOINV was internally consistent, with the model confirming and adding to the results of the many in-situ observational studies. Because the circulation is a time averaged circulation, in active areas of the Southern Ocean, there are several interesting features. For example, the stationary western eddy associated with the Agulhas Current, that is the sum of the many eddies that have been observed in this region that pinch off from the main Agulhas Current. The cyclonic eddy in the south west corner of the Argentine Basin is another example.

Quantitatively, the model has mixed success. It was shown that while the velocities were highly smoothed, a result of the optimal interpolation, and as small as 10% of observed velocities, the total net transports were comparable to observations. In the east-west direction, the SOINV estimate is approximately 30% smaller than the currently accepted values of eastward transport, but fall within the range of published estimates (see Table 7.1). In the north-south direction across 30°S, the estimates fall within the range of published estimates (see Table 7.1). These are pleasing results because, although the model grid spacing is high compared to previous inverse studies, the grid spacing is still relatively coarse and together with the degree of required smoothing tends to remove velocity extremes and reduce estimated mass transports.

The circulation field developed by the SOINV can be used in many ways not usually possible with observational data. The inverse circulation has been compared to EKE values derived from the Topex/POSEIDON altimeter. This

| Direction | Location | SOINV Estimate | Accepted Estimate | Range of Estimates |
|---|---|---|---|---|
| E-W | Drake Passage | 92 Sv | 130±13 Sv [Nowlin and Klinck 1986] | -15 Sv [Foster 1972] to 237 Sv [Reid and Nowlin 1971] |
| | 30°, South of Africa | 92.5 Sv | 130±13 Sv [Nowlin and Klinck 1986] | -15 Sv [Foster 1972] to 237 Sv [Reid and Nowlin 1971] |
| | 145°E, South of Tasmania | 104 Sv | 146 Sv pers. comm. Rintoul [1995] | |
| N-S at 30°S | Indian | -14.5 Sv | | -2 Sv to -20 Sv [Macdonald 1993] |
| | Pacific | 14.7 Sv | | 10 Sv to 15 Sv [Macdonald 1993] |
| | Atlantic | <-1 Sv | <-1 Sv [Coachman and Aagaard 1988] | |

Table 7.1: Model transports across key sections compared to observational estimates of transport. By the assumption that there is no net transport into the Atlantic, it is generally assumed that the transport south of Africa is equal to Drake Passage. Positive directions are east and north.

comparison reinforces our confidence in the SOINV circulation, and highlights several regions of the worlds oceans that are unstable with large EKE values, but more importantly, highlights regions of the world's oceans that appear to be very stable, even in areas of strong currents and varying topography.

At 1°× 1° grid scale, the SOINV can start to be compared to high resolution ocean circulation models. In this thesis, the SOINV results have been compared to the results of a circulation model based on Semtner and Chervin's [1988] model and reported by Smith et al. [1996]. The two models, while generally in close agreement, show some subtle differences that appear to arise from differences in the physics of the two models. This comparison suggests that while the high resolution numerical model is useful to show circulation features not usually observable with observational data, it is not clear that the numerical model circulation is statistically consistent with the observational data.

From the SOINV circulation, it is also possible to investigate the existence of the Deacon Cell. It was shown that while there was a Deacon Cell like circulation present, the size and shape was somewhat different to previous publications. The size of the SOINV circulation was much smaller than those presented by Doos and Webb [1993]. This is thought to be a combined result of the SOINV not explicitly solving for a vertical exchange, and the FRAM model having an excessive vertical exchange. The shape of the SOINV cells also suggests that there are inconsistencies between the FRAM circulation and the observational data.

Using the SOINV circulation to inspect surface velocities and dynamic height of the Southern Ocean shows that, compared to the smoothed circulation of Nowlin and Klinck [1986], the SOINV surface velocities are in close agreement with those presented by Nowlin and Klinck [1986].

From discussions in chapter 6, it is clear that the SOINV has not been

completely successful in diagnosing the heat and freshwater transport of the Southern Ocean. The main concern is the northward transport of heat associated with the Pacific Ocean. It is also clear that the global heat transport is northward and conflicts with the notion that the oceans must transport heat away from the equator in order to balance global heat [Toole and Raymer 1985]. From the discussion in section 6.4, it became clear that the inverse model presented in this thesis will need some additional constraints on the heat and freshwater circulation if the thermohaline circulation is to be investigated.

## 7.1 Model improvements and future work

From the discussions above, it has become clear that there is a need to improve the inverse model presented in this thesis to correct some inconsistencies that are currently present within the circulation.

The present model has been developed as a single layer inverse model, manipulating depth integrated transports. This configuration was primarily controlled by the limits imposed by local computer resources. By utilising the larger computer resources now becoming available, the inverse model could be divided into several layers, divided by either density or neutral surfaces or as Martel and Wunsch [1993] chose to do, on geographical co-ordinates. Switching to a multi layer model also allows for the model to explicitly include vertical exchanges of properties in a similar manner to previous inverse studies [Wunsch 1994].

From the discussion on mass transport, it appears that the smoothing of the hydrographic data removes a significant part of the signal, even though the $T'$ and $S'$ terms have been included. This is particularly evident in the eastward transport estimates, and suggests that some additional constraints on the circulation are required. These constraints could simply prescribe a transport

through a section, ie Drake Passage, or could take the form of including additional conservative properties. Given that the current dataset only includes temperature, salinity and oxygen, the type of properties to be conserved would include heat, freshwater and oxygen conservation equations using surface heat flux, rainfall data or oxygen flux data from atmospheric general circulation models or from compilations of surface flux data. As it was shown that the heat circulation is unsatisfactory in the present model, adding the constraint of heat conservation would be an important first step.

Throughout the presentation of mass circulation, it was clear that the transport associated with the major boundary currents was consistently underestimated, this is despite most observations in the Southern Ocean being located in these regions. It is also the case that the circulation through Drake Passage is underestimated even though there are many observations in the area. It would be interesting to investigate decreasing the grid spacing in these regions, say to $\frac{1}{2}^\circ \times \frac{1}{2}^\circ$, particularly through Drake Passage, up the east coast of South America, around the coast of South Africa and possibly near the coast of Australia, although the data density near Australia may be marginal. This decrease in grid spacing would also allow for a decrease in length scales associated with the optimal interpolation, making better use of the available data, and hopefully resolving the boundary currents more accurately than in the present model. Consideration would need to be given to how the decreased grid spacing would influence the propagation of the boundary mass conservation signal throughout the model domain.

The Southern Ocean is possibly the most poorly sampled ocean in the world. It would be exciting to utilise the observations in other basins to apply the model to a world inverse model, possibly with several layers.

# Appendix A

## Southern Ocean Topography

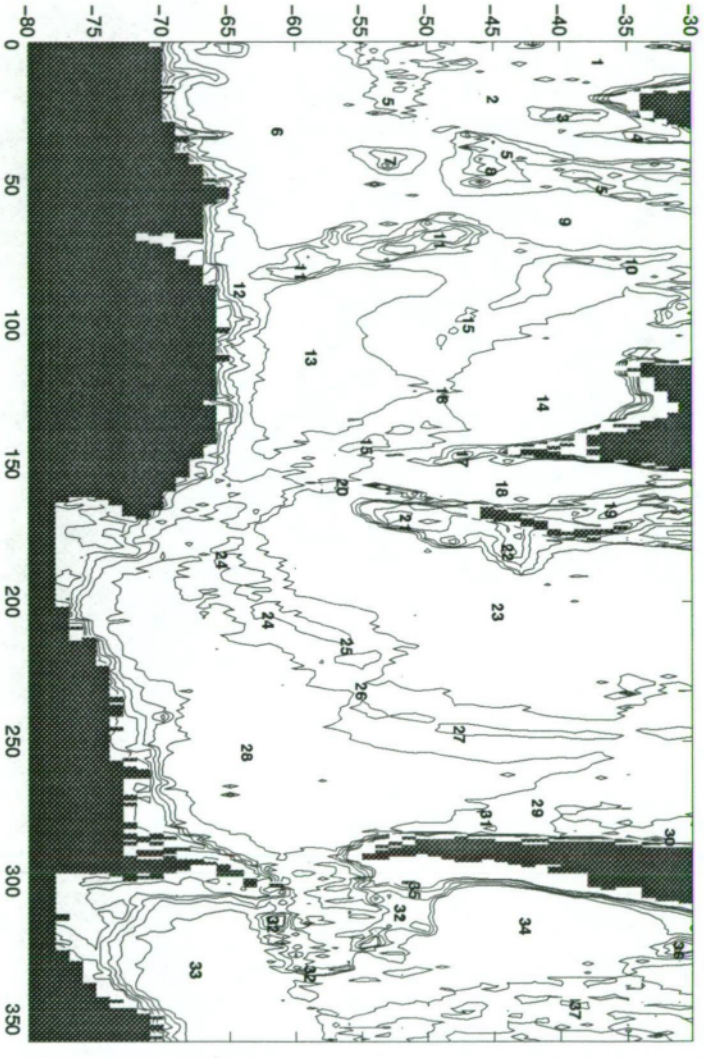


Figure A.1: Bathymetry of Southern Ocean with bathymetric features discussed in the text marked and named in Table A

| Topographic Features | | | |
|---|---|---|---|
| Numeric Order | | Alphabetic order | |
| 1 | Cape Basin | 2 | Agulhas Basin |
| 2 | Agulhas Basin | 3 | Agulhas Plateau |
| 3 | Agulhas Plateau | 34 | Argentine Basin |
| 4 | Mozambique Plateau | 13 | Australian-Antarctic Basin |
| 5 | South-West Indian Ridge | 16 | Australian-Antarctic Discordance |
| 6 | Atlantic-Indian Basin | 15 | Australian-Antarctic Ridge |
| 7 | Conrad Rise | 6 | Atlantic-Indian Basin |
| 8 | Crozet Plateau | 21 | Campbell Plateau |
| 9 | Crozet Basin | 1 | Cape Basin |
| 10 | South-East Indian Ridge | 29 | Challenger Fracture Zone |
| 11 | Kerguelen Plateau | 22 | Chatham Rise |
| 12 | Princess Elizabeth Trough | 30 | Chile Basin |
| 13 | Australian-Antarctic Basin | 31 | Chile Rise |
| 14 | South Australian Basin | 7 | Conrad Rise |
| 15 | Australian-Antarctic Ridge | 9 | Crozet Basin |
| 16 | Australian-Antarctic Discordance | 8 | Crozet Plateau |
| 17 | South Tasman Rise | 27 | East Pacific Rise |
| 18 | Tasman Basin | 26 | Eltanin Fracture Zone |
| 19 | Lord Howe Rise | 35 | Falkland Plateau |
| 20 | Macquarie Ridge | 11 | Kerguelen Plateau |
| 21 | Campbell Plateau | 19 | Lord Howe Rise |
| 22 | Chatham Rise | 20 | Macquarie Ridge |
| 23 | South-West Pacific Basin | 37 | Mid Atlantic Ridge |
| 24 | Pacific Antarctic Ridge | 4 | Mozambique Plateau |
| 25 | Udintsev Fracture Zone | 24 | Pacific Antarctic Ridge |
| 26 | Eltanin Fracture Zone | 12 | Princess Elizabeth Trough |
| 27 | East Pacific Rise | 36 | Rio Grande Plateau |
| 28 | South-East Pacific Basin | 32 | Scotia Ridge |
| 29 | Challenger Fracture Zone | 14 | South Australian Basin |
| 30 | Chile Basin | 10 | South-East Indian Ridge |
| 31 | Chile Rise | 28 | South-East Pacific Basin |
| 32 | Scotia Ridge | 5 | South-West Indian Ridge |
| 33 | Weddell Abyssal Plain | 23 | South-West Pacific Basin |
| 34 | Argentine Basin | 17 | South Tasman Rise |
| 35 | Falkland Plateau | 18 | Tasman Basin |
| 36 | Rio Grande Plateau | 25 | Udintsev Fracture Zone |
| 37 | Mid Atlantic Ridge | 33 | Weddell Abyssal Plain |

Table A.1: Topographic features discussed in text as located on figure A.1

# Bibliography

Bennett, A. F., 1978: Poleward Heat Fluxes in Southern Hemisphere Oceans., *J. Phys. Ocean.*, **8**, 785 – 798.

Bianchi, A. A., C. F. Giulivi and A. R. Piola, 1993: Mixing in the Brazil-Malvinus Confluence., *Deep-Sea Res.*, **40**(7), 1345 – 1358.

Bigg, G. R., 1985: The Beta Spiral Method., *Deep-Sea Res.*, **32**(4), 465 – 585.

Bindoff, N. L., and T. J. McDougall, 1994: Diagnosing Climate Change and Ocean Ventilation Using Hydrographic Data., *J. Phys. Ocean.*, **24**(6), 1137 – 1152.

Bingham, F. M., and L. D. Tally, 1991: Estimates of Kuroshio transport using an inverse technique., *Deep-Sea Res.*, **38**(suppl. 1), S21 – S43.

Boland, F. M., and J. A. Church, 1981: The East Australian Current 1978, *Deep-Sea Res.*, **28A**(9), 937 – 957.

——, and B. V. Hamon, 1970: The East Australian Current, 1965 - 1968., *Deep-Sea Res.*, **17**, 777,794.

Braccio, P., 1995: Parrallel Ocean Program Simulation Web Page., http://dubhe.cc.nps.navy.mil/ braccio/. [Accessed Aug. 1995].

Bretherton, F. P., R. E. Davis and C. B. Fandry, 1976: A technique for objective analysis and design of oceanographic experiments applied to MODE-73, *Deep-Sea Res.*, **23**, 559–582.

Bryan, K., 1969: A numerical model for the study of the world ocean., *J. Comput. Phys.*, **4**, 347 – 376.

Bryden, H. L., 1979: Poleward heat flux and conversion of available potential energy in Drake Passage., *J Mar. Res.*, **37**(1), 1 – 22.

——, and R. A. Heath, 1985: Energetic Eddies at the Northern Edge of the Antarctic Circumpolar Current in the Southwest Pacific., *Prog. Oceanogr.*, **14**, 65 – 87.

Bryden, H. L., and R. D. Pillsbury, 1977: Variability of Deep Flow in the Drake Passage from Year-Long Current Measurements., *J. Phys. Ocean.*, **7**, 803 – 810.

——, D. H. Roemmich and J. A. Church, 1991: Ocean heat transport across 24°N in the Pacific, *Deep-Sea Research*, **38**(3), 297 – 324.

Callahan, J. E., 1971: Velocity Structure and Flux of the Antarctic Circumpolar Current South of Australia., *J. Geophys. Res*, **76**(24), 5859 – 5864.

Carmack, E. C., 1990: Large scale physical oceanography of Polar Oceans, in *Polar Oceanography, Part A: A Physical Science*, edited by W. O. Smith, Jr., Academic Press Inc., San Diego, California.

——, and T. D. Foster, 1975: On the flow of water out of the Weddell Sea., *Deep-Sea Res.*, **22**, 711 – 724.

Cheney, R. E., J. G. Marsh and B. D. Beckley, 1983: Global Mesoscale Variablility from collinear tracks of SEASAT Altimeter Data., *J. Geophys. Res*, **88**(C7), 4343 – 4354.

Church, J. A., G. R. Cresswell and J. S. GodfreyThe Leeuwin Current, Internal paper reviewed by J Reid,.

Coachman, L. K., and K. Aagaard, 1988: Transports through Bering Strait: Annual and interannual variability., *J. Geophys. Res*, **93**, 15,535 – 15,539.

Coleman, R., 1984: Investigations of the Tasman Sea by Satellite Altimetry., *Aust. J. Mar. Freshw. Res.*, **35**, 619 – 633.

Colton, M. T., and R. P. Chase, 1983: Interaction of the Antarctic Circumpolar Current with bottom topography: An investigation using satellite Altimetry., *J. Geophys. Res*, **88**(C3), 1825 – 1843.

Cox, M. D., 1984: A primative equation three-dimensional model of the world ocean., *Tech. Rep. 1*, , Geophys. Fluid Lab. NOAA., Princeton Univ., Princeton, N. J.

Cresswell, G. R., 1991: The Leeuwin Current - observations and recent models., *J. Royl. Soc. W. A.*, **74**, 1 – 14.

——, and R. Legeckis, 1986: Eddies off southeastern Australia., *Deep-Sea Res.*, **33**(11/12), 1527 – 1562.

de Szoeke, R. A., and M. D. Levine, 1981: The Advective flux of heat by mean geostrophic motions in the Southern Ocean., *Deep-Sea Res.*, **28A**(10), 1057 – 1085.

deSzoeke, R. A., 1987: On the Wind-Driven Circulation of the South Pacific Ocean., *J. Phys. Ocean.*, **17**, 613 – 630.

Doos, K., and D. J. Webb, 1993: The Deacon Cell and the Other Meridional Cells of the Southern Ocean., *J. Phys. Ocean.*, **24**, 429 – 442.

England, M. H., J. S. Godfrey, A. C. Hirst and M. Tomczak, 1993: The Mechanism for Antactic Intermediate Water renewal in a world Ocean Model, *J. Phys. Ocean.*, **23**, 1553 – 1560.

Evans, D. L., S. R. Signorini and L. B. Miranda, 1983: A Note on the Transport of the Brazil Current., *J. Phys. Ocean.*, **13**, 1732 – 1738.

Fahrbach, E., G. Rohardt, M. Schroder and V. Strass, 1996: Transport and Structure of the Weddell Gyre., In press, Ann. Geophys.

Fiadeiro, M. E., and G. Veronis, 1982: On the determination of absolute velocities in the ocean., *J. Mar. Res*, **40(sup)**, 159 – 182.

Fine, R. A., 1985: Direct evidence using tritium data for throughflow from the Pacific into the Indian Ocean., *Nature*, **315**(6), 478 – 480.

——, 1994: Circulation of Antarctic Intermediate water in the south Indian Ocean., *Deep-Sea Res.*, **40**, 159 – 182.

Fine, R. A., M. J. Warner and R. F. Weiss, 1988: Water mass modification at the Agulhas Retroflextion: Chloroflouromethane studies., *Deep-Sea Res.*, **35**, 311 – 332.

Foster, L. A., 1972: Current Measurements in Drake Passage, M.s., Dalhousie University, Halifax, N.S. Canada.

Foster, T. D., and E. C. Carmack, 1976: Frontal zone mixing and Antarctic Bottom water formation in the southern Weddell Sea., *Deep-Sea Res.*, **23**, 301 – 317.

Fu, L., 1981: The general circulation and meridional heat transport of the subtropical South Atlantic determined by inverse methods., *J. Phys. Ocean.*, **11**, 1171 – 1193.

Fu, L.-L., 1986: Mass, Heat and Freshwater Fluxes in the South indian Ocean., *J. Phys. Ocean.*, **16**(10), 1683 – 1693.

Gandin, L. S., 1963: *Objective Analysis of Meterological fields*, p. 287, Gidrometizdat, Leningrad, (In Russian), English translation No. 1373 by Israel Program for Scientific Translations, (1965), Jerusalem, 242pp.

Garzoli, S. L., 1993: Geostrophic velocity and transport variability in the Brazil-Malvinas Confluence., *Deep-Sea Res.*, **40**(7), 1379 – 1403.

Georgi, D. T., 1981: Circulation of bottom waters in the southwestern South Atlantic., *Deep-Sea Res.*, **28A**(9), 959 – 979.

——, and J. M. Toole, 1982: The Antarctic Circumpolar Current and the oceanic heat and freshwater budgets., *J. Mar. Res*, **40(sup)**, 183 – 197.

Gill, A. E., 1973: Circulation and Bottom water production in the Weddell Sea, *Deep-Sea Res.*, **20**, 111 – 140.

——, 1982: *Atmosphere-Ocean Dynamics*, vol. 30 of *International Geophysics series*, p. 662, Academic Press, California.

Godfrey, J. S., and T. J. Golding, 1981: The Sverdrup relation in the Indian Ocean, and the effect of Pacific-Indian through flow on Indian Ocean circulation and on the East Australian Current., *J. Phys. Ocean.*, **11**, 771 – 779.

——, and K. R. Ridgeway, 1984: Title Unknown., *Trop. Ocean.-Atmos.*, **26**, 16–17.

Godfrey, J. S., and K. R. Ridgway, 1985: The large-scale environment of the Poleward-flowing Leeuwin Current, Western Australia: Longshore Steric Height Gradients, wind Stresses and Geostrophic Flow., *J. Phys. Ocean.*, pp. 481 – 495.

Gordon, A., and P. Tchernia, 1972: Waters of the continental margin off Adelie coast, Antarctica., *Antarctic Oceanology II: The Australian -New Zealand Sector. Antarctic Research Series.*, **19**, 59 – 69.

Gordon, A. L., 1985: Indian-Atlantic Transfer of Thermocline Water at the Agulhas Retroflection., *Science*, **227**, 1030 – 1033.

——, and C. L. Greengrove, 1986: Geostrphic circulation of the Brazil-Falkland confluence., *Deep-Sea Res.*, **33**(5), 573 – 585.

Gordon, A. L., E. J. Molinelli and T. N. Baker, 1982: *Southern Ocean Atlas*, p. lots, Amerind Publishing Co., New Delhi.

——, R. F. Weiss, W. M. Smethie Jr and M. J. Warner, 1992: Thermocline and Intermediate Water communication betyween the South Atlantic and Indian Oceans., *J. Geophys. Res*, **97**(C5), 7223 – 7240.

Grundlingh, M. L., 1980: On the volume transport of the Agulhas Current., *Deep-Sea Res.*, **27A**, 557 – 563.

Hamon, B. V., 1970: Western Boundary Currents in the South Pacific., in *Scientific Explorations of the South Pacific*, edited by W. S. Wooster, pp. 50 – 59, National Acadamy of Sciences., Washington, D.C.

Hastenrath, S., 1982: On Meridional Heat Trasnports in the World Ocean., *J. Phys. Ocean.*, **12**, 922 – 927.

Heath, R. A., 1981: Oceanic fronts around southern New Zealand, *Deep-Sea Res.*, **28A**, 547–560.

Hellerman, and Rosenstein, 1983: Normal monthly wind stress over the world ocean with error estimates, *J. Phys. Ocean.*, **13**, 1093 – 1104.

Hogg, N. G., 1987: A least-squares fit of the advective-diffusive equations to Levitus Atlas data., *J. Mar. Res*, **45**(2), 347 – 375.

Hsiung, J., 1985: Estimates of Global Oceanic Meridional Heat Transport., *J. Phys. Ocean.*, pp. 1405 – 1413.

Lawson, C. L., and R. J. Hanson, 1974: *Solving Least Squares Problems*, p. 340, Prentice-Hall series in Automatic Computation, Prentice-Hall Inc., Englewood Cliffs N. J.

Levitus, S., 1982: Climatological Atlas of the World Ocean., *Tech. Rep. 13*, , NOAA prof. paper.

Macdonald, A. M., 1993: Property fluxes at 30°S and their Implications for the Pacific-Indian throughflow and the Global Heat Budget., *J. Geophys. Res*, **98**(C4), 6851 – 6868.

Manabe, S., K. Bryan and M. J. Spelman, 1990: Transient response of a global ocean-atmosphere model to a doubling of atmospheric carbon dioxide., *J. Phys. Ocean.*, **20**(6), 722 – 749.

Mantyla, A. W., and J. L. Reid, 1983: Abyssal characteristicsof the World Ocean Waters., *Deep-Sea Res.*, **30**, 805 – 833.

Marshall, D., 1995: Topographic Steering of the Antarctic Circumpolar Current, *J. Phys. Ocean.*, **25**, 1636 – 1650.

Martel, F., and C. Wunsch, 1993: The North Atlantic Circulation in the Early 1980's - An Estimate from Inversion of a Finite Difference Model., *J. Phys. Ocean.*, **23**, 898 – 924, Department of Earth, Atmospheric and Planetary Sciences, MIT.

McCartney, M., and J. Zemba, 1988: Thermocline, intermediate and deep circulation in the southwestern South Atlantic., in *SAARI Meeting Report,*, pp. 28–29, Lamont-Doherty Geological Observatory of Columbia University, Palisades, New York.

McCartney, M. S., 1977: Subantarctic Mode Water., in *A Voyage of Discovery.*, edited by M. Angel, pp. 103 – 119, Pergamon Press., Oxford.

McDougall, T. J., 1987: Thermobaricty, Cabbeling, and Water-Mass Conversion., *J. Geophys. Res*, **92**(C5), 5448 – 5464.

McIntosh, P. C., 1990: Oceanographic Data Interpolation: Objective Analysis and Splines., *J. Geophys. Res*, **95**(C8), 13,529 – 13,541.

Mellor, G. L., C. R. Mechoso and E. Keto, 1982: A diagnostic calculation of the general circulation of the Atlantic Ocean., *Deep-Sea Res.*, **29**(10A), 1171 – 1192.

Menke, W., 1984: *Geophysical data analysis: discrete inverse theory*, p. 260, Academic Press, Orlando.

Mestas-Nunez, A. M., D. B. Chelton, M. H. Freilich and J. G. Richman, 1994: An evaluation of ECMWF-Based climatological wind stress fields, *J. Phys. Ocean.*, **24**, 1532 – 1549.

Meyers, G., R. J. Bailey and A. P. Worby, 1995: Geostrophic transport of Indonesian throughflow., *Deep-Sea Res.*, In Press.

Morrow, R., R. Coleman, J. Church and D. Chelton, 1994: Surface Eddy Momentum Flux and Velocity Variances in the Southern Ocean from Geosat Altimetry., *J. Phys. Ocean.*, **24**(10), 2050 – 2071.

Morrow, R. A., 1992: Surface eddy variability and eddy momentum flux in the Southern Ocean from GEOSAT altimetry., Ph.D. thesis, Marine Studies Centre, University of Sydney.

Mulhearn, P. J., 1987: The Tasman Front: A Study using Satellite Infrared Imagery., *J. Phys. Ocean.*, **17**, 1148 – 1155.

Murray, S. P., and D. Arief, 1988: Throughflow into the Indian Ocean through the Lombok Strait, January 1985 - January 1986., *Nature*, **333**(2), 444 – 447.

Nof, D., 1995: Choked Flows from the Pacific to the Indian Ocean, *J. Phys. Ocean.*, **25**, 1369 – 1383.

Nowlin, W. D., and J. M. Klinck, 1986: The physics of the Antarctic Circumpolar Current, *Rev. of Geophys.*, **24**(3), 469 – 491.

Office., U. H., 1958, 1959: *Oceanographic Atlas of the Polar Seas. Parts I and II*, Washington, DC., h.o. pub. no. 705 edition.

Olbers, D., 1989: Diffusion Parameterizations for the climatological circulation of the North Atlantic and the Southern Ocean, in *Parameterization of Small-Scale Processes*, edited by P. Muller, and D. Henderson, 'Aha Huliko'a Proceedings, pp. 181 – 204, Monoa, University of Hawaii.

——, G. Gouretski, J. Seiss and J. Schroter, 1992: Hydrographic Atlas of the Southern Ocean, *Tech. rep.*, , Alfred Wegener Institute, Bremerhaven, FRG.

Olbers, D. J., M. Wenzel and J. Willebrand, 1985: The inference of North Atlantic circulation patterns from climatological data., *Rev. Geophys.*, **23**, 313 – 356.

Orsi, A. H., W. D. Nowlin Jr and T. Whitworth III, 1993: On the circulation and stratification of the Weddell Gyre, *Deep-Sea Res.*, **40**(1), 169 – 203.

Park, Y.-H., L. Gamberoni and E. Charriaud, 1993: Frontal structure, Water Masses, and Circulation in the Crozet Basin., *J. Geophys. Res*, **98**(C7), 12,361 – 12,385.

Peterson, R. G., 1990: On the volume trasnport in the southwestern South Atlantic Ocean., *EOS*, **71**(17), 542.

——, and L. Stramma, 1991: Upper-level circulation in the South Atlantic Ocean, *Prog. Oceanog.*, **26**, 1 – 73.

Pickard, G. L., and W. J. Emery, 1990: *Descriptive Physical Oceanography*, p. pp320, Pergamon Press, Potts Point, Australia, 5 edition.

Piola, A. R., and D. T. Georgi, 1982: Circumpolar properties of Antarctic Intermediate Water and Subtropical Mode Water., *Deep-Sea Res.*, **29**, 687 – 711.

——, and A. L. Gordon, 1984: Pacific and Indian Ocean upper-layer salinity budget., *J. Phys. Ocean.*, **14**, 747 – 753.

Pond, S., and G. L. Pickard, 1983: *Introductory Dynamical Oceanography*, p. 329, Pergamon Press, New York.

Read, J. F., and R. T. Pollard, 1993: Structure and Transport of the Antarctic Circumpolar Current and Agulhus Return Current at 40°E, *J. Geophys. Res*, **98**(C7), 12,281–12,295.

Reid, J. L., 1973: Transpacific hydrographic sections at lats. 43°S and 28°S: the SCORPIO Expedition -III Upper ter and a note on southward flow at mid-depth., *Deep-Sea Res.*, **20**, 39 – 49.

——, 1986: On the Total Geostrophic Circulation of the South Pacific Ocean: Flow Patterns, Tracers and Transports., *Prog. Oceanog.*, **16**, 1 – 61.

Reid, J. L., and W. D. Nowlin, 1971: Transport of water through the Drake Passage., *Deep-Sea Res.*, **18**, 51 – 64.

Rhines, P. B., 1983: *Lectures in geophysical fluid dynamics*, vol. 20 of *Lectures in Applied Math.*, pp. 3 – 58, Am. Math. Soc.

——, and W. R. Young, 1982: Homogenization of potential vorticity in planetary gyres., *J. Fluid. Mech.*, **122**, 347 – 367.

Ridgway, K. R., and J. S. Godfrey, 1994: Mass and heat budgets in the East Australian current: A direct approach, *J. Geophys. Res*, **99**(C2), 3231 – 3248.

Rintoul, S. R., 1988: Mass, Heat and Nutrient Fluxes in the Atlantic Ocean determined by Inverse Methods, Ph.D. thesis, Woods Hole Oceanographic Institution, Massachusetts Institute of Technology.

——, and C. Wunsch, 1991: Mass, heat, oxygen and nutrient fluxes and budgets in the North Atlantic Ocean., *Deep-Sea Res.*, **38**(Suppl. 1), S355 – S377.

Roemmich, D., 1983: Optimal Estimation of Hydrographic Station Data and Derived Fields., *J. Phys. Ocean.*, **13**, 1544 – 1549.

——, and B. Cornuelle, 1990: Observing the Fluctuations of gyre-Scale Ocean Circulation: A Study of the Subtropical South Pacific., *J. Phys. Ocean.*, **20**(12), 1919 – 1934.

Roemmich, D., and ——, 1992: The Subtropical Mode Waters of the South Pacific Ocean., *J. Phys. Ocean.*, **22**, 1178 – 1187.

——, and T. McCallister, 1989: Large Scale circulation of the North Pacific Ocean., *Prog. Oceanog.*, **22**, 171 – 204.

Roether, W., R. Schlitzer, A. Putzka, P. Beining, K. Bulsiewicz, G. Rohardt and F. Delahoyde, 1993: A Chlorofluoromethane and Hydrographic Section across Drake Passage: Deep water ventilation and Meridional Property Transport., *J. Geophys. Res*, **98**(C8), 14,423 - 14,435.

Savchenko, V. G., W. J. Emery and O. A. Vladimirov, 1978: A cyclonic Eddy in the Antarctic Circumpolar Current South of Australia: Results of Soviet-American Observations aboard the R/V Professor Zubov., *J. Phys. Ocean.*, **8**, 825 - 837.

Schmitz, W. J., 1995: On the interbasin-scale thermohaline circulation, *Rev. of Geophys.*, **33**(2), 151 - 173.

Schott, F., and H. Stommel, 1978: Beta spirals and absolute velocities in different oceans, *Deep-Sea Res.*, **25**, 961–1010.

Semtner, A. J. J., and R. M. Chervin, 1988: A simulation of the global ocean circulation with resolved eddies., *J. Geophys. Res*, **93**, 15,502 - 15,522.

Semtner, B., 1995: Modeling Ocean Circulation., *Science.*

Shum, C. K., R. A. Werner, D. T. Sandwell, B. H. Zhang, R. S. Nerem and B. D. Tapley, 1990: Variations of Global Mesoscale Eddy Energy Observed from GEOSAT., *J. Geophys. Res*, **95**(C10), 17,865 - 17,876.

Sievers, H. A., and J. W. D. Nowlin, 1984: The Stratification and Water Masses at Drake Passage., *J. Geophys. Res*, **89**(C6), 10,489 - 10,514.

Silva, N. S., and S. Neshyba, 1979: On the southernmost extension of the Peru-Chile Undercurrent., *Deep-Sea Res.*, **26A**, 1387 - 1393.

Sloan, S. W., 1986: A Fast algorithm for constructing Delaunay Triangulations in the plane, *Tech. rep.*, , Deptartment of Civil Engineering and Surveying, The University of Newcastle.

Smith, R. D., R. C. Malone, M. Maltrud and A. J. Semtner, 1996: Global eddy-resolving (1/6 x 1/4) ocean simulations driven by 1985 - 1994 atmospheric fields., In preperation.

Smith, R. L., A. Huyer, J. S. Godfrey and J. A. Church, 1991: The Leeuwin Current off Western Australia, 1986-1987, *J. Phys. Ocean.*, **21**, 323 – 345.

Stevens, D. P., and P. D. Killworth, 1992: The Distrobution of Kinetic energy in the Southern Ocean: a comparison between observations and an eddy resolving general circulation model., in *Antarctic and Environmental Change.*, vol. 388, edited by D. J. Drewty, R. M. Laws, and J. A. Pyle, pp. 251 – 257, Royal Society of London., Great Britain.

Stramma, L., Y. Ikeda and R. G. Peterson, 1990: Geostrophic transport in the Brazil Current region north of 20°S., *Deep-Sea Res.*

——, and R. G. Peterson, 1989: Geostrophic transport in the Benguela Current region., *J. Phys. Ocean.*, **19**, 1440 – 1448.

Stramma, L., —— and M. Tomczak, 1995: The South Pacific Current., *J. Phys. Ocean.*, **25**, 77 – 91.

Tchernia, P., 1980: *Descriptive regional oceanography*, p. 253, Pergamon Press, Oxford, England.

Thompson, R., and G. Veronis, 1980: Tranport calculations in the Tasman and Coral seas., *Deep-Sea Research*, **27A**, 303 – 323.

Toole, J. M., 1981: Sea Ice, Winter Convection, and ther temperature Minimum Layer in the Southern Ocean., *J. Geophys. Res*, **86**(C9), 8037 – 8047.

——, and M. E. Raymer, 1985: Heat and freshwater budgets of the Indain Ocean - revisited, *Deep-Sea Res.*, **12**(8), 917 – 928.

Toole, J. M., and B. A. Warren, 1993: A Hydrographic section across the subtropical South Indian Ocean, *Deep-Sea Res.*, **40**, 1973 – 2019.

——, S. E. Wijffels, M. S. McCartney, B. A. Warren, H. L. Bryden and J. A. Church, 1995: WOCE Hydrographic Section P6 across the subtropical South Pacific Ocean., Conference Presentation.

Trenberth, K. E., J. G. Olson and W. G. Large, 1989: A global Ocean wind stress climatology based on ECMWF Analysis, *Tech. rep.*, , Climate and global dynamics division, National Center for Atmospheris Research, Boulder, Colorado.

van Ballegooyen, R. C., M. L. Grundlingh and J. R. E. Lutjeharms, 1994: Eddy fluxes of heat and salt from the southwest Indian Ocean into the southeast Atlantic Ocean: A case study., *J. Geophys. Res*, **9**(C7), 14,053 – 14,070.

Vassie, J. M., A. J. Harrison, P. L. Woodworth, S. A. Harangozo, M. J. Smithson and S. R. Thompson, 1994: On the temperal variability of the transport between Amsterdam and Kerguelen islands., *J. Geophys. Res*, **99**(C1), 937 – 949.

Warren, B. A., 1973: Transpacific hydrographic sections at lats. 43°S and 28°S: the SCORPIO Expedition -II Deep water., *Deep-Sea Res.*, **20**, 9 – 38.

——, and K. G. Speer, 1991: Deep circulation in the eastern South Atlantic Ocean., *Deep-Sea Res.*, **38 Sup**, S281 – S322.

Whitworth, T., 1980: Zonation and geostrophic flow of the Antarctic Circumpolar Current at Drake Passage., *Deep-Sea Research*, **27A**, 497 – 507.

——, and W. D. Nowlin, 1987: Water Masses and Currents of the Southern Ocean at the Greenwich Meridian., *J. Geophys. Res*, **92**(C6), 6462 – 6476.

Wijffels, S. E., R. W. Schmitt, H. L. Bryden and A. Stigebrandt, 1992: Transport of freshwater by the Oceans, *J. Phys. Ocean.*, pp. 155 – 162.

Wilkin, J. L., and R. A. Morrow, 1994: Eddy kenetic Energy and momentum flux in the Southern Ocean: Comparison of a global eddy-resolving model with altimeter, drifter, and current-meter data., *J. Geophys. Res*, **99**(C4), 7903 – 7916.

Wolff, J.-O., and D. J. Olbers, 1989: The dynamical balance of the Antarctic Circumpolar current studied with an eddy resolving quasigeostrophic model., in *Mesoscale/synoptic coherent structures in geophysical turbulence.*, edited by N. J, pp. 435 – 458, Elsevier Science Pub.

Wooster, W. S., and M. Gilmartin, 1961: The Peru-Chile Undercurrent., *J. Mar. Res.*, **19**, 97 – 122.

——, and J. L. Reid Jr, 1963: Eastern Boundary Currents., in *The Sea.*, vol. Volume 2, edited by M. N. Hill, pp. 253 – 280, InterScience, London.

Wunsch, C., 1978: The North Atlantic General Circulation West of 50 ° W, Determined by Inverse Methods, *Reviews of Geophysics and Space Physics*, **16**(4), 583–620.

——, 1984: An eclectic Atlantic Ocean circulation model, I, The meridional flux of heat., *J. Phys. Ocean.*, **14**, 1712 – 1232.

Wunsch, C., 1994: Dynamically consistant hydrography and absolute velocity in the eastern North Atlantic Ocean, *J. Geophys. Res*, **99**(C7), 14071–14090.

——, and B. Grant, 1982: Towards the general circulation of the North Atlantic Ocean., *Prog. Oceanog.*, **11**, 1 – 59.

Wunsch, C., D. Hu and B. Grant, 1983: Mass, Heat, Salt and Hutrient Fluxes in the South Pacific Ocean., *J. Phys. Ocean.*, **13**, 725 – 753.

——, and J.-F. Minster, 1982: Methods for Box Models and Ocean Circulation Tracers: Mathematical Programming and Nonlinear Inverse Theory., *J. Geophys. Res*, **87**(C8), 5647 – 5662.

Wyrtki, K., 1961: Physical Oceanography of the Southeast Asian Waters., *Tech. Rep. 2*, , NAGA, Inst. of Ocean., Wash.

Zemba, J. C., and M. S. McCartney, 1988: Transport of the Brazil Current: It's bigger than we thought., *EOS*, **69**(44), 1237.

Zhang, H.-M., 1995: Application of an inverse model in the community modeling effort results., Thesis, Massachusetts Institute of Technology and the Woods Hole Oceanographic Institute.